MODELING ENERGY SUPPLY UNIT OF ULTRA-LOW POWER DEVICES WITH INDOOR PHOTOVOLTAIC HARVESTING

To attain the academic title of: *Dr.-Ing.*

Accepted dissertation from
Faculty of Mechanical Engineering,
TU Dortmund University

By: **Mojtaba Masoudinejad**
From: Dezfool, Iran

Oral examination: 3 July 2020

Supervisors:
1. Prof. Michael ten Hompel (TU Dortmund University)
2. Prof. Luca Benini (ETH Zurich)

Dortmund, 2020

dedicated to great men:
***Mostafa, Azim and Qasem** . . .*

تقدیم به مردان بزرگ:
مصطفی، عظیم و قاسم ...

Acknowledgements

I wish to express my deepest appreciations to Professor Luca Benini who provided me with guidance during the course of this research. In addition, I am grateful for all help from Dr. Michele Magno who advised me with his deep insight within the field of low power embedded systems. I also have to thank Professor Michael ten Hompel who gave me the chance to pursue this research within his chair.

Financial support by means of research assistant has been provided partially from German Research Council (DFG) within Collaborative Research Center (SFB876) *Providing Information by Resource-Constrained Data Analysis*, project A4 and partially by the Federal Ministry of Education and Research of Germany as part of the *competence center for machine learning ML2R* (01|S18038A) through chair of Materials Handling and Warehousing (FLW) of TU Dortmund University.

I am indebted to all my fellow researchers in FLW from TU Dortmund University and IIS from ETH Zurich who have supported me scientifically and motivated me for the best practice research.

Finally, without the complete understanding and support of my family, specially my dearest wife, Fatemeh, this work would have been much difficult or perhaps impossible to finish.

Mojtaba Masoudinejad
July 2020, Dortmund

Abstract

Challenges in the field of logistics have pushed development and integration of cyber-physical systems in these applications. PhyNode as one of these systems has shown promising results for enabling a transportation box with intelligence. However, engineering shortcomings during its development and implementation have shown potential for further research topics. Among them, balancing the Energy Supply Unit (ESU) to avoid periodic battery recharge is the main motivation of this work addressed by its modeling.

For a systematic analysis of PhyNode's ESU, two types of models are developed for each of its three modules, including: Indoor photovoltaic harvesting (IPV), power management device and the battery. First type of models are computationally lightweight for on-board monitoring implementation. In contrary, system level detailed models are more advanced and computationally intensive. They are used to properly dimension the hardware or optimize the operational process during system design phase.

At first IPV devices are analyzed extensively to highlight their differences from solar applications. In addition to the development of a high precision measurement platform for measurement of IPV behavior, collected data is used for model development. Due to wide range of signals, a normalized space is introduced in addition to guidelines for model's parameters estimation. Moreover, a new evaluation criteria is suggested enabling comparison of model's performance in different environmental situations.

A battery measurement setup is introduced for analyzing battery with ultra-low power loads. In addition to the comparison of different battery identification methods, effect of aging on the battery performance has been analyzed. By measurement of PhyNode's load, both developed models are evaluated showing error less than 0.5 % on estimation of the models' output.

Furthermore, internal structure of power management device designed for ultra-low power applications is analyzed. Converter and maximum power point tracking as two main parts of this system are modeled separately. Despite suggestion of a partial model based on physical principles of converter, lack of design information leads to a black-box modeling approach. Therefore, two machine learning based models are developed for these parts. Combined model of them is tested on an evaluation data-set, showing a performance with a RMSE of 1.2 %.

Finally, a holistic model including all modules builds the overall structure of PhyNode's ESU. This model is tested with real data from different hardware combinations of PhyNode in action for long time periods showing a MAPE less than 1 %. Due to the high accuracy of developed model, it is used for simulation of PhyNode in a real world scenarios. In addition, potentials of holistic model are shown by simulating energy balancing after different changes in either hardware or operational process of PhyNode.

Contents

List of Figures

List of Tables

List of Abbreviations

ADC	Analog-Digital Converter
AE	Algebraic Equation
AES	Algebraic Equation Set
ANN	Artificial Neural Network
BJT	Bipolar Junction Transistor
BMO	Burst Mode Operation
BMS	Battery Management System
CCM	Contineous Conduction Mode
CFT	Constant off Time
CMPT	Current-Mode Pulse Train
CNT	Constant on Time
CPPS	Cyber-Physical Production System
CPS	Cyber Physical System
DAE	Differential-Algebraic Equation
DC	Direct Current
DCM	Discontineous Conduction Mode
DE	Differential Equation
DoD	Depth of Discharge
ECM	Equivalent Circuit Model
EH	Energy Harvesting
EPH	Endocochlear Potential Harvesting
ESS	Energy Storage System
ESS-TF	Elliot Symmetric Sigmoid transfer function
ESU	Energy Supply Unit
FF	Fill Factor

FOCV Fractional Open Circuit Voltage

HTS-TF Hyperbolic Tangent Sigmoid transfer function

I2C Inter-Integrated Circuit
IC Integrated Circuit
IGBT Insulated Gate Bipolar Tansistor
IoT Internet of Things
IPV Indoor Photovoltaic
IR Infra-Red

KiBaM Kinetic Battery Model

LDO Low Dropout
LED Light Emitting Diode
LMM Levenberg-Marquardt Method
LS-TF Logarithmic sigmoid transfer function
LSq Least Square Method
LTI Linear Time-Invariant
LuT Look-up Table

MAE Mean Absolute Error
MANE Mean Absolute Normalized Error
MAPE Mean Absolute Percentage Error
ML Machin Learning
MLE Maximum Likelihood Estimation
MNB Main Board
MOSFET Metal Oxide Semiconductor Field-Effect Transistor
MPP Maximum Power Point
MPPT Maximum Power Point Tracking
MPTC Multi-Pulse Train Control
MSE Mean Square Error

NRM Newton Raphson Method

OC Open-Circuit
OCV Open Circuit Voltage
ODE Ordinary Differential Equations
OV Over-Voltage

PCC Peak Current Control
PCD Periodic Charge Difference
PCM Pulse Current Modulation
PDE Partial Differential Equations
PFM Pulse Frequency Modulation

PL-TF	Pure Line transfer function
PMIC	Power Management IC
PNGV	Partnership for a New Generation of Vehicles
PSM	Pulse Skipping Modulation
PSO	Particle Swarm Optimization
PSS	Periodic Steady-State
PTC	Pulse Train Control
PV	Photovoltaic
PVNS	Photovoltaic Normalized Space
PWM	Pulse Width Modulation
RF	Radio Frequency
RFID	Radio Frequency Identification
RMS	Root Mean Square
RMSE	Root Mean Square Error
SC	Short-Circuit
SCPI	Standard Commands for Programmable Instruments
SMU	Source Measurement Unit
SoC	State of Charge
SoD	State of Discharge
SoH	State of Health
SPDT	Single Pole Double Throw
SPST	Single Pole Single Throw
SSB	Swappable Slave Board
SVM	Support Vector Machine
SwC	Switched Capacitor
SwI	Switched Inductor
TEG	Thermo-Electric Generator
TI	Texas Instruments
ULP	Ultra-Low Power
VMPT	Voltage-Mode Pulse Train
WSN	Wireless Sensor Networks

Nomenclature

δ	[-] Error
η	[%] Efficiency
κ	[-] Conversion ratio of converter
λ	[nm] Wavelength
$\mathcal{C}$	[A s] Capacity of the battery
$\mathcal{C}_n$	[A s] Nominal capacity of battery
$\mathcal{C}_r$	[A s] Remained capacity of battery
$\mathcal{D}$	[A s] Battery depth of discharge
$\mathcal{L}$	[s] Battery lifetime
$\mathcal{T}$	[s] Time duration of a complete switching period of converter
μ_h	[-] Number of high peaks in a complete cycle of multi pulse converter
μ_l	[-] Number of low peaks in a complete cycle of multi pulse converter
ρ	[-] Relative error
σ	[%] Standard deviation of the battery's state of charge
τ_h	[s] Time duration of a high peak pulse of a converter
τ_l	[s] Time duration of a low peak pulse of a converter
τ_{rc}	[s] Time constant of a RC pair
φ_1	[-] Charge phase of converter
φ_2	[-] Pump phase of converter
φ_3	[-] Idle phase of converter
ϑ	[%] Periodic charge difference
$\boldsymbol{\alpha}$	[-] Vector of tuning factor in a model
$\boldsymbol{\psi}$	[-] PV model vector of unknowns
ξ	[A m^2] Ratio of maximum power point current change due to the PV surface change
ζ_a	[-] Battery aging factor
ζ_c	[-] Battery current factor
a	[-] Ideality factor including the series cell effect
B	[J K^{-1}] Boltzmann's constant ($1.380\,650\,3 \times 10^{-23}$)
C	[F] Capacitor

D	[-] Duty ratio of converter
E	[lm m^{-2} or W m^{-2}] Light intensity
E_G	[eV] Band gap energy
E_λ	[eV] Photon's energy at wavelength λ
E_e	[W m^{-2}] Irradiance
E_v	[lm m^{-2}] Illuminance
I	[A] DC current
i	[A] Current
I_{80}	[A] Current value at the 80% of the V_{oc}
I_ϵ	[A] Infinitesimal current for battery
I_b	[A] Terminal current of battery
I_d	[A] Diode's current
I_g	[A] Photo-generated current of PV module
I_h	[A] PV harvested current
i_l	[A] Inductor current of converter
I_M	[A] Current at maximum power point of PV transducer
I_n	[A] Nominal battery current
I_{ph}	[A] Inductor's higher peak current level
I_{pl}	[A] Inductor's lower peak current level
I_{pn}	[A] Demanded current by PhyNode
I_p	[A] Inductor peak current of converter
I_{sc}	[A] Short circuit current
I_s	[A] Diode saturation current
k	[-] Counter index of discrete systems
K_v	[V] Fractional voltage factor value of maximum power point tracking
L	[H] Inductance
n	[-] Diode's ideality factor
N_p	[-] Number of parallel cells in PV module
N_s	[-] Number of series cells in PV module
N_h	[-] Number of neurons in a hidden layer of an artificial neural network
P_h	[W] PV generated power
P_M	[W] PV generated power at maximum power point
Q	[A s] Total capacity of battery
q	[C] Electric charge (1.602×10^{-19})
q_c	[C] Capacitor electric charge
Q_n	[A s] Normalized total capacity of battery
R_0	[Ω] Series internal resistance of battery
R_{sh}	[Ω] Shunt resistance of PV model
R_s	[Ω] Series resistance of PV model
s	[*] General representation of a signal
S_{pv}	[m^2] Surface of PV module
T	[K] Temperature
t_d	[s] Depletion time of battery

T_s	[s] Sampling time
V	[V] DC voltage
v	[V] Voltage
v_b	[V] Terminal voltage of battery
V_e	[V] Electromotive force of battery
V_h	[V] PV harvested Voltage
v_l	[V] Inductor voltage of converter
V_M	[V] Voltage at maximum power point of PV transducer
V_{oc}	[V] Open circuit voltage
V_{ref}	[V] Reference voltage of converter
v_{str}	[V] Storage voltage of BQ device
V_T	[V] Thermal voltage of PV transducer
y	[%] Battery state of discharge
z	[%] Battery state of charge

Chapter 1
Introduction

Don't listen to the person who has the answers;
listen to the person who has the questions.

—Albert Einstein

Abstract
This chapter as the opening of this work provides an abstract overview of the logistics and challenges this sector of industry is facing. Modularization and decentralization by use of cyber-physical systems as a sub-section of Industry 4.0 and IoT are commonly accepted as solutions to tackle these challenges which are briefly reviewed here.

PhyNode as a successful experiment for integration of cyber-physical systems into the unit transportation box used in the field of materials handling and warehousing is analyzed including its hardware specification and modular design. PhyNetLab as a test platform for the evaluation of futuristic warehouses including a network of more than 200 PhyNodes is introduced as well.

Analysis of PhyNode's energy with focus on the energy supply unit is explained as the main goal of this work and tasks are defined toward this aim. Borders of this work are clarified afterwards and the overall outline of this work is justified.

1.1 Logistics and Industry 4.0

Logistics in its general substance can be considered as all sets of services covering the planning, organization, management, control and execution of flowing goods and information [1]. It includes multiple tasks, from purchasing, production, warehousing and freight transport to added value services, distribution and reverse logistics in the whole supply chain [2, 3]. Based on this definition, logistics is a vital section of industry. The estimated potential market volume of the logistics sector of the European Union member states in 2018 was about 1120 billion Euro [4] while transport and warehousing are representing the majority of the added values [3]. According to investigations [3], the European logistics sector is dealing with three clear problem areas as:

- continuous rise in costs
- external (non-logistics) effects such as energy and emission
- quality and quantity of the relevant staff.

Moreover, there are some not critical issues pushing this sector to continuously improve. According to [5] some of these aspect are:

- transparency and integrity control along the whole supply chain
- real time detailed shipment tracking
- integrity control for sensitive goods
- assets control and monitoring for analysis and optimization.

Industry 4.0 which is sometimes redundantly called industrial Internet of Things (IoT) [6] is seen as an umbrella concept helping to address most of these concerns. The term Industry 4.0 refers to a wide collective range of researches which precise distinction of each is not possible [7]. However, it roots into the field of IoT [6], first mentioned in 1999 by Kevin Ashton within the supply chain management context [8]. The early versions of this concept were using Radio Frequency Identification (RFID) in the form of sensor networks [9]. Nonetheless, this concept has expanded its territory into multiple other applications, from pure technical matters to even social issues [10].

Nowadays, IoT devices have a wide range from fitness tracker and health monitors to drones, smart grids and logistics [11]. Nevertheless, its definition has been summed up into “enabling the machine perception of the real world and seamless interaction with it” [10]. This perception can result from both physical or virtual *smart things* that have identities, attributes, services and interfaces which should seamlessly integrate together [12]. Understanding about the concept of being *smart* in the context of the Industry 4.0 and IoT can be explained in different ways. However, most of them are focusing on two main aspects including:

1. reliable functionalities embedded in a single system
2. ability to communicate

These two aspects are basically the definition of two other research trends, namely embedded device and Cyber Physical System (CPS). Embedded devices have been always held as highly reliable and predictable compared to the general-purpose computing systems [13]. While embedded devices focus more on the computing and process level, CPS has a strong perspective on the communication and interconnection in between. Unlike traditional embedded systems mostly designed for the stand-alone operation, CPS is focusing on the networking of multiple devices. Within the Industry 4.0 concept, this communication can be within different levels; from closed local Wireless Sensor Networks (WSN) to globally spread devices communicating over the internet. This possibility of data exchange is the key differentiation of devices in the Industry 4.0 era [14] from former systems.

In addition to the expansion of IoT into many facets of today's life, next generation of computing is going to be outside of the traditional systems realm with stationary computing devices [9]. Consequently, integrated embedded devices and CPS are getting developed and integrated in diverse fields of applications. During the last few years, number of these devices has been growing rapidly [15]. This is making an explosion of small computing platforms for commercial, consumer and industrial use cases [11].

In the Industry 4.0 vision, an efficient smart manufacturing system or production line is made of multiple modules made as CPSs. These modules communicate with each other as well as their environment. Moreover, they interact with products as well to influence the manufacturing configuration and can manipulate and control the production process [16]. This is mainly required to realize the individual production in the batch size of one while maintaining the economic feasibility of mass production [7]. It makes production and materials flow topologies more fluid that automatically reconfigure themselves instead of having a production process with fixed rules and structures [16], mainly designed by humans.

This concept exactly fits to the requirements of future logistics which sees system flexibility as an asset [17, 18]. Modularization as a priority for flexibility, requires to decompose logistics systems into basic functions and introduce proper module for each, while able to communicate with others. Therefore, using a CPS which is able to understand its condition and react based on that will tackle the flexibility issue [12]. Concurrently, this reduces the operating challenge in the highly dynamic Industry 4.0 environment [19]. Modularization of logistics tasks using CPS will also reduce the need for central systems and makes them much more dynamic [20]. This will reduce the need for human interaction required to continuously reconfigure systems based on new demands. In addition, for those cases where human operators are still essential, these solutions can improve the working quality and reduce the injury risks at the workplace. It also helps them to decide more efficiently and reduces the chance of failure [1].

1.2 CPS for materials handling

Flexibility and modularity of systems have always played a major role in the field of materials handling and warehousing [21]. As mentioned before, smart objects that are able to understand and react on their environment are a key solution to achieve this flexibility [12]. As a part of the overall IoT revolution during the last years in the field of materials handling, embedded devices and CPS are used to realize such smart entities [18].

For in-house applications, nun-bulky materials are mostly transported in a units which can be a carton, a bag or a container. Therefore, providing *smart* solutions for these modules is the first step toward the Industry 4.0 revolution. Traditionally, these units are only a carrier of the materials with related data stored in a central system, while all keypoints are printed on a paper sticked to the bin. With advancements in the field of hardware miniaturization, this paper-based information system can be replaced with an electronic board. This intelligent module stores all related data locally and makes them available at all time, traveling with the bins. In this sense, system will be modular and does not rely on a central data-bank. An abstract overview of some examples developed in this concept can be found in [1].

One of the first trials to embed electronics into a load carrier has been started in 2009. Autonomous load carrier embodied as *Intelligent Bin* (inBin) [21] was developed to fulfill the growing demand for smart carriers and containers [12]. Two subsequent versions of this smart object are shown in Fig. 1.1.

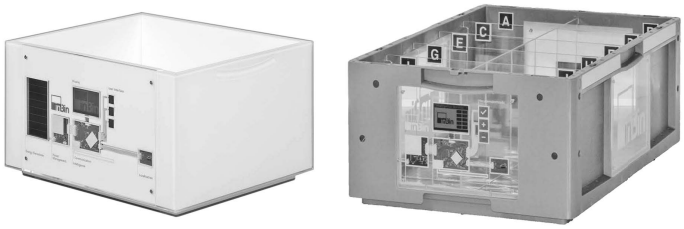

Fig. 1.1 Two generations of inBin over time. Left: 2009; Right: 2012.

It is a container with the ability of storing data about its contents' attributes, showing data on its display, in addition to interaction with an operator through an input panel. Although each inBin can be seen as a stand-alone device, its main use-case is in a group as one connected subsystem inside a materials handling system. Meanwhile, by storing the content data in the inBin, there would be no need for a central warehouse management system.

In spite of success of the inBin, it had the compatibility issue with the standard containers used commonly in industry. In addition, integration of hardware inside the container increased its initial cost, made its update roughly impossible and very hard to maintain. Therefore, instead of further iterations, a more modular concept named *PhyNode* has been introduced.

PhyNode

PhyNode is a CPS made specifically for research and development in logistics application. Its form-factor is to be simply mounted on a typical industrial container unit without requiring any extra mounting utility. In addition, its design is based on a modular principle enabling its update over the time. It also includes multiple redundancies for research purposes. Its modules can be fine-tuned or even removed based on the industrial application. A picture of the developed PhyNode is shown in Fig. 1.2.

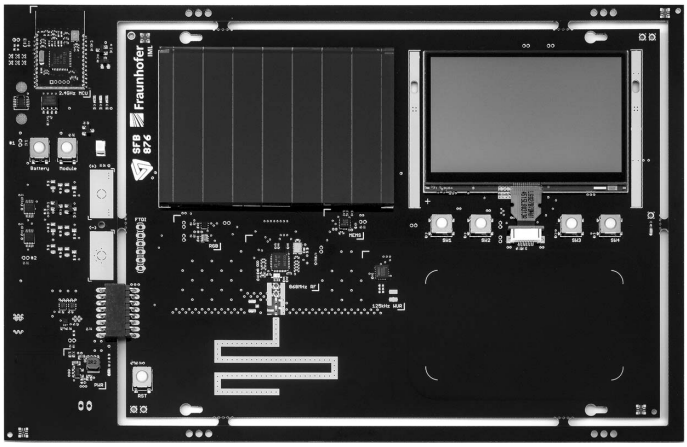

Fig. 1.2 Overview of PhyNode's front side.

The main research goal of PhyNode is the evaluation of different logistics CPS nodes in diverse structures and scenarios. In one hand, a large number of them are needed to replicate a real scale system; on the other hand, they have to be modifiable to represent different nodes and applications. Therefore, a design with two sections is considered. Each PhyNode is made of a Main Board (MNB) and a Swappable Slave Board (SSB). This separation can also be seen in Fig. 1.2 which shows physical detachment of inner part of the board from the section on the left. These two parts are attached through an optically separated 8 bit connection. MNB is considered as the basement of each PhyNode and will stay the same while design and structure of SSB advances over time. An abstract view of the PhyNode's MNB is presented in Fig. 1.3.

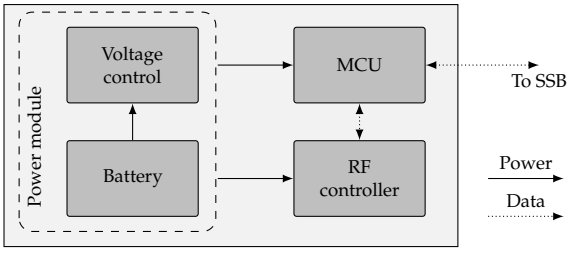

Fig. 1.3 Schematic structure of PhyNode's MNB.

MNB is a minimal system to assure communication and update of the SSB, regardless of its design. It is made of a Radio Frequency (RF) communication module at 2.4 GHz using Zigbee. This decision is mainly due to the low power demands of this system. It also has a low power 8051 micro-controller which enables communication with the SSB.

On the other hand is the SSB which can be modified to integrate different hardware designs. It can be simply modified to fulfill diverse requirements of different applications. Although five dissimilar configuration of SSB are developed, structure of the complete version including all parts is shown in Fig. 1.4.

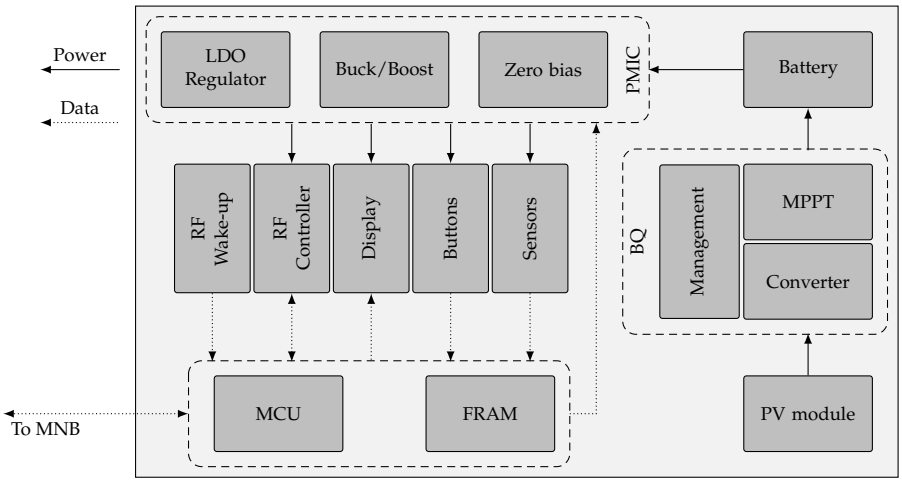

Fig. 1.4 Schematic structure of PhyNode's SSB.

All versions use a *MSP430FR5969* Ultra-Low Power (ULP) processor from Texas Instruments (TI) with 64 kB of FRAM. Also they all include a *CC1200* RF communication module from TI which is able to communicate at 868 MHz. In addition, they have a 125 kHz wake-up receiver which is able to react to a specified pattern. Using this wake-up system, a turned off PhyNode comes back alive only when its operation is necessary.

All PhyNodes are equipped with a power unit including a battery, a power management unit (BQ) and a Photovoltaic (PV) module for Energy Harvesting (EH). Push buttons enable possible interaction with an operator. In spite of these common items, the rest of components on PhyNodes may not be available on some versions. There are five on-board sensors including ambient sensor measuring RGB and Infra-Red (IR) in addition to the temperature. Also a 3-axis accelerometer provides acceleration information for detection of any possible movements. Some versions of PhyNode use a display as a visual interaction device for the user as well. A more detail explanation of PhyNode's hardware can be found in [22].

PhyNetLab

In logistics applications, different analysis have to be done before deployment of a new system. Though simulation and emulation tools provide understanding of a system, they do not mimic all complexities of a real working network. Some of these dynamics in addition to the logistics scenarios complexities are:

- radio interference
- resource limitations
- energy constraints [22].

These dynamics has to be analyzed before any large-scale deployment which can be in the size of some hundred or even thousands of entities.

PhyNetLab, is a research test-bed with more than 600 m^2 surface replicating a real world industrial materials handling and warehousing facility. In addition to its physical space, its hardware platform provides a variety of wireless communication possibilities with protocols on the sub 1 GHz band in addition to the 2.4 GHz band. It is developed to deploy a ULP WSN and test different decentralized in-house material flow scenarios. In addition, it enables evaluation of different logistics CPS modules in action. While evaluating logistics CPS modules, PhyNetLab provides an opportunity to test different technical aspects as well, such as radio configuration and routing algorithms. Moreover, different debatable topics such as security, privacy, business structure and integration to other available IT infrastructure can be analyzed in PhyNetLab under real-world condition. [23]

In PhyNetLab, different types of CPS nodes can operate hand in hand on the field level. That is one of the reasons for having different configurations of PhyNodes which enables replication of complex scenarios. All in all, more than 200 PhyNodes in five different configurations are operational in PhyNetLab for different types of tests and evaluations.

Due to the nature of materials handling process a transportation method is always required to move objects. Therefore, five mobile robots from *Robotnik* are included in PhyNetLab which are able to lift a rack up and displace it into a new position. These racks are designed in a way that a box equipped with PhyNode can be mounted on top. Not only these robots sense their environment with laser-scanners to avoid any safety concerns for humans, they can localize themselves using a camera-based indoor localization system. This system, commonly known as *motion-capturing* indoor localization is made of multiple cameras sensitive to the IR light. A ring of IR light sources around each camera emits light that can be reflected by specific spherical markers. Any object which has to be tracked inside PhyNetLab is marked with at least three of such markers. From reflections seen by cameras and using stored relative coordination of markers, position of objects can be found in software with sub-milimeter accuracy and a rate up to 200 Hz. Further information regarding PhyNetLab can be found in [23, 24].

1.3 Energy concerns of CPS

Regardless of specific definition and application field of CPSs, there are similarities in between them. In addition to the processing unit required for any CPS, some kind of communication interface is necessary as well. Moreover, as seen for the PhyNode, based on the field of application, it is very common that some kind of data collection or sensors be included as well. Nonetheless, all these parts require electrical energy which its scale will be dependent to the design specifications. An overview of some main device categories with their energy requirement is depicted in Fig. 1.5.

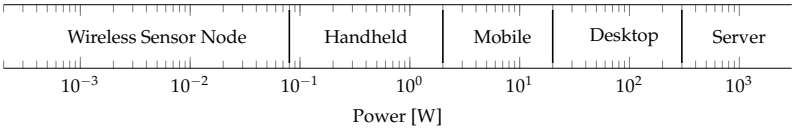

Fig. 1.5 Power consumption scale of different classes of devices. From [25].

In spite of differences in the size, specification and application domains, an Energy Supply Unit (ESU) is required to fulfill this energy demand. Although intensive actions such as computation or communication were traditionally very limited on non-stationary devices, advancements in the field of CPS design and embedded systems, has made the realization of smart objects running on low power possible [20]. This trend have been expanded by further introduction of ULP devices, bringing energy requirements to the edge.

Battery has been traditionally a reliable power source used for multiple non-stationary systems. However, there are challenges for the use of batteries as the sole power supply. At first, battery life is a systematic operational bottleneck, limiting an entities' life span. Although it is possible to use larger batteries, limitations on the size and weight of most entities make their implementation hard, if not impossible. Second, changing or recharging batteries increases the operational and maintenance cost of an entity [26] and can even disgrace the whole feasibility of a solution in some cases. For instance, changing battery of some thousands of PhyNodes in a warehouse is not acceptable. Moreover, these entities operate in dynamic environments with continuous changing condition [15] which may cause a device to be in an extreme remote location for a long period. This makes access to the device much harder and even impossible in some cases. Hence, maintenance and running cost of the system will be higher. Furthermore, this will reduce reliability of the system since lack of battery change or late access will cause system failure and/or data loss.

A method to tackle these issues is an EH system in combination to the battery. Regardless of harvesting type, the general concept of EH is considered a promising option to degrade battery replacement challenges [26]. Furthermore, a properly designed ESU can be energy-neutral in a way that the harvested power from the EH module fulfills all demands of the system. However,

reaching this point requires accurate design for matching energy harvest and demand. Moreover, to optimize the performance of the harvesting and the battery, some extra components are required to manage these two parts making ESU more complex. An abstract flow of energy in this structure is presented in Fig. 1.6. From a system design point of view, this unit has to be analyzed in detail to enable energy-neutral operation.

Fig. 1.6 Schematic flow of energy in the ESU with an EH module.

1.4 Motivation and goals

An energy-neutral CPS such as what is aimed for the PhyNode has to be accurately designed to balance the harvested and demanded operational energies. This balance has two sides which both can be dynamic. Harvested energy is dependent not only on the selected device, but also on the environmental condition. On the other hand, demand is dependent on the selected hardware and operational process. Hardware selection aspect is a procedure happening during the design of the CPS, mainly done by system engineers. In contrary, operational behavior are decided during a phase when the system is already built and operating. Understanding of this condition is mainly important for software designers trying to develop the operational algorithm of the system and process engineers interested on the performance.

As a general scientific approach, models are used to analyze systems without testing each real experiment on the hardware. Therefore, a model is required which explains the behavior of the ESU including its EH. However, it has to be noted that according to the required perspective, aim of the model will be different. Process engineers deal with a hardware structure. Hence, a model explaining behavior of the ESU will satisfy their needs. On the other hand, system designers are more interested in general modeling methods which can be applied on different hardware. In this way they can apply these methods as tools analyzing different combination of hardware and test their performance before finalizing a hardware design.

Within this work both perspectives will be addressed. However, PhyNode as the case-study is used for the development of both models and methods of modeling. It has to be noted that PhyNode is a fixed hardware combination already available and development of methods can be simply tested on that. Moreover, both EH and Energy Storage System (ESS) include a large set of different technologies with diverse properties. Therefore, this work will only concentrate on the used class of devices in PhyNode which are the PV EH and Lithium Polymer batteries for storage. Although PhyNode is the used

case-study here, its overall ESU structure shown in Fig. 1.6 is very common for such type of systems. Consequently, modeling methods have to be kept as general as possible to make them applicable to other systems.

A system designer requires a model which can be used to check if the ESU can balance the harvest and demand. According to inclusion of all parts, this type of model will be called *detailed model* in the rest of this work. Concurrently, this model has to be as modular as possible that in case of change in one component, the whole model structure remains and can be tuned using specification of new component with minimum effort. For instance, if the battery is changed into a larger battery, model of the rest of system has to remain intact. This forces a modular modeling strategy that provides models and methods for that class of components regardless of the rest.

Since battery is used in PhyNode, energy storage of the whole ESU can be monitored using terminal voltage of the battery. As long as this voltage is higher than the minimum allowed voltage, PhyNode will be operational. This is a critical fact for unbalanced environments which the harvested energy is not always constant. Therefore, at some time periods system will be discharged due to negative balance; while during positive energy balance times battery will be recharged. Consequently, as long as the minimum allowed voltage during the negative balance phase is not reached, system can be considered as energy-neutral. Hence, the output of the detailed model can be defined as the terminal voltage of the battery. According to this, overall goal of the detailed model will be:

Goal:

Developing a modular model to estimate terminal voltage of PhyNode's battery at each time, in different environmental and operation conditions.

According to the usage of this model by system engineers during the design phase, this model has to be highly accurate while it has no implementation limitation. In contrary to this model, are those models which are used during the operation of PhyNode. While these models are used inside PhyNode during operation, they will be called *on-board model* hereafter. These models must have a very limited memory footprint and computation resource requirements due to PhyNode's constraint. In addition, based on the memory and computational need, a process designer may be interested on the model of only some sub-parts of the ESU. Therefore, a modular concept has to be used here as well. According to the extreme resource restrictions of PhyNode, it is very common that only the battery status monitoring model be integrated. This model behaves similar to the battery percentage of a cell phone. However, to keep generality of the methodology, modular on-board models will to be developed for all compartments of PhyNode's ESU.

Focus of this work is mainly on the modeling of the ESU. However, there are multiple relative and interesting aspects which are not dealt with during this work. Some of these topics are:

- Process of hardware selection for the ESU
- Power demand analysis of PhyNode
- Task scheduling and energy optimization of PhyNode

1.5 Outline

According to the overall modular principle used for the modeling, the main goal can be divided into three sub-tasks as:

1. modeling the PV EH module
2. modeling the battery
3. modeling the management device in between

For each of these items both on-board and detailed model have to be addressed separately. In addition, a holistic model has to be suggested by combination of modular detailed models to assure system analysis as a whole during the design procedure.

To fulfill these tasks and build required models, the road-map of this work will be as following: at first in Chapter 2, some basics of the modeling including the definition of a model and its types are explained. Signals and systems and their representation as fundamentals of this work are addressed. Afterwards, some basic statistical terminology used in the rest of this work is mentioned. For a reader with knowledge about modeling in addition to the signal and systems, this chapter can be skipped.

Chapter 3 as the first modeling part focuses on PV EH systems. Some basics of PV harvesting are explained which are required for the development of a model. Common techniques available for modeling PV modules are reviewed. To evaluate these techniques (mainly developed for the outdoor applications) in the indoor environment, a measurement platform is explained and used for accurate data collection. These data is used not only to evaluate available knowledge, but also for advancement of this know-how to be fitted into the indoor condition. Both model types are generalized and applied on PhyNode's PV module. At the end, developed models are applied to a separate data-sets collected from PhyNode in PhyNetLab for the evaluation.

In Chapter 4 focus is on the modeling of the battery. At first, different technologies of ESS are shortly compared and selection of batteries is discussed. Basics of battery operation is explained afterwards. Next, state-of-the-art modeling of batteries and its common methods are surveyed. Later on, specifications of PhyNode's battery are provided and its model is developed using measured data. Then, two different perspectives on the model are mentioned which can be used for both target implementation of models.

Chapter 5 aims on the modeling of the management device in between the battery and the PV EH module. Available solutions and state-of-the-art modules for this purpose are reviewed. Internal structure of the used solution in PhyNode is explained. Afterwards, models for this system are developed and evaluated using collected data from the device.

Although model of each module is evaluated in its corresponding chapter, Chapter 6 focuses on merging the detailed models together to build a holistic model. Then this holistic model is evaluated using PhyNode within a new environment. After quantization of the holistic model's performance, it is used to evaluate different operational and hardware situations. Not only this shows how the holistic model can be used in reality, but also it presents flexibility of the modular concept.

Finally, models from this work are summed up in Chapter 7. All contributions are listed and some future possible topic are suggested for interested researchers.

This text is written in a coherent way that there is a central overall story-line around the PhyNode case-study. However, due to interdisciplinary nature of this work, each chapter can be read as a stand-alone work as well.

Chapter 2
Fundamentals of Modeling

We have no idea about the 'real' nature of things . . .
The function of modeling is to arrive at descriptions which are useful.

—Richard Bandler, John Grinder

Abstract
This chapter focuses on the information required for understanding the rest of this work. Basics of modeling including its terminology and methodology are reviewed in a very abstract form.

Signals and systems as key tools for model development are reviewed. Different properties of systems which are useful during the modeling procedure are defined. Possible representation and formulation of a system are explained. Then, common perspectives for building a model are described.

Finally, in the last part of this chapter, statistical terminologies used in the rest of work are mentioned.

2.1 What is a model?

Science has been always about studying properties of the reality by constructing models for it [27]. Consequently, modeling has become a central endeavor to most engineering and scientific disciplines [28]. However, understanding and analyzing the reality of physical world as a single whole is extremely hard and perhaps impossible. This had led to division of science into different fields according to the slice of the reality which is being analyzed or modeled. In spite of differences in scientific disciplines, there are basic methodologies about model building. Yet, before any discussion on techniques, a common understanding of a model is essential.

Due to the necessity of modeling for different disciplines, multiple definitions have been suggested. In most definitions of models such as those explained in [27–29], it is defined using some other terms such as system and experiment. To avoid complexities of defining these terms simultaneously, a general definition of model is proposed here as:

Definition: *Model*

A model is a *tool* for understanding and explaining the behavior of a *segment of reality* in a *specific situation*.

In this way, models are used in different aspect of daily life. For instance, when a person is defined as kind, it is a model of that person. Such a model predicts higher probability of a yes answer to a favor. This model provides knowledge about that person's behavior without really asking for the favor. It is an intuitive tool built upon impressions of that person from past experiences. However, changes in the situation may prove us wrong showing the limited validity of our model in some situations. Moreover, it is critical to note that this model is only valid for the purpose it is built upon. For instance, such a mental model gives no answer to the driving skills of that person.

It is important to recognize that a part of reality can be described in dissimilar ways or models according to the point of view and intention of the model developer [30]. For instance, an electrical engineer is interested in a model describing voltage-current behavior of an electric board while a control engineer describes it in dynamic form using its inputs-outputs. The same board would be modeled in a mechanical way for a car-producer interested in its operation in a harsh thermal or vibrating condition.

In spite of general explanation of a model including all possible aspects, it is founded on three key points:

- A model is a *tool* specifically developed for a particular goal.
- A model explains information about a *limited section* of reality.
- A model is only valid in a *limited situation*.

Based on these factors different types of models can be considered.

In a simple and general way, the main aim of modeling can be classified into two major groups [31]:

- To satisfy curiosity by understanding the nature of reality.
- To study and understand order of reality to build it or build upon it.

The first category is mostly used by experimental scientist while the later is used in engineering disciplines, such as what is aimed in this work. Moreover, three major types of models can be defined as *mental*, *verbal* and *mathematical* models [27]. The way a person rides a bike without falling is a mental model learned from experiments available in the biker's brain. A verbal model is mostly a sentence explaining an if-then clause, such as: if the heater is turned on, temperature goes up. It is important to differentiate these two types from each other. An example is that although a person may be able to ride a bike, it may not be possible to describe this model in words.

A mathematical model explains the relations between quantities or variables and how they affect each other in the form of mathematical formulation [27, 32]. For instance, Newton's second law is a model explaining the relation between an object's mass and acceleration due to the net applied forces. Most physical laws fit into this category of modeling which is the main focus for the rest of this work, but from an engineering point of view.

2.2 Signals and systems

Two physical phenomena have to be modeled in engineering fields; namely, physical *systems* and *signals* [29]. A system defines that portion of the real world which has to be modeled while signals are required to explain the situation which the system is operating in. These phenomenons are discussed here with more details as the basement of modeling.

Engineers define a situation in the physical realm by providing information about variables. From a mathematical perspective, this information (or a set of their combination) provides the definition of a signal as:

Definition: *Signal*

A signal is a representation of information. In the form of a function or a set of values [33].

A variable s can have a quantitative value representing a specification. However, in most engineering tasks a signal provides values of the parameter according to the time as the independent variable. In case this representation provides the value for all time instants, it is called a time continuous signal and will be shown using $s(t)$. In most modern applications with digital devices, storing a continuous signal is impractical and theoretically impossible.

Therefore, the value of a signal would be sampled in a periodic manner leading to a time discrete signal presented as $s[kT_s]$. Where T_s is the sampling period and k shows the index of sample. This can be simplified to $s[k]$ while the sampling time T_s is mostly kept constant. To be noted that in this text a set of multiple signals will be presented as a vector using a bold character as **s** with the vertical distribution as:

$$\mathbf{s}(t) = \left[s_1(t),\, s_2(t),\, \ldots,\, s_m(t)\right]^{\mathsf{T}} \tag{2.1}$$

Moreover, a signal can be single or multi dimensional, with both real or imaginary values. According to this representation of signal, **s** will be able to express possible condition of reality which is aimed to be modeled.

System has been defined in different terms according to the field of application. For instance, Bernard Zeigler explains it as: "...a potential source of data" [28]. Ross Ashby defines it as: "...not a thing, but a list of variables" [28]. However, Brian Gaines simple expression of a system makes more sense in this context. "The largest possible system of all is the universe. Whenever we decide to cut out a piece of the universe such that we can clearly say what is inside that piece (belongs to that piece), and what is outside that piece (does not belong to that piece), we define a new system" [28]. It has to be considered that in this definition, separation of a section of reality is not necessarily a cutting in the physical realm. It is only bordering a limited section for modeling abstraction. Therefore, for the modeling context in the mathematical form, a system is defined as:

Definition: *System*

A system is a limited section of the real world relating some signals with each other.

According to this definition, a system can be presented in different ways. A very common and simple method is to graphically represent a system in an abstract form of Fig. 2.1.

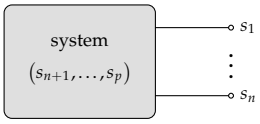

Fig. 2.1 General representation of a system including both external and internal signals.

In addition to the environmental signals, a system may have some internal parameters which effect its behavior as well. Considering these internal parameters, this graphical representation can be written in a general mathematical form as:

$$\mathbf{f}\left(s_1^{(m)}(t),\ldots,s_1^{(1)}(t),s_1(t),s_2^{(m)}(t),\ldots,s_2(t),s_p^{(m)}(t),\ldots,s_p(t),t\right)=0 \tag{2.2}$$

when $s^{(j)}$ is the jth order derivation of signal s according to the time. Moreover, it has to be noted that this presentation has a vector form as a set of functions collected in the **f**.

For the modeling, it is always easier to work with simplified principles. Therefore, signals are divided into different groups [27] according to their properties and relation to the system. Terminology used here is as:

Constant: a signal (quantity) which does not change.
System parameter: a constant given from the system.
Design parameter: a constant defined by designer to give the system a special property.
Variable: a normal signal which changes over time.
Output: a system variable the designer is interested in, shown by $y(t)$.
External signal: a signal affecting the system, not affected by other variables.
Input: an external signal which can be modified and affects the system behavior, shown by $u(t)$.
Disturbance: an external signal which cannot be modified, shown as $w(t)$.
Internal signal: a system's variable which is neither input/output nor external signal.

By this categorization of signals, a model representation can be modified into the general form presented graphically in Fig. 2.2.

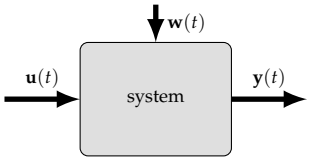

Fig. 2.2 Abstract representation of a general system and its signals.

Using this system representation, general mathematical form of a model from (2.2) can be rewritten into (2.3). Obviously this is a generic form of a model and some elements of this representation may not be available in some cases.

$$\mathbf{f}\left(\mathbf{y}^{(m)}(t),\ldots,\mathbf{y}^{(1)}(t),\mathbf{u}^{(m)}(t),\ldots,\mathbf{u}^{(1)}(t),\mathbf{w}(t),t\right)=0 \tag{2.3}$$

According to the number of signals related to a system, it may be classified as single or multiple input/output. Moreover, according to the representation of relations between signals, a system may be continuous or discrete from time point of view. In the discrete time form, differentiates are used instead of the derivations commonly used for continuous time domain.

According to the form of equations **f** in (2.3), a system may have different mathematical properties. For instance, it may be either implicit or explicit. Consequently, handling the model will require different mathematical tool-sets. Some key properties of the mathematical model of a system which are required in this work are explained hereafter.

Linearity

A system is considered linear when its mathematical representation has a linear form. In another word, a system with single input and single output is linear when its graphical representation of relation between input and output has a line form. However, to prove linearity, a system has to accomplish the superposition criteria defined as:

Definition: *Superposition*

Superposition applies on a system when its output to a linear combination of inputs complies with the corresponding combination of outputs to the individual input signals.

Time variance

As it is clear from the naming, a time invariant system gives the same output to an input, disregarding the time of experiment. This can be formulated as:

Definition: *Time-invariant system*

A system is time-invariant when its output to a delayed input is the same output to the original input with a correspondingly time delay.

Combining linearity and time invariance definitions, a large group of systems can be defined as Linear Time-Invariant (LTI).

Causality

System causality is defined according to the cause and effect of the input and output signals. A causal system can be defined as:

Definition: *Causal system*

A system is causal when no output instant of the system depends on any of its future instants of inputs.

In the mathematical representation, when the general form of a system relation as $S : U \times Y$ changes into $S : U \rightarrow Y$, system will be causal [34].

Memory

It is possible that one or more internal signals or outputs of a system have some kind of memory effect. For instance, height of liquid in a tank has a memory effect because it is an integration of all incoming and outgoing liquid volume over time. Therefore, a memory-less system can be defined as:

Definition: *Memory-less system*

A system is memory-less when its independent variables for each given value of input(s) is only dependent on that specific time [35].

Basically all systems with *accumulator* or *summing* elements have memory, such as a battery or a capacitor in an electric circuit.

Static/Dynamic

A system is considered dynamic when its changes are related to the time. Therefore, its mathematical representation requires differential or difference equations according to the time. Consequently, a static system is defined as:

Definition: *Static system*

A static system can be explained without any need for inclusion of time. Neither in its signals nor in the system description.

Therefore, static systems are sometime considered as steady-state because its signals and their relation are not time dependent.

2.3 System representations

Regardless of physical nature of a system, a model is a representations of the system being analyzed. Many branches of science have developed their own method of system representation. However, they can be somehow categorized into two major groups of *graphical* and *mathematical* representations. Perhaps mathematical representation is the most accepted and common method which spans a very diverse range of fields. On the other hand, graphical models try to represent the system in a more visual way which helps to understand the connections in a system easier.

Graphical representation

There are many graphical representation of systems which have been developed over time for each discipline of science. For instance, an electric circuit can be either a real representation of a system or an equivalent circuit replicating the behavior of a non-electrical system. An example of this case is the heat dissipation of an electrical board presented as an electrical circuit in spite of its thermodynamic nature. This duality between thermodynamic parameters and electrical elements is traditionally used by electrical engineers because it is more familiar for them to analyze circuits.

In addition to the field specific graphical presentations, two common generic methods are available which can be applied in different areas.

Block diagram method is based on the flow of signals shown as arrows. Modification of any signal happens when it passes through a system shown by a block. Each block can be considered as a system receiving one or more signals, operating on them and pass the result(s) out. Block diagrams always require causality included while all blocks have at least one input and one output [30]. This representation technique is commonly used by control engineers and system designers due to diversity of systems dealt with. Further information regarding this type of representation can be found in most signals and systems sources such as [35].

Simulink package of the software *MATLAB* uses this representation of system for the purpose of simulation.

While block diagram is founded on the concept of signals, a *bond graph* is made of components which exchange energy or power through their connections [30]. Therefore, these representations are made of components and bonds. In contrast to the signal exchange in block diagrams, bond can be bidirectional while signal is omnidirectional. In another word, there is no necessity for the system causality in bond graph representation.

Each bond transports power or a flux of energy which is a product of *effort* and *flow* variables. These two variables are generalized parameters of physical phenomena with similar principles. This similarity can be seen for few common fields in Table 2.1.

Table 2.1 Bond variables in different physical fields.

	Electrical	Mechanical	Hydraulic	Thermal
effort	voltage	force	pressure	temperature
flow	current	velocity	flow	energy flow

Beside effort and flow as two fundamental variables, there are two other generalized variables namely *displacement* and *momentum*. A detail explanation of these variables and relation between different fields can be found in [30]. In addition to the bidirectional energy and power flow which simplifies system representations compared to the block diagrams, bond graph has the benefit of modeling and simulation of multi-domain systems.

Multiple softwares use this concept of system representation such as *Modelica*, *PSpice* and *Simscape*.

Mathematical representation

A mathematical model is a single equation or a set of them which are able to describe a system [32]. These equations can be algebraic, differential or partially differential. In addition, based on the system specification they may be linear or not, time based or dependent. Hence, representation in (2.2) is a very generic form and can be explained more specifically. According to the complexities for analytical solution of high order differential equations, this single high degree

differential equation can be rewritten as a system of first order differential equations. For this purpose, a set of internal variables known as *states* (shown by x) are used. A state is a variable explaining a fundamental principle of the system at each given time. Minimum number of states in a system is equal to the order of differential systems to completely explain its behaviors. For instance, number of states in electrical systems is equal (but not always) to the number of energy storage devices.

Using a vector $\mathbf{x}$ of states, system model can be presented by a sets of equations as $\dot{\mathbf{x}} = \mathbf{f}(\mathbf{u}, \mathbf{x})$, when $\dot{x}$ is the derivation of x according to the time. Since system outputs are always some of the states, this representation mostly has a secondary equation as $\mathbf{y} = \mathbf{h}(\mathbf{u}, \mathbf{x})$ to explain the outputs. Consequently, a state space model can be defined as:

Definition: *State space model*

when:
$\mathbf{x}(t)$: n-dimensional column vector of *states*,
$\mathbf{u}(t)$: p-dimensional column vector of *inputs*,
$\mathbf{y}(t)$: q-dimensional column vector of *outputs*.
a state space model is presented by:

$$\dot{\mathbf{x}} = \mathbf{f}(\mathbf{u}, \mathbf{x}) \tag{2.4a}$$
$$\mathbf{y} = \mathbf{h}(\mathbf{u}, \mathbf{x}) \tag{2.4b}$$

This type of models are called lumped parameter models [28] because they are made of Ordinary Differential Equations (ODE). In contrary is another type of models, known as the distributed parameter models, described by Partial Differential Equations (PDE). In a PDE, derivation is according to the parameters other than time.

A common form of model is a lumped model for a LTI system in a continuous time form which its matrix representation would be as:.

$$\dot{\mathbf{x}}(t) = A \cdot \mathbf{x}(t) + B \cdot \mathbf{u}(t) \tag{2.5a}$$
$$\mathbf{y}(t) = C \cdot \mathbf{x}(t) + D \cdot \mathbf{u}(t) \tag{2.5b}$$

Both ODE and PDE model representations can be written in the discrete time domain as well using difference instead of derivation. The general representation of system in discrete time will change to $\mathbf{x_{n+1}} = \mathbf{f}(\mathbf{x_n}, \mathbf{u_n}, t_n)$.

In some cases (both natural system or human-made) it is possible that system states are related together without a time aspect described by difference or derivation or integration as the inverse form. A common example of such relation is the voltage current relation of a resistor as $v = i \cdot r$. Where the voltage at each time instant is only dependent on the current at that specific time and the resistor value as a *constant* in the model. This type of relations

is a consequence of a *static* system as explained formerly where relation is formulated as an Algebraic Equation (AE) without need for time or derivation according to time. It has to be noted that this relation may be nonlinear as well. Therefore, based on the system characteristics, formulation of function from (2.3) may be a set of Differential Equation (DE), AE or a combination known as Differential-Algebraic Equation (DAE).

In reality, casual systems have a chain of cause and effect showing some essence of time and dynamic. However, scale of this time and its relation to the modeling aim is crucial for the mathematical representation. When the concerned time scale of the system for the model, is much larger than its causal (cause and effect) procedure, it is possible to ignore the dynamics and simply conceive the static representation of the system. Further information about the scale of time and this consideration according to the modeling can be found in [27].

Up to here, continuous and discrete models had been presented according to the time. However, two other types of models can be considered as well, namely *qualitative* and *discrete-event* models. A qualitative model is by nature a discrete time model, though it is not necessarily a periodic time instant with equidistant time periods. However, the key factor is discretization of dependent variable (states) in such a system [28]. In a discrete-event system, changes in the states are not managed by time but dependent on the occurrence of an event within the system. Therefore, in a finite time, possible number of state changes is a finite value [28]. Nevertheless, both time and state axes may be timely continuous or discrete.

2.4 Model building

Different steps have to be passed for the development of a model. Before starting any of these steps, modeler has to define the goal of the modeling and its outcome. According to the definition of the model, next step is to define the boundary of the system and its margins from the environment. Afterwards, there are two key steps ahead: at first a model structure has to be defined which in the mathematical form will be a parametric model. Then, the final step is use of a method or algorithm to estimate model's parameters according to the system in experiment.

The last two steps require experiments and system analysis. It is mostly in this way that different experiments are designed within the system boundaries to monitor the system and collect information regarding its behavior. According to these information, a system structure has to be built. There are different approaches to develop the structure of a model. It relies on the source of knowledge about the system and method of analyzing and formulating that knowledge. However, these methodologies can be classified into two groups of *deduction* and *induction* which are shortly explained.

Deduction

This approach is used when a model is developed based on prior knowledge and insight to the system behavior. Deduction is used when the knowledge about a process is available from experiments on a similar process [30]. An example of this knowledge can be the physical laws explaining the relation between variables in the ideal form such as Newton's laws. According to this principle, deductive modeling starts from a general form and narrows to the specific case for the system.

In addition to the relations between parameters, prior knowledge may reveal further information about the system structure. This may help for selecting the proper states or sub-systems of the overall system.

Induction

In many cases prior information about a system model are not available, leading into model induction. Within these techniques sometimes known as identification, focus of modeling is on finding parameter values inside the model [30]. However, this is also possible when a model structure be assumed, including input/output signals, system order, linearity and so on. In this perspective, a selection criteria has to be defined to select the best model according to the modeling aim.

A system structure may be selected from some predefined set of forms or being generated empirically based on observations from the system. For instance, it is common for system experts and control engineers to consider a first or second order of differential function to develop a PID controller regardless of the real structure of the system. On the other hand, statistical induction mostly tries to find an initial guess about distribution of the system data to fit a class of regression to that.

Degree of inductivity

In case a complete model of a system is explained only by deduction using prior knowledge and physical facts, it is called a *white-box* model [30]. This naming is mostly because all internal behaviors of the system are clearly known and system structure is transparent through the model.

In contrary is when no internal information is available. Proposed model only provides a formulation for explaining a relation between input and output signals. However, this formulation may or may not be related to the real nature of the system. Such a model is commonly called a *black-box* model [30].

In between there is *gray-box* modeling. It is when some aspects of the system can be explained using prior knowledge while others are not known and has to be induced using observations from measurements and experiments. Of course, amount of knowledge about a system depends on the field of work and available know-how about the system. [30]

Regardless of chosen method for selecting a system structure, a parameter tuning is necessary afterwards. It is mainly because two similar systems which follow the same structure behave slightly different due to difference on their properties. For instance, while two cars from the same manufacturer have very similar structure, they still have some differences in the way they behave. For an accurate model, these differences have to be included in the model and be tuned based on each specific case. While this is a clear step for deducted models, in some inductive modeling it cannot be applied while the model is built for that specific system.

One fact to be bared in mind is that it is very common to repeat the data collection and system structure design steps to reach a final model.

2.5 Statistical terminology

According to use of signals and their of measurement during modeling, different statistical principles are commonly necessary. Although very simple and general principles are used here, utilized terminology is explained shortly for the consistency and simple understanding of the rest of this work.

When a general measured signal is presented using s, its prediction by the model will be shown using $\hat{s}$. Using this representation, error (δ) can be simply defined as the difference in between by:

$$\delta(s) = s - \hat{s} \tag{2.6}$$

Sometimes the range of a signal within the boundary is large and errors from different experiments cannot be compared directly with each other. Therefore, a relative error can be defined. Within this work a percentage error will be used as in (2.7) which scales all errors according to the original signal value.

$$\rho(s) = 100 \cdot \frac{s - \hat{s}}{s} \tag{2.7}$$

Normally a system behavior is evaluated at different points. While error for each instant of signal can be found, some more abstract criteria is necessary. Although it is possible to use the average of errors, it has the problem that positive and negative signed errors will compensate each other. Therefore, Mean Absolute Error (MAE) is defined as:

$$MAE(s) = \frac{1}{m} \sum_{i=1}^{m} |s_i - \hat{s}_i| \tag{2.8}$$

In addition to absolute value of error, it is possible to use the square of error which has the benefit to exaggerate large errors. Using the square it is possible to define the Root Mean Square Error (RMSE) factor as:

$$RMSE(s) = \sqrt{\frac{1}{m}\sum_{i=1}^{m}(s_i - \hat{s}_i)^2} \tag{2.9}$$

In some cases such as optimization which the changes in error scale are needed and not the exact value, Mean Square Error (MSE) can be used as well.

While it is possible to calculate the RMSE for the relative error as well, Mean Absolute Percentage Error (MAPE) will be used as the alternative factor defined as:

$$MAPE(s) = \frac{100}{m} \cdot \sum_{i=1}^{m}\left|\frac{s_i - \hat{s}_i}{s_i}\right| \tag{2.10}$$

To quantify variation of a parameter from the mean value, *standard deviation* presented by σ, is formulated by:

$$\sigma(s) = \sqrt{\frac{1}{m}\sum_{i=1}^{m}(s_i - M(s))^2} \tag{2.11}$$

when $M(s)$ is the mean value of the parameter s.

Chapter 3
Modeling Indoor Photovoltaic Energy Harvesting

In the right light, at the right time,
everything is extraordinary.

—Aaron Rose

Abstract
This chapter addresses different aspects of photovoltaic energy harvesting in artificial indoor lighting. Some basics of light and its measurement comes first. General principles of light generated electrical power are reviewed. Afterward, behavior of a photovoltaic transducer is explained.

Different models from literature are reviewed. However, the main focus is on the white-box models based on the physical principles of a photovoltaic transducer. Not only different methods for parameter extraction on these models are mentioned, but also effect of light intensity and temperature as the key environmental elements affecting transducer's performance and its model are reviewed extensively.

In the third part of this chapter, available methodologies developed mainly for outdoor applications are evaluated and improved for the indoor photovoltaic energy harvesting. This is done using collected data from an indoor photovoltaic measurement platform explicitly built for this purpose.

Developed methodology is used afterwards for modeling the behavior of PhyNode's photovoltaic module. Finally, developed model is evaluated using collected data within PhyNetLab. On-board models can predict all keypoints of the PV curve with a mean relative error less than 0.3 % while mean normalized error of the system level detailed model is about 1.3 %.

3.1 Introduction

Different EH techniques are available which enable environmental energy scavenging in divers fields and scales. PV, thermo-electric, wind/air flow, pressure variations and vibrations are only some of them to be named. Each of these methods has its own pros and cons, making it more desirable for some specific applications. Although few works such as [36] has shown higher harvested energy by mechanical vibration, a survey in [12] shows better results using PV harvesting. However, this is only when warehousing application is considered specifically for stationary CPS similar to PhyNode.

PV EH has a long tradition for scavenging energy from the environment. It has been used for multiple applications by converting sunlight into the electrical energy and different works had addressed this behavior under diverse environmental conditions. With the rise of IoT devices, many small embedded systems designed for indoor usage rely on PV energy harvesting to operate as an energy-neutral system or reduce the need for recharging. In the last few years, even some systems have been developed for industrial application [1] relying on this energy sources. Not only some applications such as in [20] use this principle in the indoor environments, but also PhyNode [24] brings the Indoor Photovoltaic (IPV) harvesting to the extreme by using them in ultra-low light conditions of a warehouse.

Modeling techniques developed for solar harvesting are mostly mature and their usage is extensively analyzed in the last decades. Although the general model of PV module is deduced from the physical knowledge of PV semiconductor profile, its application and parameter extraction in indoor condition has to be validated thoroughly.

This chapter focuses on the modeling of PV transducers for indoor applications. This model has to provide an accurate estimation of the PV transducer's output at each environmental condition. Among different physical parameters, only light intensity (E) and temperature (T) are known to affect the performance and behavior of a PV transducer. Considering these aspects, an abstract representation of the desired model is shown in Fig. 3.1. When V_h and I_h are subsequently parameters representing the harvested voltage and current seen at the transducer's terminal.

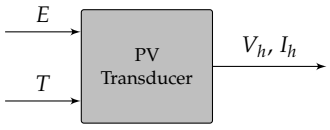

Fig. 3.1 An abstract block-diagram representation of the desired model for a PV module.

Temperature definition and its measurement techniques are well established. However, light measurement complexities in addition to its vitality for PV systems requires a deeper understanding of this physical principle. Therefore, a general introduction to the light and its measurement is provided.

3.1.1 Light

Light is a small section of the electromagnetic spectrum between the ultraviolet and infrared radiation with visible portion for the human eye's perception between 380 nm to 780 nm as presented in Fig. 3.2.

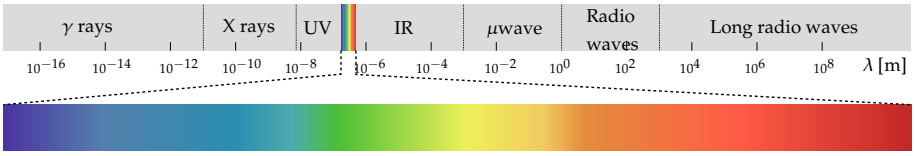

Fig. 3.2 The overall electromagnetic spectrum and highlighted section visible for the human eye's perception.

In addition to the physical spectrometry definition, light can be defined according to the human perception. For instance, the Illuminating Engineering Society of North America defines light as: "radiant energy that is capable of exciting the retina and producing a visual sensation" [37].

Regardless of the wave form definition of light, it is possible to explain it as energy packages called *photon* carrying a specific amount of energy. Scale of this energy is dependent on the properties of the light source.

Light can be measured in two different perspectives according to its rays' direction which may be *emitted* from or *falling* on a surface. While units based on emission are more desired for light generation, falling units are more sensible for the PV applications and will be used here. This measurement can be in two different ways due to perception definitions mentioned before.

Radiometry: is the measurement of light power at all wavelengths
Photometry: light measurement with respect to a human eye sensitivity

Irradiance (E_e) as the radiometry parameter is measured in $\mathrm{W\,m^{-2}}$ within the SI unit system. *Illuminance* (E_v) is the photometry parameter measured in $\mathrm{lm\,m^{-2}}$ or simply lx. It is possible to explain the illuminance as the normalized irradiance according to the human eye's light response. However, illuminance may be different in some physical systems according to the definition of human eye's light response. Moreover, real human eye perception is dissimilar within different light conditions according to the adaptation to the light intensity. A more detailed explanation of this principle can be found in [38]. Considering these definitions, conversion from irradiance to the illuminance is possible. For instance, with a monochromatic light at 555 nm, 1 W is equal to 683 lm. However, it is not possible to convert illuminance into the irradiance due to two reasons. At first, while no standard eye's light response is available. Secondly, while this curve is limited to a range of the spectrum, its application is destructive and cannot be reversed.

Both lighting parameters can be measured for each single wavelength to deliver a spectrum. Another possibility of light measurement is using

integrative devices which accumulate the spectrum and provide a single value as the light intensity. In contrast to the spectrometer, integrative light sensors are much smaller and easier to handle. However, not only these sensors do not deliver any information about each wavelength's intensity, no conversion between measurement systems is possible. Furthermore, it is possible that different lighting specifications be presented for the same value of irradiance/illuminance.

Integrative photometry sensors are commonly manufactured as Integrated Circuit (IC). These sensors are very well developed for inclusion in embedded devices such as cell phones. There are also radiometry integrative sensors which collect light and provide the integrative irradiance. These sensors commonly known as *pyranometer* are mostly used in solar farms for analysis of the outdoor light intensity. Although pyranometers are commonly more accurate compared to the photometry sensors, they are much more bulky and expensive. Therefore, illuminance is more accessible for embedded devices and will be used hereafter when light intensity is addressed, except when explicitly mentioned.

3.1.2 PV harvesting principles

In the beginning, a PV device can be defined as:

Definition: *PV transducer*

A *PV transducer* is a semiconductor device generating electrical power when illuminated with photons.

These semiconductors have weakly bounded electrons in the valence energy band. Any photon falling on the cell with higher energy than the band gap energy can break the bound and cause free movement of the electron to the conduction band which is able to pass the electricity through the material. A source for conquering the band gap energy can be supplied by photons to free the electrons. As long as light falls on the surface and photons hit the electrons, valence band breaks and pumps them into the conduction band. Therefore, photon's energy is transferred into electric energy, generating electric current in the semiconductor. A specially designed contact collects these electrons to drive them into the output terminal. These electrons return to the cell by a secondary contact when they loose their energy by doing work in the external circuit. Electrons return to the valence band with the same energy as they left. [39] Due to this nature, PV cells are able to generate Direct Current (DC).

All photons with less energy travel through the cell and get absorbed at the rear side, generating heat on the panel. Consequently, performance of a cell is dependent on balancing the threshold energy with the photon's energy. As mentioned before, the energy of photon is dependent on the light specification. Hence, a PV cell has to be designed according to the specification of light which

will be falling on it. A key aspect on the selection of a PV technology for indoor applications is this match between sensitivity of the transducer (commonly known as spectral response) and available spectrum of the light. Actually, this analysis has to be done by comparing the band gap energy of cell's material and energy of wavelength in the spectrum. A detailed analysis for common IPV technologies can be found in [40, 41].

Silicon (Si) has a good absorption characteristic in relation to the radiation while its fabrication technology is well developed. Consequently, Silicon specially in its crystalline form (c-Si) is used for most of the current PV cells. Meanwhile, other semiconductors are available, able to absorb light and convert it to electric current. However, these materials are less advanced compared to the Silicon and are still in development and commercialization phases. Thin-film semiconductors such as amorphous silicon (a-Si), copper indium gallium diselenide (Cu(InGa)Se2 or CIGS) and cadmium telluride (CdTe) are some of them which get most of the attention. [39]

3.1.2.1 PV transducer's behavior

From electrical point of view, a PV module is an electric source which can behave as either a current or voltage source. To analyze its behavior, it is common to check its characteristics at different voltage-current combinations. Hence, the I-V and P-V curves of a PV device in their first quadrant (as a source) are presented in Fig. 3.3.

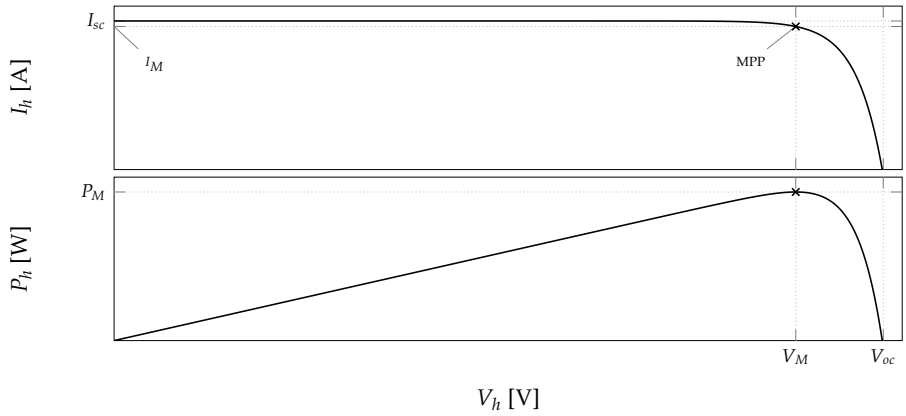

Fig. 3.3 I-V and P-V characteristics of a PV cell in (semi-)ideal form.

There are critical points in these curves which play major role on the understanding of the PV behavior. The first point is at Short-Circuit (SC), when the voltage is zero and current I_{sc} is the cross point at the current axis. On the x axis is the Open-Circuit (OC) point when no current is harvested with V_{oc} as the critical voltage. Moreover, there is a point where the maximum possible power is delivered, commonly known as *Maximum Power Point (MPP)*. Voltage,

current and power at this point will be subsequently shown using V_M, I_M and P_M hereafter.

To be noted that the curves in Fig. 3.3 are not the exact ideal form which is supposed to have a constant current for all voltages till the breaking point where the current instantly drops to zero. Hence, it is common to divide the curve into two different sub-behaviors as simplified in Fig. 3.4. A linear behavior acting as a current source with its amplitude known as photo-generated current (I_g) dependent on the light intensity (E). Second part is considered as the nonlinear replication of the internal structure of the PV transducer. The nonlinear curve is known as *dark-current* while it is commonly considered to be independent from the light intensity [42].

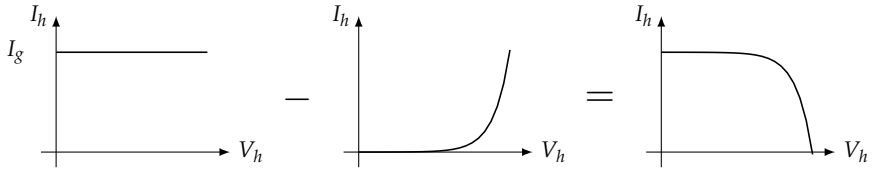

Fig. 3.4 Division of semi-ideal I-V curve into photo-generated and dark current curves.

Considering semi-ideal form of the curve in Fig. 3.4, PV cell behavior can be divided into a current source (SC till MPP) and a voltage source (MPP till OC). As can be seen, MPP plays a critical role on the behavior of the PV cell as a source. Therefore, it is reviewed with more details.

MPP

At the MPP not only the general source behavior of a PV cell is changing, but also the derivation of power according to the voltage is zero. This characteristic can be formulated as in (3.1) and is commonly used to find the MPP when the I-V curve is known.

$$\frac{\partial P_h}{\partial V_h} = \frac{\mathrm{d}I_h}{\mathrm{d}V_h} \cdot V_h + I_h = 0, \qquad \text{at: } V_h = V_M \tag{3.1}$$

While the most optimum operational I-V combination for a PV transducer is at the MPP, techniques called Maximum Power Point Tracking (MPPT) are developed to find and keep the system at this point. However, this is not a simple task, because in addition to the nonlinearity of the I-V curve, the incident radiation and the ambient temperature change the I-V curve as well [43]. Consequently, not only position of MPP differs for each transducer, but also for each environmental condition. Therefore, some kind of active MPPT system is required to adapt the transducer to the condition. Hence, many techniques are developed [44] aiming for MPPT. The number of these techniques is so large that some surveys [45–50] had tried to collect them.

These methods are in a spectrum from high accuracy at one side and low computational power and hardware requirement at the other side. Based on the MPPT design, they can be categorized into multiple subgroups. For instance, if they require prior empirical environmental data [51] which can be stored as either a Look-up Table (LuT) [52] or a mathematical formulation [53]. Or according to their accuracy, if a closed-loop system tries to continuously track the MPP using a microprocessor and repetitive measurements [54]. Since MPPT is considered as an optimization procedure, many artificial intelligence based techniques have been implemented as well. Artificial Neural Network (ANN) [55], fuzzy logic [56], genetic algorithm [57], ant/bee colony [58, 59] are only some of them.

In outdoor applications, scale of harvesting and consequently wasted energy because of non-optimal tracking is much larger than the energy demand for the MPPT. Nevertheless, in ULP IPV applications harvested energy is normally very low. Thus, the energy requirement of a complex MPPT technique can be larger than the improvement of harvesting by an exact MPPT. Consequently, quasi-seeking techniques are favored in these applications. They keep operational condition near the MPP (but not exactly at it) with a very minimal computational energy. One of the most used techniques is fractional MPPT mainly developed based on the empirical fact that the voltage and current at MPP are a fraction of V_{oc} and I_{sc} [60] which can be formulated as:

$$k_V = \frac{V_M}{V_{oc}} < 1 \qquad \text{or} \qquad k_I = \frac{I_M}{I_{sc}} < 1 \tag{3.2}$$

Voltage based method commonly known as Fractional Open Circuit Voltage (FOCV) uses a k_V reported in different literature between 0.7 to 0.8, and the suggested value for k_I is about 0.85. Nevertheless, finding the exact fraction value is a challenging issues. [44]

This direct technique requires no prior knowledge from the PV transducer. Therefore, its implementation is favorable while it widens the operational range of the harvester without worrying about the exact harvester's parameters or production tolerances. Unfortunately, detection of V_{oc} or I_{sc} requires periodical detachment of the transducer from the rest of the system causing some marginal losses. Although, some solutions such as in [60] try to avoid detachment, pure FOCV is commonly integrated in the ULP applications.

3.2 State-of-the-art PV modeling

For the modeling of a PV transducer, system is explained according to the definition of a PV transducer. Input signals are light intensity (E) and temperature (T) while outputs can be different according to the aim of modeling. Anyhow, a common goal is to find the nonlinear I-V relation of the PV transducer mathematically described by (3.3).

$$I_h = f(E, T, V_h) \tag{3.3}$$

It is also possible to replace the position of V_h and I_h according to the needs of the model. These type of models will be called *whole-curve* model hereafter while they explain the behavior of the whole range from SC till OC. In contrast, there are models which only aim for the value of this relation at specific points of the curve, such as at MPP, OC or SC. These will be called *single-point* models. Nevertheless, single-point models can be considered as simplified versions of the whole-curve model.

Both model types have a static form, because on one hand inputs changes are slow in time, and on the other hand dynamics of PV systems are mostly negligible. However, few researchers [61–64] provide dynamic models for the behavior of the PV transducer as well.

Available (static) models for PV transducers can be categorized into two major groups of *empirical* and *analytical*. Empirical models are deductive and explain the system behavior based on the available knowledge about it without analysis of the internals principles and can be considered as black-box models. For instance, [65] uses a simple model to numerically generate fits for I_{sc} and V_{oc} according to the E and T. Or, heuristic model in [40, p.89] provides the relation between E and I_{sc} and V_{oc}. A major challenge of empirical models is their dependency on the data. Although empirical models have been able to provide prediction for some solar (outdoor) cases, their implementation in indoor area cannot be assured. Because in contrast to the solar case which the sun is the main source of light, indoor lighting can extremely differ based on the buildings design. This limits the application range of an empirically developed model. Moreover, there are models such as in [66] which uses similarity of the I-V curve with the inductor current rise curve to build a model.

In contrast, analytical models are based on the knowledge of the physical principles behind operation of a PV transducer. Concurrently, analytical models from the solar applications are really mature. Hence, physical models for the explanation of PV behavior can be considered reliable and reviewed further.

3.2.1 Physical model of PV transducers

The most common model of a PV cell is based on the Shockley diode equation [67]. This model is mainly an outcome of the works done by Hall [68] and Shockley et al. [69]. In this concept, a PV cell is considered in its pure form made of a pn-junction diode. It is made of two quasi-neutral regions on either side of a depletion region while each region has an electrical contact. Typically, the heavily doped region (n-type) is called the *emitter*, and the lightly doped region (p-type) is called the *base*. Since emitter is mostly thin, most of the absorption happens in the base causing it to be sometimes named the *absorber* region [39]. Solving the minority-carrier diffusion equation with the appropriate boundary conditions provides the I-V characteristic of the PV

cell which can be found in [39, 70, 71]. Solution of these equation leads to PV terminal characteristics in (3.4), when I_{sc} is the short-circuit current, B is the Boltzmann's constant, T is temperature in Kelvin and q is the electric charge. Also, I_s is the saturation current of the p-n junction.

$$I_h = I_{sc} - I_d = I_{sc} - I_s \cdot \left[\exp\left(\frac{q \cdot V_h}{B \cdot T}\right) - 1\right] \tag{3.4}$$

This equation explains the terminal current as the combination of a short circuit current in addition to a diode's current. It can be seen that this form fits into the separation of current presented in Fig. 3.4.

While q, B and T are constant for an environmental condition, *thermal voltage* (V_t) is defined as: $V_t = B \cdot T/q$. Under standard testing conditions (operating temperature constant at 298 K), this factor will be about 25 mV. Substitution of thermal voltage simplifies diode's current in (3.4) to:

$$I_d = I_s \cdot \left[\exp\left(\frac{V_h}{V_t}\right) - 1\right] \tag{3.5}$$

According to the effect of the diode, this model is commonly known as *single diode model* (1D). Using diode current formulation from (3.5), this model has two unknowns; namely I_{sc} and I_s. According to the modesty of this model, some researchers such as [65] use this form as the PV model.

Some other works such as [39] prefer two different saturation currents in the physical representation. First current is due to recombination in the quasi-neutral region, while the second one is due to recombination in the space-charge region. This actually models the PV transducer with two diodes and is known as *double diode model* (2D). However, it is common to add the diode's ideality factor (n) to the diode's current as well. Inclusion of this factor advances the diode's current to:

$$I_d = I_s \cdot \left[\exp\left(\frac{V_h}{n \cdot V_t}\right) - 1\right] \tag{3.6}$$

A n factor between 1 to 2 is commonly accepted [72]. When it is near 1, recombination in the quasi-neutral regions dominates the diode while a value near 2 shows domination of recombination in the depletion region [39]. By inclusion of two ideality factors a 2D model explains the terminal relation as:

$$I_h = I_{sc} - I_{s_1} \cdot \left[\exp\left(\frac{V_h}{1 \cdot V_t}\right) - 1\right] - I_{s_2} \cdot \left[\exp\left(\frac{V_h}{2 \cdot V_t}\right) - 1\right] \tag{3.7}$$

It is claimed in [73, 74] that inclusion of second diode improves model performance under low illumination. Nevertheless, addition of secondary I_s as a further unknown parameter increases model complexity and requires identification of three parameters. For simplicity these parameters are presented in the vector form as $\boldsymbol{\psi}$ hereafter.

Either of these forms can be presented as an electrical Equivalent Circuit Model (ECM) as well. From signals in Fig. 3.4, a constant current source can present the photo-generated current. While diode(s) in parallel to this source build the dark current. It has to be noted that the current source is opposed to the diodes' currents which forward-bias them and represent the negative sign of signal. These ECMs are shown in Fig. 3.5.

A: 1D ECM according to (3.4) **B:** 2D ECM according to (3.7)

Fig. 3.5 Ideal equivalent circuits of I-V characteristics for a PV transducer.

The overall form of current for either of these models for a range of voltages is similar to the I-V curve of PV cell formerly shown in Fig. 3.3. Therefore, these two formulations are commonly accepted as models of PV transducers. This form can be tuned using the corresponding $\boldsymbol{\psi}$ to replicate measured I-V curve. An example of these curves is shown in Fig. 3.6.

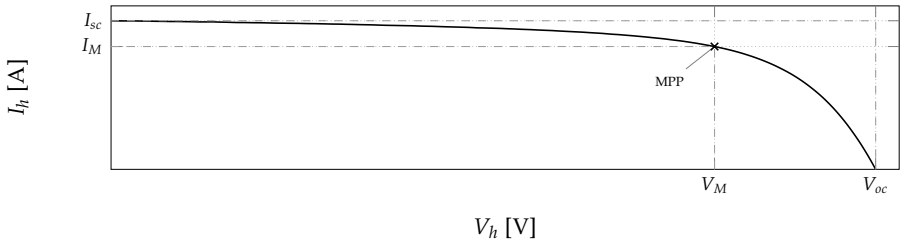

Fig. 3.6 I-V curve of a Sanyo/AM-1464 PV module measured under florescent lighting.

Comparing this measured curve with the ideal one in Fig. 3.3, it is clear that the real curve has a steeper current source region and a more flat voltage source region. To quantify these differences from the ideal case, Fill Factor (FF) is defined as a relation between the real MPP and the maximum possible MPP defined for the case that both source regions are ideal, making the MPP at the intersection of I_{sc} and V_{oc}. Therefore, FF can be explained as:

$$FF = \frac{P_M}{V_{oc} \cdot I_{sc}} = \frac{V_M \cdot I_M}{V_{oc} \cdot I_{sc}} \tag{3.8}$$

At this stage, $\boldsymbol{\psi}$ parameters in the formulation of the models are used to fit it into the measured curve. From formation of models it can be seen that the I_{sc} will only change the bias of the curve. Effect of I_s modification on an exemplary case is presented in Fig. 3.7. As can be seen, changes in this current shifts the bending point of the curve through the voltage axis without affecting the bias. Furthermore, it is possible to consider n as another tuning factor and modify it

to improve the fitting as shown in Fig. 3.7. This factor does change the bending point along the voltage axis as well with a minor change in the slope of the voltage source region. In addition, its modification changes the curvature of the bending point to some extent.

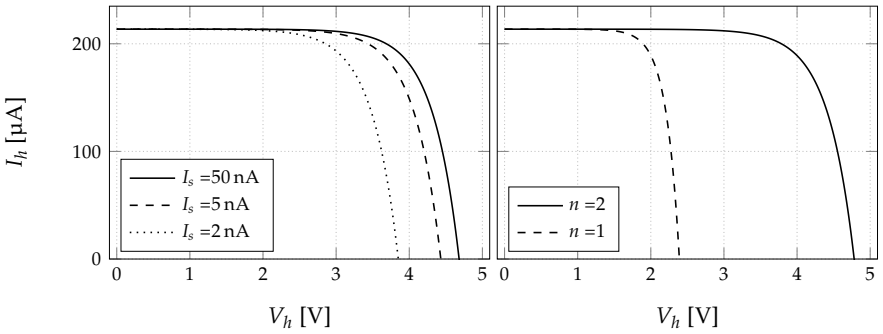

Fig. 3.7 Effect of changes in I_s (left) and n (right) on the I-V curve.

Consequently, changing factors in the tuning parameter vector $\boldsymbol{\psi}$ (including n) is very limited in the way it changes the shape of the I-V curve. Specially, slopes of the curve cannot be modified extensively to increase similarity to the real measured curve. To conquer this deficiency, further non-ideality factors have to be added to these models.

Analyzing real measured I-V curves, two extra modification factors can be imagined. Model should include factors to enable controlling the curve's slope at both ends. These factors are consequences of the non-idealities in the PV cell. In addition to the n, non-ideality in PV transducer is mostly related to the parasitic resistances in the form of one series resistance (R_s) and one shunt resistance (R_{sh}). Multiple mechanisms are responsible for these resistances. R_s main contributors are:

- semiconductor material bulk resistance
- metal contacts bulk resistance
- resistance between metal contacts and semiconductor

while R_{sh} is mainly a consequence of leakage across the pn junction around the edges and foreign impurities precipitation in the junction region.[70] Addition of these two resistances to the 2D ECM will make it as in Fig. 3.8.

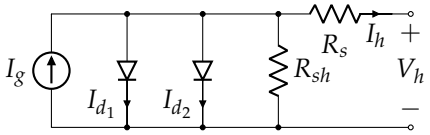

Fig. 3.8 Equivalent 2D circuit model of a PV cell including parasitic resistances.

To be noted that I_{sc} in Fig. 3.5B is replaced with I_g which is the short-circuit current with no parasitic resistance and is purely generated from the absorbed light. Analysis of parasitic resistors using Kirchhoff equations shows that the

size of R_{sh} will change the curve slope at SC. While size of R_s directly affects the slope at the OC. These effects can be seen graphically in Fig. 3.9.

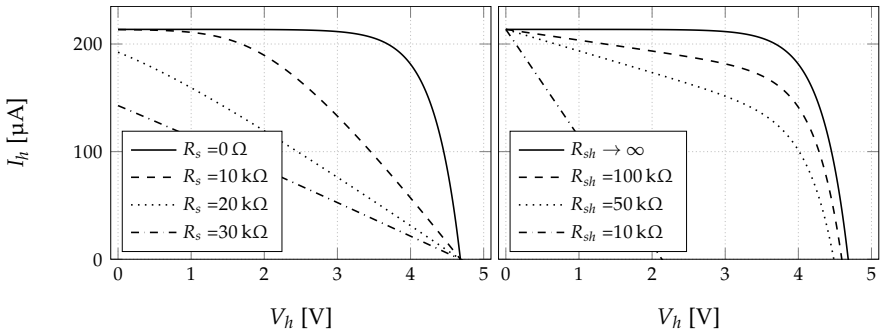

Fig. 3.9 Effect of changing parasitic resistances on the I-V curve model of a PV transducer.

Usually, the value of R_s is very small, while R_{sh} is very large to reduce the flow of current in the parallel path and enable a larger current flow through the series resistance [75].

Considering circuit in Fig. 3.8, terminal characteristic from (3.7) can be extended by adaptation of parasitic resistances to be:

$$I_h = I_g - I_{d_1} - I_{d_2} - \frac{V_h + I_h \cdot R_s}{R_{sh}} \tag{3.9}$$

Each diode's current is defined by inclusion of resistances into (3.6) and can be written as:

$$I_{d*} = I_{s*} \cdot \left[\exp\left(\frac{V_h + I_h \cdot R_s}{n_* \cdot V_t} \right) - 1 \right] \tag{3.10}$$

This equation can be considered as a full form double diode (2D) model. Its single diode (1D) version can be found by removing one of the diode currents. Considering both resistors as tuning factors, $\boldsymbol{\psi}$ has 5 elements for 1D model, while 2D model requires 7 parameters. It is also possible to increase number of diodes to add degrees of freedom for the curve tuning. For instance, [76, 77] use 3 diodes model while a 4 diodes model is proposed in [78].

Based on good physical explanation of these type of models, they are commonly used both in scientific communities and applied cases. However, the main research focus is on the number of parameters in the model, their identification method and the overall model performance. Smaller size of $\boldsymbol{\psi}$ will be easier to tune, while reducing the performance. 1D model is mostly favored compared to the 2D model because of its simplicity [79]. It is a good combination of the basic principles and provides flexibility during parameter estimation [80]. There are some models which also ignore one of the resistors to reduce number of parameters during the tuning. An abstract overview of available models and their parameter is presented in Table 3.1.

Table 3.1 An overview of physically-based PV models in some of literature including number of diodes, number of parameters and availability of resistances.

Param.	Diode	Constant n	R_{sh}	R_s	Publication
4	1	N	N	Y	[81–88]
5	1	N	Y	Y	[42, 84, 85, 89–107]
7	2	N	Y	Y	[106–113]
7	3	Y	Y	Y	[114]

There are also models such as in [115] providing a piece-wise linear model using diode and parallel bypass-resistor pairs instead of stand-alone diode(s). However, mainstream models focus on normal representation of the model and will be used here.

Tuned model after parameter extraction is able to replicate the I-V curve at a single specific environmental condition (E, T). However, changes in these factors will deviate the curve and require a separate parameter identification. Consequently, a large set of publications focus on methods to identify these parameters and replicate the I-V curve with higher accuracy. Nevertheless, before reviewing available parameters identification techniques, two aspects have to be explained. At first is the overall formulation of the physical model for multi cell PV transducers. Second is the explanation of an explicit solution for the I-V relation.

Effect of multiple cells in a module

Since a single PV cell mostly provides a small voltage and current, it is common to connect multiple cells together and build a module. When a module is made of N_s cells in series and N_p cell in parallel, its terminal I-V relation in the 1D form can be written as in (3.11) [116].

$$\begin{aligned} I_h =& N_p \cdot I_g - N_p \cdot I_s \cdot \left[\exp\left(\frac{V_h + I_h \cdot \frac{N_s}{N_p} \cdot R_s}{n \cdot N_s \cdot V_t} \right) - 1 \right] \\ & - \frac{V_h + I_h \cdot \frac{N_s}{N_p} \cdot R_s}{\frac{N_s}{N_p} \cdot R_{sh}} \end{aligned} \tag{3.11}$$

I_g, I_s, R_s and R_{sh} are parameters to be identified from measured I-V curve. Therefore, it is possible to directly merge multiple cell effects into them. Although the same principle can be used for n, according to a computational aspect (will be discussed later), this is avoided, and a simplification parameter a will be used instead of $n \cdot N_s$. Using all these considerations, the overall I-V relation representation will be as in (3.12).

$$I_h = I_g - I_s \cdot \left[\exp\left(\frac{V_h + I_h \cdot R_s}{a \cdot V_t} \right) - 1 \right] - \frac{V_h + I_h \cdot R_s}{R_{sh}} \tag{3.12}$$

Explicit I-V relations

Both models are nonlinear with no explicit form. It means signal estimation or simulation using these models has to be done in a numerical way which is computationally intensive. Not only this numerical complexity makes model integration to a ULP device extremely inefficient (or even impossible), it complicates the parameter identification process as well.

Nevertheless, it is possible to overcome this limitation for the 1D model by using the *Lambert W* or omega function. I-V relation from (3.12) can be rewritten in an explicit way [117, 118] using Lambert W as:

$$I_h = \frac{R_{sh} \cdot \left(I_g + I_s\right) - V_h}{R_{sh} + R_s} - \frac{a}{R_s} \cdot \mathcal{W}\left(\theta_i\right) \tag{3.13}$$

when $\mathcal{W}$ is the notation of Lambert W function and θ_i is defined by:

$$\theta_i = \frac{R_{sh} \cdot R_s}{a \cdot \left(R_s + R_{sh}\right)} \cdot I_s \cdot \exp\left[\frac{R_{sh} \cdot R_s \cdot \left(I_g + I_s\right) + R_{sh} \cdot V_t}{a \cdot \left(R_{sh} + R_s\right)}\right] \tag{3.14}$$

From [118] explicit formulation of voltage according to the current is:

$$V_h = R_{sh} \cdot \left(I_g + I_s - I_h\right) - I_h \cdot R_s - a \cdot \mathcal{W}\left(\theta_v\right) \tag{3.15}$$

when θ_v is defined using:

$$\theta_v = \frac{R_{sh}}{a} \cdot I_s \cdot \exp\left[\frac{R_{sh}}{a} \cdot \left(I_g + I_s - I_h\right)\right] \tag{3.16}$$

It has to be noted that the Lambert W is defined for input arguments larger than $-e^{-1}$ and lower values can cause numerical problems.

3.2.2 Parameter identification

As discussed formerly, there is a set of parameters ($\boldsymbol{\psi}$) for the whole-curve model, which has to be identified. According to the topology of the model, this vector may have different number of elements from 2 up to (theoretically) infinity. Parameter extraction for selection of $\boldsymbol{\psi}$ elements has been addressed extensively in literature. Proposed methods are very dispersed from different fields [119] which multiple surveys such as [119–121] have tried to collect the most accepted ones. These methods claim to provide a trade-off between amount of required information, accuracy of solution and required resources to solve the problem. Sources such as [122] divide the parameter extraction methods into three groups of analytical, iterative and evolutionary computational. However, it is possible to categorize them into two main groups of *analytical* and *numerical* methods while evolutionary algorithms use iterative numerical techniques as well and can be included in that group.

Numerical methods consider identification of parameters in $\boldsymbol{\psi}$ as an optimization problem with the goal of minimizing the error between current from the tuned model ($\hat{I}_h$) and the measured current (I_h). This problem can be presented using a minimization problem as in (3.17).

$$\min_{\boldsymbol{\psi}} \quad e(\boldsymbol{\psi}) = \int_0^{V_{oc}} \parallel I_h(V_h) - \hat{I}_h(V_h, \boldsymbol{\psi}) \parallel_2 \, \mathrm{d}V_h \tag{3.17}$$

Due to diversity of possible methods to solve this, different solutions have been proposed. Levenberg-Marquardt Method (LMM) [123], min optimization [20], genetic algorithm [124–126], bee colony [127], cat swarm [128], particle swarm [76, 129] are only some of these techniques. In addition to the numerical complexities including computation and power requirements, these methods also require data from the whole-curve. However, it is possible to reduce number of measured points to the number of elements in $\boldsymbol{\psi}$ to have a determined problem.

Another solution to tackle the concern of measurement points is to use a set of equations instead of an overall optimization objective function. This is the main idea behind the analytical methods to build a set of equations which only requires knowledge of limited number of points from the curve. These points are commonly OC, SC and MPP. It is possible to write the model function at these specific points based on the fact that the terminal voltage and current are zero subsequently at SC and OC. These equations for the 1D model are:

$$@SC: V_h = 0 \Rightarrow I_{sc} = I_g - I_s \left[\exp\left(\frac{I_{sc} \cdot R_s}{a \cdot V_t} \right) - 1 \right] - \frac{I_{sc} \cdot R_s}{R_{sh}} \tag{3.18a}$$

$$@OC: I_h = 0 \Rightarrow 0 = I_g - I_s \left[\exp\left(\frac{V_{oc}}{a \cdot V_t} \right) - 1 \right] - \frac{V_{oc}}{R_{sh}} \tag{3.18b}$$

$$@MPPT: I_M = I_g - I_s \left[\exp\left(\frac{V_M + I_M \cdot R_s}{a \cdot V_t} \right) - 1 \right] - \frac{V_M + I_M \cdot R_s}{R_{sh}} \tag{3.18c}$$

Using these equations, it is possible to build an Algebraic Equation Set (AES) to be solved and find the elements of $\boldsymbol{\psi}$. However, according to the size of $\boldsymbol{\psi}$, it is possible that the AES is under-determined and further equations are required. Therefore, many publications try to provide other analytical equations. The most common method is to use derivation of current according to the voltage. From (3.12), this derivation can be written for a 1D model as [130]:

$$\begin{aligned} \frac{\mathrm{d}I_h}{\mathrm{d}V_h} = & - I_g \cdot \left[\frac{1}{a \cdot V_t} \left(1 + \frac{\mathrm{d}I_h}{\mathrm{d}V_h} \cdot R_s \right) \exp\left(\frac{V_h + I_h \cdot R_s}{a \cdot V_t} \right) \right] \\ & - \frac{1}{R_{sh}} \cdot \left(1 + \frac{\mathrm{d}I_h}{\mathrm{d}V_h} \cdot R_s \right) \end{aligned} \tag{3.19}$$

Using this general form, derivation at keypoints can be written as:

$$\left(\frac{\mathrm{d}I_h}{\mathrm{d}V_h}\right)_{I_h=0} = -I_g \cdot \left[\frac{1}{a \cdot V_t} \cdot \left(1 + \left(\frac{\mathrm{d}I_h}{\mathrm{d}V_h}\right)_{I=0} \cdot R_s\right) \cdot \exp\left(\frac{V_{oc}}{a \cdot V_t}\right)\right] - \frac{1}{R_{sh}} \cdot \left(1 + \left(\frac{\mathrm{d}I_h}{\mathrm{d}V_h}\right)_{I_h=0} \cdot R_s\right) \tag{3.20}$$

$$\left(\frac{\mathrm{d}I_h}{\mathrm{d}V_h}\right)_{V_h=0} = -I_g \cdot \left[\frac{1}{a \cdot V_t} \cdot \left(1 + \left(\frac{\mathrm{d}I_h}{\mathrm{d}V_h}\right)_{V_h=0} \cdot R_s\right) \cdot \exp\left(\frac{I_{sc} \cdot R_s}{a \cdot V_t}\right)\right] - \frac{1}{R_{sh}} \cdot \left(1 + \left(\frac{\mathrm{d}I_h}{\mathrm{d}V_h}\right)_{V_h=0} \cdot R_s\right) \tag{3.21}$$

$$\left(\frac{\mathrm{d}I_h}{\mathrm{d}V_h}\right)_{\mathrm{MPP}} = -I_g \cdot \left[\frac{1}{a \cdot V_t} \cdot \left(1 + \left(\frac{\mathrm{d}I_h}{\mathrm{d}V_h}\right)_{\mathrm{MPP}} \cdot R_s\right) \cdot \exp\left(\frac{V_M + I_M \cdot R_s}{a \cdot V_t}\right)\right] - \frac{1}{R_{sh}} \cdot \left(1 + \left(\frac{\mathrm{d}I_h}{\mathrm{d}V_h}\right)_{\mathrm{MPP}} \cdot R_s\right) \tag{3.22}$$

A challenge introduced by these equations is the need for the curve slope at these keypoints. There are suggestions for estimation of these values using only measured keypoints. One of the most simple solutions for these slopes is to calculate them as a linear relation between end points and the MPP. Some researches such as [85] provide methods to estimate required I-V curve derivation only using three keypoints. There are some other methods which provide graphical suggestions for these slopes. However, all these methods can be only used for the slope at OC and SC. When only these two data can be estimated, there would be 5 equations which can be used for the building of the AES. This will be sufficient for a 1D model which has only 5 unknowns. However, further equations are necessary for higher model orders.

From MPP definition, derivation of power curve according to the voltage will be zero which using (3.1) can be written as:

$$\left(\frac{\partial P_h}{\partial V_h}\right)_{\mathrm{MPP}} = V_h \cdot \left(\frac{\mathrm{d}I_h}{\mathrm{d}V_h}\right)_{\mathrm{MPP}} + I_h = 0 \Rightarrow \left(\frac{\mathrm{d}I_h}{\mathrm{d}V_h}\right)_{\mathrm{MPP}} = -\frac{I_M}{V_M} \tag{3.23}$$

By substituting (3.23) into (3.22) a new relation can be written at the MPP according to its zero derivative power as:

$$-\frac{I_M}{V_M} = -I_g \cdot \left[\frac{1}{a \cdot V_t} \cdot \left(1 - \frac{I_M}{V_M} \cdot R_s\right) \cdot \exp\left(\frac{V_M + I_M \cdot R_s}{a \cdot V_t}\right)\right] - \frac{1}{R_{sh}} \cdot \left(1 - \frac{I_M}{V_M} \cdot R_s\right) \tag{3.24}$$

This equation does not require measurement of the curve slope at MPP. Considering this equation, it is possible to build an AES with up to 6 equations.

Although this is enough to find $\boldsymbol{\psi}$ of a 1D model, it still lacks one equation to be determined for the 2D model. That is one of the main reasons why the 1D model is more common for typical applications. Another solution to use AES alongside 2D model with measurement of only keypoints is to reduce the model order. That is why some researchers remove one of resistors while others consider one of diode's ideality factors constant.

Regardless of system size, this method has other pitfalls. At first, the general form of the main I-V equation is not explicit. Although some researchers use Lambert W equation to solve this issue, it is only applicable on the 1D model. Furthermore, in the overall general formulation of these AES, there is no explicit solution for the parameters. Therefore, it is very common to solve an AES by use of numerical methods such as Least Square Method (LSq), LMM and Newton Raphson Method (NRM).

Methodology for this problem is suggested from former decades with less powerful computational devices. In this type of solutions, some assumptions are made which help to simplify equations in a way to find an explicit solution for each parameter. In addition, most of these methods use a specific order for finding parameters while equations are dependent on the formerly found parameters. For instance, [131] provides a method for finding R_s only using the V_{oc}, I_{sc}, V_M and I_M. However, by considering R_{sh} infinite, $I_g \approx I_{sc}$ and $I_s < 10^{-10}$. Based on these assumptions, when the R_s is known, [132] provides an analytical equation to find a using I_{sc} and values at MPP. [133] uses an extra graphical line between zero point and the cross point of the V_{oc} and I_{sc} to find the a. It provides analytical relations using slope of this line for cases with all combinations of finite and infinite values of the R_s and R_{sh}. However, it uses an assumption by neglecting $I_l \cdot R_s/a$.

3.2.3 Environmental factors

Regardless of the used parameters identification method, a $\boldsymbol{\psi}$ replicates only a single I-V curve. However, light intensity (E) and temperature (T) have been mentioned to affect the I-V curve. Consequently, parameters in $\boldsymbol{\psi}$ are dependent on the incident radiation and environmental factors [82]. Accordingly, their effect on different parameters of a PV module have to be analyzed as well. A common practice for such analysis is to define a condition as the reference and explain parameters according to their value at the reference condition. Therefore, value of a parameter $\bullet$ at reference condition is noted using $\bullet^*$.

It is known from solar experiments, that the behavior of keypoints according to the environmental condition can be explained [134] by (3.25), when α and βs are light and temperature coefficients provided by the manufacturer.

$$V_{oc} = V_{oc}^* + \alpha_v \cdot \ln(E/E^*) + \beta_v \cdot V_{oc}^* \cdot (T - T^*) \tag{3.25a}$$

$$I_{sc} = I_{sc}^* \cdot (E/E^*) + \beta_i \cdot I_{sc}^* \cdot (T - T^*) \tag{3.25b}$$

In case these factors are not provided, they can be found by measuring SC and OC values at different operational conditions and fitting these models to the collected data.

However, there is discrepancy between researchers and other sources such as [132] provide different relations for these changes, such as:

$$V_{oc} = \frac{V_{oc}^*}{1 + \gamma \cdot \ln(E/E^*)} \cdot (T^*/T)^{\beta_v} \tag{3.26a}$$

$$I_{sc} = I_{sc}^* \cdot (E^*/E)^{\alpha_i} \tag{3.26b}$$

when β is a temperature effect nonlinear exponent and γ is a dimensionless coefficient dependent on the PV technology. It is considered that the I_{sc} is not temperature dependent which does not comply with (3.25b).

In contrary to the difference for the dependency of V_{oc} and I_{sc} to the environmental condition, there is a consistency on the drifts of I_g due to E. Many sources [42, 81–84, 99, 116, 135] have reported change in I_g when β_g is the temperature drift factor.

$$I_g = \frac{E}{E^*} \cdot \left[I_g^* + \beta_g \cdot (T - T^*) \right] \tag{3.27}$$

Other three types of parameters are under large debate within the literature and different explanation about their drifts from reference values are provided. Perhaps the biggest debate is on the diode ideality factors. Sources such as [136] consider it as a real quality or ideality factor. Therefore, it is a constant and not an empirical value used for fitting. Others [137–140] consider this parameter dependent on the operational condition.

The same issue is available about the diode's saturation current. Some researches explain changes in I_s dependent only on the temperature. For instance [40, 83, 116] in addition to IEC891 define changes in this current using material's band-gap energy (ϵ_G) as:

$$I_s = I_s^* \cdot \left(\frac{T}{T^*} \right)^3 \cdot \exp\left(\frac{\epsilon_G^*}{k \cdot T^*} - \frac{\epsilon_G}{k \cdot T} \right) \tag{3.28}$$

However, some others [42, 99, 135] explain this relation to follow a formulation as in (3.29) while βs are temperature drift coefficients.

$$I_s = [I_s^* + \beta_i \cdot (T - T^*)] \Big/ \left\{ \exp\left[\frac{V_{oc}^* + \beta_v \cdot (T - T^*)}{a \cdot V_t} \right] - 1 \right\} \tag{3.29}$$

Although most researchers [91, 116] consider parasitic resistances constant, [85] uses some kind of correction factor for it according to the changes in the operational condition. However, availability of minus resistance for a large section of light intensities reduces the credibility of these methods. [134] claims

improvement in the model performance in indoor condition by proposing relations for these resistance as in (3.30).

$$R_s = \frac{R_s^* \cdot \left(\frac{V_{oc}}{a \cdot V_t} - 1\right) - R_{sh}^* \cdot \left(\frac{I_{sc} \cdot R_{sh}^*}{a \cdot V_t} - 1\right)}{\left(V_{oc} - I_{sc} \cdot R_{sh}^*\right) / a \cdot V_t} \tag{3.30a}$$

$$R_{sh} = R_{sh}^* - R_s \tag{3.30b}$$

while [99] provides another dependency for the R_{sh} to the intensity as in (3.31) when R'_{sh} for silicon crystalline modules is four times R_{sh}^*.

$$R_{sh} = R_{sh}^* + \left(R'_{sh} - R_{sh}^*\right) \cdot \exp\left(-5.5 \cdot \frac{E}{E^*}\right) \tag{3.31}$$

While these formulations explain relations between parameters and environmental factors, some others use simplification assumptions to provide a single-point model explaining relations between keypoints alone regardless of the environmental conditions. For instance, by considering $I_{sc} \gg I_s$, authors of [39] are able to explain the V_{oc} using (3.32).

$$V_{oc} = V_t \cdot \ln\left(\frac{I_{sc} - I_s}{I_s}\right) \approx V_t \cdot \ln\left(\frac{I_{sc}}{I_s}\right) \tag{3.32}$$

3.3 IPV modeling

Despite maturity of solar PV applications, few researches have undertaken on the quality and quantity of indoor artificial lighting and corresponding PV cells' behavior [141]. Indoor and outdoor applications of PV cells have both similarities and differences. First, as shown in Fig. 3.10, indoor light intensity is in a much lower scale comparing to the solar lighting.

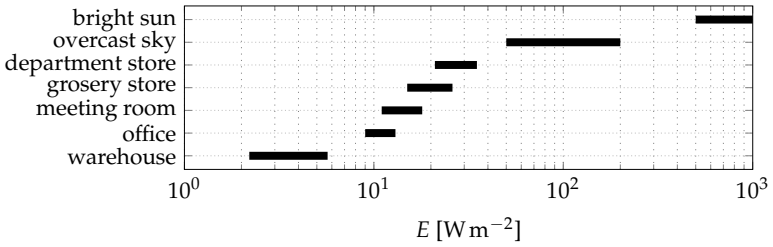

Fig. 3.10 Overview of light intensity range in different conditions. From [142]

In addition to the difference in the scale, these lighting types have totally different spectrums. This difference shown in Fig. 3.11, is due to the fact that indoor lights are specifically designed for the human eye's visible range. As a consequence, IPV module manufacturers design their modules with better response to this limited range than the whole light spectrum.

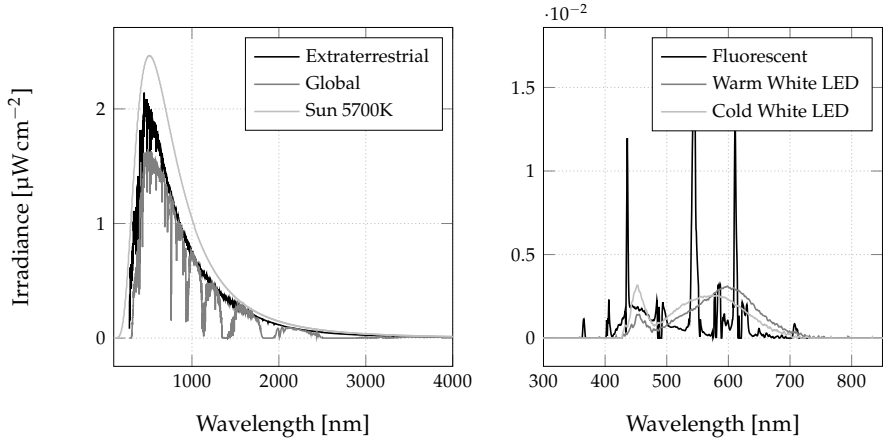

Fig. 3.11 Left: outdoor solar light spectrum [143] and sun's black body radiation at 5700 K [144]. Right: measured indoor light spectrum of three different artificial lighting.

Most of the available PV behavior analysis focus on the outdoor solar applications. While received sunlight at each point on the earth is dependent on multiple factors such as height, atmospheric condition, absorption angle and weather; sun remains the main source of light. This makes it a perfect candidate for the reference condition. That is why the sunlight with an air-mass AM1.5 delivering 1 kW m^{-2} is commonly used as the reference condition for the solar applications. Unfortunately, due to the diversity of artificial light sources and their differences from the solar spectrum, this cannot be considered as the reference condition for IPV applications.

Considering artificial light sources optimized for human eye vision, it is common to measure indoor light intensity by integrative illuminance. However, integrative nature of this measurement unit in addition to large differences in between spectrum of artificial light sources makes definition of a general reference condition roughly impossible. For instance, I-V curves in Fig. 3.12 are both measured from the same IPV cell under 248 lx at 299 K but from two different Light Emitting Diode (LED) light sources.

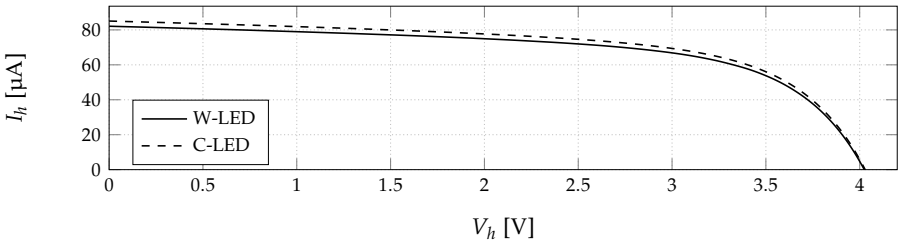

Fig. 3.12 I-V curve of the PhyNode's Solems IPV module measured under cold and warm LED light. Both sources are from the same manufacturer and both measurements are at: E =248 lx and T =299 K.

To be noted that both sources are LED type and even from the same manufacturer. However, they are designed to act at different black-body temperature causing one to feel more warm (W-LED) and the other one colder (C-LED). This difference in the performance can be simply explained by looking at their radiometry and photometry spectrum in Fig. 3.13. Although the integrative illuminance is equal for both measurements, curves have differences due to the dissimilarities of the light sources at some wavelengths.

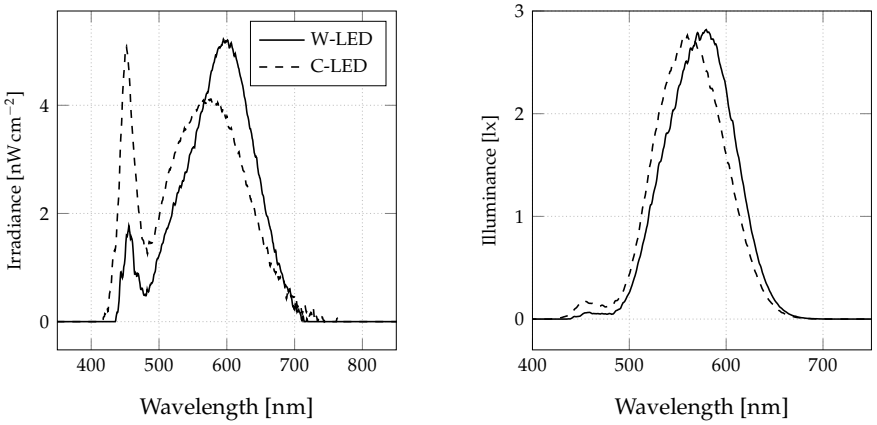

Fig. 3.13 Spectrum measured under C-LED and W-LED light both at 248 lx. In spite of equal integrative value, spectrum is different. Left: irradiance, Right: illuminance.

Up to here, its known that the formulation of environmental effects is under debate. Furthermore, differences in between solar and artificial spectrum brings complexities to the definition of the reference condition. Consequently, detailed analysis and modeling of IPV behavior is required. In this procedure, not only classical techniques for identification has to be reevaluated, but also behavior of the IPV module according to the changes in environmental condition has to be explained. A detailed model of PV system has to mimic the whole-curve I-V relation for all possible indoor environmental conditions. Therefore, a structure made of two subsequent steps with the layout shown in Fig. 3.14 is proposed.

Fig. 3.14 Two steps of a full PV whole-curve model.

In this two fold concept, initial part of the model estimates $\boldsymbol{\psi}$ parameters according to the environmental parameters. In the second part, I-V curve related to the extracted $\boldsymbol{\psi}$ is made and used for finding any specific data regarding the PV characteristics. However, this is the point where the detailed models and single-point models differentiate. Single-point models does not rely on these two steps and directly provides specific keypoints for each set of

environmental condition. Hence, it lacks insight about exact behavior of the PV module and its overall I-V curve.

Regardless of model type, both of them require accurate, reproducible and reliable data to extract and formulate models. Therefore, data collection procedure is explained hereafter.

3.3.1 Data collection

For the modeling of IPV behavior at system level, I-V curve of a transducer module has to be measured under different light intensities and temperatures. Therefore, each measurement will be a set of three elements including:

- I-V curve
- light intensity
- temperature

Procedure of measuring these elements with high accuracy is explained here, while a more detailed version can be found in [17, 145, 146].

The most key information about an IPV system is its I-V curve. According to the nonlinear behavior of the PV modules, both voltage and current have to be measured simultaneously for the whole positive range. A common practice is to change an impedance connected with a 4-wire (Kelvin) connection. Change of impedance can be applied by use of a 4-quadrant Source Measurement Unit (SMU) sweeping voltage from zero to the point where the measurement passes to the fourth quadrant. Benefit of using a SMU is its ability to measure voltage and current simultaneously while acting as a source.

Due to the artificial low light condition, generated current from IPV transducers is mostly small in the scale of some µA, requiring a very accurate and sensitive measuring device. Therefore, a *Keysight B2902A* is selected which is a two channel precision SMU with a resolution of 10 fA and 100 nV. It is able to be a source while measuring voltage and current using 4-wire connection. For the measurement of the I-V curve, IPV is connected to this measurement device. Concurrently, SMU is connected via USB to a PC running a MATLAB script controlling the device using Standard Commands for Programmable Instruments (SCPI).

Most of source devices have internal safety relays to avoid over-current. However, these relays affect the measurement in a SMU and their selection has to be done precisely to avoid measurement accuracy loss. It is known from the shape of the I-V curve that I_{sc} is the highest current in the first quadrant. Hence, over-current relay has to be selected according to the I_{sc}. Therefore, measuring I_{sc} ahead of main voltage sweep is necessary.

After setting the over-current relay, voltage sweep can start. Although it is possible to start exactly from zero voltage, collection of data from a very short range in the second quadrant will be helpful for the numerical filtering to reduce measurement noises. Therefore, sweep starts from a small negative

voltage. While signals are measured with the highest possible resolution, voltage increases till the current reaches a small negative value. This is decided for the filtering similar to the starting voltage. At this point sweep and measurement stops and data is passed to the PC for storage. The overall I-V curve measurement procedure can be seen in Algorithm 1.

Algorithm 1 Process of measuring I-V curve of an IPV module

1: Build connection to the SMU;
2: Set $V_{\text{source}} = 0$;
3: I_{sc} = Measure current ;
4: Set over-current relay to $I_{sc} + \epsilon$; {ϵ to avoide over-current for negative voltages}
5: Set V_{source} =-100 mV ; {A negative voltage as the sweep's starting point}
6: I_h = Measure current ;
7: **while** $I_h \geq -0.05 \cdot I_{sc}$ **do**
8: Set $V_{\text{source}} = V_{\text{source}} + \epsilon$;
9: I_h = Measure current ;
10: **end while**
11: Turn voltage source off ;
12: Transfer data to the PC ;
13: Disconnect SMU;

Since the overall model in indoor lighting has to be developed, both photometry and radiometry light intensities are necessary. However, roughly no embedded device is able to be advanced with a spectrometer and they use a small (and even ULP) integrative photometry IC. Therefore, collection of such measurement in parallel to the spectrometry is beneficial.

For the spectrometry, a small 2-inch integration sphere from *StellarSphere IC2* with a 180° field of view and wavelength range of 200 nm to 1700 nm is used. This sphere makes a homogeneous light probe and transfers it through a fiber optic connection to a *BLACK-Comet* spectrometer from *Stellar Inc.*. This device is able to measure a wavelength range of 200 nm to 1100 nm and transfers the data through a USB connection to the control PC. This process starts in parallel to the I-V curve measurement.

PhyNode uses a *MAX44009* [147] integrative photometry sensor from *Maxim Integrated* which is a ULP wide-range intensity integrator IC. Since this sensor is for ULP application according to its low power mode, it has a low resolution which is not optimal for the light measurement. Therefore, a *TSL2561* [148] sensor from *ams AG* is used as a secondary light integrator in parallel. This sensor delivers two values corresponding two channels. One channel representing the whole spectrum from 300 nm to 1100 nm while the secondary channel covers the IR region. Both these integrative sensors deliver digital data using Inter-Integrated Circuit (I2C) serial bus. This interface is also used for their behavior control and sample time setting.

For the temperature measurement, a *MCP9808* [149] sensor from *Microchip Technology Inc.* is used. This sensor is able to deliver the measured temperature

with high accuracy and resolution through the same I2C bus shared with the integrative light sensors connected to a Raspberry Pi. This device acts as a interface in between control PC and environmental sensors.

For a proper accurate measurement, all sensors are mounted on a board which has the exact size as PhyNode. In addition, integration sphere for the spectrometry is mounted on this board presented in Fig. 3.15.

Fig. 3.15 Developed board for the measurement of IPV data, mounted on a box. This board houses probe integration sphere and sensors in addition to the IPV module.

This board is mounted on a normal transport box holding the Raspberry Pi interface, spectrometer, SMU and a laptop as the control PC. Therefore, the overall setup is mobile and can be simply used in different fields with a single power line. The overall signaling of this setup is presented in Fig. 3.16.

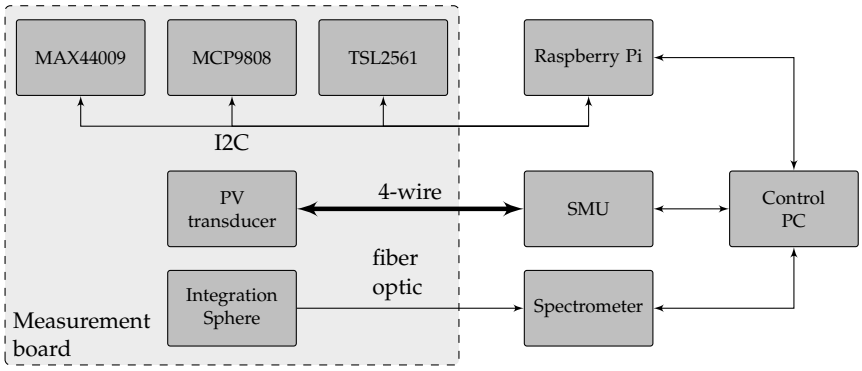

Fig. 3.16 Schematic signaling structure of the light measurement platform.

As can be seen in Fig. 3.16, Raspberry Pi is connected to the control PC and sets the sensors according to the setting from the main program. This program written as a MATLAB script, sets up all measurement devices at first. This includes finding I_{sc} for I-V curve measurement, calibration of spectrometer and setting a sampling time of 400 ms for sensors through Raspberry Pi. When all devices are initiated, measurements start in parallel. After finishing all measurements, data is read back and stored as a structure in MATLAB. The overall measurement process can be seen in Algorithm 2.

Algorithm 2 Process of a complete experiment of IPV data collection

```
Connect to the Raspberry Pi and initialize sensors ;
Initialize SMU for I-V measurement ;
Initialize spectrometer ;
Start sensors measurement through Raspberry Pi;
Start spectrometry ; {in parallel}
Start I-V measurement ; {in parallel}
while I-V measurement or spectrometry not finished do
    wait ;
end while
Stop sensors measurement through Raspberry Pi;
Read all measurements ;
Filter and store data ;
```

This portable setup is able to collect required data from a PV cell. However, for a systematic analysis and modeling, data has to be collected at reproducible environmental condition. To fulfill this requirement, a controlled light environment test-bed is developed.

Accurate modeling requires understanding of effects from each single input of the system. Therefore, measurement platform has to enable insulation and manipulation of each single parameter. Therefore, measurement must be completely under control.For the IPV measurement, platform has to be physically insulated from the outside environment to avoid interference from the normal lighting. Therefore, a shielded wooden cabinet with the size of $1100 \times 660 \times 660$mm is used as the main body of the test-bed. The whole interior is covered with professional dark light absorbing materials to avoid reflection of light, causing non homogeneous light distribution. Not only this structure enables separation of light, but also it provides a controlled temperature environment.

Although it is possible to simply mount the desired light source inside this cabinet, first trials in [17, 145] shown non-homogeneous light distribution as an effect of non-idealities in sources. Consequently, reception of similar light at the measurement devices and IPV module cannot be guaranteed. Furthermore, regulation of light intensity is required which as shown in [17, 145] cannot be achieved by dimming, distance modification and even application of optical filters. In addition, [17] shows dimming and power modulation change the light spectrum disabling reproducible experiments.

To conquer the light homogeneity and intensity control problem, an integration sphere is built. An integration sphere is an optically designed spheres with inner surface coated with highly reflective and diffuse material with multiple holes as light inputs in addition to an output hole. Holes are designed in a way that the incoming light is reflected (theoretically) infinite times before reaching the output. This design has different benefits which availability of a near perfect homogeneous output is the main one.

Designed integration sphere has a 50 cm diameter with internal coating of *Barium sulfate*. It has 5 input openings with 40 mm diameter and a single output with a diameter of 190 mm. The overall integration sphere is mounted on top of the measurement cabinet through a shielded hole providing a column of homogeneous light. Each input opening is supplied with a shielded and cooled space for mounting an artificial light source. Cooling system is added to avoid temperature increase on the light source during long measurement sessions. Not only high temperature can destroy the sensitive internal coating of the integration sphere, but also it voids the measurement while it changes the light spectrum by adding to its IR section. In addition, each input gate is equipped with a rotational diaphragm which can physically control the light entrance. Availability of multiple inputs enables creation of mixed lighting as well.

Inside temperature can be modified through an air canal on the floor of the cabinet connected to a fan. To avoid any light entrance, a light maze is installed on this opening. This temperature control is not active and is only able to keep the environmental temperature constant. The overall structure of this light measurement platform is presented in Fig. 3.17.

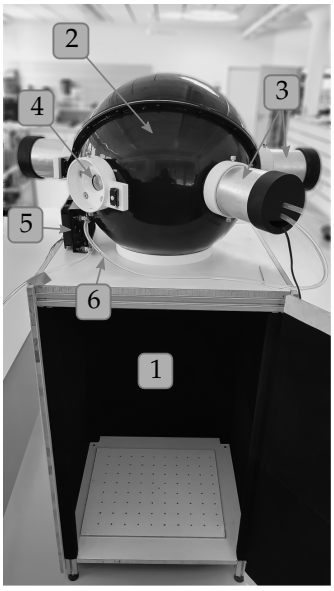

Fig. 3.17 The overall structure of the light measurement platform.
1: Interior light absorbing layer,
2: Integration sphere,
3: Input holes and light mounting device,
4: Servo controlled diaphragm,
5: Heat exchange radiator,
6: Cooling pipes

By mounting the measurement board in this cabinet, it is possible to measure IPV behavior at different lighting conditions and temperatures. To avoid excess heat, SMU, Raspberry Pi and spectrometer are mounted outside with cabling through the light maze. In addition to the Solems IPV module used on PhyNode, a monocrystalline IPV from IXYS has been measured within the light measurement test-bed as well. These modules and their abstract specification can be seen in Table 3.2.

Table 3.2 Specifications of the used IPV modules for the measurements.

Manufacturer	Model	Technology	N_s	N_p
Solems	07/072/048	Amorphous Si.	7	-
IXYS (IXOLAR)	SLMD960H12L	Monocrystalline	12	-

Both modules have been measured under W-LED from *Luminus Devices Inc.*. Moreover, PhyNode's Solems IPV module have been tested under C-LED light source as well. This enables analysis of the lighting type on the data. In addition, to check the temperature effect on the performance, data collection for Solems IPV module under W-LED source has been repeated in different temperatures. Consequently, three data-sets are available with specifications from Table 3.3 and data distribution depicted in Fig. 3.18. These data-sets are publicly accessible in [150].

Table 3.3 Specifications of the measured IPV data-sets.

Name	Module	Lighting	E [lx]	T [K]	No. of data
SWL	Solems	W-LED	10.8 to 240.5	298.8 to 304.9	130
IWL	Ixys	W-LED	23.1 to 240	299 to 299.5	25
SCL	Solems	C-LED	19.3 to 608.5	299.3 to 299.6	45

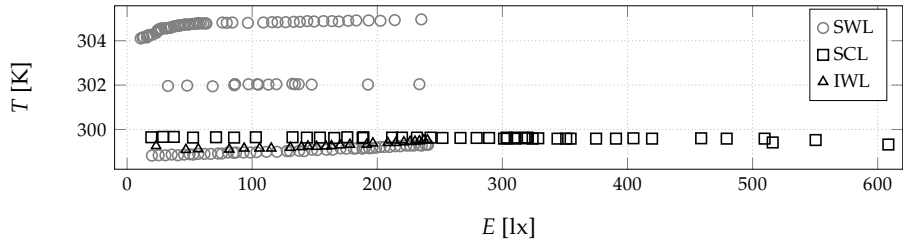

Fig. 3.18 Distribution of environmental conditions measured in different data-sets.

3.3.2 Photovoltaic normalized space

Due to large range of possible indoor light intensities, collected I-V curves are distributed in a large range which can be seen in Fig. 3.19 showing some measurements from SCL data-set. Not only this large range introduces complications to the behavior comparison, but also it causes scaling issues in numerical parameter identification. Photovoltaic Normalized Space (PVNS) is suggested to tackle this issue by normalizing the I-V curve into a unity space. This is simply done by division of each voltage to the V_{oc} of the curve and each current to the I_{sc}. Normalized notation of each parameter $\bullet$ will be shown using $\overline{\bullet}$ hereafter. It has to be noted that this is a scaling mechanism and not a mapping. Therefore, each parameter keeps its unit. Application of this method on the exemplary I-V curves can be seen in Fig. 3.19 as well.

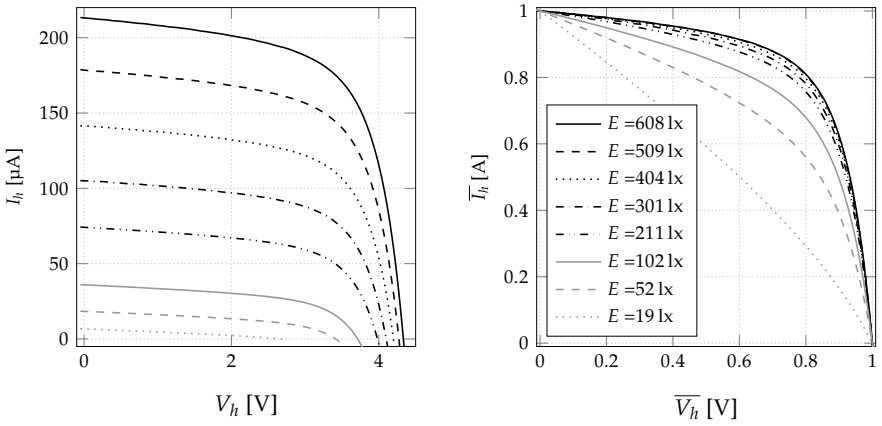

Fig. 3.19 Examples of measured I-V curves. Left: in normal space, Right: in PVNS.

Analyzing examples presented in Fig. 3.19, behavior for higher intensities is very similar, while the lower the light intensity goes, I-V curves get more flattened out. The benefit of PVNS is that any developed method for modeling can be applied on any measured I-V curve regardless of its range. The general model of a PV module in PVNS is defined as:

$$\overline{I_h} = \overline{I_g} - \overline{I_{d_1}} - \overline{I_{d_2}} - \frac{\overline{V_h} + \overline{I_h} \cdot \overline{R_s}}{\overline{R_{sh}}} \tag{3.33a}$$

$$\overline{I_{d*}} = \overline{I_{s*}} \cdot \left[\exp\left(\frac{\overline{V_h} + \overline{I_h} \cdot \overline{R_s}}{a_* \cdot \overline{V_t}} \right) - 1 \right] \tag{3.33b}$$

As can be seen, in addition to voltage and current values, resistances are scaled too. However, n and consequently a are both unit-less parameters and do not require scaling. Moreover, thermal voltage V_t has to be scaled as well due to its voltage unit. All in all, relation of all scaled parameters is as in (3.34).

$$\overline{\mathbf{P}} = \mathbf{P} \times \left[\frac{1}{V_{oc}}, \frac{1}{V_{oc}}, \frac{I_{sc}}{V_{oc}}, \frac{I_{sc}}{V_{oc}}, \frac{1}{I_{sc}}, \frac{1}{I_{sc}}, \frac{1}{I_{sc}} \right] \tag{3.34}$$

when:

$$\mathbf{P} = \left[V_h, V_t, R_s, R_{sh}, I_h, I_g, I_s \right]^{\mathsf{T}} \tag{3.35}$$

3.3.3 Evaluation criteria

Before modeling itself, a performance evaluation factor has to be defined. According to the large signal ranges, relative factors are preferred for PV models. However, finding the percentage error at the OC is impossible due to division to zero. Although it is possible to simply remove the value at OC, it is not desired according to the importance of this point. Same problem is available in all relative factors based on the individual points. To tackle this issue, Mean Absolute Normalized Error (MANE) is defined here. This factor

normalizes the percentage absolute error according to the I_{sc} and calculates the mean value for the whole curve. In this way, division to zero is avoided while the error is scaled for different light intensities. In another sense, this will be the MAE for the I-V curve in the PVNS which can be explained as:

$$\mathrm{MANE} = \frac{100}{I_{sc} \cdot V_{oc}} \cdot \int_0^{V_{oc}} |\delta(I_h)| \, \mathrm{d}V_h = 100 \cdot \int_0^1 |\delta(\overline{I_h})| \, \mathrm{d}\overline{V_h} \tag{3.36}$$

or for the case of discrete measured data with m points:

$$\mathrm{MANE} = \frac{100}{I_{sc} \cdot m} \cdot \sum_{i=1}^{m} |\delta(I_h)| = \frac{100}{m} \cdot \sum_{i=1}^{m} |\delta(\overline{I_h})| \tag{3.37}$$

This factor provides a relative performance figure and enables comparison of different signal levels without numerical problems.

3.3.4 Single-point models

At the first step, it is possible to use the collected data and develop a model explaining behavior of keypoints of the I-V curve directly according to E and T fulfilling the requirements of the on-board model. While each keypoint is explained using a separate model, this type of modeling is simply called single-point model hereafter. To do so, a formulation for each keypoint has to be found. This form has to be general with enough degree of freedom (tuning parameters) that can be applied on different IPV technologies, lighting types, light intensities and temperatures.

V_{oc}, I_{sc}, V_M, I_M are the main keypoints to model. In addition, as discussed formerly, use of FOCV from (3.2) is a common MPPT technique specially in ULP applications. Such a method simply sets operational voltage to 80 % of the V_{oc}. Therefore, estimation of this current (I_{80}) would be necessary for ULP applications such as PhyNode. These keypoints collected for all data-sets are graphically presented in Fig. 3.20 according to their light intensity.

From Fig. 3.20 comparing two data-sets for Solems IPV module, it can be said that the type of light will not change the overall behavior. Moreover, IXYS IPV module as a monocrystalline IPV has a similar form to the Solems IPV module as an amorphous Silicon module. Therefore it is possible to find a general function form for each keypoint regardless of lighting type and IPV technology. However, each single-point model has to include enough tuning parameters to reproduce the differences. Data in Fig. 3.20 specially both data-sets from Solems IPV module show a relation directly dependent to the light intensity. Nevertheless, building models according to the reference point (similar to the solar condition) helps to reduce numerical dependencies. As discussed formerly, no unique standard reference condition can be defined for artificial lighting due to the variety of the light types and spectrum. Hence, data from the highest light intensity in each data-set is considered as the reference condition

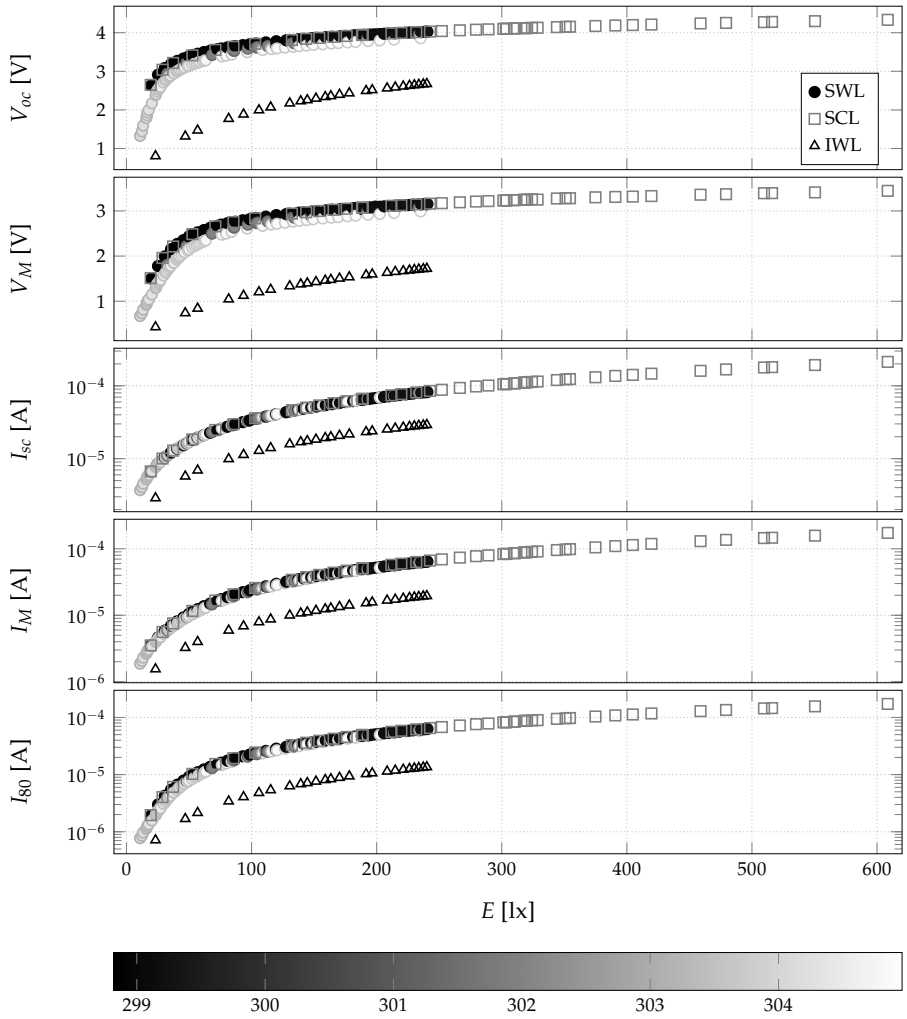

Fig. 3.20 Keypoint parameters measured for all data-sets. Color of SWL points shows temperature in K as in the color-bar.

of that specific data-set. Relative parameters are presented with $\widetilde{\bullet}$ as the ratio of the measured parameter divided to the value at the reference condition ($\bullet^*$).

Analyzing curves from Fig. 3.20, it can be found that both voltage factors (V_{oc} and V_M) simply shown by V_x have a logarithmic form according to the light intensity. This also complies with the heuristic model in (3.25a) for the solar condition. However, this form is not flexible enough to fit the curves measured from the IPV modules. Therefore, a modified version is suggested for the single-point model of voltage factors as in (3.38).

$$\widetilde{V_x} = \frac{V_x}{V_x^*} = \alpha_1 + \alpha_2 \cdot \ln\left(\alpha_3 + \frac{\alpha_4}{\widetilde{E} + \alpha_5 \cdot \widetilde{T}}\right) + \alpha_6 \cdot \widetilde{T} \tag{3.38}$$

A bare line made by (3.39) can simply reproduce I_{sc} behavior in Fig. 3.20.

$$\widetilde{I_{sc}} = \frac{I_{sc}}{I_{sc}^*} = \alpha_1 + \alpha_2 \cdot \widetilde{E} + \alpha_3 \cdot \widetilde{T} \tag{3.39}$$

Although MPP currents look similar to I_{sc}, their curves flattens out for low E. Consequently, while (3.39) is usable for the normal E range, (3.40) is necessary to estimate the overall behavior when I_x can be either of I_M or I_{80}.

$$\widetilde{I_x} = \frac{I_x}{I_x^*} = \alpha_1 + \alpha_2 \cdot \widetilde{E} + \alpha_3 \cdot \widetilde{E}^{\alpha_4} + \alpha_5 \cdot \widetilde{T} \tag{3.40}$$

Performance of single-point models are presented in Fig. 3.21 which is after tuning $\boldsymbol{\alpha}$ while temperature drifts are removed when T range is limited.

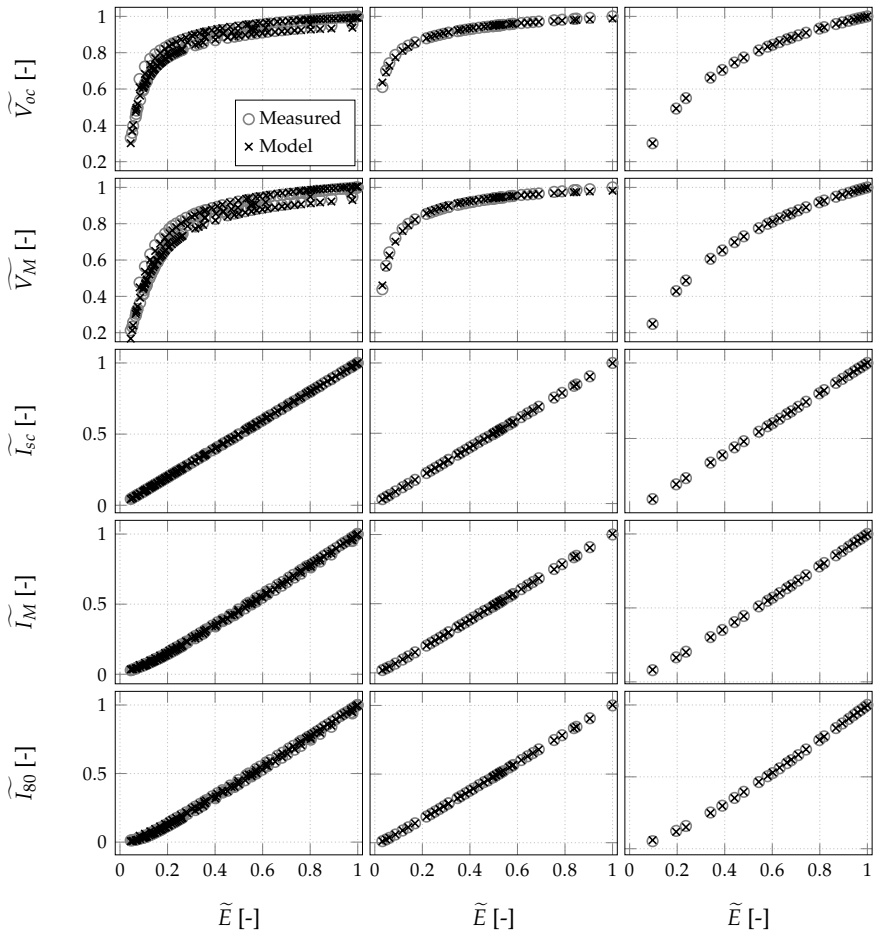

Fig. 3.21 Performance of single-point models. Left: SWL data-set with T; Middle: SCL data-set without T; Right: IWL data-set without T.

Although all models provide acceptable performance, their sensitivity to the reference point should be analyzed. In solar applications, E^* is defined very high that $\widetilde{E}$ is always less than unity. Nonetheless, highest E measured in each data-set is used here as E^* which makes a $\widetilde{E} \geq 1$ possible. Consequently, it is necessary to validate model's behavior for $\widetilde{E}$ larger than one.

To evaluate this issue, SWL data-set is simply cut out at some lower intensity. Same as before, highest available light intensity in the new data-set is used as the reference and parameters are tuned. Then the model is evaluated on the complete data-set including that section of data with higher intensities not used for the identification. Performance of two cases compared to the whole data-set performance according to the distribution of the relative error criteria can be seen in Fig. 3.22.

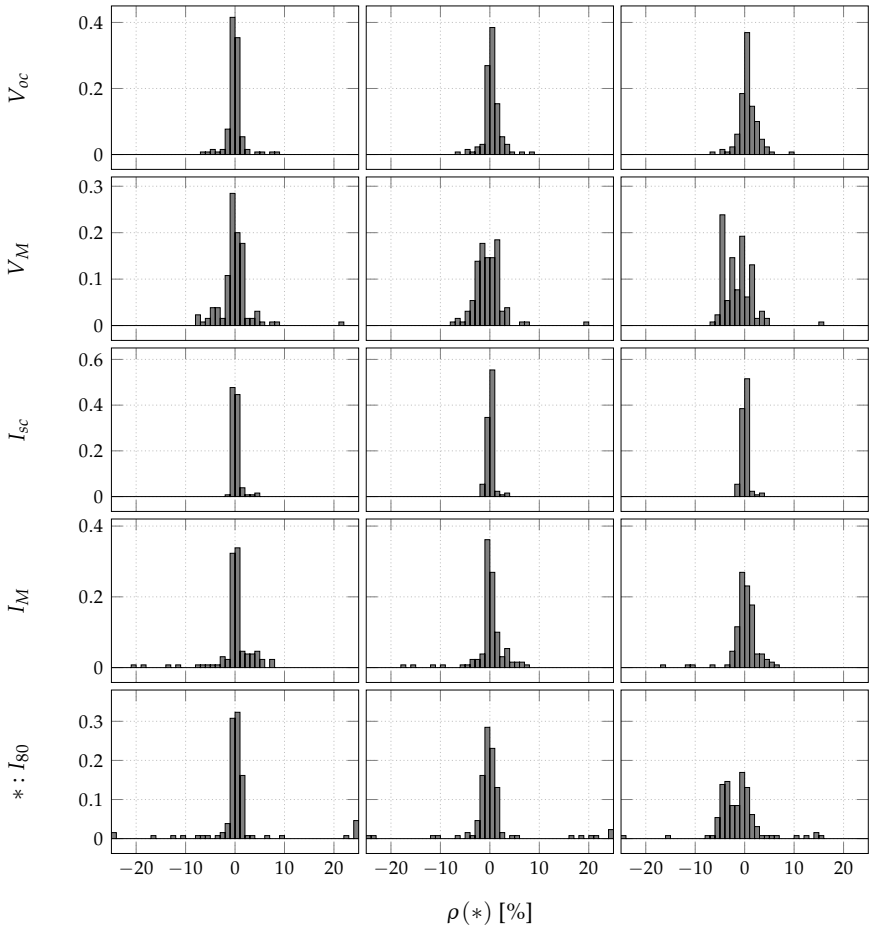

Fig. 3.22 Density of relative error distribution of single-point models. Parameters identified in models using reference at: Left: highest light intensity; Middle: 60 % of the highest light intensity; Right: 40 % of the highest light intensity.

As can be seen, although performance gets worse when reference condition is pushed to a lower light intensity, models still have a good performance with most error density around zero.

Single-point models are computationally light weight and can be used as the on-board model for embedded systems such as PhyNode. However, their lack of generality can cause concerns when the operation is deviated from the optimal condition. Therefore, a general model covering the whole I-V curve would be beneficiary to replicate all possible conditions.

3.3.5 Whole I-V curve model

Different ECMs replicating behavior of a PV module has been discussed. Although it has been claimed that 2D model is preferred for polycrystalline silicon and 1D model for amorphous silicon [119], both models will be analyzed here for the IPV application. In addition to the complexity of model, both numerical and AES based parameter identification techniques will be tested. After identification of parameters for a range of environmental conditions, general formulation for their relation will be suggested.

3.3.5.1 Numerical parameter identification

Numerical extraction of parameters in $\boldsymbol{\psi}$ is the simpler variation while it only requires the main relation of I-V in addition to some measured points from the I-V curve. However, according to the implicit I-V relation of a PV module, finding current for a voltage value adds another level of complexity. Although it is possible to reduce this with the Lambert W function for the 1D model, each current finding in 2D model requires a separate solution of implicit I-V relation. Therefore, a MATLAB function is developed which uses `fsolve` method with *trust-region-reflective* technique to solve the I-V relation for each input voltage.

In the next step, numerical optimization problem as in (3.17) has to be solved to find the parameters in $\boldsymbol{\psi}$. To make solution of this problem possible, optimization problem has to be determined. Consequently, at least data about 5 points of the I-V curve are necessary for the 1D model and 7 points for the 2D model. The most reliable selection will be to use OC, SC and MPP as the first three points. However, selection of other points can be a challenging tasks. Therefore, different combination of points has been tested.

Different methods including NRM, min optimization, nonlinear LSq and Particle Swarm Optimization (PSO) are tested to solve this numerical problem. A common outcome of all these trials with different methods is the fact that the results of these methods all depend on the initial guess. A probable reason for this phenomena is availability of multiple local minimums in the problem. Although some methods such as PSO claim to find the global minima, according to the selection of initial guesses they may require a very large number of iterations till they converge to the final global minimum point.

From different solving methods, those solutions with acceptable results reach different parameters for a single problem. However, among these solutions some values are physically not feasible, such as parasitic resistances with negative value or a very high number for n.

The first reason for these issues can be distribution of selected points from the I-V curve. Therefore, in addition to the different distribution of extra points, other dispensations such as increasing number of points distributed at every 20 % of V_{oc} has been tested. Multiple trials has shown that it is possible to find a combination of points for some specific initial guesses that help each optimization technique to reach a feasible $\boldsymbol{\psi}$. Nevertheless, it is not possible to provide a general method working on all curves in a data-set. Furthermore, it has been experienced that any increment in the number of points increases the sensitivity to the initial guesses.

To conquer these issues, 1D model is focused first here. The first issue to be analyzed is the possibility of good results with non-feasible R_s and n. Looking at effect of these parameters in Figs. 3.7 and 3.9, it can be concluded that both have influence on the OC point and the voltage source section of the I-V curve. The most related factor to this section of the I-V curve is the derivation of the curve around OC point explaining the voltage source section conduct. Therefore, to understand reason of this abnormal behavior, derivation of I-V curve around OC point has to be analyzed more deeply. To see the effect of these parameters at the derivation, it is possible [85] to reformulate the general derivation of current according to the voltage from (3.19) as in (3.41).

$$\frac{\mathrm{d}I_h}{\mathrm{d}V_h} = \frac{-\left(u + \frac{1}{R_{sh}}\right)}{1 + R_s \cdot u + \frac{R_s}{R_{sh}}}, \quad \text{when: } u = \frac{I_s}{a \cdot V_t} \cdot \exp\left(\frac{V_h + I_h \cdot R_s}{a \cdot V_t}\right) \tag{3.41}$$

Using (3.41) at OC, it is possible to explicitly explain R_s using (3.42).

$$R_s = -\frac{S_{oc} + \frac{1}{R_{sh}} + w}{\frac{S_{oc}}{R_{sh}} + w} \tag{3.42}$$

when:

$$S_{oc} = \left(\frac{\mathrm{d}I_h}{\mathrm{d}V_h}\right)_{I_h=0} \quad \text{and} \quad w = I_s \cdot \exp\left(\frac{V_{oc}}{a \cdot V_t}\right) \tag{3.43}$$

From (3.42), it is possible to analyze the changes in R_s according to the n in a way that it fulfills the slope requirement at OC. As an example, slope at OC point (S_{oc}) for the reference condition measurement of Solems IPV module is found from its I-V measurement. By solving (3.42) for different combination of other parameters, it is possible to find valid combinations of R_s and n. Result of these solutions are presented in Fig. 3.23.

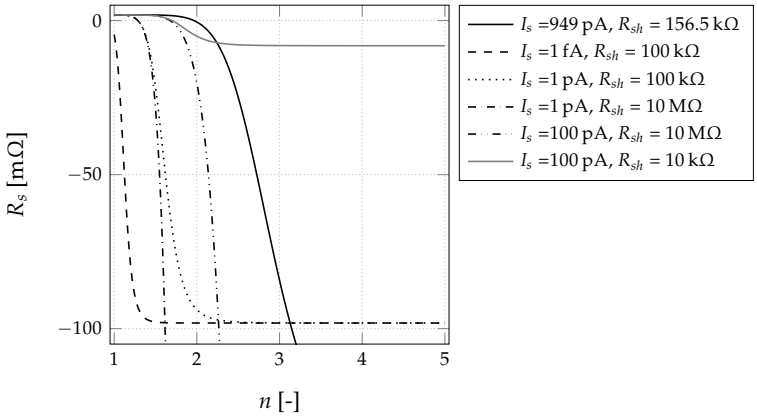

Fig. 3.23 Valid combination of R_s and n fulfilling the derivative equation at the OC point using different combinations of I_s and R_{sh}.

As can be seen in Fig. 3.23, there are a large number of possible parameter combinations. Nonetheless, multiple combinations are not feasible although they can fulfill requirements at the OC. To remove these combinations from the optimization problem, parameters boundaries have to be introduced. Consequently, only those optimization techniques are allowed which are able to handle problems with boundaries.

Different values for the boundaries have been discussed in literature. In spite of minor discrepancies, the most common values mentioned are collected in Table 3.4. However, these values are mainly suggested for the solar application with large current outputs in the scale of few amperes.

Table 3.4 Common bounds on PV model's parameters [129].

Parameter	Lower limit	Upper limit	Unit
R_s	0	0.5	[Ω]
R_{sh}	0	100	[Ω]
I_g	0	1	[A]
I_s	1×10^{-12}	1×10^{-6}	[A]
n	1	2	[-]

Although these values are commonly accepted for solar applications, there is no clear reasoning for them except for the lower limit of the resistances. In addition, use of these values on IPV data-sets leads to the saturation of parameters in multiple cases. Moreover, some of these boundaries are even not logical for IPV applications. For instance, it is very probable for a small IPV module to have an output current in the scale of few µA. Therefore, a upper limit of I_g =1 A is extremely over-scaled. Simultaneously, such a range of I_s is in the same scale of the output current. Therefore, a more general boundary definition is necessary for IPV applications.

Use of PVNS comes handy in such conditions and helps to analyze parameters regardless of their actual values and provide bounds considering a general form. In addition to the restriction on positive resistors, it is known that the R_s inversely affects the curve slope at the OC while R_{sh} modifies the slope at SC. Considering an ideal case with $FF = 1$, it can be said that the voltage source section is totally perpendicular, leading to a zero R_s. In the ideal condition, R_{sh} has to be theoretically infinite to make a totally flat current source section possible.

From measurements in ultra-low light condition seen in (3.36), it can be concluded that the I-V curve is always convex. Therefore, worst case scenario will be at $FF = 0.5$ with a direct line between SC and OC. According to the reverse relation, this will lead to a limiting bound for both resistors equal to 1 Ω. However, this will be the lower bound for R_{sh} and upper bound for the R_s. Although these are the logical boundaries for the resistances, it is possible to tighten them and improve the identification speed even further. Considering the convex form, it can be said that the lines connecting SC and OC to the MPP are always below the curve itself. Therefore, it is possible to use the slope of these lines as the limits for the resistances.

From scaling process into the PVNS, I_g has a value near the unit. Therefore, it is suggested to consider a range of 0.9 A to 1.1 A for this current.

There are multiple debates on the selection of values for the n. While a range between 1 to 2 is the most common, higher values have been suggested [151, 152] up to 5 [72, 153] and even 8.6 [154]. However, application of the upper limit of 5 has shown saturation for many low lighting conditions. Therefore, use of 10 as the higher limit for this value is suggested. Nonetheless, all values larger than 5 have to be considered with extra care. It has to be added that this pre-knowledge about n is the main reason for the usage of a and not including N_s into the n value.

The only physical knowledge available for the selection of bounds for I_s is that it has to be a small positive value and not larger than the I_g. Therefore, suggestion for this parameter is the range of $[\epsilon, I_g]$. Consequently, boundaries for the parameters in $\boldsymbol{\psi}$ in the PVNS are presented in Table 3.5.

Table 3.5 Suggestion for bounds for PV model's parameters in the PVNS.

Parameter	Lower limit	Upper limit	Unit
I_g	0.9	1.1	[A]
R_s	ϵ	$(V_{oc} - V_M)/I_M$	[Ω]
R_{sh}	$V_M/(I_{sc} - I_M)$	∞	[Ω]
I_s	ϵ	1.1	[A]
n	1	10	[-]

Implementation of nonlinear LSq with *trust-region-reflective* in MATLAB is used for solving the optimization while it is able to handle the boundaries.

Next step is a general suggestion for the initial values assuring convergence to the minimum, regardless of other factors. According to the large difference in the scale of data, providing fix values applicable on the whole data-set is not possible and initial values have to be extracted from the I-V curve. For the I_g, the easiest value would be use of the I_{sc} which simply can be considered as unit in the PVNS.

Value of resistances directly affect the slope at SC and OC. Therefore, best suggestion will be use of slopes. In case only single-points are available, these values will be simply the boundary values from Table 3.5. However, when the measurement of the whole I-V curve is available, this can be calculated with more accuracy. This is a reason why in Algorithm 1 current is measured for a bit further than these limits. Anyhow, in case non of these methods is possible, use of 1 is the simplest value for these parameters.

For the saturation current I_s, no exact value can be logically argued. However, multiple trials on the available data-sets had shown 1 pA a proper suggestion for the curves in the PVNS. In the case of 2D model, values of 1 nA and 1 mA in the PVNS can be suggested .

Same as for the I_s, no explicit initial value for the n can be defined. However, based on different trials, using half of the upper bound of the n (equal to 5) is a good initial guess in the PVNS. For the 2D model, a unit secondary n can be suggested.

Using PVNS in addition to the mentioned bounds and initial values, it is possible to identify parameters in $\boldsymbol{\psi}$ using nonlinear LSq. These settings have shown very reliable performance for even higher number of points fed to the optimizer. Therefore, a set of 200 equidistant points over the voltage axis are used for each I-V curve to be tuned. Performance of both 1D and 2D models on two extreme examples from SCL data-set are presented in Fig. 3.24.

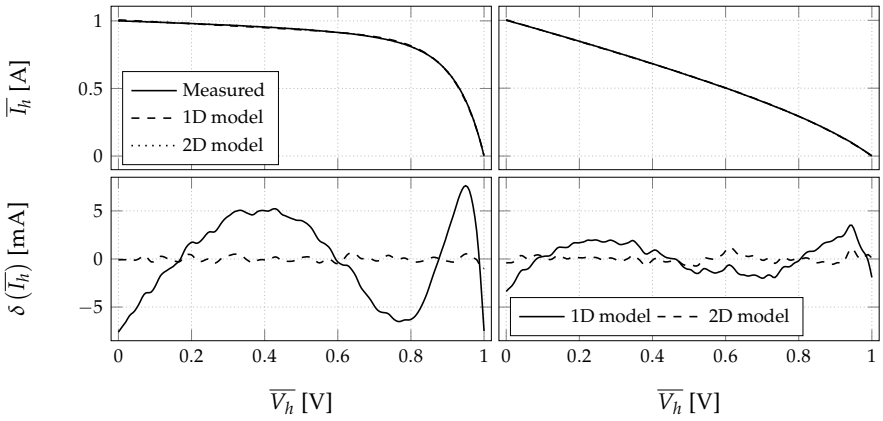

Fig. 3.24 Performance of numerically tuned 1D and 2D models on two extreme examples of I-V curves from SCL data-set presented in PVNS. Left: at 608.5 lx, 299.3 K; Right: at 19.4 lx, 299.7 K.

As can be seen in Fig. 3.24, both models perform with errors in the scale of few thousands of the signal. However, a general trend can be seen in the 1D model through all data-sets, while 2D model's error seems to be only the remaining noise. Even though, it should not be forgotten that the 1D models are still in a very good performance range. Therefore, a trade-off has to be done based on the application in between accuracy and model's complexity. Distribution of relative error factor MANE for both models applied on all data-sets is presented in Fig. 3.25.

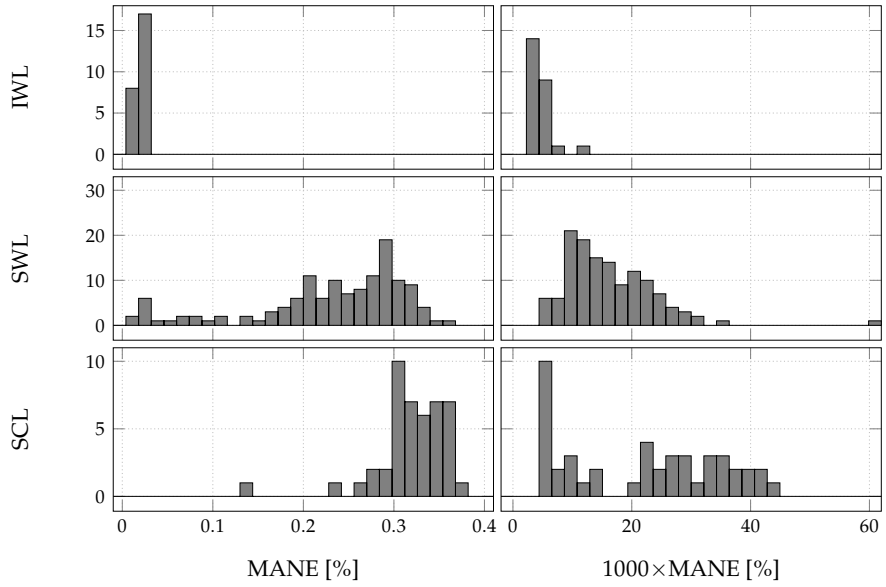

Fig. 3.25 Density of MANE distribution for: Left: 1D model; Right: 2D model.

Considering these distribution of performances, it can be seen that all relative errors are in very small range, less than 1 % of MANE. In addition, it is clear that the 2D model is doing a much better job compared to the 1D model due to its extra degrees of freedom. There are few examples of the 2D model which the performance is worse than the rest. Though, even these cases have better performance compared to their 1D model alternatives.

Next step after parameter identification is to find a relation for each parameter according to the changes in the environmental conditions. The behavior of each parameter for all data-sets can be seen in Fig. 3.26.

Analyzing these graphs, except a very limited number of points, parameters of all data-sets show a specific pattern. I_g has a linear behavior with its slope dependent on the IPV module. As can be seen, the slope is the same for both data-sets of the Solems IPV module while slope of the IXYS IPV module is different in spite of similar lighting source as for the SWL data-set.

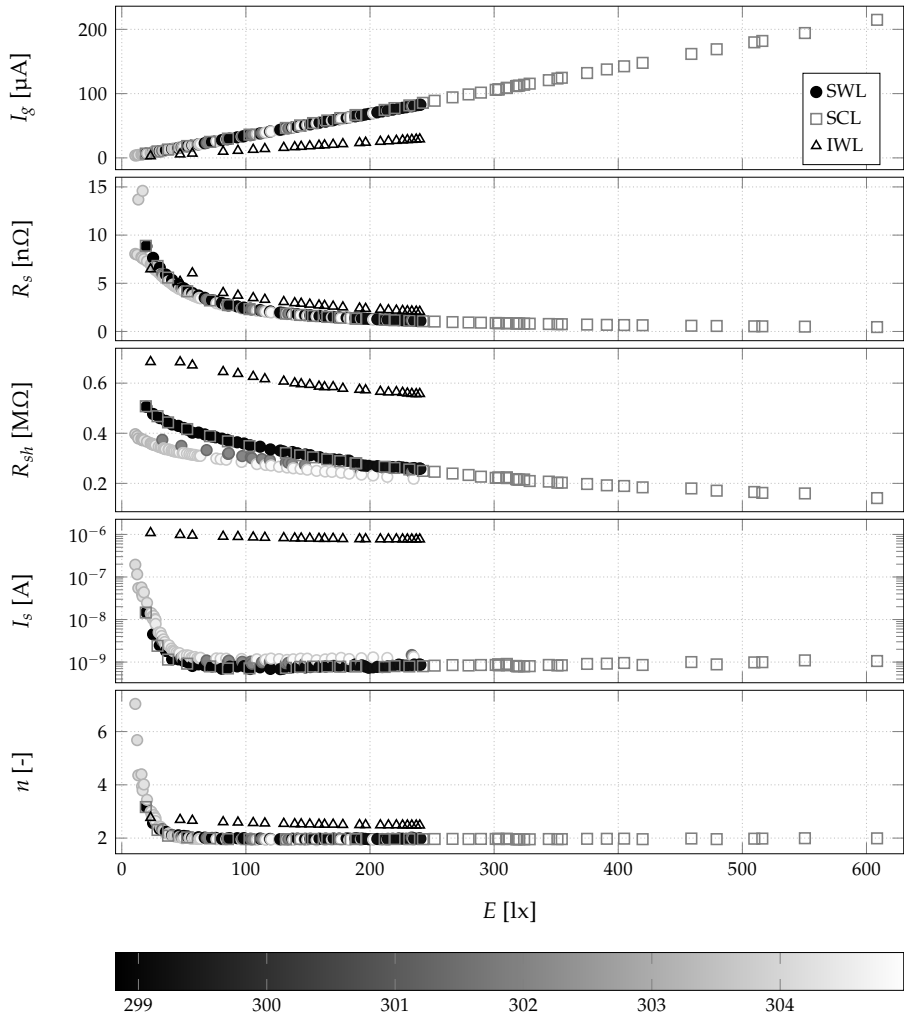

Fig. 3.26 Changes in 1D model parameters according to the light intensity for all data-sets. Color of SWL points shows temperature in K as in the color-bar.

R_s for all data-sets have the same behavior while the bias is different according to the IPV technology. While R_{sh} has also a clear behavior, effect of IPV type and the temperature are more visible. Finally, both I_s and n show a roughly similar behavior, specially for the low light condition, though at totally different scales.

Due to claims for the better performance of the 2D model, it will be beneficiary to use these parameters for the environmental behavior. Hence, behavior of the parameter for the 2D model extracted from all data-sets are presented in Fig. 3.27.

Monitoring changes in these parameters, it can be said that the behavior of the I_g remains linear similar to the 1D model. However, R_s has different

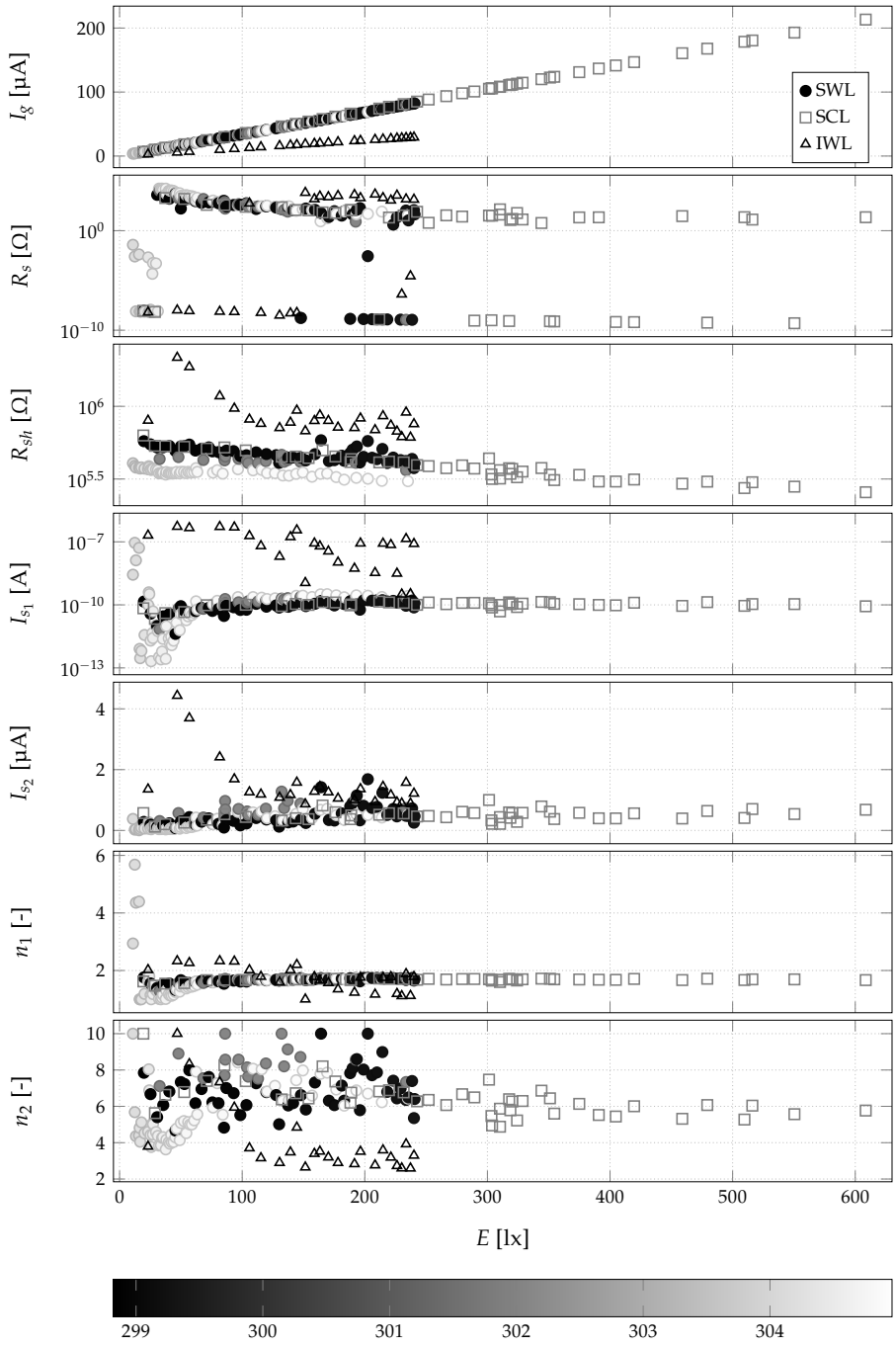

Fig. 3.27 Changes in 2D model parameters according to the light intensity for all data-sets. Color of SWL points shows temperature in K as in the color-bar.

behaviors even with totally different scales. R_{sh} has a more unified behavior with some dependencies to the temperature as well.

Behavior of the I_{s_1} is roughly clear for the normal lighting conditions. Nonetheless, its behavior for low light condition with less than 100 lx is not specific, even for the same temperature range. In contrast, I_{s_2} can be considered more linear for the Solems IPV module with some temperature effect on the slope of line. However, its behavior for the IXYS IPV module is not clear.

For the n_1, a roughly linear behavior can be seen in the normal lighting condition, with upward changes for the low light condition. Furthermore, except few examples which the n_2 is saturated to the higher bound, it can be considered that the value is roughly constant for each IPV module.

Considering all these behaviors it is hard to clearly define explicit formulations for 2D model's parameters. This can be a sign that the number of available degrees of freedoms in the 2D model are more than the real physical parameters explaining the behavior of an IPV module. Consequently, optimizer uses these extra possibilities to numerically tune the parameters into the best possible result. Yet, this is with the cost of ignoring the big picture of the internal behavior. This phenomena is also known as *over-fitting* in numerical regression systems. Anyhow, it is possible to use analytical tuning method, namely AES-based identification which perhaps is able to solve this concern. Therefore, this method comes hereafter.

3.3.5.2 AES parameter identification

An alternative method to identify parameters in $\boldsymbol{\psi}$ is to rely on the analytical formulas extracted from the model's physical knowledge as was explained in (3.18), (3.20) to (3.22) and (3.24). This set of equations can be implemented to reduce the number of points required for the identification of parameters. Considering this set, equations in (3.18) are basically same as the numerical method while they rely on the exact values of keypoints. However, rest of equations in this set replicate the behavior of the I-V curve obviating the need for values at further points. Techniques are available to find slopes without measuring extra points. However, they all add another source of inaccuracy to the parameter identification. Hence, exact extraction of slopes are used here while the whole I-V curve is available in the data-sets.

Although it is possible to calculate the derivation at exact points, availability of noise in measurements can cause large errors. To conquer this issue, it is better to use a larger section of the curve and find an average slope at each of them. Yet, this range has to be selected very carefully due to major difference in the slope. As an example, slopes found using deviation of 5 % and 20 % from the V_{oc} are compared in Fig. 3.28.

After multiple trials on all data-sets, best reliable performance is when the slope at SC is found with deviation of 20 %, 2 % at OC and 6 % at MPP. All these deviations are in relative voltage according to the V_{oc}.

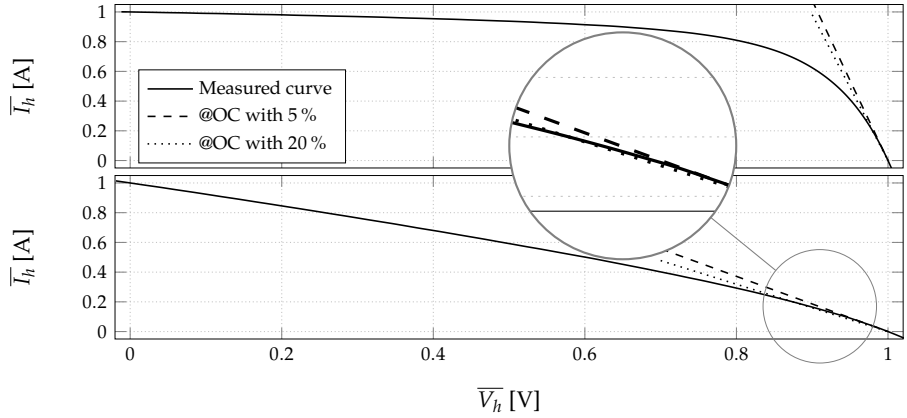

Fig. 3.28 Slope finding at the OC points and resulted slope for high and low light intensity examples using 5 % and 20 % deviation from OC.

Next, parameters have to be tuned to reduce the error found for each equation. However, errors are in different scales because of dissimilar nature of equations. For instance, small R_s leads to a large slope at OC and an error in the scale of 10×10^6. In contrary, large value of R_{sh} leads to small values on the slope equation at SC. Therefore, a normalization is added to bring errors into the same scale. Hence, signal values are divided to the I_{sc} while each slope equation is divided to the measured slope at the related point.

With use of six equations, actually an over-determined set of equations is made for the 1D model which has only five unknowns in $\boldsymbol{\psi}$. Hence, it is possible to leave a slope equation out and make a determined equation set. Comparison of tuned models with distinct equations on an example I-V curve can be seen in Fig. 3.29 presenting difference in performances.

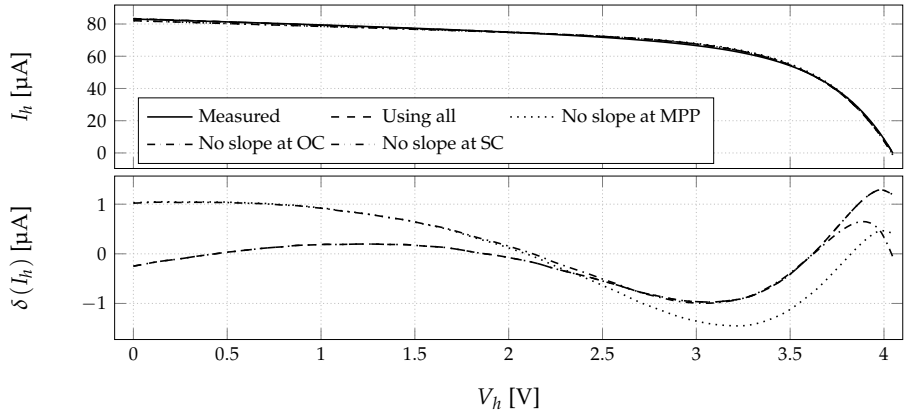

Fig. 3.29 Different 1D models' according to inclusion of slope equation in the AES.

To compare the performance of these different sets of equation, MANE factor for these four combinations in addition to the numerical method are presented in Fig. 3.30 for SWL data-set.

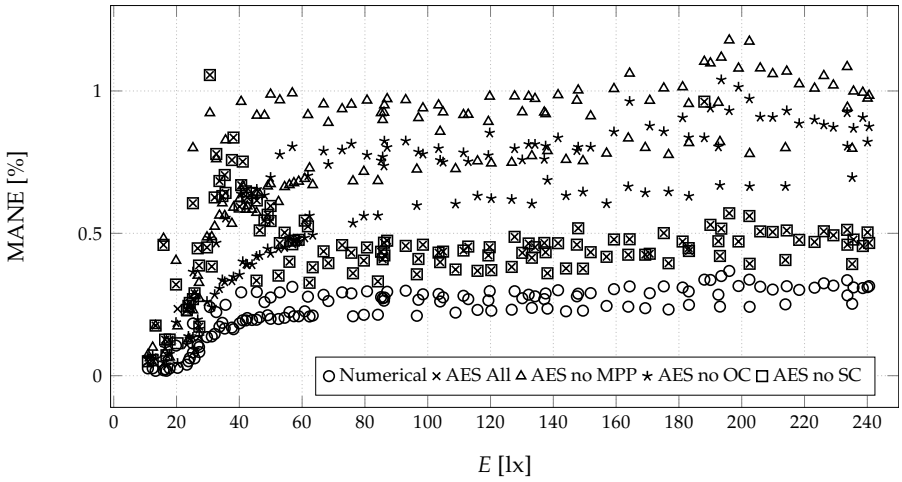

Fig. 3.30 Performance of over-determined and different determined AESs after removal of extra equation, compared with the performance of numerically tuned 1D models.

From Fig. 3.30 it can be seen that the performance of AES with all equations is exactly the same as the case when the the derivation equation at SC is not used. Therefore, it can be concluded that this equation has no effect on the performance of the 1D model in the IPV case. In addition, it is clear that the use of derivation at OC is critical and its removal increases the overall error specially for the normal lighting range. Furthermore, removal of derivation at MPP makes the performance the worst possible. All in all, in case AES tuning has to be used for 1D model, it can be suggested to use all equations or remove the derivation at SC for the computational simplicity. In addition, it can be said that the overall error is lower for low light condition. However, its increase flattens out after a bending point where the common lighting intensities are.

In the next step, found parameters between two methods have to be compared. Therefore, Fig. 3.31 shows comparison of all identified parameters from numerical method and the over-determined AES including all equations. It can be concluded that the overall behavior of all parameters is similar, regardless of the identification method. However, there are small tuning differences in some parameters which can be simply ignored. In these cases found parameters from numerical method are more reliable because it is based on more points from the curve.

There is a complexity when AES based identification has to be applied on the 2D model. While seven parameters have to be identified, only six equations are available; three equations based on the single points value and three based on their derivations. However, by using (3.24) which is based on the fact of

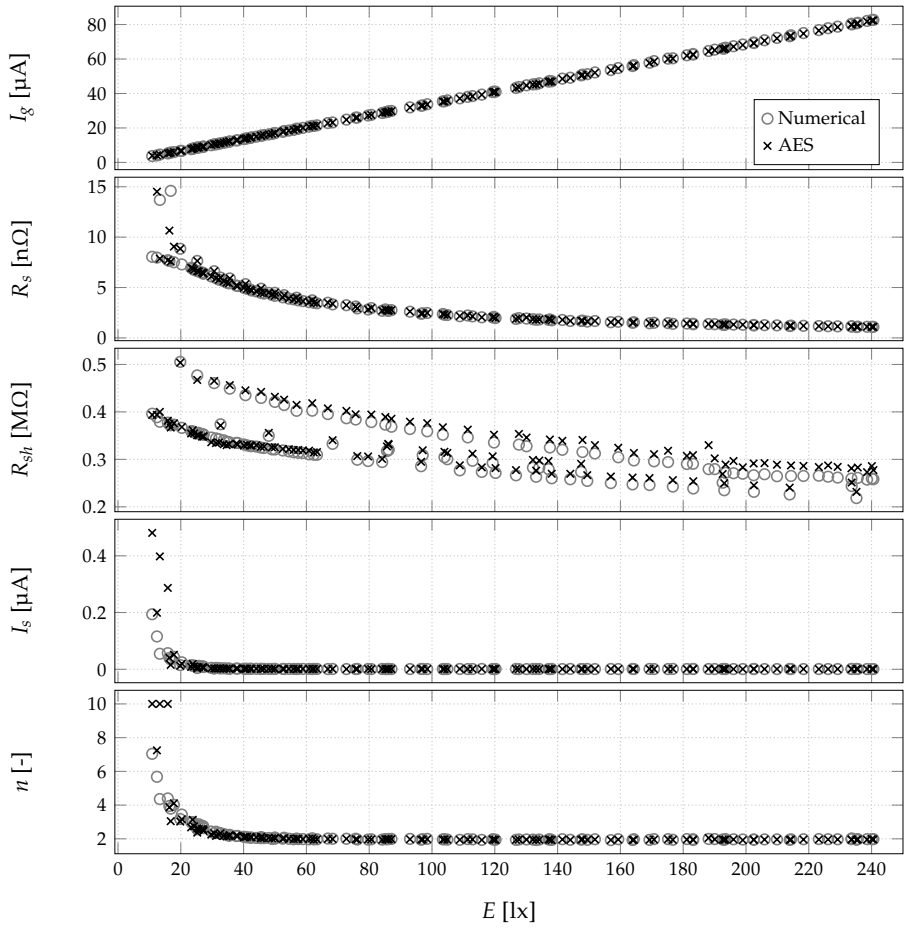

Fig. 3.31 Comparison of identified parameters for the 1D model using AES with all equations and numerical method for SWL data-set.

zero derivation of power curve according to the voltage, a determined AES with seven equations can be made. Using this set of equations in addition to the boundary conditions and suggested initial values, parameters for SWL data-set as in Fig. 3.32 are extracted.

Comparing these identified values with the values found from the numerical tuning in Fig. 3.27 it can be seen that the behavior of I_g and R_{sh} are exactly the same. Although R_s is in both methods divided into two branches, AES-based identified R_s are more in the lower branch and a more acceptable range. Behavior of diode's parameter have to be analyzed together. As can be seen, n_1 has a roughly constant value around 2. But, it reduces slowly for smaller E values and gets saturated to the lower bound of 1 for intensities lower than 40 lx. This results in limited I_{s_1} as well, though there is a high limit on this

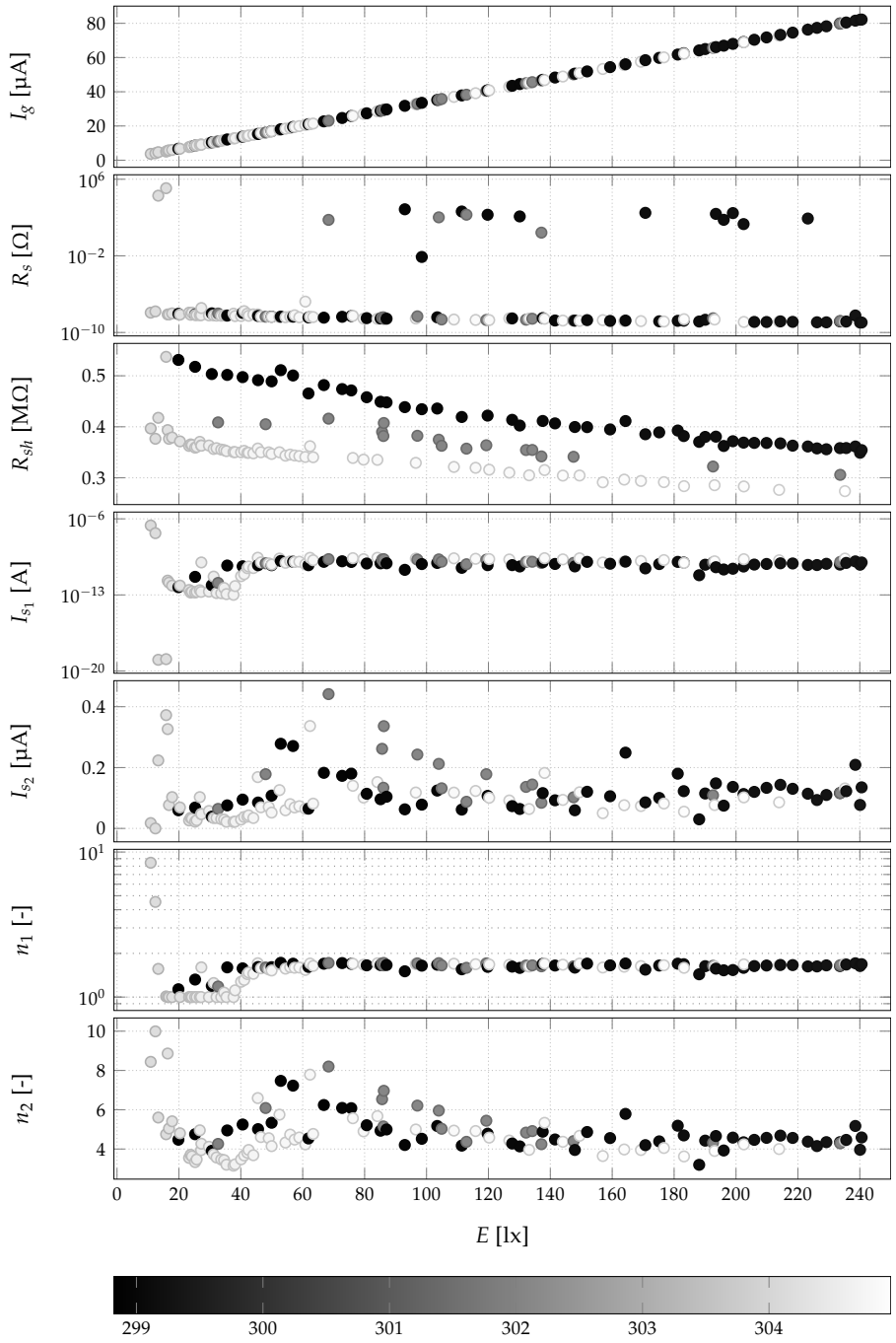

Fig. 3.32 Distribution of 2D model's parameters identified using AES-based optimization for the SWL data-set. Color shows temperature in K as in the color-bar.

value. Nevertheless, behavior of secondary diode looks promising and shows some kind of logical behavior.

Considering all these aspects, accuracy of different models and methods, in addition to the need for the validity of model for the whole range, it is decided to use 1D model. Not only it reaches similar outcome regardless of identification method, it provides a more smooth behavior for the whole light intensity range. Moreover, in addition to its simplicity, it is possible to formulate it in an explicit way as discussed formerly. This will make its implementation less resource intensive. Therefore, relation of the parameters in $\boldsymbol{\psi}$ for a 1D model according to the environmental factors as shown in Fig. 3.26 will be formulated.

Comparison of Solems IPV module behavior under two different lighting types (in Fig. 3.26) shows direct dependency to E. However, for the consistency of the methodology with the single-point method, relative parameters will be used here. While relative temperature can be explained similar to the single-point models, multiple trials have shown easier formulation when temperature difference is used. This difference can be simply defined according to the temperature at reference condition by $\Delta T = T^* - T$.

Considering behavior of relative parameters, multiple form of functions have been evaluated and finally empirical forms as in (3.44) for all parameters can be suggested.

$$\widetilde{I_g} = \frac{I_g}{I_g^*} = \alpha_{g1} \cdot \widetilde{E} + \alpha_{g2} \cdot \Delta T \tag{3.44a}$$

$$\widetilde{R_s} = \frac{R_s}{R_s^*} = \frac{\alpha_{s1} + \alpha_{s4} \cdot \Delta T}{\alpha_{s2} + \alpha_{s3} \cdot \widetilde{E}} \tag{3.44b}$$

$$\widetilde{R_{sh}} = \frac{R_{sh}}{R_{sh}^*} = \frac{\alpha_{p1} + \alpha_{p6} \cdot \Delta T}{\alpha_{p2} + \widetilde{E}} + \ln\left(\alpha_{p3} \cdot \widetilde{E} + \alpha_{p5}\right) \tag{3.44c}$$

$$\widetilde{I_s} = \frac{I_s}{I_s^*} = \alpha_{i1} + \alpha_{i2} \cdot \widetilde{E} + \frac{1}{\alpha_{i3} \cdot \widetilde{E}^{\left(\alpha_{i4} + \alpha_{i5} \cdot \widetilde{T}\right)}} + \alpha_{i6} \cdot \Delta T \tag{3.44d}$$

$$\widetilde{n} = \frac{n}{n^*} = \alpha_{n1} + \alpha_{n2} \cdot \widetilde{E} + \frac{1}{\alpha_{n3} \cdot \widetilde{E}^{\left(\alpha_{n4} + \alpha_{n5} \cdot \widetilde{T}\right)}} + \alpha_{n6} \cdot \Delta T \tag{3.44e}$$

Prediction of parameters using these equations after tuning $\boldsymbol{\alpha}$ values for SWL data-set are presented in Fig. 3.33. To be noted that parameters of the I-V curve with maximum light intensity are used as the reference point.

Considering this good performance, 1D model in its general form in addition of changes in its parameters according to (3.44) can be accepted as a valid model for the IPV applications. These models will be used for the evaluation of the PhyNode's IPV in the context of PhyNetLab.

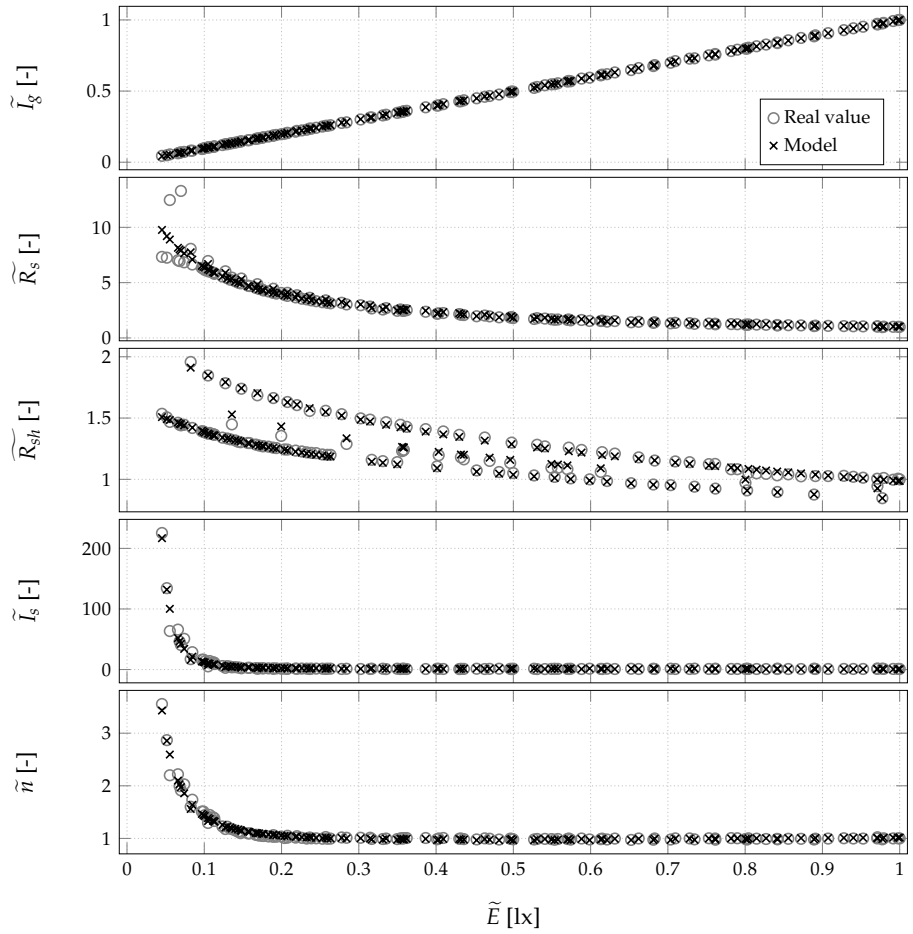

Fig. 3.33 Performance of parameters' models at different environmental conditions on SWL data-set including temperature effect.

3.4 Modeling PhyNode's IPV in PhyNetLab

For evaluation of the proposed models (single-point and detailed whole-curve) in real world, PhyNetLab is used as a warehouse test-bed. At first, overall light intensity of the lab in different heights, positions and orientation is measured. For this purpose a simplified version of the board from Fig. 3.15 is used. This version is able to measure integrative photometry light intensity and temperature using the Raspberry Pi in a remote way without the need for a main PC. Two of this boards are mounted on a materials handling box with IR reflective markers attached which are used within the motion capturing indoor localization system. To span the whole PhyNetLab, this box is mounted on a mobile robot which drives automatically. The overall setup of this light measurement system is shown in Fig. 3.34.

Fig. 3.34 Mobile setup for automatic measurement of environmental parameters in PhyNetLab. Two measurement boards enable measurement at different radius from the center point. Box has a set of IR reflective markers which enable exact positioning of the box at each time in PhyNetLab.

Robot is programmed in a way that it starts at a corner and measures in a raster form at specific points. It drives to the first measurement point, triggers the measurement on the board and rotates 360°. After a complete rotation, it stops the measurement and drives to the next point in the raster and repeats this procedure till the whole PhyNetLab is spanned. Measured integrative photometry light intensity collected in this way is presented in Fig. 3.35.

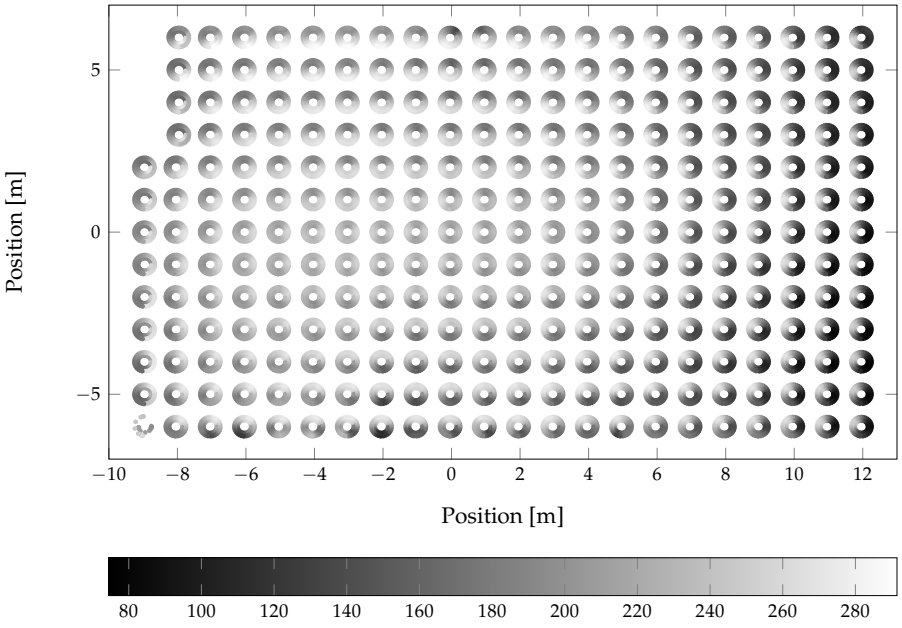

Fig. 3.35 Measured integrative light intensity at the lowest level in PhyNetLab. Similar measurement is done on other levels. Color of each point shows E according to the values from color-bar in lx.

This procedure is repeated for different levels of boxes to have information for all possible operational points of PhyNode. Not only this data can be

used for simulation purposes in the future light analysis, it provides an understanding of the light intensity in a real application field. Using this data, it had been found that the light is not homogeneous and changes in a range between 50 lx to 500 lx in different positions and heights.

In addition, to analyze the I-V curve and extract models' parameters, complete measurement setup as in Fig. 3.15 is used again afterwards. Employing information from Fig. 3.35, the I-V measurement setup has been placed in different positions of the lab and more than 120 experiments including I-V curve, integrative and spectrometry light intensity and temperature have been measured as the real world evaluation data. These data is collected during multiple days to avoid any daily bias or temperature drifts. This data-set includes light intensities between 244 lx to 494 lx and temperature between 298 K to 302 K. Distribution of this data-set can be seen in Fig. 3.36.

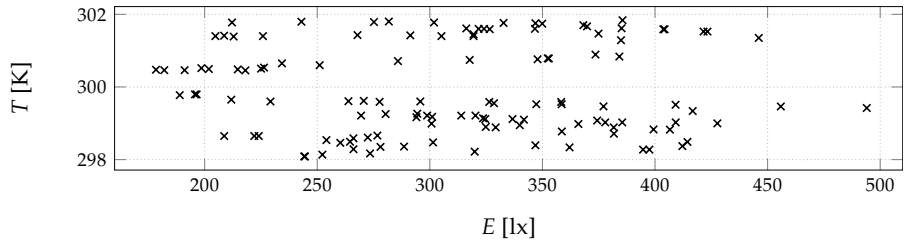

Fig. 3.36 Distribution of environmental conditions of measured examples in PhyNetLab.

Although this is a roughly large data-set, it is more acceptable to divide it into two parts for tuning and evaluation. Therefore, 30 % of measured data is randomly selected as the tuning set while the whole set is used for the evaluation. In this way, application of models is more realistic and evaluation can be considered more reliable.

3.4.1 Application of single-point model

Using 37 examples selected randomly from the data-set in PhyNetLab, parameters for all single-point models explained in (3.38) to (3.40) are tuned. Performance of tuned models on the complete data-set is as in Fig. 3.37.

As in Fig. 3.37, all single-point models are able to predict keypoint values with a very good performance for the whole data-set. Larger relative current errors are due to very small value of I_{sc} (around 170 µA at highest).

It has to be noted, this is just one example of multiple possible selection of tuning sets. Repeating this random selection multiple times, it had been found that the relative errors are always lower than 5 % for all keypoints as long as 30 % of data-set is used for tuning. Although it is possible to reduce number of measurements in the tuning data-set, it has to contain at least 6 measurements to enable a determined set of equations for the tuning. Anyhow, it is suggested

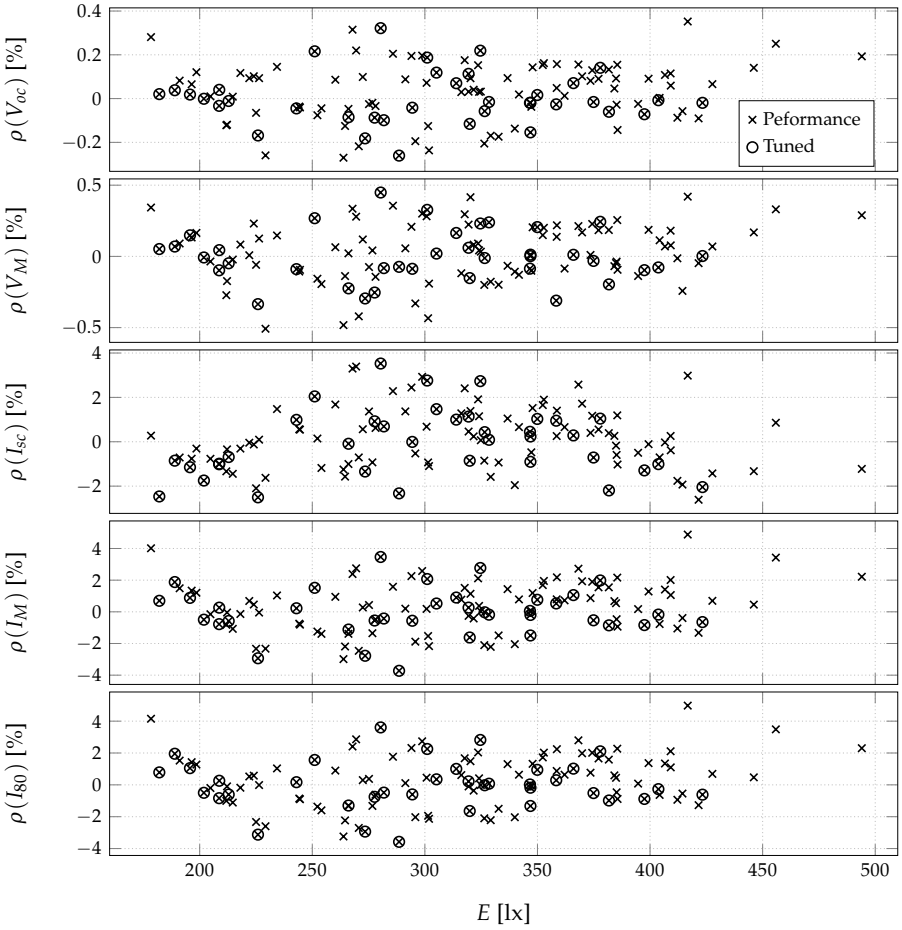

Fig. 3.37 Performance of single-point models on the PhyNetLab evaluation data-set. Only randomly selected 30 % of data shown with circles are used for parameter tuning.

to include at least double this size with a roughly unified distribution over the whole range of E and T.

3.4.2 Application of whole-curve model

In the last step, performance of the whole-curve model for the PhyNetLab data-set has to be evaluated. Same as for the single-point models, a 30 % subset of data is used for the tuning of the parameters in $\boldsymbol{\psi}$ and $\boldsymbol{\alpha}$ subsequently. Top layer of the model calculates the $\boldsymbol{\psi}$ using tuned $\boldsymbol{\alpha}$ parameters and pass them to build a 1D I-V relation. Current value found using this relation is compared with the measured I-V curve to find the MANE for that specific curve. Application of this method on the whole data-set shows distribution of error as presented in Fig. 3.38 with an average MANE value of 1.2947 %.

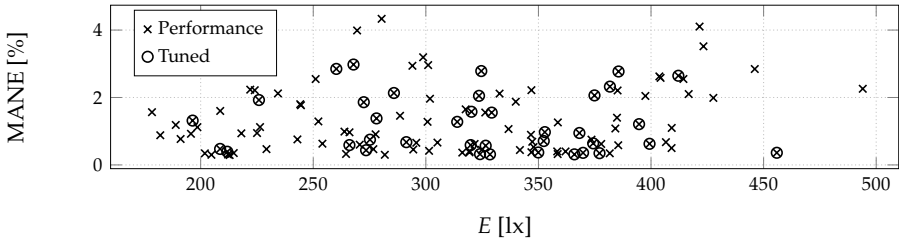

Fig. 3.38 MANE of whole-curve model on the evaluation data-set collected inside PhyNetLab. Only randomly selected 30 % data shown with circles are used for parameter tuning.

Same as for the single-point evaluation, this procedure has been repeated multiple times with different random tuning experiments, always reaching a highest MANE less than 6 %. In addition, for tuning parameters in (3.44) at least 6 examples are required to have a determined LSq problem. However, it is again suggested to use at least double this amount of I-V curves.

Chapter 4
Battery Modeling

. . . , not everybody runs on batteries, Tony!

—Pepper Potts

Abstract
This chapter is to provide models for the behavior of PhyNode's battery. For this development, first a comparison of available energy storage systems is provided. Then, basic principles of battery systems and common terminology for this chapter are explained. State-of-the-art research for modeling batteries is reviewed afterwards in addition to the typical methods for estimation of the battery's state of charge.

Focusing on the PhyNode's battery, its specifications are reviewed in addition to the analysis of its real power demand measured during operation. Next, a setup used for accurate measurement amid modeling and evaluation is explained. After measurement of the battery terminal voltage under different loads, relation between voltage and state of charge is analyzed in both continuous and discrete manners. Then differences of both methods are explained by comparing the outcoming relation from them.

For the model implementation, effects of aging and current are explained and formulated to enable estimation of the state of charge as accurate as possible. Model is completed by identification of dynamic parameters for the whole range of the battery operation.

To evaluate both on-board and detailed models battery signals are measured while two different load types are applied to it. Both models are evaluated on these measurements. Meanwhile performance of the detailed model is improved further by application of a dynamic aging factor during a discharge process.

Application of on-board model on the PhyNode's evaluation data-set has a RMSE of 0.3832 % to predict the battery status while system level detailed model performance has a RMSE of 0.075 % on the relative error.

4.1 Introduction

Advancement in the ULP devices has reduced energy requirements of modern embedded system. Yet, that small energy demand still has to be supplied from a source. Furthermore, size and weight restrictions specially for IoT systems, makes possible cable-based solutions not desirable. Consequently, use of small and lightweight ESS has been analyzed. While integration of EH is suggested to tackle the energy balancing issue, some form of ESS is still required as a buffer. Though, its size is mostly reduced compared to a solution without EH. This ESS is to assure uninterrupted operation during periods which the harvested energy cannot directly fulfill the demand.

Energy can be stored in different forms, classified into mechanical, electrochemical, chemical, electromagnetic and thermal [155]. This diversity makes selection of an appropriate storage solution for each application non-trivial [40]. System designers have to consider multiple factors and balance them with the storage's characteristics. The most critical factor for an ESS is the available energy, measured in joule (J) or watt hour (W h). Another key element is the density of this energy based on the size. Therefor, *specific energy* combines them as a ratio of the energy to the weight.

For embedded solutions, power has to be sufficiently available in the electric form. Although maximum current load can be used to show this factor, maximum deliverable power at each time instant is more common due to non constant voltage of some ESS. Similar to the energy, power density can be defined using the *specific power* as a ratio of the power to the weight.

A practical tool to compare ESS with each other is the *Ragone plot* showing relation between specific power and specific energy [156]. An example of such plot for embedded systems' storage devices is presented in Fig. 4.1.

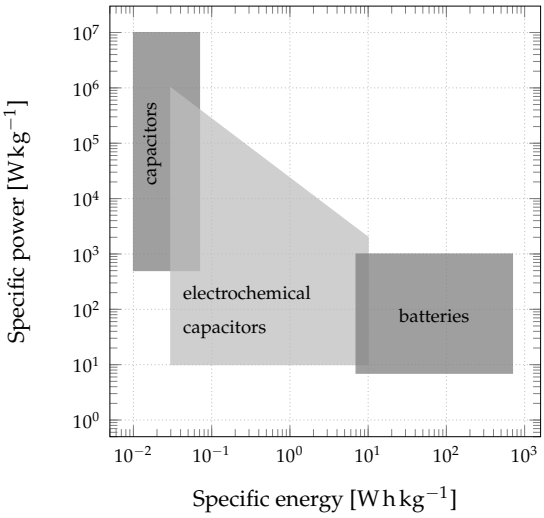

Fig. 4.1 Ragone plot for common ESS devices used in embedded systems design, comparing specific energy and specific power. Reproduced from [25].

From Fig. 4.1, capacitors provide a high specific power at low specific energy. They can be optimal for cases with very short operational duration and high peak current demands. This is common for applications with periodic short burst actions commonly known under the name of battery-less applications. They are in a wide range from contact-less smart cards and RFID tags to wildlife population monitoring [157]. Capacitor based ESS has the benefit of lower weight and size, cheaper production, high reliability while it can be disposed more environmentally friendly.

Looking at Fig. 4.1, batteries and super-capacitors are somehow in the hot-spot. They are well balanced and can provide an acceptable power while having higher specific energy than capacitors. System designers have to decide between these two types according to their requirements. Super-capacitors are commonly selected when current demand is high, while batteries can gear up a more lasting system due to the higher specific energy.

Considering smaller specific energy of capacitors, their use in combination with EH solutions is more feasible. However, balancing the harvested energy, capacity and power demand is critical. In case that not enough energy can be harvested in time, it is very probable to miss an operation cycle in a battery-less system. While this is tolerable in some applications, others such as industrial case of PhyNode cannot afford this reliability reductions. Consequently, batteries are used in PhyNode and will be considered hereafter.

4.1.1 Fundamentals of batteries

Batteries have different technologies according to their design and field of use. However, regardless of the design, they can be divided into two major categories of *primary* and *secondary*. Their key difference is the possibility of reversing the internal process to recharge.

Batteries are galvanic cells storing and releasing electric energy from electrochemical reactions through alteration of chemical bonds [25, 158]. They are made of two chemically different electrodes with an ion-conducting electrolyte in between [25]. Main responsibility of the electrolyte layer is to prohibit migration of electron while allowing transfer of ion [158]. Each electrode is responsible for one bond operating complementary to the other. Oxidizing with respect to reducing happens at the positive electrode (*cathode*) while reducing with respect to the oxidizing is referred at the negative electrode (*anode*) [158]. These electrodes are connected to the current collectors which are the battery terminals. As soon as a load is connected to the terminals, chemical reactions occur and build a voltage between electrodes, making ions travel through the electrolyte. Simultaneously, electrons flow through the external circuit from anode to the cathode. In secondary batteries, possible reverse reaction is induced due to the incoming energy to the battery.

It is common to name batteries according to the material used for their electrolyte. Though less liquid electrolyte becomes generally less ionically

conductive, few exceptions are available which are currently a hot research topic [158]. Semi-solid gel, solid polymer or even solid crystalline material are some of these electrolytes [158]. Using these electrolytes enables production of thinner batteries.

Lead-acid batteries are a very common secondary battery type, mostly known for their integration in automobile electric systems. They can provide energy during start phase and get recharged using a generator coupled into the combustion engine. Meanwhile, there are diverse technologies available for building secondary batteries such as Li-ion, nickelmetal hydride (NiMH) and nickelcadmium (NiCd). Ragone plot in Fig. 4.2 shows an abstract general comparison of some of these technologies.

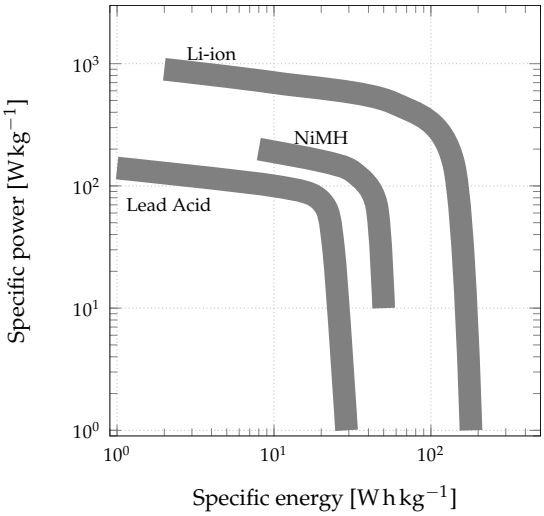

Fig. 4.2 Ragone plot for comparison of common secondary battery technologies. Based on [156, 159].

Considering Fig. 4.2, Li-ion batteries can be considered as the winners compared to the others. The main reason behind higher energy density of Li-ion cells is their higher voltages (about 4 V) reached by use of non-aqueous electrolytes. In contrast, most aqueous cells can reach less than 2 V [160]. There are claims such as in [156] that Li-ion batteries are on top of any comparison chart. However, their advantages comes with a share of disadvantages. For instance, they require protection circuits due to safety risks. Moreover, the charging voltage of Lithium-based batteries has to be limited to 4.2 V because of safety reasons [161]. In addition, Lithium-based batteries are typically more expensive than NiMH batteries [161]. Regardless of all these aspects, their usage is widely spread from mobile phones to electric vehicles. In short, almost all consumer and power electronics, communication, as well as transportation domain use these batteries [156]. PhyNode uses a Lithium polymer battery as well. For further reading a detailed discussion of operational electro-chemical principles of batteries can be found in [156, 160].

4.1.2 Battery terminology

There are parameters and traits which are fundamental for analyzing batteries. Some of them required within this work are explained here.

Regardless of common understanding of a *full* or *empty* battery, their exact definition is critical for the purpose of modeling. A fully charged battery is commonly defined as:

Definition: *Fully charged battery*

A battery is considered as *fully charged* when its maximum allowed voltage is reached, while being charged with an infinitesimal current at the room temperature [162].

Although this theoretical definition explains the fully charged state, it is dependent on the definition of the infinitesimal current (I_ϵ). Charging a battery with too small currents takes a long period and is impractical in reality. On the other hand, although use of too large current will shorten the charge time, amount of the overall energy pumped into the battery can be increased when charging with lower currents. Therefore, it is common to make a trade-off for the selection of I_ϵ which will be discussed with more details later.

Complementary to the charge process, discharged case is defined as:

Definition: *Fully discharged battery*

A battery is considered as *fully discharged* when its minimum allowed voltage is reached, while being discharged with an infinitesimal current at the room temperature [162].

Same as for the charging, it is very probable that the load current is not very small and cannot be considered as infinitesimal. Therefore, instead of theoretical definition of fully discharged, concept of *depleted* battery will be used here which can be explained as:

Definition: *Depleted battery*

A battery is *depleted* as soon as its minimum allowed voltage is reached for the first time during a discharge process.

As discussed formerly, a key aspect of a battery is the amount of energy it can deliver. Moreover, an ideal battery can be considered as a voltage source with a specified voltage. In this ideal case, terminal voltage (V_b) drops to zero as soon as this predefined energy is delivered. Nevertheless, this is not the case in reality and V_b changes according to the amount of charge still available.

Therefore, it is common to ignore the voltage and define *capacity* of a battery ($\mathcal{C}$) according to the remained charge as:

Definition: *Battery capacity*

Capacity of a battery is the amount of charge drained from it, starting from a fully charged state, till it is depleted.

While capacity has a very general definition, its measurement is dependent on the current used for discharge, and commonly higher currents lead to a smaller capacity. However, measured capacity with I_ϵ can be called the *total capacity*. This value shown with Q is defined by (4.1) when t_d is the time required till the battery gets depleted, starting from a fully charged state.

$$Q = \int_0^{t_d} I_\epsilon \, \mathrm{d}\tau = I_\epsilon \cdot t_d \quad [\mathrm{A\,s}] \tag{4.1}$$

On the other hand, *nominal capacity* ($\mathcal{C}_n$) is the capacity when the battery is discharged at the nominal current (I_n). Using this definition, $\mathcal{C}_n$ can be defined as in (4.2) when starting from a fully charged initial state.

$$\mathcal{C}_n = \int_0^{t_d} I_n \, \mathrm{d}\tau = I_n \cdot t_d \quad [\mathrm{A\,s}] \tag{4.2}$$

Nominal capacity provided by manufacturers is generally measured in a pessimistic manner to include production tolerances. Consequently, capacity of a new battery is mostly higher than $\mathcal{C}_n$. However, similar to the total capacity, nominal capacity reduces over time, as a consequence of the aging process. Hence, it is common to consider end of life for a battery when it reaches 80 % of the $\mathcal{C}_n$. Therefore, health of a battery in relation to this point can be defined using State of Health (SoH) as:

Definition: *State of Health*

State of Health is the relation of the present capacity to a scale between capacity of a new battery and its aged state reaching 80 % of the nominal capacity, presented as a percentage.

Same as fully charged and discharged conditions explaining two states of the battery, it is possible to define a *state* for any position in between. However, state of a battery is commonly defined as a relative parameter showing its present condition according to one of the end cases of fully charged or discharged. When starting from the fully charged condition, state can be shown as the amount of charge drained to reach the present point. This definition leads to the Depth of Discharge (DoD) explained as:

Definition: *Depth of Discharge*

Depth of Discharge shows the amount of charge drained from a fully charged battery to reach the present state.

This definition can be formulated as in (4.3), starting from the fully charged state at initial time with I_b showing the battery's terminal current.

$$\mathrm{DoD}(t) : \mathcal{D}(t) = \int_0^t I_b(\tau)\,\mathrm{d}\tau \quad [\mathrm{A\,s}] \tag{4.3}$$

According to the general definition of capacity, it is possible to show any state using *remained capacity* ($\mathcal{C}_r$) as well. It actually explains amount of charge which can be drained from the battery till it is depleted. In contrast to the DoD, this definition uses the fully discharged condition as the measurement base. Although it is possible to use this charge value as an absolute state parameter, State of Charge (SoC) is defined as a relative state formally explained by:

Definition: *State of Charge*

State of Charge is the relation between remained capacity to the total capacity of a fully charged battery [163].

SoC is a unit-less relative quantity presented as a percentage, and will be noted using z hereafter which can be formulated as:

$$\mathrm{SoC}(t) : z(t) = 100 \cdot \frac{\mathcal{C}_r}{\mathcal{C}} \quad [\%] \tag{4.4}$$

In other words, when the battery is fully charged, its SoC is 100 % and when fully discharged it has a 0 % SoC. This is the common factor used for most consumer products such as cell phones to show the battery state. According to the definition of $\mathcal{C}_r$, it is possible to reformulate the SoC as:

$$z(t) = 100 \cdot \left(1 - \frac{1}{\mathcal{C}} \cdot \int_0^t I_b(\tau)\,\mathrm{d}\tau\right) = 100 \cdot \left(1 - \frac{\mathcal{D}(t)}{\mathcal{C}}\right) \quad [\%] \tag{4.5}$$

This is actually a complementary definition of SoC used when starting measurement of the SoC from the fully charged state. Furthermore, the minus sign of the integral is according to the current sign definition that a discharge current has a positive sign while charging current is signed negative.

To be noted that in (4.4) and (4.5) capacity of the battery (in the denominator) is supposed to be measured at a constant discharge rate. However, total capacity is supposed to be used in the ideal form. This issue will be discussed further later, in the SoC finding section.

To provide a comparable relative state for the DoD as a relation to the fully charged state, State of Discharge (SoD) can be explained using:

$$\mathrm{SoD}(t) : y(t) = 100 - z(t) \quad [\%] \tag{4.6}$$

While a current value can be addressed directly, normalize currents according to the capacity are very common for batteries to simplify comparison of different batteries with each other. A relative current explanation is commonly used, addressed by C-rate as:

Definition: *C-rate*

C-rate is the relative measure of the discharge rate to the nominal capacity.

According to this definition, $1C$ is the discharge current rate which takes 1 h till a fully charged battery depletes. Similarly, discharge with $C/2$ and $C/5$ will subsequently take 2 h and 5 h till a full depletion.

4.2 State-of-the-art battery modeling

Current researches in the field of battery analysis can be categorized into two main sections, though not separated from each other. First branch provides different types of models to represent battery's behavior. Second group is made of methodologies for estimation of the SoC as a key parameter.

4.2.1 Battery modeling

Battery is a system with memory and dynamic behaviors. In addition, it is a time variant system due to its aging. Modeling of a battery is to describe its dynamic behavior using states through mathematical equations [164] which may cover diverse aspects of the battery. Main considered factors are states, capacity, impedance, available power or the remaining lifetime [163]. However, recent battery modeling focuses mainly on the development of Battery Management System (BMS) which is able to take care of its safety and health. Specially, advancement in the field of electric and hybrid vehicles has extensively contributed to this perspective. Anyhow, different models are developed for diverse fields of applications [165] that can be categorized into few main groups as:

- Empirical
- Electrochemical
- Analytical
- Equivalent electrical circuit (ECM)
- Stochastic

Empirical models

Earliest mathematical models of batteries were simple relations between its empirical parameters [164]. These models are black-box representations, interpreting a battery regardless of its internal structure. They are easy to configure and provide fast predictions of the behavior. However, according to the low physical insight from the battery, they have low accuracy [166]. Nevertheless, many of these models are still in use because of their simplicity.

Perhaps the most famous empirical model is the *Peukert's law* introduced in 1897, providing a nonlinear relation between current and runtime [164]. In spite of its foundation for lead-acid batteries, it has been evolved for other types of batteries and is in use for several decays in the industry. In an ideal case, battery lifetime ($\mathcal{L}$) is linearly related to the capacity and inversely to the drained current. According to this law, lifetime and capacity are related using (4.7) when $\alpha > 1$ is an empirically fitted dimensionless constant [167].

$$\mathcal{L} = \frac{\mathcal{C}}{I_b^{\alpha}} \tag{4.7}$$

Also advanced version of (4.7) for a variable load is explained [165] as:

$$\mathcal{C} = \mathcal{L} \cdot \left(\frac{1}{\mathcal{L}} \cdot \int_0^{\mathcal{L}} I_b(\tau)\, \mathrm{d}\tau \right)^{\alpha} \tag{4.8}$$

These models have low accuracy [166] due to lack of any insight from internal behaviors [168]. For instance considering (4.8), all current profiles with the same average current should lead to the same lifetime. However, it has been experimentally proven that this is not the case [165]. One of examples proving this issue is the *recovery effect*. It is basically the fact that the voltage of a battery increases inverse exponentially when left idle without any current transmission [165]. Consequently, in case a load profile includes some rest time, battery will last more than the same load profile applied without the rest.

Typical form of Peukert's model provides information only about the battery's lifetime. Meanwhile, there are other empirical models providing a relation explaining the voltage, such as *Shepherd* model [169, 170] as:

$$V_b[k] = V_0 - R \cdot I_b[k] - \frac{\alpha}{z[k]} \tag{4.9}$$

when V_0 is the Open Circuit Voltage (OCV) of the fully charged battery and R the internal resistance. To be noted that (4.9) is a discrete representation which is the reason for the $[k]$ notation. Parameter α is a tuning factor found empirically or from battery's internal specifications. By modification of this parameter, *Unnewehr* model [171–173] is described using (4.10).

$$V_b[k] = V_0 - R \cdot I_b[k] - \alpha \cdot z[k] \tag{4.10}$$

Furthermore, *Nernst* model [174] explains voltage as:

$$V_b[k] = V_0 - R \cdot I_b[k] - \alpha_1 \cdot \ln(z[k]) + \alpha_2 \cdot \ln(1 - z[k]) \tag{4.11}$$

As can be seen, all these models have dependency to the SoC as an internal state which requires a separate finding method which will be discussed later. There are further modified empirical models available which an overview of them can be found in [175].

Electrochemical models

Electrochemical models are developed based on a combination of the physical, electrical, chemical and electrochemical principles of the battery. They are built around complex nonlinear differential equations which describe an exact internal process [176]. These extensive level of deduction leads not only to ODEs but also PDEs in addition to a large set of parameters. For instance, one of the most recent models for Lithium-based batteries presented in [156] includes 9 constants, 7 ODEs and 15 AEs in its simplified version. Alternatively Doyle's electrochemical model [177] is made of 6 coupled nonlinear ODEs. Due to this extensive knowledge required, they are mostly used for the battery design [165] in a wide range of applications aiming different outcomes, from state estimation to capacity finding and terminal voltage. While these models are beneficial for manufacturers, they are too complex for system designers with no knowledge of the internal parameters [168].

There are different softwares e.g. *Dualfoil* as a freeware [178], which directly use these types of models to simulate a battery. Nonetheless, they still require a large number of parameters which has to be provided [165]. Furthermore, solving such a large set of equations requires extreme time and computation.

Analytical models

Analytical models are simplified version of the electrochemical models providing an understanding of the nonlinear capacity effects with reduced equation order [176]. Kinetic Battery Model (KiBaM) [179] is a very common analytical model which was originally developed by Manwell and McGowan based on the lead-acid batteries. It uses a two tank fluid structure to explain the available charge using a kinetic formulation.

Another group of analytical models are diffusion-based [180] which are founded on the diffusion of the ion inside the electrolyte. In spite of different initial definition of these two models, it has been shown in [165] that the KiBaM is an approximation of the diffusion model.

Although these models include recovery effect in addition to the capacity rate effect, they do not describe the terminal characteristics of a battery [176]. All in all, this type of models provides a good estimation of the remained charge by use of a set of ODEs.

Equivalent circuit models

An ECM is designed in a way to replicate a real battery's behavior. According to the extent of included behaviors, form of an ECM changes; leading to different circuits. Nevertheless, some fundamental components are the same in all of them. Experiments show that voltage of a battery depends on its SoC and temperature. Consequently, a dependent voltage source is a common component in ECMs with the value presented by *Electromotive Force* (V_e). Although this seems equal to the OCV, it is defined differently due to the recovery effect. However, it can be assumed that these two voltage values will be equal at an infinite recovery period. Anyhow, V_e can be explained as:

$$V_e(t) = f(z(t), T(t)) \tag{4.12}$$

Second component of ECMs is a series resistor (R_0) to reproduce the voltage drop as soon as a current passes through the battery. Considering these two essential components, *Rint model* [181] is made as depicted in Fig. 4.3A. It is also possible to use two parallel branches (each including a resistor and a diode) instead of a single resistor. This topology is able to represent different voltage drops for the charge and discharge conditions. This ECM has no dynamics and can be formulated as a static linear equation. However, in addition to the recovery effect, experiments show that the step response of a current to a battery includes dynamics in V_b. To build this behavior, *Thevenin model* adds a parallel *RC* set as presented in Fig. 4.3B [182]. Similar to the Rint model, different values of *RC* during charge and discharge are possible. In addition to the dynamic behavior, use of *RC* enables reproduction of the recovery effect.

According to the internal specification of a battery, it is possible that more *RC* time constants are required, leading to multi *RC* models. Number of these *RC* sets can be increased to improve the replication of the dynamic behaviors in a model. Fig. 4.3C shows an example of a double *RC* set model.

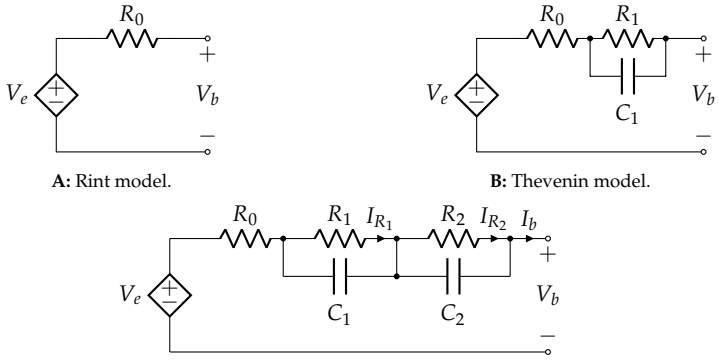

A: Rint model. **B:** Thevenin model.

C: Double *RC* model.

Fig. 4.3 Different ECMs used to present a battery.

Furthermore, many other models are available such as: Partnership for a New Generation of Vehicles (PNGV) model [183], General Non-Linear (GNL) model [182] and Randal's model [184].

Benefit of ECM is the possibility to use the mathematical representation of each circuit using Kirchhoff equations. Consequently, according to the representation of equations, output of these models can be different. For instance, in case of knowledge about the SoC, it is possible to find V_b or the other way around. Many models use a version of ECM in combination with feedback loops on V_b to estimate the SoC. According to the ECM topology and application, model's equations may be from a simple linear relation up to a set of ODEs. Furthermore, comparing these representations with empirical models (e.g. Rint and Shepherd), it can be seen that similarities are available and empirical models include the essence of some ECMs.

Stochastic models

Stochastic battery models mainly published by Chiasserini and Rao from 1999 to 2001 are based on discrete-time Markov chains and have a much higher abstraction level compared to the electrochemical models and ECMs [165]. Each state number in the chain defines number of charge units remained in the battery. Some stochastic models [185–187] even explain the battery behavior including recovery effect as a Markov process. Probabilities in these process are related to physical and electrochemical factors of the battery [176]. Although models such as in [188] describe behavior of Li-ion in a good qualitative way, they are unable to handle varying and arbitrary discharge load currents [176] which is common for most IoT applications.

4.2.2 SoC estimation

As explained by definition of the SoC, it is similar to the fuel gauge of a car, giving a quantitative feeling about the remaining energy. It plays an essential role in most models and its estimation is a fundamental aspect of the battery modeling. There are different methods available in literature to estimate the SoC, which according to [163] the most common techniques are:

- Ampere-hour
- OCV-based
- Model-based
- Impedance-based
- Based on static characteristics
- Non conventional

Considering the definition of the SoC and its formulation from (4.5), the most obvious method to find it would be the ampere-hour technique. This method requires only accurate current measurement over time, starting from a known initial state value. However, in applications with dynamic currents,

formulation of (4.5) has to be modified into a more general form. Therefore, capacity as the denominator has to be replaced with the total capacity as a more constant value which is less dependent on the discharge current.

It is known that the charge drained from a battery during a continuous discharge is dependent on the current rate. On the other hand, based on the definition, SoC has to be zero at depletion. Therefore, a scaling (efficiency) factor has to be added into the general SoC formulation to match the present remained capacity ($\mathcal{C}_r$) to the total capacity (Q). Considering these aspects, SoC in the general form for dynamic currents can be explained by (4.13). Since scaling factor η is dependent on different factors changing by time, it is shown as a time dependent parameter included in the integral.

$$z(t) = z_0 - \frac{100}{Q} \cdot \int_0^t \eta(\tau) \cdot I_b(\tau)\, \mathrm{d}\tau \tag{4.13}$$

Although this is a simple and effective method for finding the SoC with low computational power, it has two main drawbacks. It is dependent to the initial point and its cumulative concept can cause integration of error in case of low accuracy current measurement.

It is shown that the relation between SoC and V_e is very distinct for most of Lithium-based batteries and changes very slightly over the lifetime [163]. Using a high accuracy measurement system combined with the Ampere-hour method, it is possible to find this relation for a battery. However, there are specific consideration for the use of this relation, specifically for online applications. At first, to detect the OCV, current has to be detached from the battery which may be unacceptable for some applications. Second, recovery effect shows that the measured OCV is not constant and changes over time. It is also not equal to the V_e but will be reached at (theoretically) infinite time. Therefore, some techniques [189–192] have been developed to estimate the V_e according to some empirical relations found from the OCV relaxation curve. Anyhow, this method still has disadvantages of the Ampere-hour method while integration is still used for the identification of the relation.

Considering the idea from OCV-based methods, it is possible to use the battery model to find out V_e from the measurement of the terminal voltage. Use of ECM fits to this concept very well to build such a relation using a circuit topology. However, for using circuit relations in addition to V_b, information about the battery current is necessary as well. In addition, identification of parameters plays a critical role on the estimation performance. Moreover, noise in measurement and other environmental factors can cause errors in the estimation. However, it is possible to use feedback mechanism to tackle these issues. Multiple techniques such as different versions of Kalman filters [193–197], H_∞ [198–200] and particle filters [201, 202] are suggested to improve accuracy of such models with a feedback loop. Furthermore, it is possible to use different types of observers such as sliding mode [203, 204],

Luenberger [205, 206], adaptive [207, 208] and many more to estimate the SoC using the battery model.

Dependency of battery impedance to the SoC has motivated some researchers to use it for the SoC estimation of different batteries [163]. However, this technique has some major drawbacks. At first, this dependency changes over the battery's lifetime. Second, impedance is much more sensitive to the temperature than the SoC. Therefore, this method requires high accuracy measurement configuration to compensate this effect.

Voltage, current and temperature of a battery remained in a static condition for a sufficient time period can be used for the estimation of the SoC [163]. These information stored in the form of a LuT or an empirical function can be used to find the SoC. However, it can be used only in those cases where the dynamics of load are too small and can be ignored.

There are non-conventional methods available such as fuzzy logic [209–211], ANN [202, 212] and Support Vector Machine (SVM) [213, 214]. Different publications provide solutions to estimate SoC using impedance [215] or current, voltage and temperature [216] based on fuzzy logic methods. ANN based methods can be used in multiple manners. It can be applied to directly estimate the SoC using available measured parameters. Also it is possible to combine it with model-based techniques.

4.3 Modeling PhyNode's battery

PhyNode uses a Li-ion Polymer battery produced by *Blue TaiYang* with the model No. *LP632670*. It has a nominal capacity of 1250 mA h, nominal voltage of 3.7 V with a typical 4.2 V Over-Voltage (OV) limit and a cut-off voltage of 3.0 V. Its nominal charge and discharge rates are $C/5$ with a $1C$ maximum rate. It is shipped with a protection board to avoid over and under voltages. Manufacturer claims an impedance of $\leq 65\,\mathrm{m}\Omega$ for the battery pack. It also assures a capacity higher than 80 % of the $\mathcal{C}_n$ (end-of-life) after 300 cycles with I_n at $23\pm2\,^{\circ}\mathrm{C}$. In addition, its retention capability is more than 85 % of the capacity for 28 days of storage at $20\pm5\,^{\circ}\mathrm{C}$ after a full charge.

As discussed in Chapter 2, before starting with the modeling, it has to be clearly defined what is the main aim of the model. Similar to the overall concept of the modeling for PhyNode, two different goals are supposed for the battery model here. First, it has to be possible for the PhyNode's software to estimate the battery state (z) which helps planning the PhyNode's operation. In the context of PhyNetLab, this will enable PhyNode not only to inform operators with a recharge request, but also deciding about possibility of requests fulfillment.

According to the PhyNode hardware, only a single Analog-Digital Converter (ADC) is available which can be used for the measurement of a single voltage. Therefore, on-board model has to provide the SoC using only a direct V_b

measurement. Nevertheless, a SoC with integer accuracy will be enough for a general operational planning. Therefore, the on-board battery model can be presented in the abstract form of Fig. 4.4.

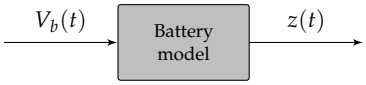

Fig. 4.4 An abstract representation of the desired on-board model for the PhyNode's battery.

Contrary to the on-board model, a system level detailed model is necessary with the V_b as its output. Knowledge about V_b is required due to the effect of the battery voltage on the nonlinear behavior of the EH system as discussed in Chapter 3. A combination of V_b with the model of the PV harvester in addition to the load demanded by PhyNode hardware enables an off-board simulation when the life-span of PhyNode has to be estimated. Input to this model will be the current flow from/to the battery and its general form can be presented as in Fig. 4.5.

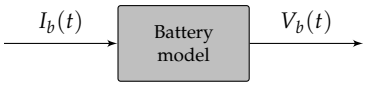

Fig. 4.5 An abstract representation of the detailed battery model for the system level analysis.

Current flow to the battery in Fig. 4.5 is a combination of load required from the rest of PhyNode hardware and the input charge harvested by PV module. Analysis of light and environmentally generated current in PhyNetLab (discussed in Section 3.4) has shown generated currents in the range of 30 µA to 140 µA. However, PhyNode demand has to be checked to know the system borders before modeling.

4.3.1 PhyNode power demand

Analyzing PhyNode's sub-modules demands in [217] had shown highest current load happening during send procedure of the communication module. Considering operational condition of this module, highest measured current demand is about 32 mA which is the maximum power for sending. Processor of PhyNode requires 100 µA per each MHz with the maximum of 16 MHz; leading to the highest demand of 1.6 mA [218]. By including some overhead for other components, 35 mA is a feasible maximum demand.

It is known that PhyNode's components have different supply voltage levels. Hence, a *TPS65290* Power Management IC (PMIC) from TI is used to match voltage levels. This device includes a Low Dropout (LDO) converter in addition to a buck-boost converter enabling voltage leveling in both directions. Furthermore, this device enables software controlled voltage selection by processor using an I2C bus. PhyNode's processor controls the voltage output of the PMIC based on the device being fed. Considering this PMIC, the abstract energy supply chain of PhyNode is shown in Fig. 4.6.

Fig. 4.6 Abstract representation of PhyNode's power delivery including PMIC.

It is common for switching-based converters to require some cycles to stabilize the output voltage after each change. Meanwhile, some devices such as PhyNode's communication module (specially during the send period) require a large current burst for a very short period of time. Therefore, providing this device from a switching based converter can cause interruptions according to the reaction time of the converter. This is the main reason for using a PMIC with an LDO to assure reliable operation. Unfortunately, LDOs are less efficient due to the excess power dissipation through heat. Therefore, in case the LDO is active, power demand seen by battery do not scale directly with the voltage level. Hence, instead of simple summation of the current demands, it is better to measure the real currents of PhyNode.

To check the real load, aforementioned SMU is connected to the PhyNode's power supply port (instead of the battery) using a 4-wire connection. SMU acts as a voltage source, emulating a fixed voltage battery. Concurrently, a program on PhyNode spans through all possible operations in cycles. Measurement of this procedure is repeated with supply voltages starting from 4.2 V with 0.1 V reducing steps. Measured current (I_{pn}) during a complete cycle at some exemplary voltage levels is presented in Fig. 4.7.

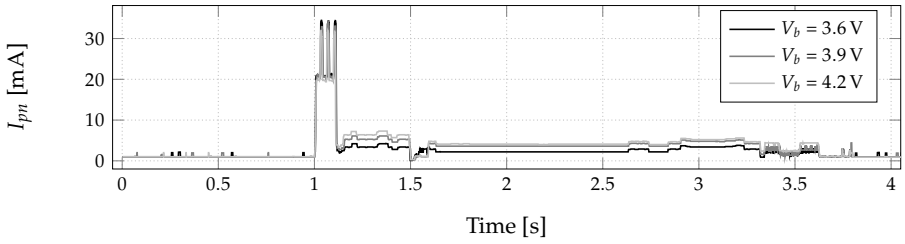

Fig. 4.7 Measured current of PhyNode at different operational voltages.

These measurements confirm the 35 mA guess as the highest current. During peaks caused by the communication module, changes in voltage has minimal affect on current. However, during the rest of the cycle, lower voltage levels require also less current. This can be analyzed further by examination of the PMIC which is out of scope of this work. Nonetheless, the idle current demand at the end is about 900 µA and is independent from the source voltage.

Furthermore, it has been found that reducing voltage to the battery cut-off value is not possible because PhyNode cannot start all parts of the system for voltages lower than 3.54 V and will not be operational. This effect can be seen in its current demand shown in Fig. 4.8, where it repeats a section of the initial check loop and cannot proceed to the normal operation.

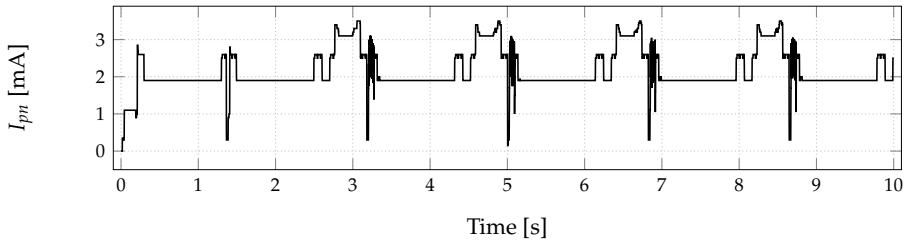

Fig. 4.8 PhyNode's demand current at 3.53 V remaining in the starting mode unable to finish the initial check loop and repeating a part of the check-up.

Considering these measurements, PhyNode's operational range is from 3.54 V to 4.2 V. In addition, perhaps this version of PhyNode cannot be considered as an energy-neutral device within PhyNetLab environmental condition. This is mainly due to higher current demand (minimum 900 µA during idle) compared to the harvested current with a maximum of 140 µA in PhyNetLab. Therefore, battery will be continuously drained even during idle mode. On one hand, it is probable that the improvements in the drivers (specially communication device) reduce the idle current demand. On the other hand, it is better to keep the battery model as general as possible. Hence, maximum current of 35 mA with the whole battery voltage range are the system boundaries used for the detailed modeling.

4.3.2 Measurement setup

Different battery specifications have to be measured required for its modeling. Commercial instruments known as *cycler* are available for measuring these factors. Although some special purpose cyclers are designed for small batteries in ULP applications, their high cost range makes them inaccessible for many normal users and system designers. Therefore, an alternative solution has to be developed which is accessible, cost efficient and accurate.

For the battery analysis, mostly a current is applied to the battery while its terminal voltage and current are measured. Therefore, the same SMU used up to here for measurement of PV modules can be exploited instead of a cycler. However, all experiments have to be programmed individually to fulfill the measurement requirements. Hence, battery is attached to the SMU via a 4-wire connection. Also a MATLAB script is written for each measurement sending SCPI commands to the SMU through a USB connection.

Although it is possible to detach the BMS board from the battery, it is kept mounted during measurements while the behavior of the battery at normal condition has to be analyzed. For safety reasons, a *keysight U2941A* test fixture holds the battery inside a metal box. Furthermore, while all measurements are done within an office with a regulated temperature, effects of temperature is ignored and temperature measurement is not required.

4.3.3 Charge process

In addition to the capacity measurement, calculation of both DoD and SoC are dependent to the fully charged state as the initial point. Hence, charging process is critical during the identification and modeling. Using definition, charging to the fully charged state is supposed to be with infinitesimal current. Within this work $C/100$ (equal to 12.5 mA) is considered as the infinitesimal current. However, use of such a small current will lead to at least 100 h for each charge cycle which is neither practical nor feasible. Consequently, a charge process is defined which makes a compromise for the required charging time.

Charge process is made of two parts; initial charge phase increases V_b in a fast manner. Then, second phase includes charge with small currents and finally I_e to assure reaching the fully charged state. Fast charge is made of applying a 1 A current till the OV limit of 4.2 V is reached. At the end point, source switches to a constant voltage source and keeps the voltage at this value for 20 minutes. After a 5 min rest period for partial stabilization, second phase subsequently applies a set of small currents till OV limit reaches for each one.

Internal hysteresis effect of batteries shown in [219, 220], causes different voltage values at a charge based on the current direction. Nonetheless, while the fully charged state is supposed as the origin point, it is more convenient to remove this hysteresis effect. Suggested method to get rid of this hysteresis is application of a voltage chirp around the desired voltage [219]. Chirp is a sinusoidal signal which its frequency increases over time. Application of this signal causes battery to switch continuously between charge and discharge. Increase of the frequency makes this changes faster over the time, leading to the removal of the hysteresis. A chirp applied to the PhyNode's battery is presented in Fig. 4.9. Incremental frequency increases the upper current bound that the overall average stabilizes around zero at the end.

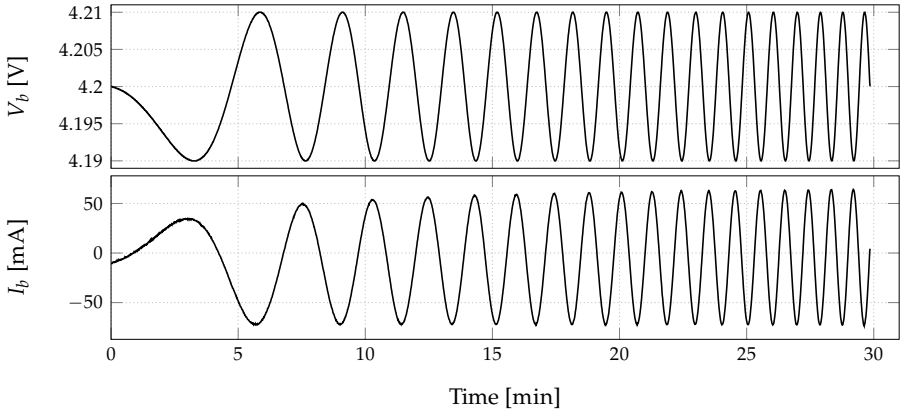

Fig. 4.9 An example of chirp signal applied to the PhyNode's battery during a charge process to reduce the effect of battery hysteresis.

After hysteresis removal, it can be considered that the maximum possible input charge is already pumped into the battery. However, due to the recovery effect, battery rests for 1 h to stabilize its internal reactions. At the end of this rest period battery can be considered as fully charged in a systematic way that can be repeated. Considering all these steps, the overall full charge process can be summarized as in Algorithm 3.

Algorithm 3 Process of fully charging the battery.

while $V_b \leq 4.2\,\text{V}$ **do**
    charge with 1 A as a constant current source ;
end while
for 20 min **do**
    act as a voltage source with $V_b = 4.2\,\text{V}$;
end for
rest for 5 min ;
for each $I_b \in \{250\,\text{mA}, 125\,\text{mA}, 62.5\,\text{mA}$ and $25\,\text{mA}\}$ **do**
    while $V_b \leq 4.2\,\text{V}$ **do**
        charge with I_b as a current source ;
    end while
    rest for 5 min ;
end for
rest for 10 min ;
while $V_b \leq 4.2\,\text{V}$ **do**
    charge with I_e =12.5 mA as a current source ;
end while
apply chirp to remove hysteresis ;
rest for 1 h ;

4.3.4 SoC-V_e relation

Both types of PhyNode's battery models require a relation between the battery voltage and its SoC. For the on-board model, it is needed to estimate the SoC by measuring V_b, while V_b has to be identified from the SoC for the detailed model. Therefore, finding SoC-V_e relation is essential here.

Two methods are commonly used for extraction of this relation. First technique finds it by voltage measurement during a discharge curve with a very small current to avoid activation of dynamics. Then measured voltage is used to find the V_e, while the SoC is found from the DoD. Second method measures V_e directly by stopping the discharge process and measuring OCV after a long rest period. Consequently, based on the current form, these methods will be addressed by *continuous* and *discrete* hereafter.

While discrete method can provide the relation only at distinct SoC points, continuous discharge can be considered more detailed. Yet, by measuring OCV during the recovery period of the discrete method, dynamic parameters of the battery can be identified as well. According to the rest period, discrete method measurement may require a very long time. Though, based on the scale of

discharge current, a measurement of continuous method may be very time consuming as well.

In ULP applications demand can be in the same scale as the current in continuous method, requiring a detailed evaluation of this method. Hence, both methods are compared here to provide guidelines for possible similar cases.

4.3.4.1 Continuous discharge method

To avoid activation of battery dynamics, [162, 219] suggest to apply a current at a rate of $C/30$ for the continuous method. In the case of PhyNode's battery, this rate is a current of 41.6 mA which is even higher than the maximum current demand. Therefore, a set of currents are used in a wide range to select the proper current criteria. Battery voltage measured over time for these cases is presented in Fig. 4.10.

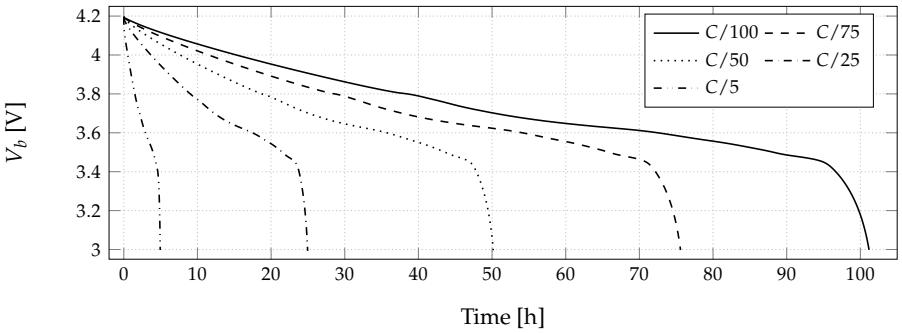

Fig. 4.10 Terminal voltage measured during continuous discharge with different currents.

It is known that current drainage from the battery causes a drop in the terminal voltage from V_e which can be explained using Rint model according to (4.14). However, this is only valid in the case of no dynamics in the behavior which explains reasoning for the assumption in this method.

$$V_e = V_b + R_0 \cdot I_b \tag{4.14}$$

Although V_b and I_b in (4.14) are directly measured, R_0 has to be found. Therefore, current is applied as a step with zero initial level. In this way, it is possible to find the drop in V_b and identify the R_0. Consequently, it is possible to calculate the V_e by assuming a constant R_0 during the whole discharge period for that current. Using this procedure, V_e is found for all curves in Fig. 4.10. To be noted that this will cause lack of data between the new end voltage and the real cut-off voltage. However, it is possible to extrapolate the data with a very small error because this difference has to be marginal according to the assumption of small current.

Next, according to the SoC definition in (4.5), DoD is converted into the SoC for each curve. Repeating this procedure, SoC-V_e relation for I_e and difference of the curve from other currents are shown in Fig. 4.11.

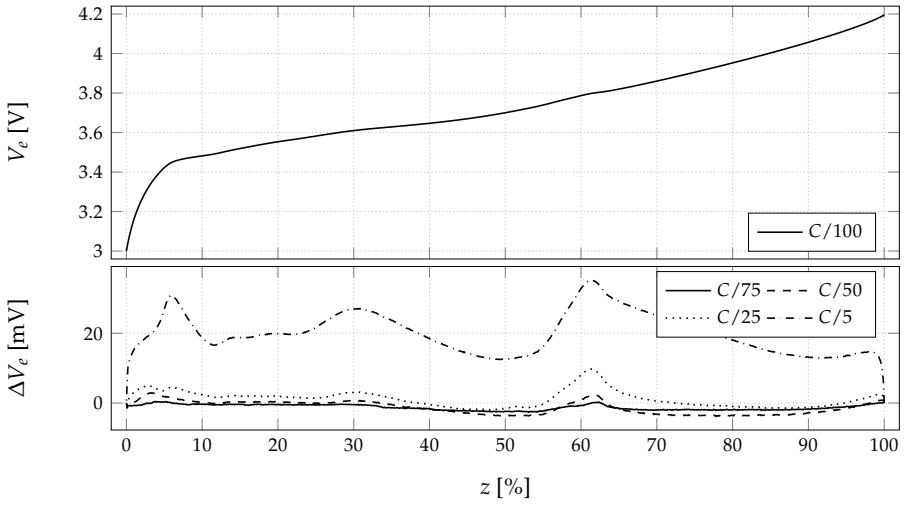

Fig. 4.11 Identified SoC-V_e relation from infinitesimal current and difference of curves with other discharge currents from this curve.

It can be seen from Fig. 4.11 that the SoC-V_e relation is made of two major sections which are typical characteristics of Lithium-based batteries. One (semi) linear part from peak voltage till the bending point around 3.46 V, followed by a hyperbolic section. Moreover, Fig. 4.11 shows that larger currents leads to larger difference in the measured voltage. Nonetheless, except for the nominal current of $C/5$, difference between curves is small. Anyhow, there is no clear criteria to define which curve is explaining a more reliable SoC-V_e relation. However, according to the definition of V_e, the most accurate value can be found using discrete method.

4.3.4.2 Discrete discharge method

In the discrete method, measurement starts from the fully charged state by application of a discharge current pulse. Both initial and end wing of the pulse have zero current and while the initial one is short, the end wing is long enough that the OCV is stabilized and V_e is reached. After measurement of V_e, the process of applying pulses repeats till the battery is depleted.

Step response is always a handy method in the dynamic modeling. Hence, analysis of the battery pulse behavior enables extraction of its dynamic characteristics. While internal parameters of the battery are mostly dependent to the charge state, this identification process has to be repeated for each pulse. Among both steps in each discharge pulse, the second one is suitable for the identification because in the first step battery state is changing and identified

values can not be related to any exact SoC. In contrast, SoC is constant during the rest wing of the pulse due to zero current transmission.

By selection of the pulse amplitude and its duration, amount of charge drained from the battery can be controlled. Ratio of this charge to the capacity defines the change in the charge state or the sampling rate of the SoC. Thus, specifications of the pulses define the fineness of the SoC-V_e relations. An example of such pulse measurement is presented in Fig. 4.12.

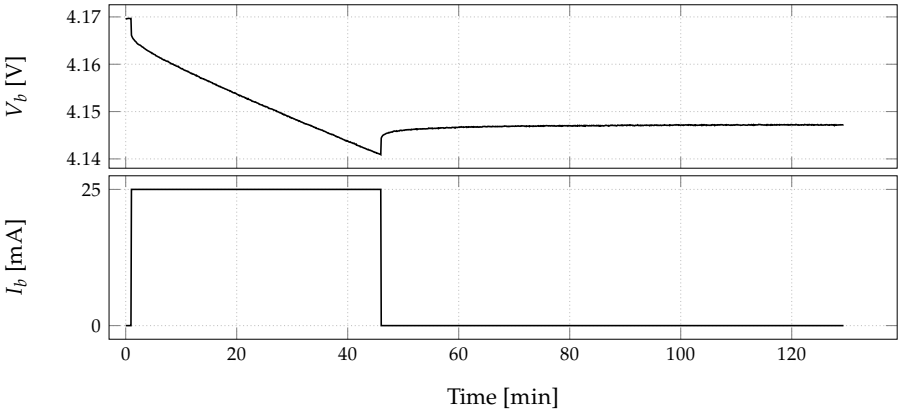

Fig. 4.12 Voltage and current of the battery measured during a single discharge pulse for the discrete identification of SoC-V_e relation.

As can be seen in Fig. 4.12, voltage is roughly stabilized at the end of recovery period. However, different trials have shown that with voltage in the hyperbolic section of the curve, recovery period has to be continued to reach the V_e. Although the recovery period can be simply extended, inclusion of data storage during this period is not possible due to the limited memory of the SMU. While it is possible to enlarge the sampling time of the SMU, it will reduce the accuracy for the detection of the dynamic parameters. This negative effect is specially important for the resistances identified by the jump at the application of the steps. Therefore, a workaround is used that the recovery period extends based on the position at the overall SoC-V_e curve. However, data storage is only for a limited section of this recovery period. These periods will be called initial and secondary recovery periods. To find the realistic V_e, battery voltage is measured at the end of the secondary recovery period and stored additionally.

While duration of pulse tail is critical for the dynamic parameter identification in addition to find the V_e, pulse amplitude and length will define the sampling rate of the SoC. Smaller distance will make a more accurate SoC-V_e curve, while extra pulse will increase the overall identification experiment time. Therefore, a trade-off has to be done in between accuracy and time. Furthermore, it is known that the hyperbolic section of the SoC-V_e curve has a very steep shape. Therefore, sampling has to be more dense in this section to

provide enough data. Consequently, a non-constant sampling rate according to the SoC is used. Experiment is programmed in a dynamic way with parameters as defined in Table 4.1.

Table 4.1 Used parameters for pulses in discrete identification of SoC-V_e relation.

V_e [V]	Amplitude [mA]	Duration [min]	1st Recovery [s]	2nd Recovery [min]
3.84–4.2	25	45	5000	10
3.48–3.84	25	45	5000	15
3.36–3.48	12.5	30	5000	30
3.24–3.36	12.5	20	5000	40
3–3.24	12.5	10	5000	60

Using these settings, measured OCV at the end of both recovery periods is presented in Fig. 4.13 according to the change in the DoD.

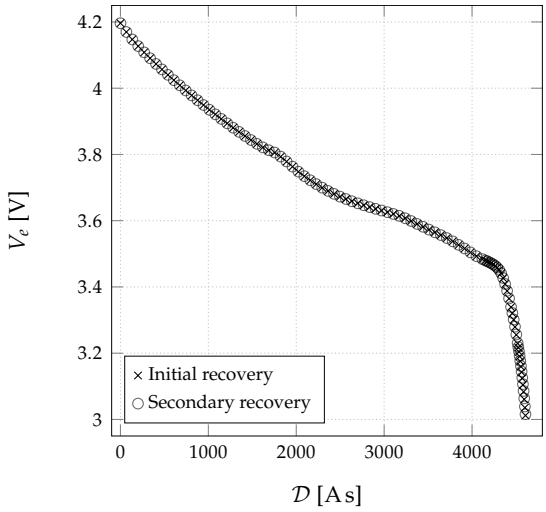

Fig. 4.13 V_e after both recovery periods measured during discrete identification method.

From Fig. 4.13, the overall curve is very similar to the continuous method in Fig. 4.11. In addition, sampling points are distributed through the whole curve in a roughly uni-distance form with extra points at the bending section. Although voltages after initial and secondary recovery periods look very similar, they have a small difference specially in the hyperbolic section. In spite of small scale of this difference, it has to be taken care of, specially in ULP applications which the changes are mostly very small as well.

While this data is according to the charge drained during each pulse, it has to be converted into the SoC. Similar to the continuous method, it is possible to simply consider this data-set as a standard condition and use the available capacity for the SoC calculation. However, as can be seen in Fig. 4.13, the last measured voltage is marginally higher than the cut-off voltage of 3 V. By extrapolation of the curve, DoD at this voltage can be found which is the

representation of the capacity. Afterwards, the SoC is calculated for each point by division of the DoD to this capacity. Comparison of this curve with the SoC-V_e curve from continuous I_ϵ discharge is presented in Fig. 4.14.

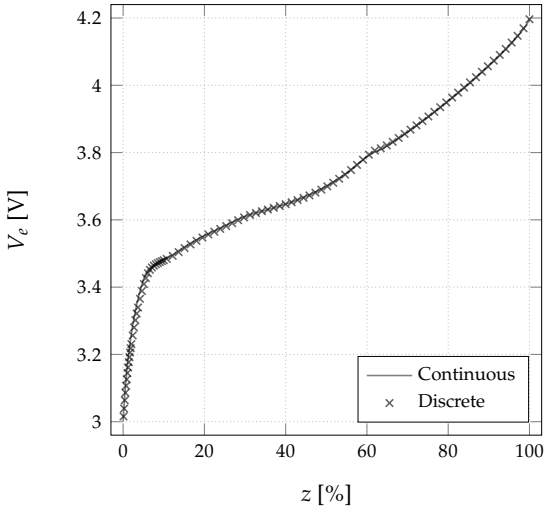

Fig. 4.14 Comparison of SoC-V_e relation identified from both identification methods.

Fig. 4.14 shows that the discrete curve fits to the continuous curve with very small differences, mostly in the hyperbolic section of the curve. The main debate at this point is to clarify if this difference is a consequence of measurement or a systematic discrepancy between these two methods. Looking at the hyperbolic section of Fig. 4.14, it is clear that the voltage of discrete method is less than the other curve. Generally, this has to be the other way around because of the recovery effect. In addition, discrete curve has been measured before continuous curve with I_ϵ which should normally lead to higher voltage for the discrete curve due to the aging effect. Consequently, it can be concluded that the shape of curve in the hyperbolic section has changed.

Finally differences in between two methods is smaller than the changes in the characteristics of a low-budget battery such as the case for the PhyNode's battery. Therefore, these methods can be redundantly used for such applications and conditions. Anyhow, before use of any of these curves one extra aspect has to be considered which is removal of the hysteresis effect.

4.3.4.3 Hysteresis effect

To compensate the hysteresis effect, it is suggested in literature [219] to measure the curve in both directions. Therefore, before measurement of a charge curve, battery is depleted with I_ϵ, followed with a chirp signal. After a 1 h rest period battery is stable at the fully discharged condition. Next, battery is charged with a constant current till it reaches the OV level. Example measurement from PhyNode's battery in both direction is shown in Fig. 4.15.

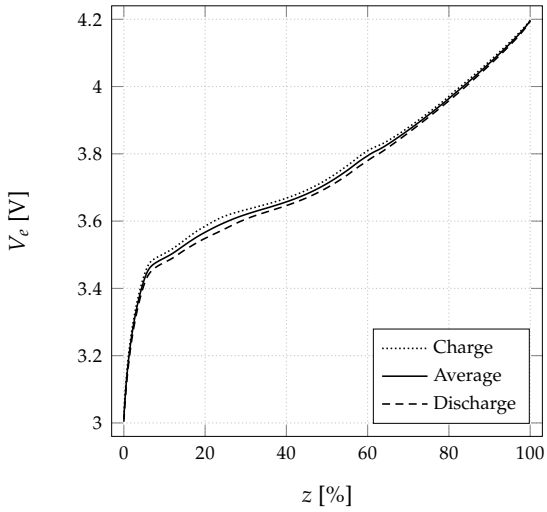

Fig. 4.15 Measured data for removal of hysteresis effect from SoC-V_e relation.

As can be seen in Fig. 4.15, there is a difference in between curves as a consequence of the hysteresis. This effect is commonly removed by using an averaged curve. This curve can be considered as the identified SoC-V_e relation used for the rest of modeling procedure.

4.3.4.4 Implementation of SoC-V_e relation

Developed battery model should be applicable on all PhyNodes in PhyNetLab regardless of production tolerances. Therefore, the SoC-V_e relation is found for five batteries as presented in Fig. 4.16. In spite of very small differences between these curves, average voltage value for each SoC is used for further steps of modeling.

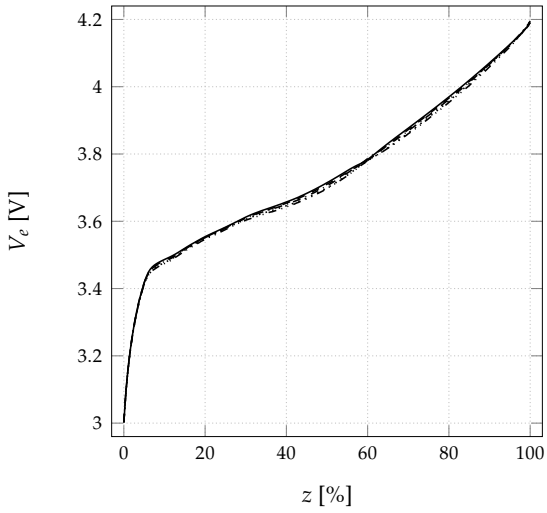

Fig. 4.16 Comparison of SoC-V_e relation identified from five different batteries.

It is common within researcher community to store a SoC-V_e relation as a LuT. For the detailed model, this LuT can be simply stored with high accuracy and used in the model. Although such LuT will not be large, it can be still memory intensive for some resource constrained applications such as PhyNode. In these cases, it is better to find a mathematical representation, replicating the behavior in an algebraic way. For the on-board model, SoC will be the outcome of the model while the only available signal from the battery is the V_b. Therefore, this algebraic function has to explain the SoC dependent to the voltage. Due to lack of current value, a model using SoC-V_b relation will be more accurate than the SoC-V_e relation. Though a relation between voltage and SoC without consideration of the current is not accurate, V_b from continuous method with I_ϵ =12.5 mA will be used further. This is mainly because this value is more near to the average of PhyNode load.

Different mathematical structures are tested to replicate SoC-V_b curve. First suitable solution is a combination of three Gaussian functions which their tuned form for the curve of PhyNode's battery is as:

$$\begin{aligned} z(V_b) =& 118.8 \cdot \exp\left[-\left(\frac{V_b - 1.778}{1.795}\right)^2\right] - 24.41 \cdot \exp\left[-\left(\frac{V_b - 1.482}{0.8579}\right)^2\right] \\ &+ 12.8 \cdot \exp\left[-\left(\frac{V_b + 0.2128}{0.5952}\right)^2\right] \end{aligned} \tag{4.15}$$

This form uses common operations to find the SoC and requires storage of only nine values. However, it still needs calculation of three exponential functions. Another possible form is a rational polynomial function with a tuned form for PhyNode as in (4.16).

$$z(V_b) = \frac{80.49 \cdot V_b^3 + 484.8 \cdot V_b^2 + 983.1 \cdot V_b + 811.6}{V_b^4 - 3.164 \cdot V_b^3 + 7.405 \cdot V_b^2 + 9.33 \cdot V_b + 14.86} \tag{4.16}$$

Performance of these two explicit formulations with the tuned parameters on the overall range of voltage can be seen in Fig. 4.17.

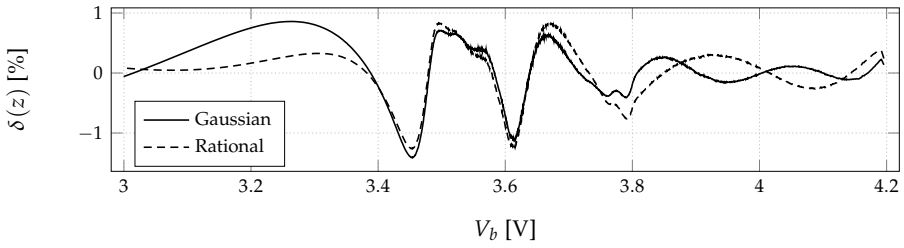

Fig. 4.17 Estimation error of explicit equations for the relation of SoC and V_b.

Model with the Gaussian form has a RMSE of 0.46 % while rational polynomial model performs with a RMSE of 0.50 %. However, Gaussian formulation requires storage of nine floating points with calculation of three exponential functions. In contrary, rational model needs storage of one parameter less and requires main algebraic operations. Therefore, use of rational polynomial model is preferred in comparison to the Gaussian model.

Although this formulation provides a complete representation of the relation, it is not directly applicable for the operational range of PhyNode, limited to the 3.54 V. Hence, SoC scale has to be adapted to the new range showing zero state at this voltage. Tuning similar rational polynomial leads to a function as:

$$z(V_b) = \frac{7107 \cdot V_b^3 + 23790 \cdot V_b^2 + 26575 \cdot V_b + 10194}{V_b^4 + 24.68 \cdot V_b^3 + 247.3 \cdot V_b^2 + 394 \cdot V_b + 186.8} \tag{4.17}$$

Good performance of tuned (4.17) presented in Fig. 4.18 has a RMSE of 0.1392 % for the limited range of PhyNode's operational voltage.

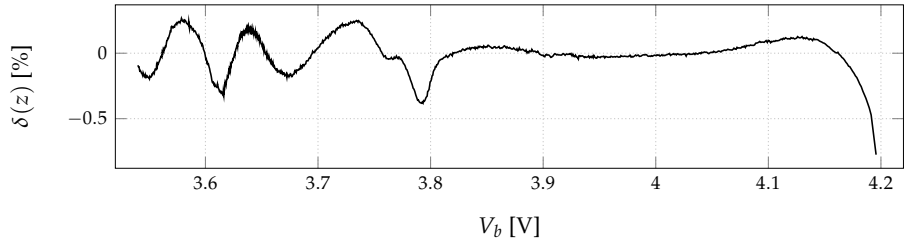

Fig. 4.18 SoC estimation error of (4.17) for the PhyNode's operational voltage range.

4.3.5 SoC estimation

Up to here, SoC has been always found based on the knowledge about the capacity. However, detailed model requires a method for the estimation of the SoC based on the current without any information about the overall capacity. As discussed in Section 4.2.2, different methods are available to estimate the SoC. Considering definition of the SoC with simplicity of the ampere-hour method, in addition to availability of high accuracy SMU for measurements, this method will fit perfectly for PhyNode.

Using (4.13), calculation of the SoC requires the scaling factor in addition to the total capacity (Q) found from a discharge with I_ϵ. However, measurements of SoC-V_e relation from both methods have shown that the measured capacity of discrete method is even higher than the continuous discharge with I_ϵ. This is mainly a consequence of the recovery effect which helps the battery to deliver more total charge. In some sense, it can be considered that the discrete curve is a continuous discharge with a zero current. Hence, using the capacity of discrete curve is a more suitable choice for the estimation of Q.

Three different aspects affect the capacity during a discharge process, demanding the efficiency factor (η). These are namely: discharge current rate, temperature and SoH. Temperature effect can be simply ignored here because applications are limited to the indoor environments with limited temperature changes. Nonetheless, the other two still have to be analyzed with more details.

Although changes in the capacity due to the aging are small, they can play a role because of small scale of ULP devices. Therefore, a *standard test* is defined to estimate the aging status of the battery. It is made of a discharge with I_n (250 mA) starting from the fully charged states till depletion.

A standard test on a new PhyNode's battery has shown a capacity of 4584.45 A s. Comparing this value with the end of life with 80 % of $\mathcal{C}_n$ (3600 A s), a roughly large difference can be seen. This difference is a consequence of using low-budget batteries to keep the production cost of IoT devices minimal. These batteries have mostly a shorter end of life and can handle less number of cycles. For instance, capacity difference of PhyNode's battery divided to its 300 cycles lifetime leads to capacity loose of about 3.28 A s per cycle. While this is a very small value of the overall capacity, comparing it to the current scale of PhyNode shows a totally different image. This difference leads to more than 100 s extra operation of PhyNode with its highest current or about one extra hour of idle operation. Consequently, aging factor and its inclusion in SoC estimation is critical for such applications.

To define the aging status of the battery, $\mathcal{C}_n$ is used as a reference point. Comparing the capacity measured from a standard test to this reference, aging efficiency can be explained by:

$$\eta_a = \frac{1}{\mathcal{C}_n} \cdot \int_0^{t_d} I_n(\tau)\,\mathrm{d}\tau = \frac{I_n \cdot t_d}{\mathcal{C}_n} \tag{4.18}$$

According to (4.13) with scaling factor multiplied to the DoD, it is better to define the aging factor (ζ_a) as the inverse of η_a using:

$$\zeta_a = \frac{1}{\eta_a} \Rightarrow \zeta_a = \frac{\mathcal{C}_n}{I_n \cdot t_d} \tag{4.19}$$

In this formulation, if a discharge measurement with I_n be scaled into the reference point, nominator and denominator of the SoC relation will be equal when the battery is depleted. This simply leads into a SoC equal to zero which is the main reason for adding the aging factor. To be noted that this is not an exact conversion method because the standard test itself will cause some extra aging as well. Consequently, in case a more detailed SoH curve is available, it is better to be used instead of the standard test. Another solution which can be used for cases such as for the PhyNode's battery without SoH data, is to repeat the standard test before and after each measurement. In this way it is possible to have a more realistic value for the aging factor during each

measurement. Therefore, standard test has been applied before and after of all measurements for the identification of the SoC-V_e relation. In this way it is possible to normalize curves and remove the aging factor to make them directly comparable with each other. This process is applied not only on discharge curves from continuous, but also to the discrete method.

To find the effect of current, normalized capacity of each normalized curve has to be compared to the normalized curve of the total capacity using:

$$\eta_c(I_b) = \frac{\zeta_a(I_b)}{Q_n} \cdot \int_0^{t_d(I_b)} I_b(\tau)\,\mathrm{d}\tau \tag{4.20}$$

when Q_n is the normalized total capacity defined by (4.21) with $\zeta_a(d)$ presenting the aging factor of the curve from discrete method.

$$Q_n = \zeta_a(d) \cdot Q \tag{4.21}$$

Considering constant current during a discharge curve, (4.20) can be simplified into:

$$\eta_c(I_b) = \frac{\zeta_a(I_b)}{Q_n} \cdot I_b \cdot t_d(I_b) \tag{4.22}$$

Similar to the aging scale factor, by defining current scale factor (ζ_c) as the inverse of the current efficiency from (4.22), each discharge curve can be related to the total capacity in the normal condition using:

$$Q_n = \zeta_a(I_b) \cdot \zeta_c(I_b) \cdot \int_0^{t_d} I_b(\tau)\,\mathrm{d}\tau \tag{4.23}$$

In this way, capacity of each discharge curve at the normalized condition will be equal to the normalized total capacity. To find the ζ_c for each discharge curve, it is possible to restructure (4.23) and substitute (4.21) which leads to:

$$\zeta_c(I_b) = \frac{\zeta_a(d)}{\zeta_a(I_b)} \cdot \frac{Q}{t_d \cdot I_b} \tag{4.24}$$

Using (4.24) current factor for each of the discharge currents in continuous method has been calculated. Distribution of these factors is shown in Fig. 4.19.

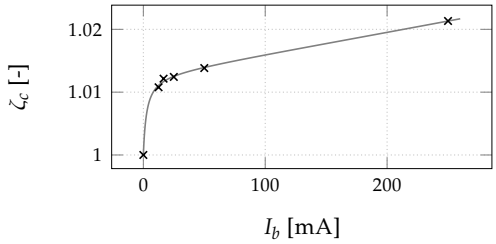

Fig. 4.19 Found current factors from continuous discharge curves. Solid continuous line presents a tuned inverse exponential form to the found points.

To be noted that in Fig. 4.19, zero current is for the current factor of the discrete method which is used for the calculation of the Q. As can be seen, a ratio of exponential relations can explain the relation between current and ζ_c. Tuned version of this relation will be:

$$\zeta_c(I_b) = \frac{0.5287 \cdot \exp(1.089 \cdot I_b) - 0.5271}{0.5545 \cdot \exp(1.025 \cdot I_b) - 0.553} \tag{4.25}$$

Using this relation, it is possible to have an estimation of the capacity effect for each current. Therefore, each state during discharge curve can be explained using the complete SoC formulation as:

$$z(t) = z_0 - 100 \cdot \frac{\zeta_a}{Q_n} \cdot \int_0^t \zeta_c(\tau) \cdot I_b(\tau)\, \mathrm{d}\tau \tag{4.26}$$

After finding the SoC-V_e relation and explanation of the method for finding the SoC, detailed model has to be built by identification of dynamics.

4.3.6 Identification of dynamic parameters

According to the flexibility and simplicity of ECMs, they will be used here. However, topology of the ECM (number of RC pairs) has to be found and their parameters need to be identified. In this step, data collected during the recovery tail of discrete identification method can be used. Analyzing pulse responses such as the one presented in Fig. 4.12, it can be clearly seen that some dynamics are available. Hence, at least one RC pair has to be included in the ECM. Nonetheless, to find the exact number of RC pairs it is better to analyze performance of ECMs with different sets. To do so, dynamic relation between voltage and current of the battery has to be explained.

Considering a simple Thevenin model from Fig. 4.3B, terminal voltage can be written using Kirschhof equations as:

$$V_b = V_e(z(t)) - R_1 \cdot i_{R_1}(t) - R_0 \cdot I_b(t) \tag{4.27}$$

when $i_{R_1}(t)$ can be found using ODE in (4.28) which can be found by solving equations for the circuit.

$$\frac{\mathrm{d}i_{R_1}(t)}{\mathrm{d}t} = \frac{1}{R_1 \cdot C_1} \cdot \left(I_b(t) - i_{R_1}(t)\right) \tag{4.28}$$

Solving this ODE will lead into an exponential function. Since data measurement and analysis are both in the discrete time, this solution in addition to the voltage relation from (4.27) can be written as (4.29) in a discrete form.

$$i_{R_1}[k+1] = \exp(-\tau_{rc}) \cdot i_{R_1}[k] + [1 - \exp(-\tau_{rc})] \cdot I_b[k] \tag{4.29a}$$

$$V_b[k] = z[k] - R_1 \cdot i_{R_1}[k] - R_0 \cdot I_b[k] \tag{4.29b}$$

when τ_{rc} is the time constant of a RC pair explained by:

$$\tau_{rc} = \frac{\Delta t}{R_1 \cdot C_1} \tag{4.30}$$

This can be expanded for higher orders of RC as well. Therefore, the overall general model of order m in combination of the relation for the voltage finding can be formulated in discrete time as:

$$\tau_{rc_j} = \frac{\Delta t}{R_j \cdot C_j} \quad , \quad j \in \{1, \dots, m\} \tag{4.31a}$$

$$i_{R_j}[k+1] = \exp(-\tau_{rc_j}) \cdot i_{R_j}[k] + \left[1 - \exp\left(-\tau_{rc_j}\right)\right] \cdot I_b[k] \tag{4.31b}$$

$$V_b[k] = V_e[k] - \sum_{j=1}^{m} \left(R_j \cdot i_{R_j}[k]\right) - R_0 \cdot I_b(t) \tag{4.31c}$$

Using this general formulation, it is possible to fit the model into the recovery tail of pulse response and analyze how good each degree of the model performs. Thus, a MATLAB script is programmed using LSq method to fit models with 1 to 3RC sets. Comparison of error for these three tuned models on an example recovery period is presented in Fig. 4.20.

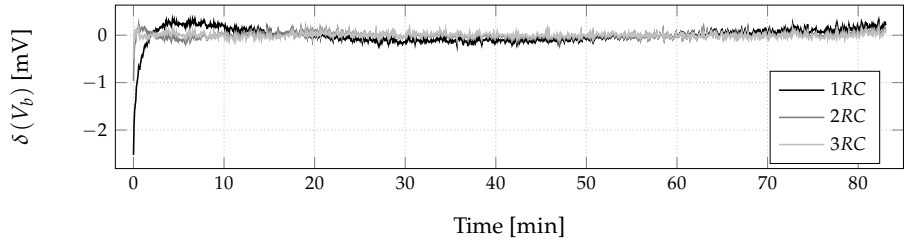

Fig. 4.20 Error of models with different number of RC sets tuned to the recovery period of an identification pulse in the discrete method.

It is clear from Fig. 4.20 that the 1RC model has order deficiency and overshoots largely in the beginning. This model underestimates the voltage in the middle and jumps high again at the end. This behavior has been seen for other pulses in the data-set as well. While 3RC removes this systematic failure and error is distributed more uniformly, 2RC model is positioned somewhere in between. Although it partially has an initial overestimation, the rest of the recovery curve can be predicted very well. According to the simplicity of 2RC model and marginal performance difference with 3RC, it is used hereafter.

During this tuning, LSq optimizer finds out the best selection of parameter values in the model explained in (4.31) which is actually the identification of dynamic parameters as well. Therefore, it is possible to apply this method on all measured recovery data in the discrete measurement data-set to find model's parameters at each experiment.

From a similar method used during the SoC-V_e identification, SoC for each set of identified parameters can be calculated as well. Using this SoC set, identified parameters for a 2*RC* ECM are presented in Fig. 4.21 for the whole charge range.

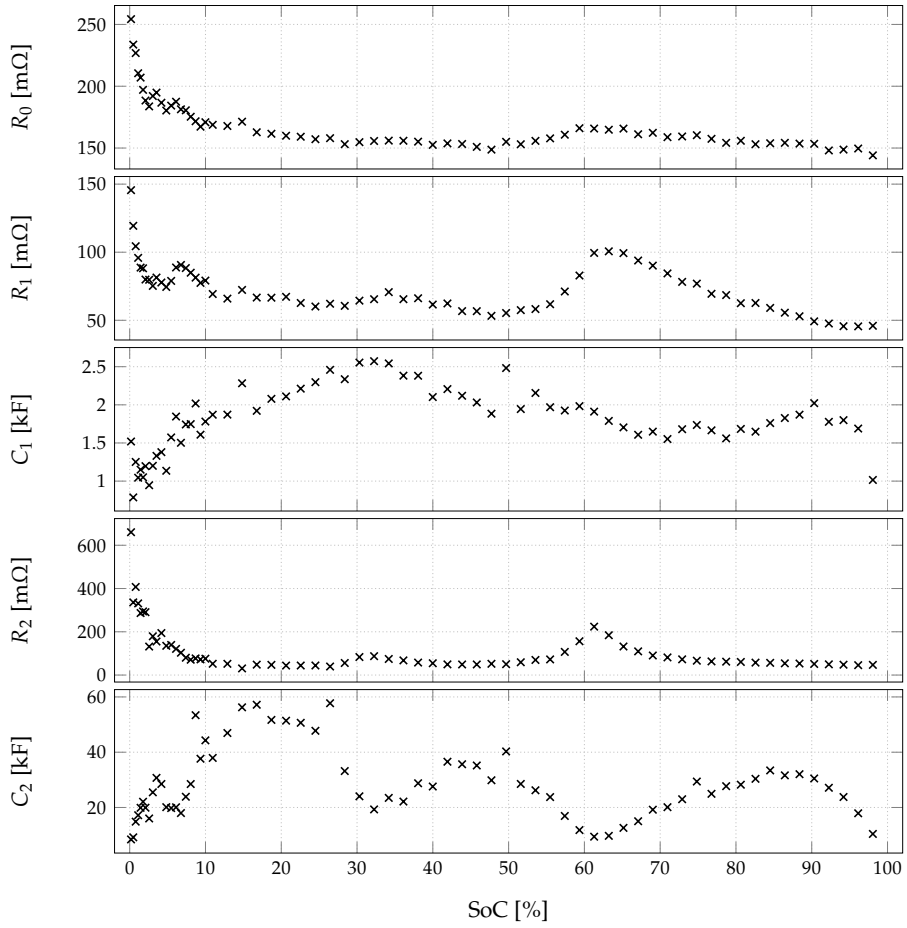

Fig. 4.21 Identified parameters for the 2*RC* model according to the related SoC.

As can be seen, parameters behavior include some dynamics according to the SoC. Therefore, the value of these parameters have to be stored in addition to the SoC-V_e relation. While these parameters are only necessary for the detailed model running on a normal computer, these values can be stored as some simple LuTs. It has to be noted that there are few outlier points in the identified data such as C_1 around 50 % and 100 % of SoC. Although it is possible to apply some outlier removal techniques or smoothing filter to remove such points, the exact measured values are used further in the model for consistency.

4.4 Models evaluation

Fundamentals of both PhyNode's models are built up to here. While on-board model is described in Section 4.3.4.4, detailed model with current as input and V_b as output has been made by an ECM with $2RC$ sets presented in Fig. 4.22.

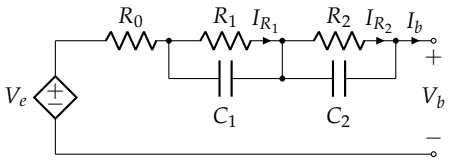

Fig. 4.22 Representation of ECM used for dynamic model of the PhyNode's battery.

The terminal voltage in this ECM can be explained in discrete time by:

$$\begin{aligned} V_b[k] =& V_e[k] - R_0(z[k]) \cdot I_b[k] - \\ & R_1(z[k]) \cdot I_{R_1}[k] - R_2(z[k]) \cdot I_{R_2}[k] \end{aligned} \tag{4.32}$$

when:

$$\chi[k] = \mathrm{LuT}_\chi(z[k]), \quad \chi \in \{V_e, R_0, R_1, R_2, C_1, C_2\} \tag{4.33a}$$
$$z[k+1] = z[k] - 100 \cdot \zeta_a \cdot \zeta_c[k] \cdot I_b[k] \cdot \Delta t / Q_n \tag{4.33b}$$
$$I_{R_1}[k+1] = \exp(\tau_{rc_1}[k]) \cdot I_{R_1}[k] + (1 - \exp(\tau_{rc_1}[k])) \cdot I_b[k] \tag{4.33c}$$
$$I_{R_2}[k+1] = \exp(\tau_{rc_2}[k]) \cdot I_{R_2}[k] + (1 - \exp(\tau_{rc_2}[k])) \cdot I_b[k] \tag{4.33d}$$
$$\tau_{rc_1}[k] = -\Delta t / (R_1(z[k]) \cdot C_1(z[k])) \tag{4.33e}$$
$$\tau_{rc_2}[k] = -\Delta t / (R_2(z[k]) \cdot C_2(z[k])) \tag{4.33f}$$

To enable evaluation of this model in addition to the on-board model, two validation experiments are designed. First test is a more general experiment in the context of PhyNode while the secondary one is specifically designed for the present status of PhyNode's operation. Performance of models on each of these experiments is evaluated separately.

4.4.1 Random load test

As a general evaluation experiment, current pulses with random amplitude and duration are applied as demand to the battery. Therefore, this experiment is named *random load test*. According to the overall demand of PhyNode, maximum load can be around 35 mA while highest charge current in PhyNetLab is about −150 µA. Hence, amplitude of the applied pulses will be in this range. While pulse duration can be between 1 s to 120 s.

Pulses are subsequently applied with voltage and current measured with a 100 ms sample time. Due to limited SMU memory, it is not possible to collect a complete discharge process started from the fully charged state. Therefore, this validation is divided into multiple sub-experiments. To avoid voltage jump in between two subsequent experiments, as soon as the memory is full

enough that only measurement of one extra hour can be stored, no further pulse is applied. During the remaining hour no current exchange happens while OCV is measured. In this way it can be assured that during the switch to the next experiment, voltage will not change. Furthermore, to allow detection of the initial state, OCV is measured in the beginning of each experiment for a duration of 1 min. This helps to find the initial state of the battery when each experiment is being analyzed standalone. Measured voltage and current during one such exemplary experiments are depicted in Fig. 4.23.

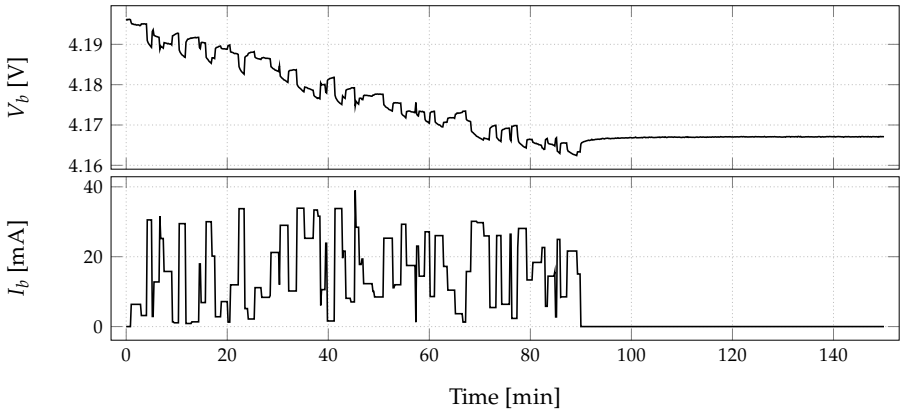

Fig. 4.23 Measured voltage and current during a random load experiment.

Complete data-set includes 50 of these measurements which are concatenated to build a complete discharge curve. Nevertheless, the whole experiment takes more than 120 h with more than 4.45×10^6 sample points.

4.4.1.1 On-board model

For the evaluation of the on-board model, measured V_b enters model in (4.16) to calculate the SoC. While the real SoC cannot be measured, original definition of SoC in (4.5) is used. This method uses present capacity to assure the most accurate SoC for the experiment. Model's error from this SoC is presented in Fig. 4.24 in addition to the error for using the LuT model.

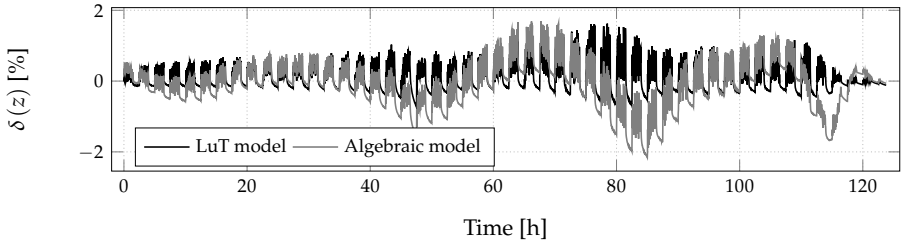

Fig. 4.24 Performance of the on-board model on the random load test.

As can be seen, SoC estimation has a small error in the whole range. It has to be considered that this model is using only the V_b without any feedback or current measurement. Lack of data about current is also the reason why error increases during rest periods at the end of each single experiment. During this rest phase V_b (which is actually the OCV) is increasing because of the recovery effect while the SoC is constant. However, model has no information about the current to include any dynamics and predict this behavior. Nevertheless, since this is a hardware limitation from PhyNode, this model is the best compromise which can be made. This algebraic based model has a RMSE of 0.61 % and LuT based model has a RMSE of 0.4 %.

4.4.1.2 Detailed dynamic model

Detailed model is presented as an ECM in Fig. 4.22 and formulated using a set of equations in (4.33). Only input to the model is I_b to predict the V_b. For evaluation, this model is applied on the random load evaluation data-set which its performance is presented in Fig. 4.25.

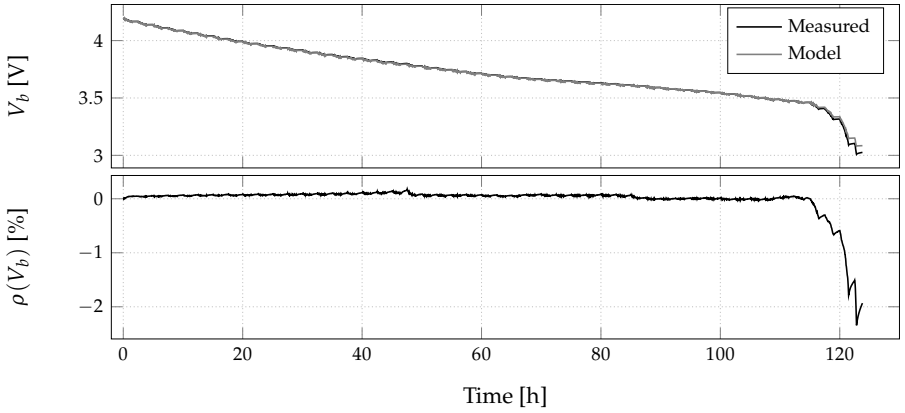

Fig. 4.25 Performance of the detailed dynamic model on the random load test data-set.

As can be seen in Fig. 4.25, errors are in a very small range with a RMSE of 6.1 mV and the maximum relative deviation of about 2 %, specially at the end of curve. It is clear that the model overestimates the voltage at the end, leading to the largest voltage difference. This difference can be a consequence of two reasons, namely: non accurate dynamic model or problematic estimation of the V_e. Deeper analysis of all single experiments in this data-set shows that this trend is vice-versa in the starting experiments and model predicts lower V_b values for them. For instance, in Fig. 4.26 data from the first experiment of the validation is presented, showing that the estimated voltage at the end of experiment is much lower than the real value.

In this region, model under-estimates the voltage, causing a value lower than the real V_b. However, looking at Fig. 4.26 shows that the dynamic behavior

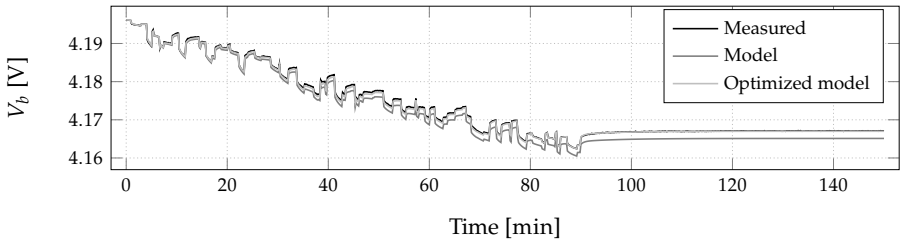

Fig. 4.26 Performance of the model on a single example of the random load test and a secondary model with optimized ζ_a for this specific experiment.

is very similar to the battery behavior. In case the reason for this mismatch be a bad dynamic model, still measured voltage at no current phase (during the end tail of this experiment) has to be equal to the V_e. Nevertheless, Fig. 4.26 shows that this is not the case and source of error is within the estimation of the V_e.

As discussed formerly, SoC-V_e relation changes slowly over the time, causing some errors in the model which cannot be fixed without long term analysis of the SoC-V_e relation which is out of scope of this work. However, another reason for this deviation can be considered which is within the way SoC is being calculated. More specifically, it is due to the changes in the aging factor ζ_a during the experiment. To show this effect more clearly, aging factor is optimized in a way that the model's voltage at the end of the first experiment fits into the measured value. Performance of this optimized model is also shown in Fig. 4.26 as well. It is clear that the dynamic model is performing perfectly and tracks all changes as it should. However, when this model with optimized ζ_a is applied on the whole evaluation measurement, the overall performance gets much worse, as depicted in Fig. 4.27.

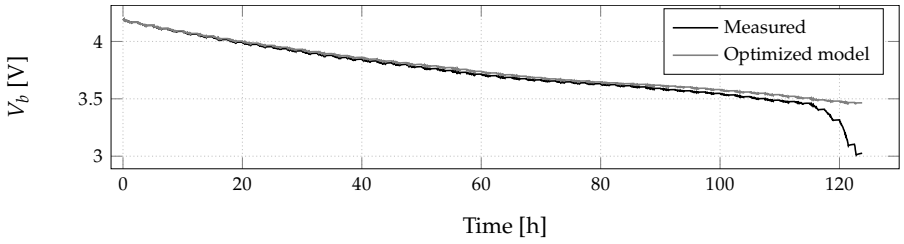

Fig. 4.27 Performance of the model on the whole random load test with optimized ζ_a for the first single experiment.

In this condition, model is always over-estimating the voltage. This is mainly a consequence of ζ_a calculation method which is tuned optimally based on the beginning of the whole evaluation experiment. However, since battery is aged during the discharge process as well, selecting the initial factor as a constant for the whole curve is inappropriate. That is also the reason for the errors in the overall experiment. It under-estimates the voltage in the beginning and overestimates it at the end because ζ_a is simply selected as the average

of standard tests before and after. This average value is a representation of somewhere in the middle of the curve and not the whole discharge process.

Using standard test principle (which is also common for finding the SoH curve) only a single parameter for each discharge curve is available. This value is actually an estimation of the overall aging during one complete cycle, including both charge and discharge. Therefore, based on the real aging process (which can be only explained with electrochemical models), this value can be accurate only for a small portion of the curve. For all times before this section, SoC is being under-estimated and over-estimated for points after that. This theory can explain the inaccuracy in the performance of the SoC estimation. Anyhow, the main question arising at this point is:

How to estimate the aging factor for low-budget batteries in ULP application?

To overcome this challenge, aging factor cannot be considered as a constant value for the whole period and has to change dynamically. However, there is no exact knowledge about the way that aging proceeds during a discharge curve. Therefore, a simple linear behavior is considered here helping to update (4.33b) into:

$$z[k+1] = z[k] - 100 \cdot \zeta_a[k] \cdot \zeta_c[k] \cdot I_b[k] \cdot \Delta t / Q_n \tag{4.34}$$

when:

$$\zeta_a[k+1] = \zeta_f + \frac{z[k]}{100} \cdot \left(\zeta_f - \zeta_l\right) \tag{4.35}$$

while ζ_f is the aging factor from former standard test and ζ_l is the estimated factor for the whole curve as the average of both standard tests. The average value is selected because the single capacity of standard test can be related to the end of a discharge procedure. However, there are a charging phase after each discharge as well in each standard test.

Inclusion of this dynamic ζ_a into the complete model improves the overall performance of the model which is presented in Fig. 4.28.

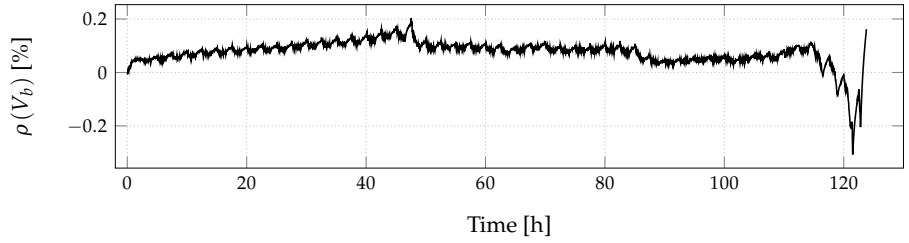

Fig. 4.28 Relative error of the improved model with dynamic ζ_a on the random load test.

As can be seen, this is able to reduce the maximum error from about 2 % for the constant ζ_a shown in Fig. 4.25 into about 0.2 %. The RMSE for the overall experiment is 3.29 mV and 0.08 % for the relative error.

4.4.2 PhyNode load test

For the final evaluation of models, present behavior of PhyNode is considered. For this purpose, a simplified load cycle of PhyNode is made based on the load profile measured and shown in Fig. 4.7. In this load, small changes in the curve are filtered to build the load shown in Fig. 4.29.

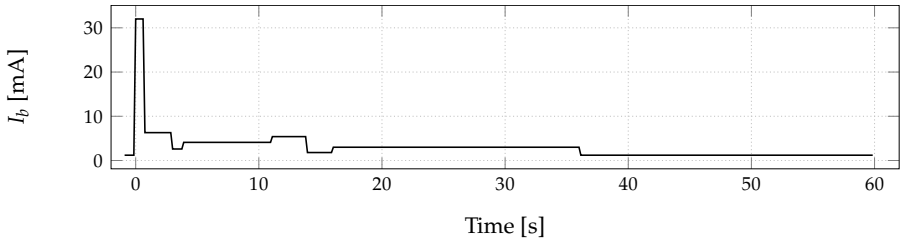

Fig. 4.29 A single simplified cycle of PhyNode's load profile.

This load is continuously applied to the battery till V_b reaches 3.53 V as the lowest allowed voltage for the present status of PhyNode, taking more than 15 days. This data-set is used to evaluate performance of battery models based on the operational situation of PhyNode.

4.4.2.1 On-board model

As mentioned, limited voltage range of PhyNode requires a modified SoC-V_e relation. Using tuned model from (4.16), error of the on-board model for the PhyNode range is presented in Fig. 4.30.

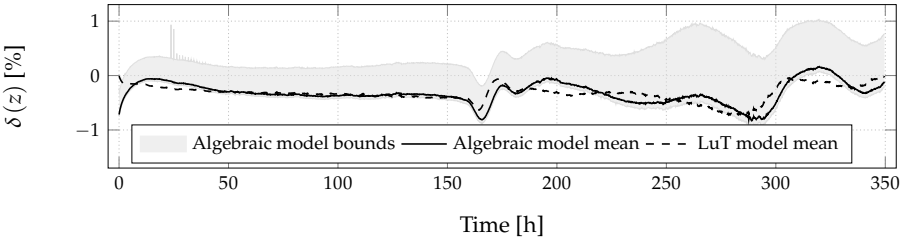

Fig. 4.30 Performance of the on-board model on the PhyNode load test.

Due to very short scale of a single PhyNode load period to the overall duration of the experiment, more than 25×10^6 points are available in the data-set. Consequently, graphical representation of error would be a thick bulk of signal. Therefore, mean of this error signal in addition to its bounds are presented in Fig. 4.30. For comparison, it shows the mean error for the modified LuT as well. As can be seen, explicit algebraic equation has a roughly similar performance. RMSE for the algebraic and LuT models are subsequently, 0.3832 % and 0.3676 %. Consequently, the relation in (4.16) can be considered

as a valid model for the on-board usage of PhyNode with V_b as input and SoC as output.

4.4.2.2 Detailed dynamic model

Final evaluation is to apply the detailed dynamic model on the PhyNode data-set. Relative error of this experiment is presented in Fig. 4.31.

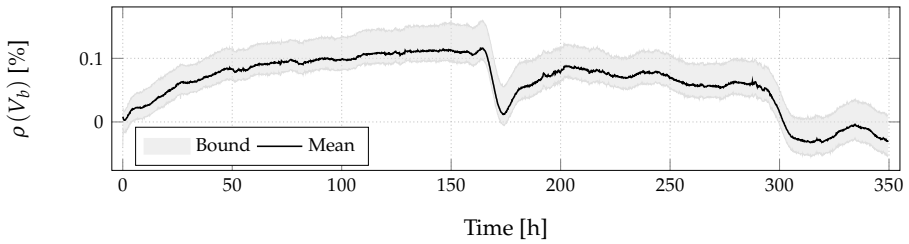

Fig. 4.31 Relative error of the detailed model on the PhyNode load test.

Similar to Fig. 4.30, in addition to the mean, both bounds of the error are presented here. In this experiment, worst condition has an error of less than 6 mV. The overall RMSE of this combination is 2.9 mV or 0.075 % on the relative error.

Looking at Figs. 4.28 and 4.31 error curves show a roughly similar behavior which can be a sign for a systematic inaccuracy. However, this is a consequence of using the averaged SoC-V_e relation from multiple batteries to compensate production tolerances. As can be seen in Fig. 4.16, there are two protrusion sections in some curves which are exactly at the same areas as in the error curve and follow the same pattern.

Finally, it has to be noted that these models are both developed in an open loop manner due to the system design restrictions and their performance should not be compared to models with a closed loop structure.

Chapter 5
Modeling Power Management System

Energy cannot be created or destroyed, it can only be changed from one form to another.

–Albert Einstein

Abstract
This chapter focuses on the modeling of the management device connecting a PV module and a battery together. In the beginning, general operational principles including a DC-DC converter, an MPPT mechanism and battery controller are addressed. In addition to the review of common converter techniques, differences between these methods and systems for EH applications specifically with ULP restrictions are reviewed and State-of-the-art devices are surveyed.

For the analytical modeling of the used device, its internal design is mentioned. By monitoring its switching mechanism, different criteria are extracted explaining converter's control mechanism. However, complexities in the controller, availability of multiple abnormal operations in addition to the inclusion of noise makes its complete deductive modeling impossible. Therefore, machine learning based strategies are used afterwards. A scenario is designed which measures the periodic steady-state behavior of the converter in different possible operational conditions. Using this data, an artificial neural network and a decision tree are trained to replicate converter's behavior. Using statistical analysis on the data-set, a single efficiency approach for the converter is exploited as its on-board model.

Measured data-set is used for extraction of MPPT behavior. It defines the selection criteria for the operational voltage of the PV module according to the open circuit voltage. In addition to a simple mathematical formulation, an artificial neural network and a decision tree model are provided for the MPPT mechanism as well.

While each single model is evaluated using the data-set, a separate scenario is designed for the final evaluation of them. In addition to the randomly selected points in the whole operational range, experiments have been measured and checked in the operational range of PhyNode as well.

5.1 Introduction

Energy storage and harvesting devices have been analyzed till here. To power an IoT device with recharging from an EH module, a simple configuration of joining them with a direct connection depicted in Fig. 5.1 can be considered .

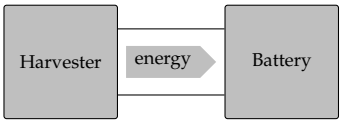

Fig. 5.1 Direct connection of EH transducer and a battery. PV operational voltage is defined and forced by battery.

In this configuration, operational voltage of the EH transducer is equal to the battery's voltage. It is known that battery's voltage slowly but continuously changes during operation. This voltage is dependent to the demand from the IoT device, supply from harvester and battery's internal states. Moreover, supplied power from the EH module is variable and nonlinear according to the environmental condition. It is possible during the design phase to select operational condition of the battery near the EH transducer's MPP. However, according to the nonlinear dynamic nature of both sides, even a well matched system will be optimal only in a limited range of conditions. Hence, a direct connection configuration is not optimal for ULP applications.

To conquer this performance deficiency, a middle-ware is required matching voltage levels of two sides while each one operates at its optimal voltage. Such a device named *converter* is able to match systems with different voltage levels by pushing voltage up or down with a conversion rate (κ) defined in (5.1) when V_i and V_o are subsequently input and output voltages of the converter.

$$\kappa = V_o / V_i \tag{5.1}$$

Based on the value of κ, three common types of converters are:

Boost: increasing the voltage level ($\kappa > 1$)
Buck: decreasing the voltage level ($\kappa < 1$)
Buck/Boost: operation in both modes ($\kappa > 0$)

which designers may select based on the system requirements. Some EH transducers such as vibrating or wind harvesters generate AC output, requiring an additional AC-DC converter. Furthermore, as discussed in Chapter 4, it is common that components of an IoT device operate in different voltage levels than as the storage's voltage. In these cases, a secondary converter or PMIC is necessary to match the battery output voltage to the rest of the system. Considering all modules, the overall ESU can be abstracted in Fig. 5.2.

Fig. 5.2 A complete ESU using EH for an IoT device.

In the case of PhyNode no AC-DC converter is required due to DC generation from PV module. To match the MPP voltage from harvester to V_b, a BQ25505 chip produced by TI is used which will be modeled in the rest of this chapter. This device is a multi purpose component designed to do MPPT and act as the DC-DC converter while safely operating the battery. Its converter is designed for boost condition in low power input range. It is a reliable solution considering low voltage level of the PV harvesting in PhyNetLab mostly lower than the battery voltage of PhyNode. Addition of this component completes PhyNode's ESU as presented in Fig. 5.3.

Fig. 5.3 Schematic representation of PhyNode's complete ESU.

5.2 Principles of DC-DC conversion

Voltage conversion from one level to another voltage can be implemented using different techniques. In most applications the output voltage has to be controlled at a desired value regardless of the current demand while the input voltage is constant. This is a common case for most battery driven devices which the demand may variate based on the operations of the device while battery voltage remains roughly constant. A simple method for conversion is to dissipate the excess power using a voltage divider. Not only this will have a very low efficiency, but also it is only applicable as a buck converter. Furthermore, it is only able to deliver a fixed ratio of the voltage. Hence, output voltage cannot be controlled directly except by manipulation of resistors.

To conquer this issue, switches are added to the design. A simple design using a single switch commonly known as *linear converter* controls the timing of the current passed to the output. A voltage feedback from the output side is used to generate the timing control signal based on the amplified error. Two realization of this principle including a LDO are presented in Fig. 5.4.

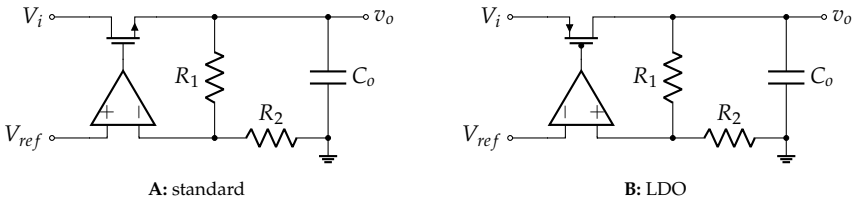

Fig. 5.4 Common linear converter topologies. From [221].

To be noted that the output voltage notation (v) is different from the input (V). This difference is to show inclusion of oscillations around the DC voltage as a consequence of switching. Therefore, the capacitor (C_o) is added at the output

side to filter fast harmonics. This notation will be used in the rest of this work to show availability of oscillations.

Using linear converters conquers the output voltage control issue. However, these designs still have the limitation to only reduce the voltage with low efficiency. To solve this deficiency, addition of an active component to the design is common. Based on the relative positioning of switch and this active component, different operational phases are possible. In the first phase, this component stores incoming energy to build up a higher voltage. During the second phase, stored voltage is added on top of the input voltage and passed to the output. According to the timing of these phases in addition to the topology of the circuit, this system can push the voltage either up or down. Furthermore, this principle has better efficiency because no power is being wasted as heat.

Capacitors and inductors are two active elements to store energy. Designs with capacitors are addressed with Switched Capacitor (SwC) while inductor based designs can be named Switched Inductor (SwI). In contrast to capacitors, charging process of inductor is not intrinsically lossy [222]. This means the charging process of an (ideal) inductor does not involve energy loss. While this is not the case for capacitors even in case of considering all charging elements of the circuit ideal [222]. Consequently, inductor based design of converter is commonly preferred for converters, specially for ULP applications and will be followed hereafter.

A SwI DC-DC converter uses inductor(s) as the active energy storage component while the energy state is controlled by some switching mechanism. Three possible phases for the inductor are:

Charge Phase (φ_1): Energy flows into the inductor, current flow increases and stores energy in the magnetic field.

Pump Phase (φ_2): Stored energy in the magnetic field flows out of the inductor and current flow decreases.

Idle Phase (φ_3): Energy balance of the inductor does not change, leading to a constant current flow.

It is common in the circuit representation to use a Single Pole Double Throw (SPDT) switch for changing the energy flow. Two common designs of SwI converters using a SPDT are presented in Fig. 5.5.

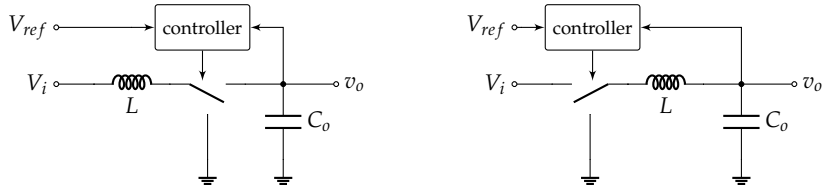

A: boost topology **B:** buck topology

Fig. 5.5 Two main SwI converter topologies.

Considering Fig. 5.5A as a general form of the boost SwI converter, two operational conditions can be possible. To analyze them, understanding inductor and its changes are necessary. It is known from the basic physics that the I-V relation of an inductor can be explained by:

$$v_l(t) = L \cdot \frac{\mathrm{d}i_l(t)}{\mathrm{d}t} \tag{5.2}$$

In the boos converter case, when the SPDT is in its lower connection, a positive voltage is available at the inductor. According to (5.2), this voltage causes increase of current, leading to the charge phase. On the other hand, when the SPDT is in its top state, a negative voltage would be applied to the inductor causing reduction of inductor's current. This makes energy transfer to the output side and can be considered as the pump phase.

A SPDT enables selection of one of two possible routes which can be simply charge or pump. Different realization of switching are possible with an overview available in [223]. Anyhow, a SPDT can be implemented using two separate Single Pole Single Throw (SPST) switches, realized using semiconductor power electronic components. Although passive semiconductor such as diode may be useful for some specific applications, active switches with a control terminal are preferred. Bipolar Junction Transistor (BJT) and Insulated Gate Bipolar Tansistor (IGBT) switches are two common realizations of an active switch. These switches are single-quadrant according to their reverse-blocking characteristics. However, Metal Oxide Semiconductor Field-Effect Transistor (MOSFET) are able to conduct reverse direction current, and are used when a two-quadrant realization is necessary. In some applications a two-quadrant switching element is required with the ability to conduct current of both polarities. Therefore, a body diode is built into the MOSFET allowing current in the reverse polarity. Two most common realization possibilities using MOSFET are shown in Fig. 5.6.

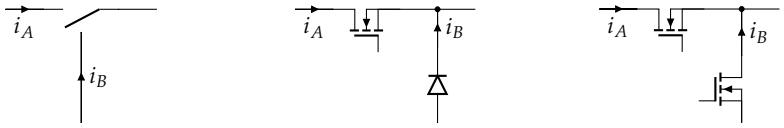

A: SPDT switch **B:** asynchronous **C:** synchronous

Fig. 5.6 A SPDT switch (A) and its possible realizations using MOSFET (s).

In the realization with the help of the freewheel diode in Fig. 5.6B, only one period (when i_A flows) can be controlled by controller. While diode current i_B depends on the voltage levels and cannot be controlled directly by controller. Therefore, this realization is mostly called an *asynchronous* design. In contrary, a *synchronous* design shown in Fig. 5.6C allows control of currents separately in addition to an idle phase.

It has to be noted that in the synchronous design, freewheel diode is still needed to prevent simultaneous conduction of both transistors [224] because of the dead time between changing the switching states. However, it is possible to use a body diode which typically provides a better performance compared to an external diode [224].

Typically, diode conduction loss increases when the output voltage is reduced [223]. Therefore, an asynchronous design would have lower efficiency in applications operating in lower voltage levels [223]. Consequently, synchronous realization of SPDT is more feasible for ULP application and will be used hereafter. Using synchronous realization, the overall boost converter of Fig. 5.5A will be realized as in Fig. 5.7. For simplicity, feedback mechanism is not presented here. However, a measurement of the output voltage is fed to the controller as well to enable tracking of the reference voltage.

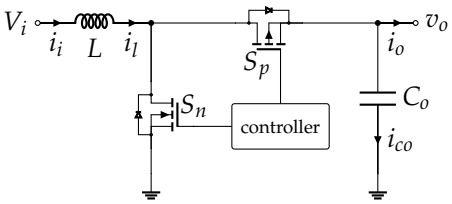

Fig. 5.7 Synchronous realization of a boost SwI converter.

Considering design in Fig. 5.7, feasible combination of switches and converter's phases can be explained as in Table 5.1, while Fig. 5.8 presents circuit topology of each phase.

Table 5.1 Feasible switching states for a synchronous boost SwI converter.

State	charge (φ_1)	pump (φ_2)	idle (φ_3)
S_n	close	open	open
S_p	open	close	open

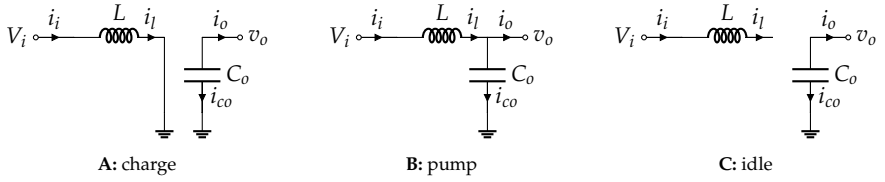

Fig. 5.8 Representative circuit of a boost SwI converter in different switching phases.

During the charge phase (φ_1), two sides of the converter will be separated from each other while the S_p is open. Consequently, current flows through the inductor and its value increases exponentially over the time with a rate dependent on the input voltage and the inductor value. Meanwhile, the output is only fed from the output capacitor, discharging exponentially with corresponding reduction in v_o. Using basic Kirchhoff laws, circuit states can be

explained by:

$$v_i(t) = L \cdot \frac{\mathrm{d}i_l(t)}{\mathrm{d}t} \tag{5.3a}$$

$$i_{co}(t) = \frac{\mathrm{d}v_{co}(t)}{\mathrm{d}t} \tag{5.3b}$$

In the pump phase (φ_2), the S_p is closed, pumping stored energy from inductor to the output. Circuit states of the converter can be explained by:

$$v_i(t) - v_o(t) = L \cdot \frac{\mathrm{d}i_l(t)}{\mathrm{d}t} \tag{5.4a}$$

$$i_{co} = \frac{\mathrm{d}v_{co}(t)}{\mathrm{d}t} \tag{5.4b}$$

During the idle phase (φ_3), both switches are open and no energy passes to the output through the inductor. Meanwhile, the output is fed from C_o which its voltage reduces over time. These change can be formulated by:

$$i_l = 0 \tag{5.5a}$$

$$i_{co} = \frac{\mathrm{d}v_{co}(t)}{\mathrm{d}t} \tag{5.5b}$$

According to the control scenario, controller toggles switches to move from one state to the other. After a change in the controlled signals, controller will adapt the switching till the reference voltage (V_{ref}) is reached. This time required for reaching the V_{ref} is commonly known as the *start-up*. In contrary, the state when system's general behavior is not changing anymore is called the *steady-state*. During the steady-state, controller simply repeats a specific pattern.

Based on ODEs explaining signals in each phase, converter's signals can be seen from two different perspectives. Dynamic analysis can explain the I-V behavior of the converter at each time instant, including the start-up period. On the other hand, is the Periodic Steady-State (PSS) mode which only examines the overall average behavior of the system and ignores small oscillations. When PSS behavior of switching systems is analyzed, signals can be divided into one DC value in addition to a small-signal which includes all non-zero components of the signal's Fourier transform. It can be considered that the output capacitor filters the non-DC part of the signal and only average signal or the DC value is used. Although it is possible to use the Root Mean Square (RMS) value of the signals, average signals in PSS are used while the DC analysis is desired here. The average PSS value of a signal $s(t)$ is shown as $\langle s \rangle$ which can be found using (5.6), when $\mathcal{T}$ represents a complete switching cycle of the signal. This notation is explicitly used to show availability of non DC components in a real signal in contrast to a pure DC signal.

$$\langle s \rangle = \frac{1}{\mathcal{T}} \cdot \int_0^{\mathcal{T}} s(t)\,\mathrm{d}t \tag{5.6}$$

PSS analysis is based on the fact that the energy balance during each complete steady-state period has to be zero. This actually follows the inductor volt-second balance as:

Principal: *Inductor volt-second balance*

For a constant inductor in the steady-state operation, the incoming energy stored inside is equal to the delivered energy from the inductor.

Based on this principle, as long as the inductor is constant, the net current change through it during a period is zero. A similar principle is also valid for a capacitors' balance in steady-state, called *capacitor amp-second balance*. More detailed explanation of these principles can be found in [222] and in most physics textbooks. Based on this principle for a SwI converter, inductor's current at the end of a cycle would be the same as its value in the beginning. Considering the SwI converter from Fig. 5.7 with only one charge phase followed by a single pump phase, this principle can be formulated as:

$$i_l(\mathcal{T}) - i_l(0) = \frac{1}{L} \cdot \int_0^{\mathcal{T}} v_l(t)\,\mathrm{d}t = \frac{1}{L} \cdot \left(\int_0^{t_1} v_l(t)\,\mathrm{d}t + \int_{t_1}^{t_2} v_l(t)\,\mathrm{d}t \right) = 0 \tag{5.7}$$

when $\mathcal{T}$ is made of $\tau_{\varphi 1}$ and $\tau_{\varphi 2}$ for the charge and pump periods subsequently with the inductor current as in Fig. 5.9.

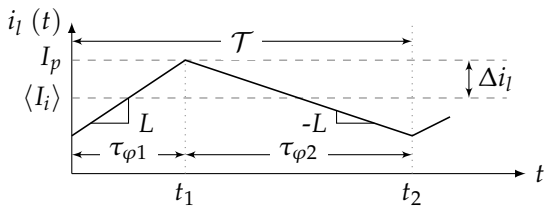

Fig. 5.9 Linearized inductor's current of a SwI converter in PSS condition.

To be noted that this is a linearized representation of the inductor's current which is exponential in reality according to the solution of (5.2). For this simple converter, the average PSS inductor's current would be equal to the input current while the small-signal changes (ripples) can be explained by:

$$\Delta i_l = \frac{\langle V_i \rangle}{2L} \cdot \tau_{\varphi 1} = \frac{\langle V_o \rangle - \langle V_i \rangle}{2L} \cdot \tau_{\varphi 2} \tag{5.8}$$

It can be seen from (5.8) that the inductor's current ripples (Δi_l) is only dependent on the voltages in addition to the timing, rather than the input current ($\langle I_i \rangle$). Considering Fig. 5.9, if $\langle I_i \rangle$ is reduced, a point can be imagined that the peak current (I_p) is exactly two times of the $\langle I_i \rangle$. In this situation,

current would be exactly zero at the end of each cycle. Furthermore, when $\langle I_i \rangle$ is less than half of the I_p, idle phase will be added to the system. Accordingly, two different categories of operation can be defined based on the current flow during a complete switching cycle. Those cases with continuous flow such as the one shown in Fig. 5.9 are called Contineous Conduction Mode (CCM). In contrast is the case when an idle phase is also available with a time period of zero inductor's current which is called Discontineous Conduction Mode (DCM). Using these definitions, the case shown in Fig. 5.10 presents the border of these two conduction modes.

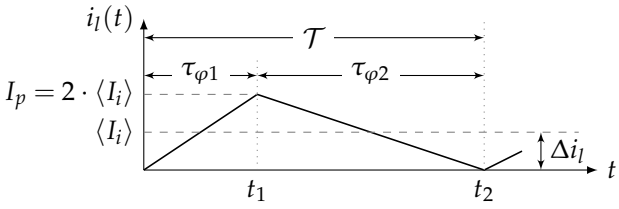

Fig. 5.10 Linearized PSS currents of a SwI converter when the peak current is exactly two times of the PSS input current. This is the border case between CCM and DCM.

5.3 Control mechanism

Physical structure of a boost SwI converter is explained and signals behavior during each phase are known. The key differentiation between performance of these systems lies in the way that the control mechanism switches in between different phases. In spite of diversity in control techniques, they can be categorized into two major classes of:

Pulse Width Modulation (PWM): Control mechanism only modifies the ratio between phases while the overall cycle duration remains constant.

Pulse Frequency Modulation (PFM): Control mechanism uses different frequency of switching which leads to not fixed cycle durations.

5.3.1 Pulse width modulation

PWM category of control mechanism is more common because of its simpler analytical concept for the design and implementation. The overall concept is based on the control of the *duty cycle* as a ratio between phases, while the overall cycle duration is kept constant. Based on the converter type, duty cycle is defined using the fraction of charge or pump period over the whole cycle time. To avoid misunderstanding, it is more common for PWM analysis to use the *active time* instead of charge or pump times. Active time is the period that the output gets energy from the input. Consequently, duty cycle is defined as:

$$D = \frac{t_{active}}{\mathcal{T}} \tag{5.9}$$

There are multiple controller designs for the regulation of the duty cycle. The most common way is to compare the error with a saw-tooth signal to generate the duty cycle and switching signals. Implementation, stability analysis, transient behavior and signals in addition to the converter's transfer function calculation can be found in [222, 223].

A secondary group of PWM control strategies use the peak current instead of the saw-tooth signal. Due to use of current for control, this group is commonly known as *current controlled*. The main advantage of these controllers is their simpler dynamics. Nonetheless, their sensibility to the noise works against this type of control. Anyhow, different converters with this control mechanism are commercially available as IC [223, p. 441].

PWM converters can have a high efficiency when they work at the full load. However, while many of losses are not dependent on the output current (load), it dissipates a portion of the power at light loads. When the operational point reduces, the relation between the PWM power dissipation to the load grows and becomes more significant, thereupon reducing the overall efficiency of the converter. [225]

5.3.2 Pulse frequency modulation

Second group of control techniques for converters originated in 60's is PFM [226]. This method uses short bursts of power to the output and manipulates the overall output power by controlling the frequency of these bursts. In contrary to PWM, PFM controller allows changes in the cycle time. When a higher load is required (or output voltage is dropped below V_{ref}) cycle time gets shorter while keeping the active time constant. This helps to decrease switching for lower loads and reducing loss for these conditions.

Multiple techniques are available leading to variable switching frequency which a survey including some of them can be found in [227]. However, it is possible to classify them into three main categories as:

- Hysteresis
- Time-based
- Current controlled

Hysteresis control mechanism simply compares the output voltage with the reference value including a hysteresis. Since switching is directly dependent on the error and hysteresis band, switching duration may change, building a variable frequency control.

Time-based control has two sub-groups. Some control techniques keep the on period of the switching constant while others do a constant off period. For instance, in a t_{on} control mechanism more peaks with the same on duration are fed to the output when the load goes high or the output voltage drops from the reference value.

Current controlled techniques monitor the point when the inductor current reaches a predefined value. While according to (5.3a) and (5.4a) time duration of phases are dependent to the voltages, this method manages the time of each phase indirectly by selection of the related peak current. In addition, changes in voltages will lead to change in the duration of each phase and causes not fixed cycle times and frequencies.

All in all, a large number of PFM techniques are available which Constant on Time (CNT), Constant off Time (CFT), Peak Current Control (PCC), Pulse Current Modulation (PCM), Pulse Skipping Modulation (PSM), Burst Mode Operation (BMO), Pulse Train Control (PTC) and Multi-Pulse Train Control (MPTC) are only some of them.

Generally speaking, PFM is a control scheme which reaches high efficiency for a wide load range [225]. According to the burst concept of the PFM, it only reduces the frequency of switching for low loads and power dissipation remains small compared to the light load [228]. Within the IoT application with ULP perspective, most of the harvesters are able to deliver a very limited amount of power. Therefore, using a PFM controller for the conversion of power from harvester to the battery is of big benefit.

5.4 State-of-the-art micro harvesting converters

Using a converter for ULP EH applications has some extra specification in addition to the common DC-DC converters. A converter in an EH application has to control the input voltage according to the MPPT to avoid efficiency loss. This requires a feedback loop from the input voltage side. This is in contrast to the classical converters with the feedback loop on the output side. In addition, most EH transducers have a dynamic I-V relation. Hence, voltage modification will cause changes in the current and vice versa. Therefore, a converter has to actually control the impedance of the EH transducer instead of voltage or current alone.

Contrary to the common converter design requirements, no reference value is available for the output voltage here which is connected to the battery. Therefore, as long as the battery terminal voltage is in the accepted range, system will be operable. Consequently, in normal operation of the converter, output voltage is considered constant. In other words, role of input and output is toggled compared to a typical converter. Nevertheless, converter should still have a feedback on the storage side to avoid overcharging and informing rest of the system in case of reaching the cut-off voltage. Considering these specific requirements for the micro harvesting converters, their control design would be different from the traditional ones.

In addition to the structural design differences, micro EH converters itself should have a very low power demand. Many producers of the EH transducer design their product in the voltage range with a MPP around 3 V to 5 V for

voltage matching reasons. Due to low power harvesting of these devices, generated current is in very small levels of sub-Ampere. Hence, a converter has to be optimized for operation at this range of currents. The quiescent current and power required for the converter's control mechanism has to be minimal that can be fed from the available harvested energy.

Furthermore, within most IoT applications, number of components, their price, weight and space footprint are critical factors. This has to be considered for the DC-DC converters as well. Moreover, trend toward application of IoT devices into the industry requires off-the-shelf products which can be simply purchased and integrated. Therefore, a market is available for fully integrated solutions for micro harvesting converters. Consequently, not only researchers develop such solutions, but also multiple manufacturers have produced specific ICs for this type of applications. A list of published designs from academia is available in Table 5.2, while Table 5.3 compares off-the-shelf products.[1]

Furthermore, a very wide range of products operate as converter and can be integrated for such application as well. However, some of them such as LTC3107 [229], LTC3108 [230], LTC3588-1[231], BD70522GUL [232] and EM8900 [233] do not provide any MPP tracking or control. Some of these products also are designed for specific applications and do not use the typical switched converter topologies. For instance, LTC3107 and LTC3108 use an external transformer mechanism while LTC3588-1 uses a full-wave bridge rectifier.

As can be seen from Table 5.2, some researches claim very promising results. However, IoT system designers mostly rely on available products in the market. Among products mentioned in Table 5.3, BQ25505 and BQ25570 from TI show a wide operational range while providing MPPT with very low quiescent current. Perhaps that is the reason why multiple embedded devices such as [234–239] have used one of these two for their implementation.

The difference between BQ25505 and BQ25570 is the availability of an extra buck converter at the output side of BQ25570, enabling a secondary output voltage rail. However, as formerly discussed in Section 4.3.1, use of PMIC with a LDO is preferred for PhyNode. Anyhow, the main parts including MPPT mechanism and boost converter are the same for these two devices. Therefore, it is possible to use them redundantly and apply the developed model for both of them alternatively. Thus, in the rest of this work BQ notation is used which can be interpreted as either of these devices.

[1] To be noted that these lists are complete for ULP applications, to the knowledge of author at the time of writing.

Table 5.2 Comparison of different state-of-the-art EH converter designs in research publications.

Design	Type	Mode	EH	V_i	MPPT	V_o	Best efficiency[a]	Fabrication
[240]	SwC	var. freq.	TEG[b]	>0.6 V	only TEG		82 %-70 %	0.35 µm-CMOS
[228]	SwI-syn.	DCM-PCM	TEG	20 mV-250 mV	only TEG		78 %-NA	0.13 µm-CMOS
[241]	SwI-syn.	DCM-PSM	PV	0.5 V-2 V	hill-climbing		87 %-70 %	0.25 µm-CMOS
[242]	SwI-syn.	DCM-PFM	EPH[c]	20 mV to 70 mV	Fixed	0.8 V to 1.1 V	56 %-NA	0.18 µm-CMOS
[243]	SwI-syn.	DCM-PCC	PV-TEG	80 mV-2.5 V	FOCV	3 V to 5 V [242]	NA-95 %*	NA-CMOS

[a] only converter/including the MPPT [b] Thermo-Electric Generator (TEG) [c] Endocochlear Potential Harvesting (EPH) * Not exact

Table 5.3 Comparison of different state-of-the-art EH converter available commercially.

IC	Type	Mode	V_i	V_{NO} [a]	$V_{Battery}$	MPP	I_Q	Max. P_{in}
MB39C831 [244]	SwI boost	PWM-PFM	0.3 V to 4.75 V	2.6 V	3 V to 5 V	T-FOCV[c]	41 µA	950 mW[d]
BQ25504 [245]	SwI boost	PFM (PCC)	0.3 V to 5.5 V	1.73 V	2.5 V to 5.25 V	T-FOCV	330 nA	400 mW
BQ25505 [246]	SwI boost	PFM (PCC)	0.3 V to 5.5 V	1.73 V	2 V to 5.5 V	T-FOCV	325 nA	510 mW
BQ25570 [247]	SwI boost	PFM (PCC)	0.3 V to 5.5 V	1.73 V	2 V to 5.5 V	T-FOCV	488 nA	510 mW
LTC3105 [248]	SwI boost	PFM (BMO)	0.225 V to 5 V	250 mV	1.6 V to 5.25 V	C-Fixed voltage	24 µA	NA
LTC3106 [249]	SwI buck-boost	PFM (BMO)	0.3 V to 5.1 V	300 mV	2.1 V to 4.3 V	C-Fixed voltage	1.6 µA	NA
SPV1050 [250]	SwI Boost/buck-boost	NA[e]	0.15 V to 5.3 V[f]	550 mV[f]	2.2 V to 5.3 V	T-FOCV	1.7 µA[g]	NA

[a] Min. voltage for normal operation of the converter [b] can be used with others [c] percentage setting between 50 % to 85 %
[d] calculated (not explicitly mentioned) [e] perhaps PFM, according to the maximum switching frequency of 1 MHz [f] in boost configuration
[g] only one of output LDOs running

5.5 Modeling DC-DC converters

Two main concepts are available for the modeling of DC-DC converters as a consequence of how signals are analyzed. Dynamic models describe the converter using a set of DAE based on the small-signals from the converter. These equations are commonly depicted in a state-space model representation. Nonlinear and linear small-signal models have been presented for different control strategies of switches such as in [251–253]. This modeling perspective is optimal for analyzing details in the system and is mostly the back-end of circuit simulations used in the form of Spice softwares. Although these models are well describing, extensive amount of included details makes them unsuitable for the abstract level analysis such as for the system designers. In addition, development of such models requires exact knowledge of the internal control mechanism which is mostly not available for commercial off-the-shelf products.

On the contrary are PSS average models which ignore small-signals and only reproduce the overall steady-state behavior. These models lack the information during transient phase of the converter while they are not replicating the control mechanism but only its steady-state behavior. In addition, these models cannot explain the oscillations in signals while these parts of signals are normally ignored during the modeling. Such models are only a small set of algebraic equations which can be simply solved and consequently preferred by most system designers. Another advantage of these models is the amount of knowledge required for the development. In contrast to the small-signal dynamic models, modeler should only have information about the general behavior of the converter. This can be an abstract analysis of the signals regardless of the real control mechanism. For instance, considering a simple PWM mechanism, such a model would not require to know if the feedback loop is based on the voltage or current. Although this perspective simplifies the modeling, it lacks the level of details used by small-signal models.

Regardless of modeling concept, wide variety of methods are available for DC-DC voltage conversion. Each method has its physical principles and its specific pros and cons. During design of each converter, different factors such as range of κ, maximum output power and conversion efficiency are considered [254]. Although converters' design would be different according to the type, an abstract model of them for IoT power design is shown in Fig. 5.11, while P_i and P_o are subsequently input and output powers and control signal is a set of information explaining the conversion method.

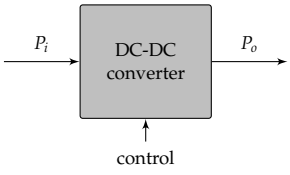

Fig. 5.11 An abstract general representation of a DC-DC converter.

For IoT system designers, two factors would be critical during design or selection of a converter. At first, κ would be considered to assure voltage matching of components together. Yet, the efficiency of a converter is more important for evaluation and system performance analysis. Efficiency can be simply defined as the ratio between output/input powers as:

$$\eta_c = \frac{P_o}{P_i} = 100 \cdot \frac{\langle V_o \rangle \cdot \langle I_o \rangle}{\langle V_i \rangle \cdot \langle I_i \rangle} \quad [\%] \tag{5.10}$$

To be noted that the PSS average signals are used here which are of interest for a system designer. This efficiency factor can be used in a more general perspective to have an overview of the available energy for the IoT device. Therefore, a model explaining this parameter has to be developed.

Similar to any other non-ideal system, the overall energy pushed into the converter will not be available at the output; leading to efficiencies less than 100 %. Hence, developed model of the converter has to provide information about the losses in it. Since these losses depend on the internal design of the converter and its parameters, abstract model can be formulated mathematically including these factors using (5.11) where $\mathbf{X}$ is a set of internal states and parameters of the converter affecting loss and efficiency.

$$P_{loss} = f\left(V_i, I_i, V_o, \mathbf{X}\right) \tag{5.11}$$

These losses can be divided into some main subcategories as:

Conduction losses: including power lost when current is passed through converter's elements due to resistive non-idealities.

Switching losses: power loss at switching period of the transistors when there is a short period of time with non-negligible current and voltage.

Gate charge losses: during each switching, stray capacitors between transistors terminals get a small amount of energy which is not recovered.

Control mechanism losses: control mechanism itself requires a small amount of power to make decisions and send control signals.

Inductor's iron losses: combination of electromagnetic energy loss of the inductor including hysteresis and Eddy-current loss.

Except for the control mechanism loss which can be considered constant, others have dependency to the converter design and control. Conduction losses are only during the period which current is passing through each element. According to the dynamic structure of circuit due to switching, calculation of this loss requires exact knowledge of each switching phase duration. Similarly, inductor's iron losses are dependent to the duration of phases. In addition, switching and gate charge losses rely on the switching frequency which is not a constant value in the PFM mode. Moreover, there would be no iron loss during the φ_3 in case a converter is operating in DCM.

Considering PhyNode, relation between input values V_i, I_i in (5.10) are known from the EH transducer. The voltage level of the battery connected to the output of the converter is also known from its model. Consequently, the model of a converter's efficiency for PhyNode presented in (5.10) is feasible. However, according to all loss dependencies, model of the BQ has to be developed specifically by analyzing its behavior at different operational conditions. Switching mechanism has to be analyzed to explain duration of each phase within a cycle. Afterwards, data has to be collected and used in combination to the switching mechanism to identify unknown internal parameters such as resistance and capacitance. Therefore, internal structure and behavior of BQ is analyzed first.

5.6 TI BQ micro harvesting converter

According to BQ25505 and BQ25570 datasheets [246, 247], these devices are specific converters for EH with MPPT and battery control. Both devices have a SwI boost converter operating in PFM mode. In addition to the battery, these devices use an alternative storage capacitor which its voltage is presented by V_{str}. This storage is mainly used to power the boost converter in cases when the battery is partially discharged. A simplified schematic of BQ25570 connected to a PV harvester is shown in Fig. 5.12.

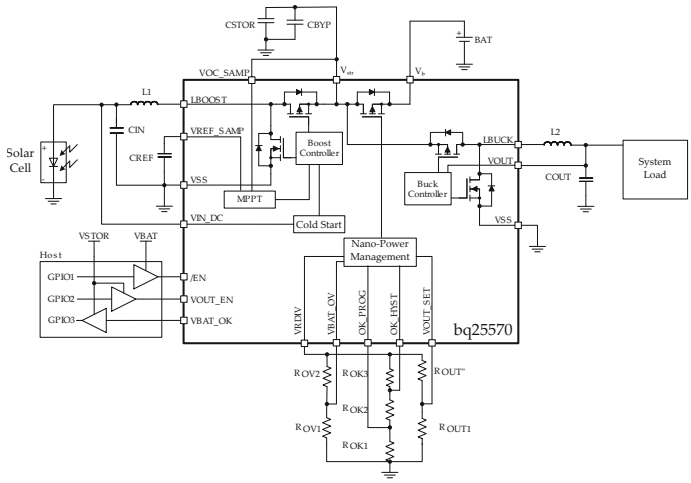

Fig. 5.12 Simplified schematic of BQ25570 for a solar EH application. From [247].

Output of the boost converter is directly connected to the storage capacitor. A separate switch can connect this voltage to the battery, according to the power management decision based on the battery voltage. Furthermore, electrical specifications of BQ from datasheets can be seen in Table 5.4.

Based on the information from datasheets, these devices have some internal state machine with a simplified structure as in Fig. 5.13. when operational

Table 5.4 Key operational parameters of TI BQ from [246, 247].

specification	min	nom.	max	unit
Input DC voltage	0.1	-	5.1	V
Input capacitance	4.7	-	-	µF
Storage capacitance	4.7	-	-	µF
Storage/battery(equivalent) pin capacitance	100	-	-	µF
Input inductance	22	-	-	µH
Total MPPT setting resistance	18	20	22	MΩ
V_{oc} for 80 % MPPT	$V_{str} - 0.015$	-	-	V
V_{oc} for 50 % MPPT	-	-	15	mV
Charger's cycle-by-cycle current limit[a]	-	230	285	mA
Input power for normal charging	0.005	-	510	mW
Maximum charger switching frequency	-	1.0	-	MHz
Storage voltage to switch from CS to NO	1.6	1.73	1.9	V
Minimum starting input power	-	15	-	µW

a) at storage voltage 4.2 V, input voltage between 0.5 V to 5 V

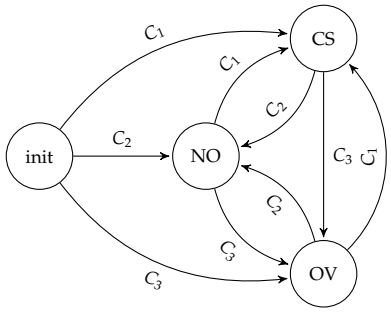

Fig. 5.13 A simplified state machine representing BQ's operational states.

states are described as:

CS: Cold Start is when there is not enough voltage to run the converter and MPPT circuit. Therefore, V_{ref} is set to 330 mV.

NO: Normal Operation is when the converter and MPPT circuit are operating while the required storage voltage is available.

OV: Over voltage protection is when the maximum defined V_o is reached and controller disables the converter to avoid overcharging the battery.

State machine in Fig. 5.13 is a discrete event model which shows changes in between states based on events defined by level of V_{str}. These event are:

C_1: $V_{str} <$1.8 V
C_2: 1.8 V$< V_{str} < V_{ov}$
C_3: $V_{ov} < V_{str}$

The maximum allowed voltage of the storage (V_{ov}) can be defined by user according to the desired hardware specifications. This setting is done by using a voltage divider using resistors as in Fig. 5.12.

In addition, Fig. 5.12 shows that the reference voltage (V_{ref}) of the boost converter is provided from the MPPT module. According to the manufacturer's

data, BQ uses a FOCV MPPT principle. Voltage defined by the MPPT is used by boost converter controller to indirectly modify the input impedance near the optimum value. However, according to the open circuit principle, this voltage is not measured continuously. A sample and hold process detaches the converter from the input side every 16 s for a duration of 256 ms and an internal circuit measures and stores the V_{oc}. A portion of this value according to the user defined percentage (implemented by an external resistor) will be used by converter till the next MPPT measuring period.

5.7 Analytical modeling of BQ converter

According to the specifications of the battery explained in Section 4.3, charging limit for BQ is set to 4.2 V. Moreover, its lowest allowed voltage is 3 V. Consequently, BQ will never be in the CS mode. Hence, in the context of PhyNode which has even smaller voltage range, only modeling of the normal operation is required. In addition, according to the cut-off limit of 3 V, it can be considered that the system will never rely only on the capacitor voltage (V_{str}), and v_o of converter is equal to V_{str} and V_b. Furthermore, using information collected from PhyNode's PV module in PhyNetLab, a value of 80 % is used for the FOCV MPPT.

From general model in Fig. 5.11 the main aim of modeling here is to find the BQ output power. However, since the converter's output voltage is equal to V_b, output of the model can be simplified into its output current.

Furthermore, converter's output voltage (equal to V_b) is a known value and can be used as an input to the model. Moreover, input voltage and current are dependent to the I-V curve of the PV module. Therefore, it is better to divide the model into two sub-parts. In the first section it is supposed that the input voltage and current values are known and given to the model. Therefore, abstract model of the converter can be depicted as in Fig. 5.14.

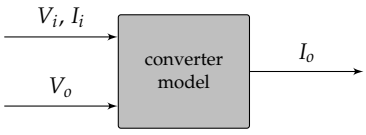

Fig. 5.14 Abstract representation of the BQ converter model.

While this model provides the PSS output current, another model is required explaining the behavior of the MPPT section of BQ. This model is supposed to state selection of V_{ref} when V_{oc} from PV module is known. This can be presented in an abstract way as in Fig. 5.15.

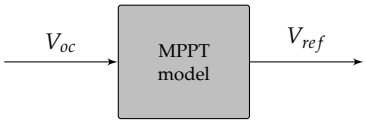

Fig. 5.15 Abstract representation of the BQ MPPT model.

5.7.1 BQ switching mechanism

As explained formerly, both converter modeling principles require knowledge of the switching mechanism. BQ datasheet mentions a PFM control for the regulation of the voltage. However, no clear definition of the exact control strategy is provided except use of three different peak currents (I_p) of 50 mA, 100 mA and 230 mA. In addition, Fig. 5.12 shows a SwI boost converter with synchronous switch implementation using two MOSFETs. Therefore, information about switching has to be collected from the system to find duration of phases in cycles required for loss calculations.

According to the converter design, monitoring inductor's current (i_l) will provide critical information about the way control mechanism manages the switching. For this purpose a measurement setup is prepared. The same SMU used formerly is utilized again for this measurements but with application of both channels. First channel acts as a current source replicating an EH source with a voltage compliance reproducing the V_{oc}. Second channel is a simple voltage source behaving similar to the battery. Simultaneously an oscilloscope with a high accuracy current probe is used to measure i_l. Some of measured currents at different input/output combinations are presented in Fig. 5.16.

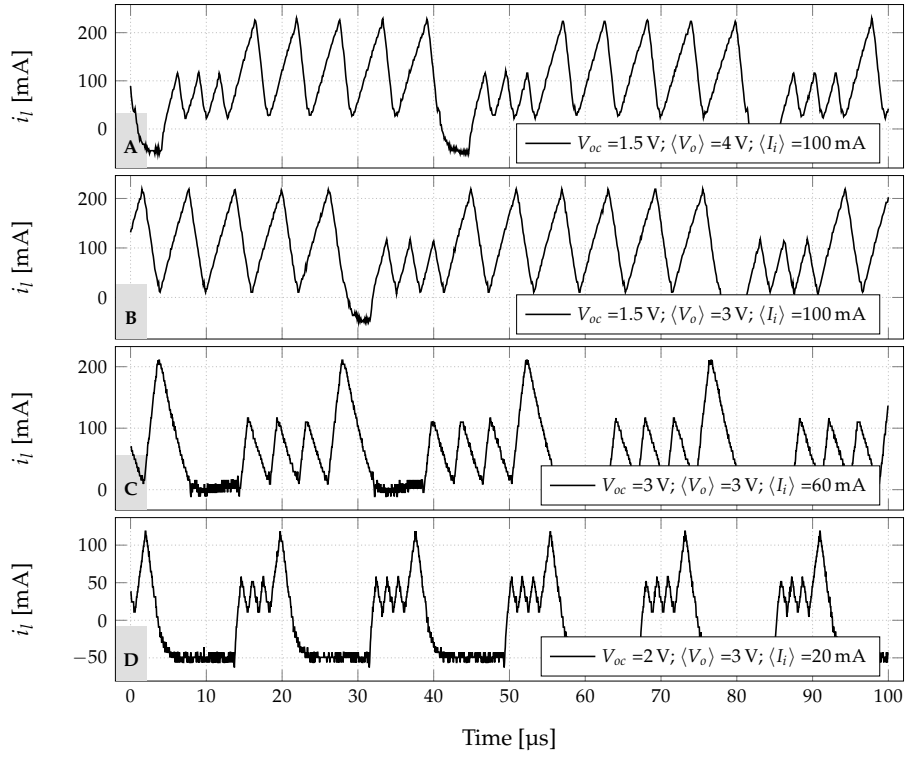

Fig. 5.16 Inductor's current of BQ25570 in some operational conditions.

To be noted that SMU signal values in Fig. 5.16 are presented in the PSS notation. This is due to the fact that although a fix value is set, real signals have a small-signal portion as well, oscillating around this DC value.

Analyzing these measurements shows a very complex switching strategy. Although all mentioned peak currents are available, each steady-state condition includes only two subsequent of them. In addition, a complete cycle is made of two sets of pulses happening after each other at the border of CCM and DCM followed with an idle phase at the end. It has to be noted that the i_l during this idle phase is not exactly zero because an LC circuit is made in this phase due to reverse body diode of S_p leading to a small current passing through the branch. Reviewing literature shows that these specifications have similarities with PTC and its advance version MPTC switching mechanism.

PTC, firstly introduced in [255–257] was mainly designed for flyback converters. It is a nonlinear control mechanism regulating voltage with the combination of two different predefined pulses [258]. Energy accounting of these pulses is in a way that burst of one type leads to the reduction of the controlled voltage while the other one increases it. Controller pushes a combination of these pulses subsequently in a manner that the oscillations are in an acceptable range around the reference voltage. Voltage-Mode Pulse Train (VMPT) and Current-Mode Pulse Train (CMPT) are two types of PTC designs. Within VMPT, the duty ratio of high and low power pulses are preset while in CMPT currents are preset [259].

Considering the PTC principle, the ratio between high and low pulses has to be selected very carefully because they affect both voltage ripple and PSS average current. Consequently, when the controlled side current has a larger range, controller has to use a larger number of pulses in some current levels. This will simply lead to a bigger voltage deviation which is generally not desired. Therefore, MPTC has been introduced in [260] which can build more than two predefined pulses. With the availability of more pulses, a larger current range is covered while keeping the voltage ripples small.

Combining these two design principle for traditional DC-DC converter with the specifications for EH application, design mentality of the TI BQ developers can be understood easier. On one hand, converter has to operate for a large range of harvested currents. On the other hand, input voltage has to oscillate very near to the reference voltage defined by the MPPT module to keep the optimal harvesting. This is mainly due to the fact that the converter of the EH transducer is controlling the impedance and not only voltage or current alone. Therefore, deviation in any of input signals will push the EH transducer to operate not at the MPP. Consequently, a mixed concept is used in the design. Three peak currents are available to operate in CMPT. This helps to expand the input current range. Meanwhile, to keep the voltage oscillations small, only two of them will be used according to the input current. This simplifies each PSS operation into a normal PTC mechanism.

However, by combination of different number of pulses, it is possible to build only some specific PSS currents. These values will be discrete and dependent on the peak current values and duration of pulses which is also dependent on the voltage values itself. To enable any current value between these specific discrete points, controller can add an idle time period at the end of the pulse train. By modification of this time, controller actually changes the cycle duration ($\mathcal{T}$) as the denominator of the PSS values in (5.6). This has the benefit that (theoretical) zero current nature of idle phase does not affect the nominator. Consequently, this combination can enable any possible input current while keeping the voltage ripple small.

Within this design, there is a hard limitation for the input current which is defined by the largest possible I_p. Considering the largest current pulse, even if no low pulse being fed to the output and no idle time, a train of only these pulses can be imagined. From boost converter circuit topology, PSS input currents is equal to PSS inductor's currents. Therefore, $I_p/2$ of the highest peak current is a hard limit for the PSS input current.

Using this theory, it is possible to explain signals measured and shown in Fig. 5.16. However, exact duration of each phase is required for the modeling and analysis of losses. Hence, it is necessary to find below aspects for each steady-state condition.

1. Selection of peak current levels
2. Number of each pulse type
3. Duration of the idle phase

5.7.2 Modeling BQ switching

Before starting to find mentioned parameters, a general analysis of each pulse will be helpful. To differentiate signals belonging to each peak current, $\bullet_l$ and $\bullet_h$ show signals for low-power and high-power pulses subsequently. When the formulation can be used for both types, a notation $\bullet_j$ is used. A general representation of a pulse is shown in Fig. 5.17.

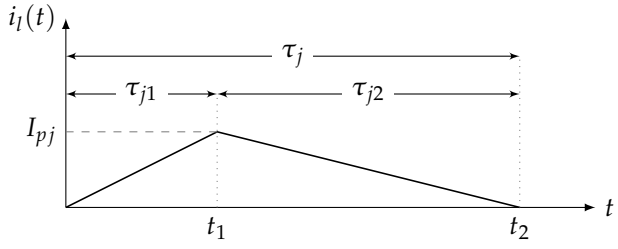

Fig. 5.17 A representation of inductor's current during a single pulse.

By considering small voltage ripples compared to the PSS input voltage, in addition to the current dynamic formulation from (5.3a) and (5.4a), duration of charge and pump phases in this pulse can be estimated using (5.12) and (5.13) subsequently.

$$\tau_{j1} = t_1 = L \cdot \frac{I_{pj}}{\langle V_i \rangle} \tag{5.12}$$

$$\tau_{j2} = t_2 - t_1 = L \cdot \frac{I_{pj}}{\langle V_o \rangle - \langle V_i \rangle} \tag{5.13}$$

Using these two equations, the overall pulse duration (τ_j) would be:

$$\tau_j = \tau_{j1} + \tau_{j2} = L \cdot I_{pj} \cdot \frac{\langle V_o \rangle}{\langle V_i \rangle \cdot (\langle V_o \rangle - \langle V_i \rangle)} \tag{5.14}$$

5.7.2.1 Selection of peak current levels

According to the definition of PSS, system behavior is in steady-state mode. Therefore, it is valid to consider a constant amount of energy being fed into the converter during each cycle. However, energy within a cycle is not balanced uniformly. During a low-power pulse, less power is passed to the output side. However, while the input power to the converter is constant, the rest of incoming energy which is not passed to the output is stored in the input capacitor. This storage leads to the increase of the voltage on the input side. On the contrary, during a high-power pulse more energy than the incoming energy to the converter is passed to the output. This will cause reduction of the input capacitor voltage. These changes in the input voltage for the capacitor can be explained using (5.15).

$$\Delta V_i = \frac{\Delta q_c}{C_i} \tag{5.15}$$

while the charge changes during a pulse can be calculated by (5.16).

$$\Delta q_c = \int_{\tau_j} (i_i - i_l)\, \mathrm{d}t \tag{5.16}$$

Quantification of charge entry to the input capacitor from (5.16) shows that deviation of input voltage is directly dependent to the difference between inductor's current and input current. While this difference is integrated over time, it is possible to simplify this into the difference between input current and $I_{pj}/2$ for the duration of a pulse. Then, it can be said that larger difference between these currents leads to a larger charge transfer to the input capacitor and consequently larger voltage oscillations. To be noted that this fact is valid for both cases of high and low power pulses. Hence, to keep the oscillations of the input voltage small, a MPTC controller has to always select the nearest peak current to the input current. Based on this fact, it can be said that the selection of I_p values is based on (5.17).

$$I_{pl} = \max\{50, 100, 230\}[\mathrm{mA}] \leq 2 \cdot \langle I_i \rangle \tag{5.17a}$$

$$I_{ph} = \min\{50, 100, 230\}[\mathrm{mA}] \geq 2 \cdot \langle I_i \rangle \tag{5.17b}$$

Use of this principle can be seen in all presented cases of Fig. 5.16. It has to be noted that this selection of current is done for modeling and is not the actual way that the controller is selecting these values because no exact knowledge of the $\langle I_i \rangle$ is available for the controller.

5.7.2.2 Number of pulses

From examples in Fig. 5.16, a complete cycle of the converter is made of two sets of pulses followed by an idle period. Number of these pulses during a complete cycle will be presented using μ_l and μ_h (both integers or $\in \mathbb{Z}$) subsequently for low and high power pulses. According to these representation, the overall cycle time can be explained by (5.18) when $\tau_{\varphi 3}$ is the duration of the idle phase.

$$\mathcal{T} = \mu_l \cdot \tau_l + \mu_h \cdot \tau_h + \tau_{\varphi 3} \tag{5.18}$$

To find the number of pulses during a cycle, an energy balancing can be used by writing energy equations. Within the boost topology, energy enters the inductor during φ_1 and pushed to the output side during φ_2 while no energy exchange happens during φ_3.

As mentioned before, half peak current can be considered as its PSS value during a single pulse. Consequently, using (5.12) to (5.14), the average PSS current $\langle I_o \rangle$ during a pulse can be defined by (5.19).

$$\langle I_o \rangle_j = \frac{I_{pj}}{2} \cdot \frac{\tau_{j2}}{\tau_j} = \frac{L \cdot I_{pj}^2}{2 \cdot \tau_j \cdot (\langle V_o \rangle - \langle V_i \rangle)} \tag{5.19}$$

Therefore, the output energy during one pulse is written as:

$$E_{oj} = \langle V_o \rangle \cdot \langle I_o \rangle_j \cdot \tau_j = \frac{L \cdot I_{pj}^2 \cdot \langle V_o \rangle}{2 \cdot (\langle V_o \rangle - \langle V_i \rangle)} \tag{5.20}$$

Consequently, in an ideal form when no energy is lost, the overall energy delivered to the output is equal to:

$$E_o = \mu_l \cdot E_{ol} + \mu_h \cdot E_{oh} \tag{5.21}$$

Unlike output, input energy is pushed to the converter during the whole cycle, regardless of its switching phases. Therefore, it can be written as:

$$E_i = \langle V_i \rangle \cdot \langle I_i \rangle \cdot \mathcal{T} \tag{5.22}$$

For an ideal converter with no energy loss and using (5.19) to (5.22), the energy balance of the converter can be written by:

$$\langle V_i \rangle \cdot \langle I_i \rangle \cdot \mathcal{T} = \frac{L}{2} \cdot \frac{\langle V_o \rangle}{\langle V_o \rangle - \langle V_i \rangle} \cdot \left(\mu_l \cdot I_{pl}^2 + \mu_h \cdot I_{ph}^2 \right) \tag{5.23}$$

For the modeling, input PSS signal values are known in this equation, while the overall cycle duration and number of pulses are unknown parameters. Yet, it is possible to represent (5.18) as the inequality in (5.24) by removing the idle time.

$$\mathcal{T} \geq \mu_l \cdot \tau_l + \mu_h \cdot \tau_h \tag{5.24}$$

By substituting pulse duration from (5.14) into (5.24) and using it in (5.23), an inequality between μ_h and other parameters can be found as:

$$\mu_h \geq \frac{\mu_l \cdot I_{pl} \cdot \left(2 \cdot \langle I_i \rangle - I_{pl}\right)}{I_{ph} \cdot \left(I_{ph} - 2 \cdot \langle I_i \rangle\right)} \qquad \text{when: } \mu_l, \mu_h \in \mathbb{Z} \tag{5.25}$$

Although $\langle I_i \rangle$ is an input of the model and I_{pl} and I_{ph} can be found using (5.17), this inequality still includes two unknown parameters; namely: μ_l and μ_h. However, reviewing a large set of measured inductor's currents in addition to those in Fig. 5.16 shows that the control mechanism uses a constant μ_l =3. Therefore, this inequality has only one remaining unknown parameter.

Furthermore, in (5.25) it can be considered that smaller number of pulses would be preferred to keep the ripple small. Consequently, by considering $\mu_l = 3$ in (5.25), μ_h can be found by (5.26) where $\lceil \bullet \rceil$ is the *ceil* function to round the value to the next positive integer.

$$\mu_h \geq \left\lceil \frac{3 \cdot I_{pl} \cdot \left(2 \cdot \langle I_i \rangle - I_{pl}\right)}{I_{ph} \cdot \left(I_{ph} - 2 \cdot \langle I_i \rangle\right)} \right\rceil \tag{5.26}$$

Analyzing this criteria, it can be seen that the number of high peak pulses is not dependent to the voltages at all. This is mainly a consequence of ignoring the idle phase which leads to the inequality. Therefore, although this criteria is necessary, it is not sufficient to explicitly find the μ_h. Accordingly, inclusion of $\tau_{\varphi 3}$ is necessary not only to find its own value, but also to find the exact μ_h.

5.7.2.3 Duration of the idle phase

Using the capacitor amp-second balance, it can be declared that at the end of a cycle, total net current passed through the input capacitor has to be zero. Therefore, it can be formulated that the PSS input current is equal to the average inductor current. Using $I_{pj}/2$ as the average current during a pulse, it is possible to explain the PSS input current as:

$$\langle I_i \rangle = \frac{1}{\mathcal{T}} \cdot \left(\mu_l \cdot \tau_l \cdot \frac{I_{pl}}{2} + \mu_h \cdot \tau_h \cdot \frac{I_{ph}}{2}\right) \tag{5.27}$$

By substituting timing values from Eqs. (5.12) to (5.14) and (5.18) into (5.27), duration of idle phase can be written by (5.28).

$$\tau_{\varphi 3} = \frac{L \cdot \langle V_o \rangle}{\langle V_i \rangle \cdot (\langle V_o \rangle - \langle V_i \rangle)} \cdot \left[\mu_l \cdot I_{pl} \cdot \left(\frac{I_{pl}}{2 \cdot \langle I_i \rangle} - 1 \right) + \mu_h \cdot I_{ph} \cdot \left(\frac{I_{ph}}{2 \cdot \langle I_i \rangle} - 1 \right) \right] \tag{5.28}$$

Using $\mu_l = 3$, still two unknown parameters are available in (5.28) which linearly related to each other. However, there are two other necessary conditions to build a valid pulse set. While $\tau_{\varphi 3} \geq 0$, μ_h has to be a positive integer. Their importance on parameters finding can be seen in Fig. 5.18 showing relation and conditions for the case in Fig. 5.16A.

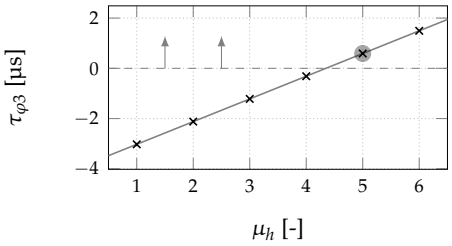

Fig. 5.18 Changes in the idle phase time according to the number of high peak pulses for the case with:
$V_{oc} = 1.5\,\text{V}$, $\langle V_o \rangle = 4\,\text{V}$, $\langle I_i \rangle = 100\,\text{mA}$.
First positive idle time with integer number of pulses is at $\mu_h = 5$.

As can be seen, first integer number of μ_h with a positive idle time is at $\mu_h = 5$. Not only this complies with the result from (5.26), but also it has the exact value from the measurement in Fig. 5.16A. However, there is a concern about $\tau_{\varphi 3}$ which is shorter than 1 µs. BQ cannot switch this fast because of its 1 MHz maximum frequency (see Table 5.4). This can be explained by the fact that all these formulations are based on an ideal case. However, in reality there are losses, noise and the fact that the i_l during idle phase is not exactly zero.

In addition, BQ is a mixed signal IC which its internal control logic design is pushed to extreme to operate in ULP. Therefore, some of decision making processes are not perfect; causing less accurate switching. For instance in examples of Fig. 5.16, pulses are finished not exactly when $i_l = 0\,\text{A}$. Analysis of this value shows no exact relation to any of converter's external signals. Specially, end of pulse is detected more accurately when the input current is higher. This shows sensitivity of zero current sensing to the input current.

To have exact understanding of all these aspects, many other factors has to be included in the model. Although some of these factors can be found by using intensive data collection and analysis, few factors (specially digital logic of the BQ) requires information from the manufacturer. After knowledge about these parameters, it is possible to estimate timing, number of pulses and duration of each. However, this data has to be used for identification of internal parameters such as resistances as well. Therefore, using this two-fold strategy adds another level of inaccuracy to the model.

In addition to inaccuracies and lack of internal knowledge for a deductive modeling, there are multiple conditions which even the general control form will not apply or reaches its limits. Some of these cases are analyzed hereafter.

5.7.3 Special switching cases

A case which can simply happen in some unfortunate operational conditions, is when the battery is roughly depleted but the light intensity is high, generating a high V_{oc}. In such situations, it is probable that the voltage matching does not fit to the boost form anymore. Inductor current for two such cases are presented in Fig. 5.19.

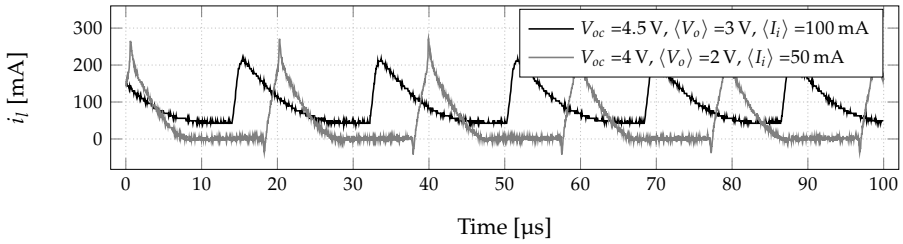

Fig. 5.19 Inductor current when input voltage is higher than the output voltage.

In these examples, considering the 80 % rule for the MPPT leads to an operational input voltage higher than the output voltage. Looking at Fig. 5.19 it is clear that the converter is not operating in the PTC mode anymore. In addition, according to the current level, it may operate either in CCM or DCM. Although it can be discussed that this is not the designed operational range of the converter, it is still plausible to have such condition.

In addition to the cases with higher $\langle V_i \rangle$ than $\langle V_o \rangle$, equal values lead to the same abnormal condition as well. According to the design of the boost converter, it can be concluded that the pump phase in this case will be theoretically infinite according to zero in the denominator of the fraction in (5.13). As depicted in Fig. 5.20, in this condition converter behaves similar to the case that input voltage is higher than the output.

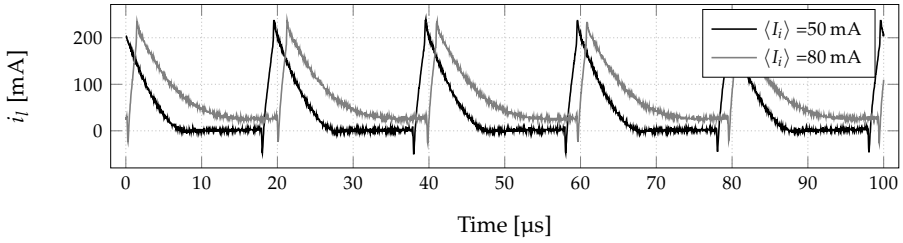

Fig. 5.20 Inductor current of the boost converter operating at the border of boost and buck condition. Set values are: V_{oc} = 4 V, $\langle V_o \rangle$ = 3.2 V

Although it is possible to ignore these conditions while the BQ is not designed for this ranges, there are multiple other cases which the switching is not completely predictable. Some of these examples are presented in Fig. 5.21.

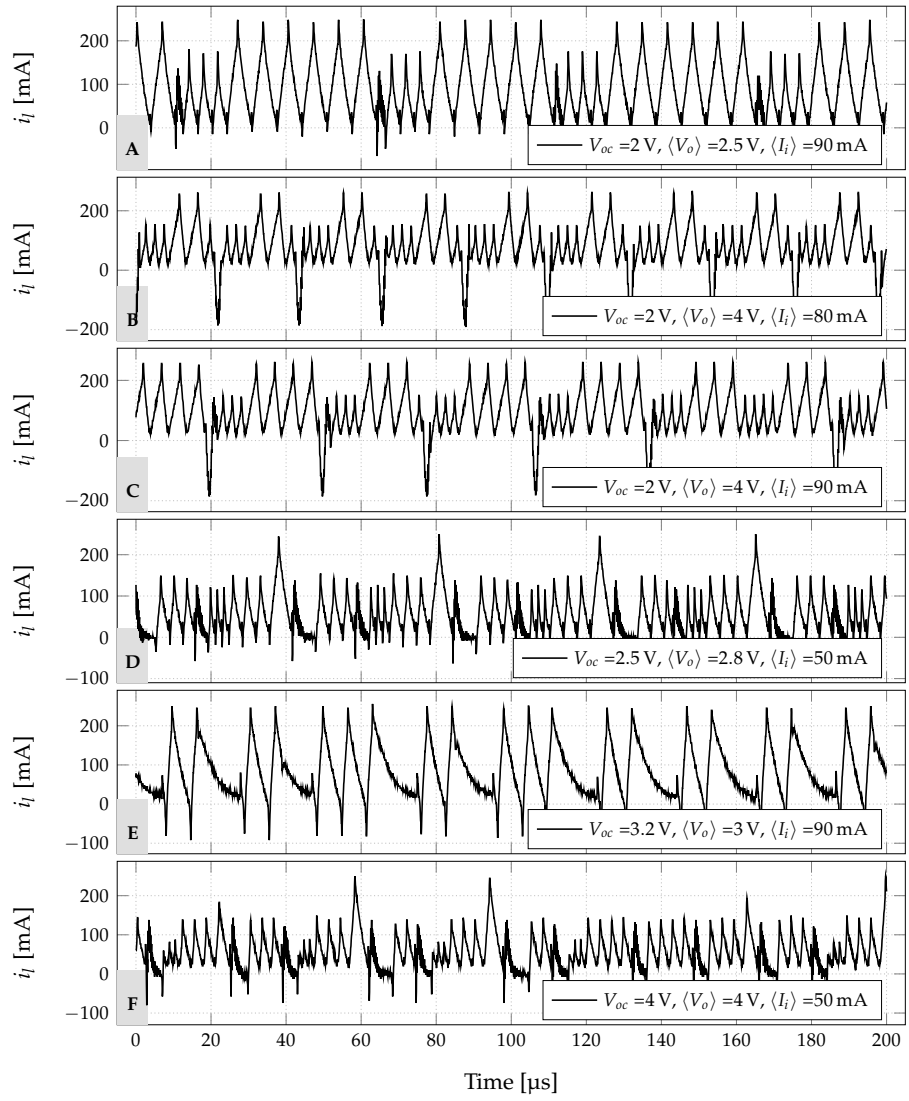

Fig. 5.21 Abnormal switching in spite of operation in normal signal range of the converter.

As can be seen, in Figs. 5.21A, 5.21C, 5.21E and 5.21F number of high peak pulses changes between cycles. In some others such as Figs. 5.21D and 5.21F more than two types of pulses are available within a cycle and cycles are irregular. Pulse forming in some cases such as Figs. 5.21A and 5.21C repeats in a macro level that a pattern repeats itself each two or three cycles. In Fig. 5.21B, after second high peak a low peak happens which is abnormal while cycles always start with a low peak and end with a high peak. Even in some cases such as Fig. 5.21E, it seems that the switching is happening in the middle of a phase while the current is not zero yet.

Detailed analysis of signals in more than 100 cases shows that all scenarios can be explained by analyzing other signals such as input and output voltages. Another reason for different behaviors is the dependency of the switching to the zero current passing, which is critical to start a pulse. Monitoring all signals shows that detection of this point is based on the voltage difference on the inductor. According to the ULP design of the device, this detection is not very accurate and as discussed formerly, is dependent to the current level. Due to this design, sensitivity to noise is high and can cause abnormal behavior.

Nevertheless, cases with macro pattern can be explained because voltages change slowly during a cycle integrally. Although a limit is not reached during a cycle, it can happen in the next one, causing dissimilar cycles. As an example, measured signals from Fig. 5.21C are presented in Fig. 5.22.

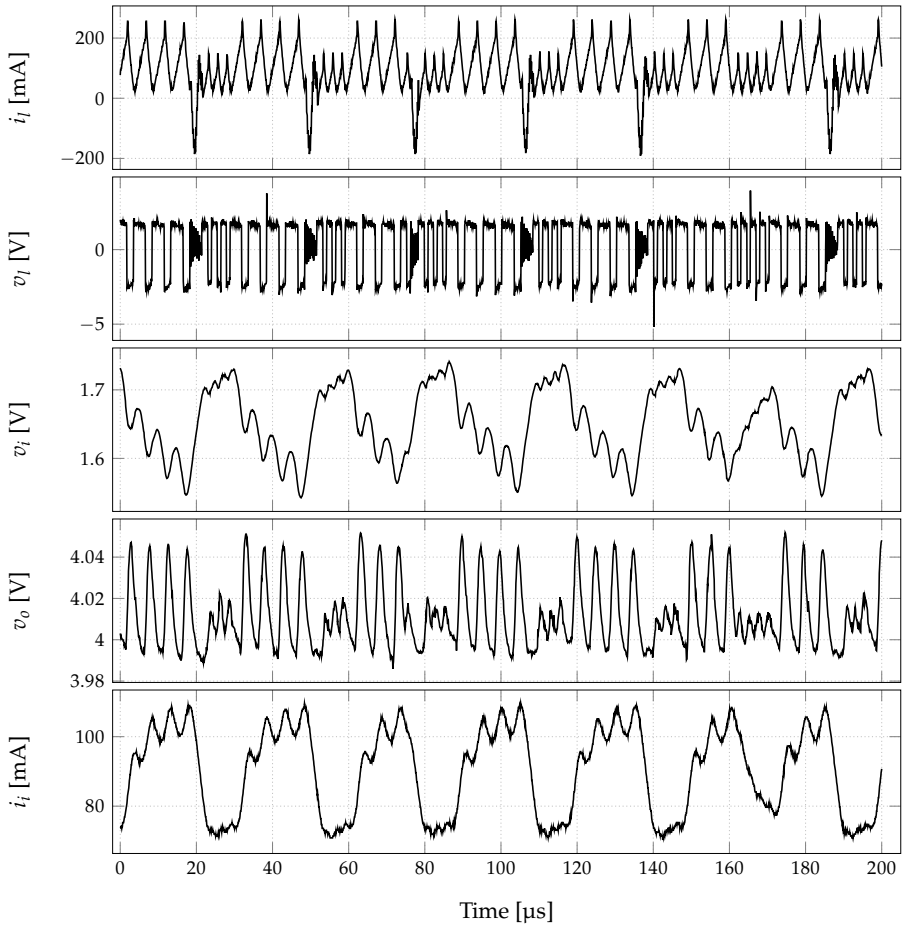

Fig. 5.22 All measured signals for a case with macro cycle pattern of switching. Set values are: $V_{oc} = 2\,\mathrm{V}$, $\langle V_o \rangle = 4\,\mathrm{V}$, $\langle I_i \rangle = 90\,\mathrm{mA}$

As can be seen in Fig. 5.22, signals have same values at the end of cycles with 3 and 4 high pulses. This is the consequence of initial condition of the cycles which is not exactly the same.

Although developing a deductive model including all these dependencies is possible, such model will actually be a dynamic model representing all small-signals. Therefore, deductive accurate model in the system level is not feasible and a data-based perspective is necessary for developing the system level model. This model will include PSS behavior of the converter ignoring small-signal level dynamics. Therefore, a reliable data-set for the whole operational range of the BQ has to be collected and used.

5.8 Data collection

For the analysis of the BQ, collected data has to be from the whole operational range. Therefore, this range is specified in the first step. Using information provided in Table 5.4, input voltage ($\langle V_i \rangle$) may vary between 0.1 V to 5.1 V. On the output side voltage range is specified by battery which will be in a range between 3 V to 4.2 V. However, to keep the modeling as general as possible, lowest voltage range in the NO state of BQ is used which is 1.8 V. Maximum peak current of 230 mA adds a limit to the input current to be smaller than half of this value. Furthermore, while input current and output voltage can be directly controlled, direct manipulation of the input voltage is not possible. Hence, it has to be modified indirectly using V_{oc} due to the MPPT mechanism.

For the measurement, both SMU channels are connected using 4-wire principle. One channel to the input and the other one to the output. To collect PSS values, measurements have to be integrative over a larger time period to cover at least one complete cycle of switching. While the fastest switching of 1 MHz puts a limit on the shortest cycle, longest time period of a cycle cannot be defined from datasheet. However, multiple tests have shown that sampling time in the scale of tens of ms will be proper for a large portion of the current range. When the input current is small (in the µA range), a cycle takes much longer and fast sampling leads to a semi periodic data collection over time. This is because in such small current levels, although controller uses the smallest I_p, its average pulse current of 25 mA is still much larger than the $\langle I_i \rangle$. Hence, it keeps the switching in φ_3 for a long period to balance the current. Use of too large sampling time can introduce another type of problem to the measurement. Since the MPPT mechanism periodically detaches the input to measure the V_{oc}, signals during this phase are not valid. Therefore, sampling time has to be selected in a way to make MPPT measurements detectable. While each V_{oc} sampling period takes 256 ms, a sampling time of 50 ms is selected which assures 5 samples. This T_s is fine for a large portion of the current range, albeit measurements with small $\langle I_i \rangle$ have to be averaged over time to cancel out point measurements within the cycle.

Although signals may have any value in the range, measuring performance at all input values is not possible and signals have to be sampled at discrete values. Considering this discretion, sample points of each signal has to be selected carefully as a trade-off between accuracy and measurement effort. Consequently, both output voltage and V_{oc} are discretized in 200 mV steps. Meanwhile, large range of input current is divided in a logarithmic way with samples at points shown in Fig. 5.23.

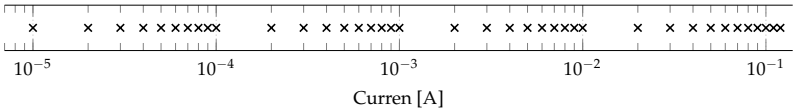

Fig. 5.23 Representation of all input current values used for sampling BQ behavior.

Stabilization period of the converter in transition is dependent on the difference between subsequent operational points. Hence, it is better to measure two operational points with small differences directly after each other to reduce the transition time into minimum. Therefore, data collection is divided into experiments which only a single parameter changes in a step-wise manner.

Each experiment is in this way that the input current and desired V_{oc} are set with an initial voltage of 4.15 V at the output side. SMU measures this condition for a period of 30 s which is enough to be sure that at least one complete cycle after a V_{oc} measurement is done. When the measurement of this condition is finished, instead of detaching the source to set new values, input settings remain the same while the output voltage changes into its next level. In this manner, the whole range of output voltage is swept during a single experiment. In the next experiment, new set of operational signals is applied and measured in the same manner. Example of measured signals during one such experiments are shown in Fig. 5.24.

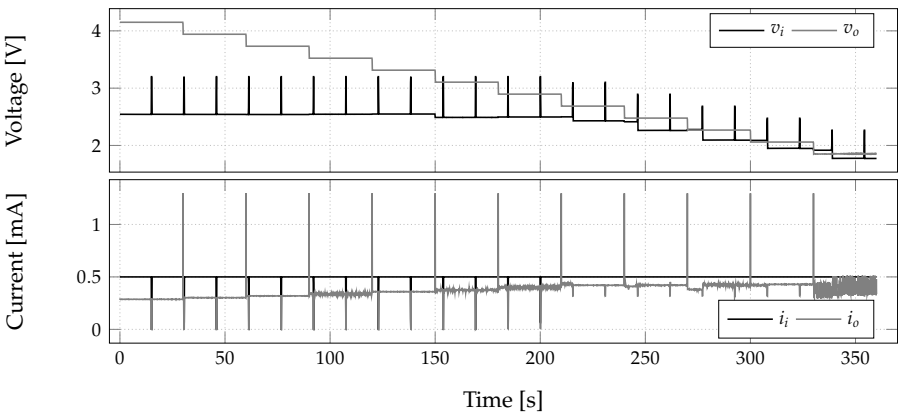

Fig. 5.24 Exemplary measured signals from BQ25505 for a complete signal set at V_{oc} = 3.2 V and i_i = 500 µA.

Two interesting aspects can be seen in Fig. 5.24. Firs are the periodic jumps in the input signals as a consequence of the MPPT measurement procedure. Second, it is clear that the reduction of the output voltage leads to increase of the output current showing a semi constant efficiency.

Data collected during most of these experiments are fine, whereas some abnormalities has been seen in the way MPPT behaves for low current experiments. Since this collected data will be used for modeling of the MPPT system as well, this requires some extra considerations. Although it is supposed that the MPPT measurement gets the present V_{oc}, its behavior includes some memory effects. This can be seen in Fig. 5.25 presenting input voltage measured during two experiments with exactly similar signals setup. The only difference between these two is the period that the BQ has been operating before storage of the data begins.

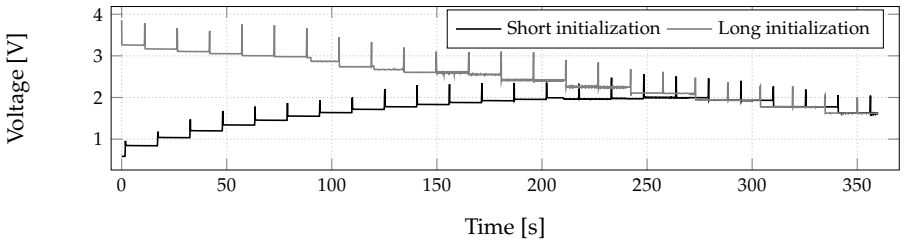

Fig. 5.25 Measured input voltage at V_{oc} = 5 V and i_i = 10 µA. Only difference is the initial time before starting the data storage.

This effect is a consequence of the way that the V_{oc} is being measured. BQ uses an internal capacitor which is being charged during the 256 ms of the V_{oc} measurement period. When the input current (can be considered as the I_{sc} or I_M of the PV module) is very small, dynamics of the capacitors requires longer period to reach the real V_{oc}. Over the time, remained voltage in the capacitor from last measurements helps it to measure more accurately. This effect can be seen in the first example in Fig. 5.25 which the measured V_{oc} increases over time. While the aim here is to provide PSS models without the dynamics, a long initial time is required for low currents till the V_{oc} measurement mechanism is stable. However, a shortcut is used here by applying a roughly large current of 1 mA for a period of 20 s before the measurement starts. This period is long enough to assure that the V_{oc} measurement of the MPPT mechanism is activated once to charge the capacitor. After this period, desired input current is applied and measurement starts. Using these specifications, 819 experiments have been measured spanning the whole normal operational range of the BQ. Each experiment includes measurement of 12 operational conditions which have to be separated from each other. In addition to separation, this raw data requires some pre-processing steps before being used for the modeling.

Pre-Processing

In the first step of pre-processing, each segment of data with similar operational condition has to be extracted. While during an experiment only v_o is being changed, its change points have to be detected. Since 12 different levels of voltage are included in one experiment, detection of largest 11 linear changes for two subsequent points will give the step points of the v_o.

As MPPT module sets the input voltage for the following period till next measurement, each section in between these subsequent MPPT measurements can be considered as a single condition. Therefore, MPPT measurement pulses have to be extracted and removed from the data. For filtering, it is known that in contrast to mean based filters, moving median filter has the benefit of removing outliers without introducing new values to the data. Furthermore, each MPPT measurement peak will be measured using 5 samples. Therefore, a window has to be selected for the moving median to assure that at each point there are more than number of outlier points on each side of the desired value. To assure this, each side of the window has to have at least 6 samples. While window has to be valid for both sides and using an odd number, a window size of 13 samples is used for the filtering. After finding difference of this filtered signal and the measured voltage signal, any outlier detection algorithm can detect all MPPT measurement peaks.

Unfortunately, there is no way to synchronize the MPPT measurements with the output voltage steps. Hence, there would be a special type of data which has to be handled differently. It is from the time that the output voltage change is applied till the next V_{oc} measurement. During this time, optimal operating condition is changed, but controller still tries to fit the input to the former optimal condition. Although it is possible to consider this as another imaginary operational condition, ignoring it will be a more safe decision to avoid compromising rest of the data-set. In addition to this section, there will be a section of data between last MPPT measurement till the change point in the output voltage which is shorter than a normal section. This type of data will be called secondary sections.

Using voltage specific points, all valid operational sections of data are extracted. To remove noise in addition to sub-cycle data for low current ranges, average value of all signals for each section is found after removal of outliers with a 25 % cut limit. After application of this procedure on all experiments in the data-set, 18 346 points of data are collected in addition of 8891 secondary sections with shorter periods.

For the converter model development, some extra cleaning process has to be applied on the data as well. At first, any data section from secondary set which are shorter than 3 s is removed because of high possibility of noise. Afterwards, main and secondary sets are combined together. Then, all portions with nonsense signal values are removed. These cases are when the output

current is negative, efficiency is more than 100 % or smaller than 5 %. In the final step, all duplicate entries with exactly similar conditions are removed. At the end, this data-set includes 22 507 entries, each presenting behavior of the BQ at one specific operational condition. Distribution of efficiency for the model's input signals in this data-set is presented in Fig. 5.26.

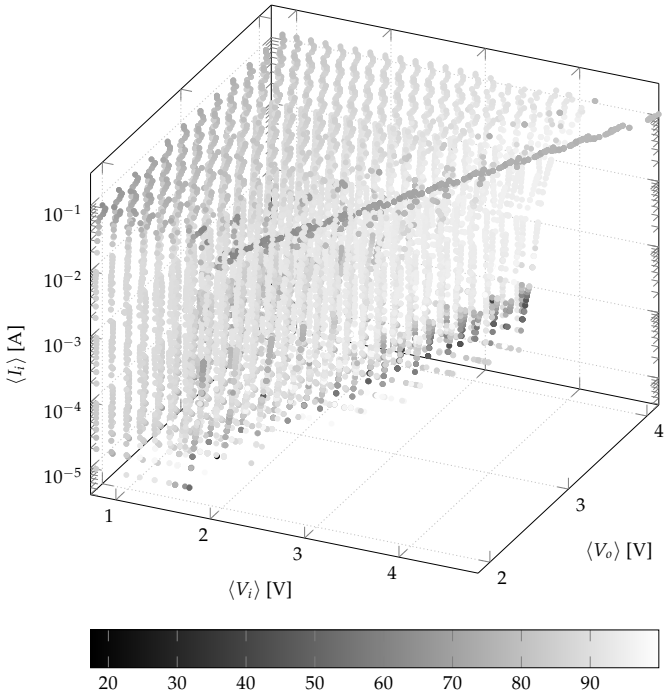

Fig. 5.26 Efficiency of the BQ converter measured for data-based modeling according to the PSS signals. Color of each point shows the efficiency according to the value in the color-bar.

Some facts can be extracted from this graphical representation of the data-set in Fig. 5.26. At first, internal behavior of the MPPT is in a way that it tries to keep the system at the boost condition or near it. This is the main reason that some kind of diagonal cut is available in the data. However, it has been seen in Section 5.7.3 that the MPPT mechanism is able to push the system into the buck condition. This can be confirmed here as well while this cut in Fig. 5.26 is not exactly at the border of boost condition and some efficiency values are in the buck condition as well. While output voltage is constant, MPPT actually decides about the depth of push into the buck condition by setting the input voltage. From Fig. 5.26 it is clear that higher currents cause deeper push to operate in the buck condition. That is actually the reason why the carving is not an exact diagonal cut.

Fig. 5.26 shows that despite high performance, reduction of the input voltage leads to lower efficiency. Perhaps this is a consequence of controller dependency

to the input voltage. In addition, increase of input current into the margin causes a reduction of the efficiency as well.

At this stage this data-set is ready for the development of the model to include all these data in a more compact form.

5.9 Data based converter model

It is known that within the operational range of the BQ converter, efficiency can have any possible value . Therefore, a model developed for such a system fits into the *regression* category of data-based models. In addition, due to the number of inputs and complex behavior of the device, it is roughly impossible to heuristically suggest a formulation for its behavior. Consequently, using Machin Learning (ML) techniques can be helpful not only to store the collected information in an abstract form, but also enabling estimation for the values in between them. Different ML based methods are available which can be used for the regression. While data about the system behavior is available which can be considered as the *training set*, this problem fits into the category of *supervised* learning. Among possible learning methods, converter will be modeled here using ANN due to the simplicity of implementation and sophistication for modeling complex behavior. In addition, decision tree will be used due to limitations on resources for the implementation of the ANN on ULP devices.

5.9.1 ANN based converter model

ANNs with a broad range of size, structure and design have been used for different applications. In this context, an ANN with one single hidden layer in between input and output is considered and modified to fit into the problem. According to the number of inputs for the model, this *shallow network* will have three inputs fully connected to the hidden layer. Since model has only one outcome, output layer is made of a single neuron. A graphical representation of this simple network known as *feed-forward* network is shown in Fig. 5.27.

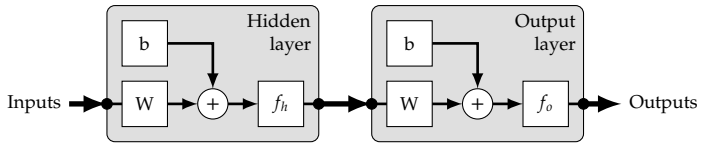

Fig. 5.27 A simple shallow feed-forward ANN with a single hidden layer.

It is known from the data-set that both converter's input and output voltage values are distributed uniformly in a limited range and scale. However, currents are distributed logarithmic in a wide range from micro to hundred of milli amperes. This makes numerical handling of the current more complex. Hence, for the input of the model, $\ln(\langle I_i \rangle)$ will be used which compresses this range and makes the distribution of data more uniform. It has to be noted that any

noisy data with negative value which can cause imaginary logarithm values is already removed. Furthermore, similar challenge is available for the $\langle I_o \rangle$ as the output of the network. However, not only use of efficiency as the model output helps to avoid this issue, but also it make evaluation of the performance more uniform which is preferred. Therefore, structure of ANN-based model will be a modified version of Fig. 5.14 as presented in Fig. 5.28.

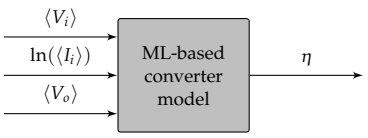

Fig. 5.28 Abstract representation of the ML-based model of the BQ's converter.

While number of inputs and output are defined by the nature of problem, number of neurons in the hidden layer (N_h) of the shallow network can be modified to reach better performances. In this step, this value is changed from 5 to 100 neurons in steps of 5. In addition, activation (or transfer) function of neurons in the hidden and output layer can change as well. Among different possible activation functions, Hyperbolic Tangent Sigmoid transfer function (HTS-TF), Logarithmic sigmoid transfer function (LS-TF) and Elliot Symmetric Sigmoid transfer function (ESS-TF) are tested for the hidden layer. For the output neuron, Pure Line transfer function (PL-TF) is used in addition to the HTS-TF and LS-TF.

For the training, performance of the model is evaluated by use of MSE while *Bayesian regularization back-propagation* training method is used. During the training, data-set is randomly divided with 70 % for training, 15 % for validation and 15 % for testing. Maximum number of epoch is set to 1×10^4 and maximum number of fails to improve the performance is equal to 50. Since performance of training can be dependent on the initial values as well, each of these networks is trained five times with different random initial values. At the end, best performing network among these five trials for each combination of transfer functions and N_h is selected. Comparison of the performance for these networks on the whole data-set can be seen in Fig. 5.29.

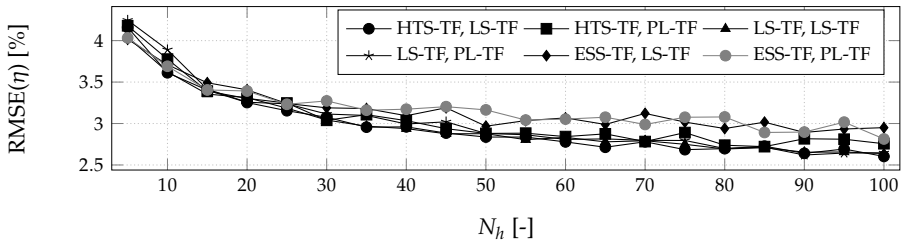

Fig. 5.29 Comparison of the BQ converter model performance for different feed-forward ANNs with distinct N_h and different transfer functions. Transfer function mentioned in the legend are in the order of hidden layer, output layer.

As can be seen, transfer function type is not critical, though increasing N_h improves the performance. In addition, improvement of the performance flattens out around 60 neurons. Hence, further increase of N_h is not feasible.

A simple modification in the design of the ANN is to use a cascade form to bypass inputs into the hidden layer in addition to the input layer. By modification of the network into this form, performances are measured again with similar settings as for the feed-forward network. Comparison of the performance on the whole data-set can be seen in Fig. 5.30.

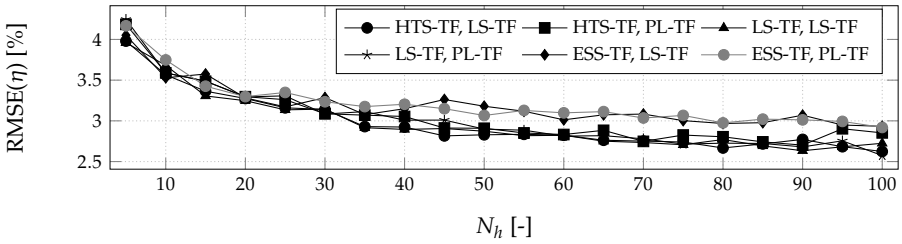

Fig. 5.30 Comparison of the BQ converter model performance for different cascade feed-forward ANNs with distinct N_h and different transfer functions. Transfer function mentioned in the legend are in the order of hidden layer, output layer.

Comparing results from cascade feed-forward with the feed-forward networks shows that in spite of additional complexity, input bypass improves the performance minimally. Nonetheless, the same trend in the cascaded networks can be seen that the type of transfer functions has a small effect on the performance and key aspect is the number of neurons in the hidden layer. Consequently, instead of increase in the single hidden layer, neurons are spread within two hidden layers in the next step.

New ANN is made of two hidden layers both with HTS-TF and the output layer with LS-TF. These transfer functions are selected because of their best performance in both shallow networks. To check different size of each layer, with the similar setting to the shallow network, number of neurons in the layers (N_{hx} for the layer x) is changed. Each network has been trained 5 times with different initialization and best results are selected. Performance of different size of network can be seen in Table 5.5.

Table 5.5 RMSE (η) [%] of applying different ANNs with two hidden layers and different N_h in each layer.

$N_{h2} \setminus N_{h1}$	10	20	30	40	50	60	70
10	2.791	2.615	2.475	2.504	2.464	2.480	2.386
20	2.691	2.441	2.500	2.363	2.409	2.311	2.458
30	2.523	2.391	2.364	2.427	2.285	2.338	2.321
40	2.453	2.404	2.395	2.476	2.330	**2.257**	2.391
50	2.473	2.311	2.313	2.316	2.373	2.298	2.356
60	2.426	2.305	2.413	2.264	2.493	2.313	2.295
70	2.400	2.377	2.331	2.462	2.260	2.318	2.416

Among all these trials, an ANN with 60 neurons in the first hidden layer and 40 neurons in the second hidden layer provides the best performing result with a RMSE of 2.257 %. However, as can be seen in Table 5.5, differences on the performances are very small, specially when compared to a shallow network. Considering results in Table 5.5 and Fig. 5.29, it can be seen that a network with a 20/10 structure has a similar performance to a shallow network with 100 neurons. However, trials with increasing depth of the network and number of neurons did not show a further significant improvement in the performance. Hence, the best performing network with two hidden layers can be used as the detailed system level model of BQ converter.

Implementation of such ANN on PhyNode is roughly impossible because of its complexity. Although use of smaller networks helps to reduce memory and calculation demands, it is still too large to be implemented on a PhyNode. It had been shown in [261] that implementation of very limited number of ML algorithms is possible on PhyNode as a consequence of extreme constraint on memory and computational resources. Among proper methods, binary decision tree has the lowest load on memory and computation of PhyNode. Therefore, it will be discussed further.

5.9.2 Decision tree based converter model

A binary decision tree is basically a set of *if-then* arguments on the input signals which builds different branches of a tree. This is the main reason for simple implementation that does not require complex computations, specially floating point mathematical operations. In this way, this algorithm breaks the data-set into smaller subsets while the tree is growing till it reaches the final nodes known as *leaf*, providing the output of the model.

Trials for training a decision tree using the data-set collected from BQ converter have shown very good performances with RMSE even as low as 1.435 % on the estimation of the efficiency. In spite of better performance of decision tree compared to the ANN model, its selection as the detailed model has to be evaluated further. This is mainly due to the fact that a decision tree will not provide a real regression similar to an ANN and it only makes decisions based on the trained data. In this case of model for the BQ converter, this can cause problems while signals are measured at specific discrete points. Therefore, some further evaluation would be useful to make a final judgment between this decision tree and the ANN model.

Regardless of performance, this trained decision tree has more than 4000 nodes and 1786 levels which its implementation on a PhyNode is still not possible. Therefore, this tree has to be pruned extensively to reduce its memory footprint and computation demand. Of course this pruning will be at the price of accuracy reduction. Exponential effect of pruning on the performance of this decision tree can be seen in Fig. 5.31.

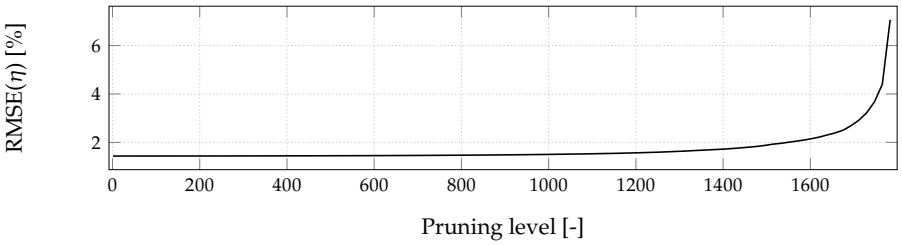

Fig. 5.31 Effect of pruning level on the performance of the decision tree based model of the BQ converter.

According to Fig. 5.31, there would be multiple levels of the decision tree which a system designer can decide between number of if-then tuples (levels) and accuracy of the on-board model. Anyhow, Fig. 5.31 shows a critical aspect that even a very extreme pruning attitude will still lead to a roughly acceptable performance with a RMSE of about 6.4 %. This shows a phenomena that the efficiency of the BQ converter is somehow more dense in a specific range that use of only few comparisons leads to a good estimation. Therefore, it is possible for some system designers to simply ignore any dynamic model and consider a constant value as the efficiency.

5.9.3 Constant efficiency for the converter

Selection of a single value as the efficiency of the converter can be based on different statistical criteria such as *average*, *median*, *mode* and others. However, before finding these factors, it is essential to assure that the input signals are distributed within the whole operational range in a uniform way. This is one of the main reasons for the selection of sampling points which can assure this distribution as already presented in Fig. 5.26. Distribution of efficiency in this data-set is shown in Fig. 5.32.

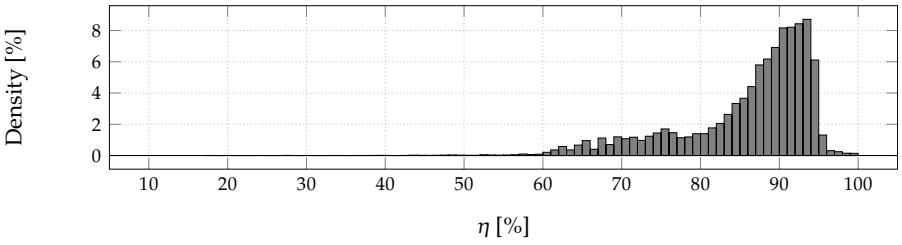

Fig. 5.32 Distribution of efficiency density for the whole operational range.

Using available data-set, different statistical parameters can be found. Among them, for the finding of the mode, frequency of none of efficiencies is higher than one due to very fine measurement. Therefore, mode is calculated using rounded value including three digits after the decimal.

According to the concept of selecting a single efficiency, use of Maximum Likelihood Estimation (MLE) also fits for finding the value. Although it is possible to consider the data in Fig. 5.32 as a Poisson distribution, no exact knowledge about it is available and this assumption will only limit the generality. Therefore, an empirical MLE is found using the maximum occurrence in the histogram. This is calculated by using histogram bins with a width of 0.001 % in efficiency. These selected efficiencies in addition to the performance of other methods are presented in Table 5.6.

Table 5.6 Statistical parameters of the BQ converter data-set and performance of each value as the single efficiency.

Method	Average	Median	Mode	MLE
Selected η [%]	85.983	88.821	91.106	92.425
RMSE [%]	8.5299	8.989	9.950	10.689
MAE [%]	6.559	6.097	6.469	7.067

As could be estimated from the distribution, no exact single value can be found based on these parameters. Therefore, an alternative method is used by finding evaluation factors MAE and RMSE directly for all possible values in the range of 10 % to 100 % which evaluation factors are presented in Fig. 5.33.

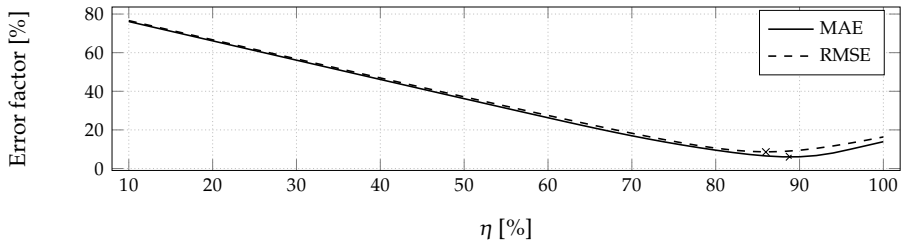

Fig. 5.33 Distribution of the error factors for different constant efficiency values.

It can be seen from this analysis that two different values can be selected based on the criteria. Lowest RMSE value happens at 85.983 % with a RMSE of 8.529 %. While lowest MAE equal to 6.096 % happens at efficiency value of 88.822 %. According to the use of RMSE here as the main criteria, single value suggestion for the efficiency of the BQ will be at 85.983 %.

To be noted that this efficiency value is decided based on the whole operational range of the BQ. In case of change in the working area, system designers have to modify the data-set by removing the irrelevant data from the data-set and redo the selection process. However, when the operational limitations of PhyNode in PhyNetLab are applied, single efficiency found is similar to the value for the whole range. This shows a similar distribution of data in the PhyNode range and the whole range. Anyhow, RMSE of this value on the modified data-set is a bit higher.

Comparing the performance of a single efficiency value with an extensively pruned decision tree, it can be seen that the improvement of the performance of decision tree has a roughly linear relation with the performance in the extensive cases. Therefore, it is suggested that a system designer use at least few top levels of a decision tree (when possible) which can simply improve the performance with a minimum computational load.

5.10 Modeling MPPT mechanism

From the FOCV principle of the MPPT mechanism in the BQ, it is supposed that the operational voltage be always at 80 % of V_{oc}. However, as seen in the data-set for the converter model, due to the ULP nature of BQ, noise can cause differences in the behavior of the system. Therefore, a more detailed analysis is necessary to model the MPPT mechanism. Using collected data for the modeling of the converter, a separate data-set is also available for the behavior of the MPPT. This data-set includes 18 330 entries for the measurement of the MPPT, with each entry including:

1. V_{oc} value set as a compliance of the SMU
2. measured V_{oc} during the MPPT measurement pulse
3. input current of the converter after measurement pulse
4. input voltage of the converter after measurement pulse

After removal of duplicates and outliers, 16 074 entries remain in this data-set. To check if the FOCV assumption for the 80 % limit is valid, operational voltage after MPP pulse according to the V_{oc} is presented in Fig. 5.34.

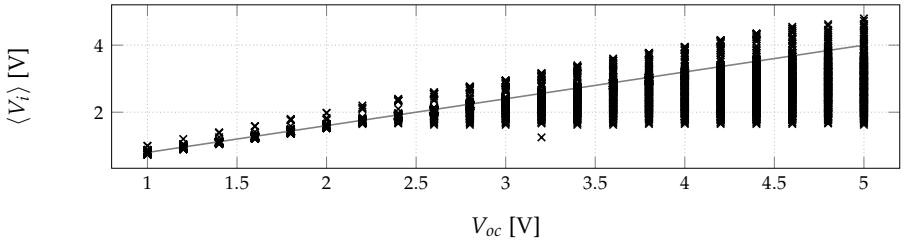

Fig. 5.34 Distribution of the operational input voltage according to the real V_{oc} set to the SMU. Line shows the 80 % limit used for the FOCV MPPT.

As can be seen, although some experiments fulfill the 80 % criteria, a section of data does not comply with this rule. Even a small portion of the data-set (about 7 %) selects an operational $\langle V_i \rangle$ larger than 80 % of the V_{oc}. While this difference is small, its extent increases for larger V_{oc} and in some cases has a deviation of up to even 900 mV. This cannot be explained explicitly, and according to its small portion and non-uniform distribution can be considered as the measurement or control noise due to the ULP system. Secondary portion of abnormal selection of $\langle V_i \rangle$ belongs to values smaller than the desired 80 %

which their distribution increases when V_{oc} gets higher. The reason for this deviation has to be analyzed while it can be a behavioral procedure of the BQ or a consequence of V_{oc} measurement. Therefore, distribution of all measured values according to the $\langle V_o \rangle$ are shown in Fig. 5.35.

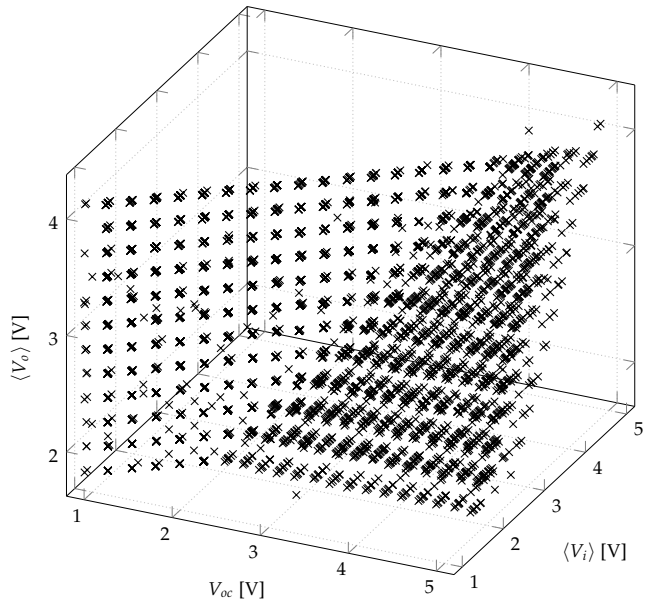

Fig. 5.35 Distribution of the operational input voltage according to the real V_{oc} set to the SMU in addition to the output voltage.

Considering the FOCV rule, data in Fig. 5.35 has to be a diagonal surface. Although this surface has to be independent from the $\langle V_o \rangle$, value of this signal in the higher ranges of V_{oc} plays a rule. A more detailed look shows that these points are actually when the the output voltage is smaller than the 80 % of the V_{oc}, pushing the converter out of boost mode. This effect appears initially when $\langle V_o \rangle$ is around 1.6 V with a V_{oc} of about 2 V. Although this setting by the MPPT can be considered as a safety mechanism, it is simply a consequence of its ULP design which is not able to measure the voltage. Looking at the measured V_{oc} during the MPPT pulse shows that the measurement mechanism is limited to values near the output voltage.

Although operation at buck condition is not the main case for BQ, as discussed formerly, it can happen within PhyNetLab. In these cases, a lower V_{oc} will be measured, causing operation at lower $\langle V_i \rangle$ than the V_M of the PV module. Consequently, drained current from the PV module will not be the I_M. This is the main reason for separation of the MPPT model from the converter model. In case of a single model for the whole BQ, these conditions lead to a much larger error while model considers PV operation at V_M and I_M. In

contrary, this two-fold mechanism finds a realistic value for the V_h and passes it to the PV model for the extraction of an accurate I_h.

Based on these principles and considering Fig. 5.35, two separate behaviors are available which can be explained with a simple model for the MPPT mechanism as in (5.29). This simple relation actually replicates two surfaces seen in Fig. 5.35 as a nonlinear formulation.

$$\langle V_i \rangle = \min\{0.8 \cdot V_{oc}, \langle V_o \rangle\} \tag{5.29}$$

This formulation can be included as the on-board model because of its simple form. However, as can be seen in Fig. 5.36 showing its application on the data-set, many points are not predicted properly with this formulation.

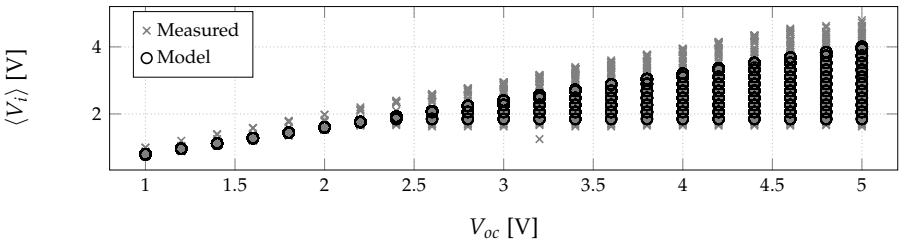

Fig. 5.36 Prediction of the simple MPPT model from (5.29) on the data-set.

This model has a RMSE of 252.3 mV or 8.97 % on the relative error. Anyhow, signals analysis shows another interesting fact with an example of it shown in Fig. 5.37. This presents measured voltages of three experiments with similar voltages but different $\langle I_i \rangle$ values. This shows that the measured voltage during a MPPT pulse is dependent on $\langle I_i \rangle$.

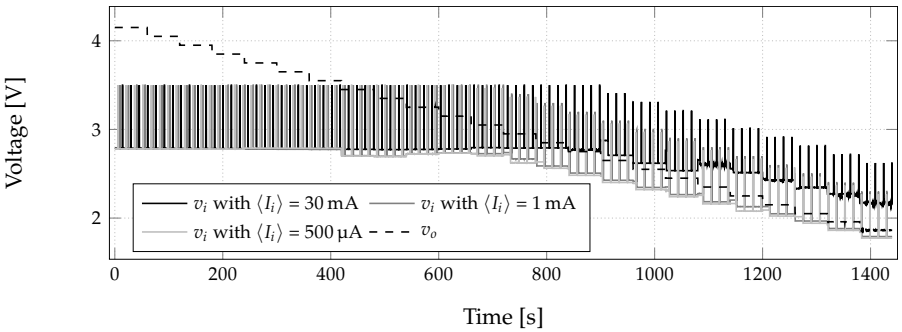

Fig. 5.37 Measured voltages at different currents, with set value of V_{oc} = 3.5 V for all of them.

While lower current levels have a roughly similar behavior, increase of $\langle I_i \rangle$ makes reading of the real V_{oc} for a much larger range of the $\langle V_o \rangle$. This is a consequence of the way that BQ measures the V_{oc}, discussed in Section 5.8. When the input is able to push more current, chance of having a more accurate voltage measurement is higher. Although the exact current passed from a PV

module to the BQ cannot be estimated, using I_M is a feasible consideration which fits to the measurements available in the data-set.

Including these specification, model of MPPT has to be modified to include $\langle I_i \rangle$ as input in addition to $\langle V_o \rangle$ and V_{oc}. Similar to the converter model, it is more convenient to use the logarithm of $\langle I_i \rangle$ as the input which reduces the magnitude range and makes data more uniformly distributed. Using these three signals as inputs to the MPPT model, its abstract representation from Fig. 5.15 has to be updated into Fig. 5.38.

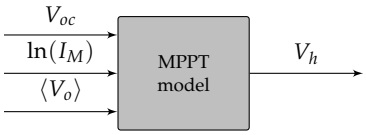

Fig. 5.38 Abstract representation of the BQ MPPT model in its full form.

As discussed in the simple model from (5.29) and seen from distribution of the data in Fig. 5.35, actually two behavior have to be included for the MPPT model. It is possible to train a single ANN to include both these conditions which will be large and roughly complex. To solve this issue, it is possible to divide the data-set into two sub-parts and train two separate networks. However, it is known that a major part of behavior can be explained by FOCV principle which actually do not require a separate network. Therefore, it is better to train a single network for the abnormal conditions when the BQ is being pushed to the buck mode. Different trials have shown that a shallow network with $N_h = 100$ will be a good compromise between computation needs and accuracy. Considering this network, the overall model for MPPT can be formulated as in (5.30), when f is representing the ANN behavior for the cases that signals push the converter into the buck mode.

$$\langle V_i \rangle = \min\{0.8 \cdot V_{oc}, f(V_{oc}, \langle V_o \rangle, \ln(\langle I_i \rangle))\} \tag{5.30}$$

A min function is used in (5.30) instead of separating the decision making based on the comparison of voltages. This is mainly because the trained ANN will always provide a larger value than the 80 % for the normal operational conditions. Using this model, the overall performance on the whole data-set has a RMSE of 22.5 mV and MAPE of 0.41 %.

In addition, using this data-set and replicating the f of (5.30) with a decision tree has a RMSE of 18.4 mV and MAPE of 0.53 %. Although it shows a better RMSE than the ANN, its relative performance is worse. Nevertheless, similar to the converter model, these models have to be tested for values between measured discrete points in the data-set.

5.11 Models evaluation

Although both types of models are tested on the evaluation section of data-set, it is better to check them with data not used during model development. This is also critical because both models are developed using data collected at discrete points. In addition, it evaluates if decision tree models are really better than their ANN counterparts. Therefore, a similar scenario is used for the data collection but with the V_{oc} and $\langle I_i \rangle$ selected randomly and $\langle V_o \rangle$ spanning the whole possible range. In this way new points will be available to provide a reliable realistic evaluation. This experiment is repeated 200 times with randomly selected values. Since PhyNode's operational range in PhyNetLab is limited compared to the whole range, another 200 experiments are measured with randomly selected values with V_{oc} in between 4.3 V to 3.8 V, $\langle I_i \rangle$ from 40 µA to 140 µA and $\langle V_o \rangle$ between 4.2 V to 3.54 V.

Using these two data-sets, it is possible to check performance of each model standalone and finally as a combination of both converter and MPPT models together. Available models for converter are ANN and decision tree in addition to a single efficiency method as the on-board model. Concurrently, in addition to the ANN and decision tree, there is a simple analytical model formulated in (5.29) as the on-board model describing the MPPT mechanism. Converter models performance factors on both ranges are presented in Table 5.7.

Table 5.7 Converter models performance on randomly selected operational points.

	Whole range			PhyNode range		
Factor	Single η	ANN	DT	Single η	ANN	DT
RMSE (η) [%]	10.407	2.159	3.855	10.295	1.381	1.327
MAPE [%]	10.946	1.402	2.106	10.558	1.169	1.076

As could be estimated, a single efficiency value has a large error for both data-sets. However, both ML-based models are performing in a good range, though selection of one over the other is not possible. Therefore, a system designer has the freedom to select one based on the preferred evaluation factor. An example of performance for these three models is shown in Fig. 5.39.

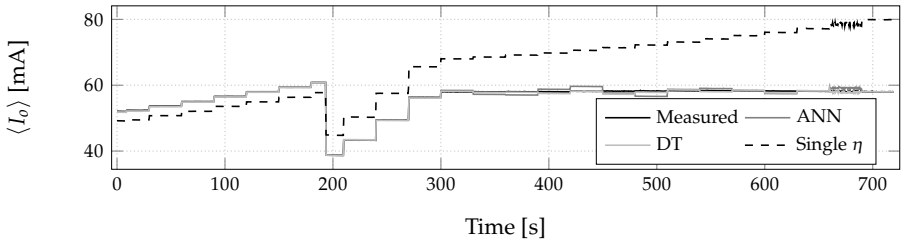

Fig. 5.39 Performance of the converter models on predicting $\langle I_o \rangle$. Setting at V_{oc} = 3.9 V, $\langle I_i \rangle$ = 77 mA. $\langle V_o \rangle$ is swept in the whole range during the experiment.

Additionally, performance of MPPT models on two data-sets with randomly selected operational points is shown in Table 5.8.

Table 5.8 Performance of MPPT models on the data-set with randomly selected operational points.

	Whole range			PhyNode range		
Factor	Simple	ANN	DT	Simple	ANN	DT
RMSE ($\langle V_i \rangle$) [mV]	311.82	201.50	208.92	174.73	110.19	118.84
MAPE [%]	6.739	3.735	4.125	3.913	1.173	1.819

One aspect which has to be noted is that these performances are a bit worse than the training. This is mainly due to the fact that the real MPPT procedure of the BQ is periodic. Consequently, it is possible that BQ is not operating optimally between two subsequent MPP measurements. However, model calculates the optimal $\langle V_i \rangle$ for each single point in the data regardless of V_{oc} measurement procedure. This effect in addition to the performance of models in a single example experiment can be seen in Fig. 5.40.

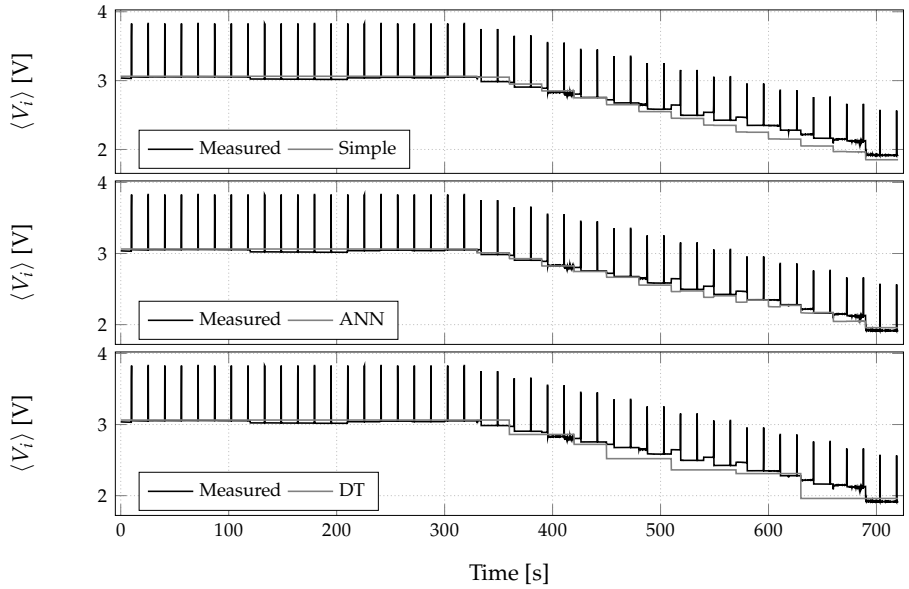

Fig. 5.40 Performance of the MPPT models on predicting $\langle V_i \rangle$. Setting at V_{oc} = 3.8 V and $\langle I_i \rangle$ = 20 mA. $\langle V_o \rangle$ is swept in the whole range during this experiment.

As can be seen, ANN based model has a better performance and can be used as the detailed system level model. However, decision tree model is not that bad and can be preferred due to faster realization. Furthermore, considering ULP limitations, even the simple model has an acceptable performance and can be used for the on-board model.

Finally, using these two models, it is possible to evaluate the overall performance of combined models together. Results of these evaluations using RMSE are presented in Table 5.9.

Table 5.9 RMSE of efficiency evaluated using combined BQ models on the data-set with randomly selected operational points.

	Whole range			PhyNode range		
MPPT \converter	Single η	ANN	DT	Single η	ANN	DT
Simple	10.407	-	-	10.295	-	-
ANN	-	4.628	5.650	-	1.229	1.291
DT	-	5.117	5.570	-	1.232	1.273

It can be concluded from Table 5.9 that all possible four combinations of ML-models have a roughly similar performance and can be used based on the preference of the system designer. In addition, on-board model made of (5.29) for the MPPT and a single efficiency for the converter have an overall estimation error of about 10 % on the efficiency. Despite high value, it is an acceptable performance considering very limited knowledge and resource required. An example of all performance on a single evaluation experiment is shown in Fig. 5.41.

In Fig. 5.41 system is operating in normal condition till the drop at about 380 s which the lowering $\langle V_o \rangle$ causes push to operation in the buck mode. As can be seen, models are all performing very well for this range and the major error is during the operation in abnormal condition. Revising the performance within both data-sets shows a similar trend for the whole operational condition. Therefore, it can be concluded that the performance of the combined model for the normal operational condition will be even better than performances mentioned in Table 5.9.

Among four possible combinations of methods, both ANN models will be used further because of consideration of the RMSE as the main performance criteria.

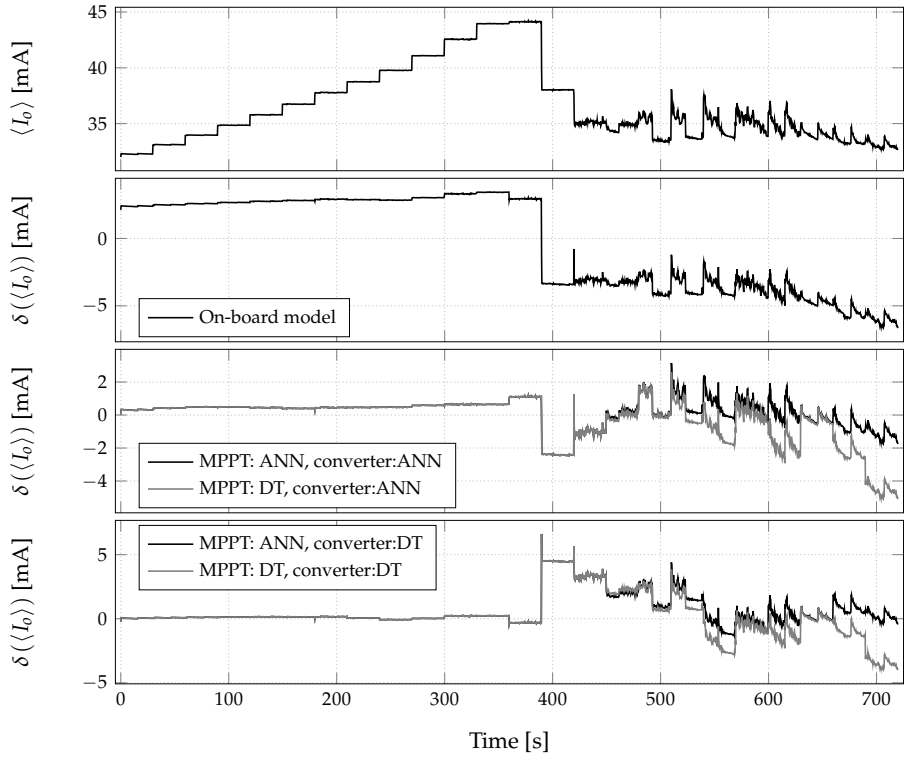

Fig. 5.41 Performance of models for the BQ on a randomly selected operational condition. Setting at V_{oc} = 3.54 V and $\langle I_i \rangle$ = 50.8 mA. $\langle V_o \rangle$ is swept in the whole range during the experiment.

Chapter 6
Holistic Model and Energy Balancing

Having a vision for what you want is not enough ...
Vision without execution is hallucination.

—Thomas A. Edison

Abstract
This chapter provides a holistic view of the overall energy supply unit of PhyNode by combining modular models developed for each device. This model only requires light intensity, temperature and PhyNode's load to provide the battery's status and voltage as its outputs. For the initialization, this model requires only the starting open circuit voltage of the battery.

For the evaluation, a totally new environment is used to avoid any effect included during model development. This also assures that the modeling techniques are universal and applicable on different environments. Using collected lighting information, PV models are tuned to the new lighting type.

Evaluation of the overall holistic model in the new environment on multiple experiments with different hardware combinations always shows a MAPE less than 1 % in the estimation of the battery voltage.

Afterwards this holistic model is used for the system design procedure to balance the energy in a materials handling process within a production system. After definition of criteria for the quantification of the performance, present status of PhyNode is evaluated. This is followed with analyzing different possible modifications on either operational process of PhyNode or its hardware.

All in all, in addition to providing the holistic model as the main goal, this chapter provides possible use-cases of the model for simulation within the field of materials handling and warehousing to modify the system and make PhyNode energy neutral.

6.1 Holistic model

All PhyNode's ESU modules have been modeled separately. In this part, they are combined to build a holistic model for the whole system. Although physical relation between these modules is known, their combined model presented in Fig. 6.1 has a more complex structure.

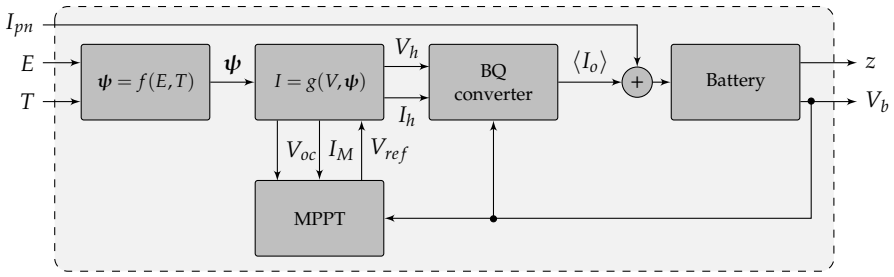

Fig. 6.1 The overall schematic structure and signaling of the holistic model.

This model has only three inputs, namely: light intensity (E), temperature (T) and demanded current by PhyNode (I_{pn}). Output of this model is the battery terminal voltage (V_b) or its SoC (z) for each iteration of the input signals. The only required value which has to be set in the model is the initial battery OCV to calculate its SoC. Knowledge about SoH and integration of its data into the battery model will help to enable aging factor. However, its implementation is not necessary for the holistic model. This model has an iterative procedure with a constant T_s and operates as described in Algorithm 4.

Algorithm 4 Process of updating battery voltage using holistic model.

1: Read inputs: E, T, I_{pn};
2: Calculate $\boldsymbol{\psi}$ for E, T;
3: Calculate I-V relation of PV model using $\boldsymbol{\psi}$;
4: Find V_{oc} and I_M from PV model;
5: Calculate $\langle V_i \rangle$ using MPPT model with V_{oc}, $\ln(I_M)$ and last V_b;
6: Find $\langle I_i \rangle$ from PV I-V relation for the $\langle V_i \rangle$;
7: Calculate $\langle I_o \rangle$ using converter model with $\langle V_i \rangle$, $\ln(\langle I_i \rangle)$ and last V_b;
8: Calculate effective current on the battery (I_b) as signed sum of $\langle I_o \rangle$ and I_{pn};
9: Find new SoC using I_b, T_s and former SoC;
10: Update V_b with the new SoC;

In case of non-constant T_s, integration procedure in the battery model has to be modified to adapt itself for each sampling. In addition, larger T_s will lead to a lower accuracy in the estimation of the system behavior.

Though each model has been evaluated during modular modeling, the overall holistic model has to be checked as well. Model of BQ and battery are not dependent on the environment and behave similarly in different conditions. However, PV model has dependencies on the environment. Therefore, evaluation of holistic model in other environments than PhyNetLab can prove

the overall validity of the PV modeling. Consequently, PhyNode is being tested in an office in Dortmund, Germany with windows looking into west.

Using the same setup as in Fig. 3.15 without the spectrometer, behavior of the PV cell has been measured every 5 min for one complete day. Using this data-set, $\boldsymbol{\alpha}$ parameters in this lighting are tuned. This data enables estimation of I-V relation for different environmental indoor condition of the office.

For the measurement of evaluation data, battery is connected to the BQ while SMU applies PhyNode's load on the battery's terminal and measures its voltage. This measurement of V_b enables a comparison between model's estimation and real condition. In parallel, Raspberry Pi measures the environmental signals.

By use of the whole-curve detailed model for the PV EH module, dynamic detailed model for the battery, ANN model for the MPPT and converter of the BQ, V_b is estimated for each measurement. Error of model for a three days duration is shown in Fig. 6.2. Similar to the performance of the battery, samples are too dense. Therefore, only moving mean of error and its bounds are shown.

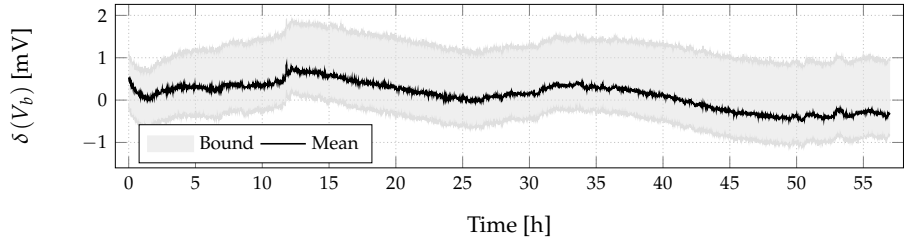

Fig. 6.2 Error of the holistic model and its bound on the evaluation experiment.

Furthermore, Fig. 6.3 shows the exact error of V_b in a short time period.

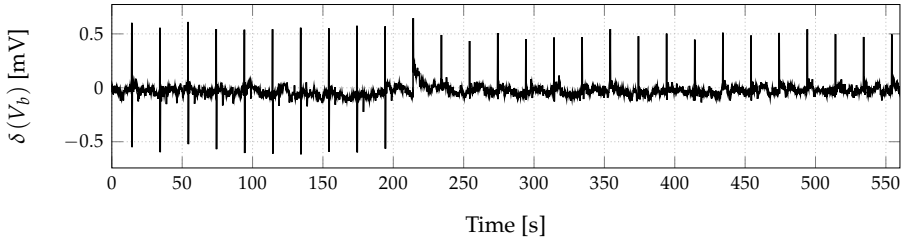

Fig. 6.3 Error behavior of the holistic model on a small part of the evaluation experiment.

The overall performance of the holistic model has a RMSE of 336.32 µV and a MAPE of 0.007 % on V_b, proving high accuracy of the holistic model. To evaluate robustness of the model to component's production tolerances, four different combination of batteries and PV cells have been tested as well, each for a similar three days period. Repeating this experiment on each device combination has shown a worst case MAPE of 0.938 % on V_b.

At this point not only model of each module is accurate, but also the overall holistic model can be trusted as well. To show possible uses of these models, dimensioning of PhyNode and its energy balance are discussed here for the application case of warehousing in PhyNetLab.

6.2 System dimensioning

As discussed in Chapter 4, present condition of PhyNode would not be energy-neutral due to harvesting/demand imbalance. However, this was based on a simple comparison between the idle demand and harvested current. Nevertheless, due to the environmental condition and load changes, a more accurate analysis of this imbalance is necessary.

Although used I_{pn} of PhyNode in Fig. 4.7 is directly measured from the board, order of operations in reality will not be the same. Based on the operational scenario, these actions will be in different orders and a real load profile is required to evaluate the energy neutrality. Hence, Cyber-Physical Production System (CPPS) [262] which is a production test platform build upon use of PhyNodes in PhyNetLab is considered. In addition to the warehousing aspects, it includes standard containers with PhyNodes as fundamental elements for transportation of objects at a production floor. It evaluates different scenarios and algorithms for production planning which can be used as a base for a more realistic behavior of PhyNodes in action. Consequently, it is possible to consider pushed events to PhyNodes in this application similar to a real industrial case. Furthermore, availability of accurate positioning system inside PhyNetLab provides tracking data for each PhyNode. Using localization data, combined with measured lighting intensity from Fig. 3.35, a realistic light profile can be generated as well. Using measured temperatures from PhyNetLab during one day, environmental conditions required for PV model are available. Considering these information, an accurate realistic profile can be made as input data for the holistic model.

Time separation of the profile has to be 100 ms which is equal to the shortest operation of PhyNode. This profile is considered for a complete day to have all possible conditions of a scenario. This duration is enough for the energy balance analysis due to indoor condition of PhyNetLab which is not affected by sunlight, geographical position and season. One extra point to be noted is the aging status of the battery which its nominal condition is used here.

Before analyzing this profile, a performance criteria is required. Therefore, Periodic Charge Difference (PCD) presented with ϑ is defined as:

Definition: *Periodic Charge Difference*

PCD shows the deviation of battery SoC of an embedded system between start and end of an operational period.

This can be simply formulated as:

$$\vartheta = z(end) - z(start) \tag{6.1}$$

Smaller ϑ value shows a better balanced system. While positive ϑ is a sign of over-production, negative ϑ resembles a system with a negative energy balance. Using this definition, it is possible to evaluate PhyNode's real behavior using profile from CPPS. Simulation of this profile with the use of holistic model is shown in Fig. 6.4. To be noted that again due to large number of measured points (more than 864 thousand) only moving mean signals are shown. This analysis proves the initial guess that PhyNode will be continuously discharged because this scenario in CPPS has a PCD of $-2.4048\,\%$.

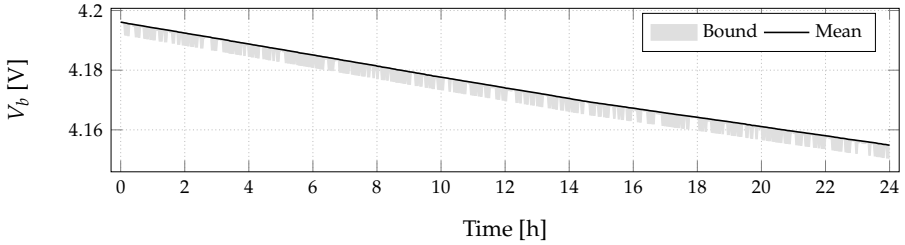

Fig. 6.4 PhyNode behavior through a complete operational day using a load profile from CPPS in PhyNetLab.

This performance is not acceptable for a system designer due to lack of power balance and need for recharge. First steps to tackle this issue is the reduction of demand. By analyzing the load, it can be seen that more than 88 % of demand is during the idle period. Although current in this phase is not high, its time duration makes it the most demanding charge. Hence, reduction of demand in this phase will improve the balance. Fortunately, this is possible by use of the wake-up system in PhyNode which allows it to turn off during no-operation period and come back when needed. In this way, by assuming a zero demand during this idle phase, experiment is repeated with the modified load profile. SoC during this simulation is presented in Fig. 6.5; showing an improved PCD, reduced to $-0.2074\,\%$.

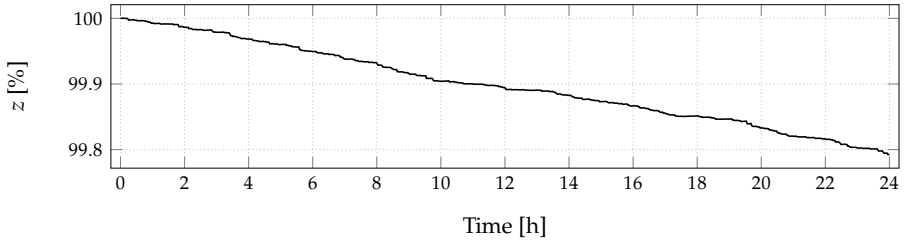

Fig. 6.5 PhyNode behavior through a complete day with zero idle current.

As can be seen, battery is being charged during some periods because the sum of currents is incoming. Regardless of these improvements, PhyNode is still not energy-neutral since net change of SoC is negative. A further change is modification of PhyNode's operational process in a way that for a portion of time bins are positioned at rest. During this period which can be a night shift with no-operation, PhyNode is turned off and will only charge.

This type of operation will lead to discharge for the operational phase and charge during the rest time. Therefore, some kind of zigzag behavior will be seen in the SoC status. While PCD provides an impression about status between both ends, another comparison factor to the PCD is required to show how imbalanced the overall operation is during this period. It is possible to simply use the standard deviation of SoC shown by σ to explain how spread the SoC values are. Larger values of σ will show a more imbalanced system.

Different rest periods at different light intensities are simulated and their outcomes are presented in Fig. 6.6. In these scenarios, the common profile is used till the rest period starts. Then the demanded current is equal to zero and a constant light intensity is applied.

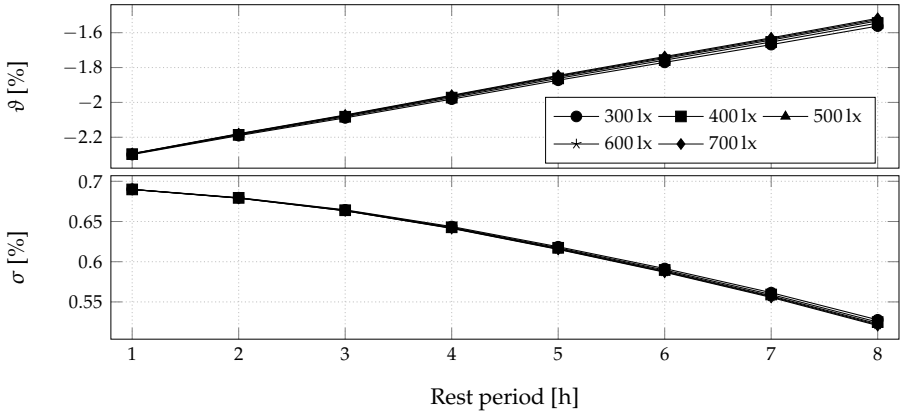

Fig. 6.6 Performance of PhyNode during a complete day with different rest periods at different lighting intensities.

As presented in Fig. 6.6, addition of a rest period during a day will improve the overall condition marginally. PCD is reduced with increase of time and system imbalance factor is reduced as well exponentially. This is mainly due to increasing rest period which reduces the depth of discharge while increasing sum of unused harvested energy.

In spite of these improvements, PhyNode still cannot be considered as an energy-neutral device and some further changes in the system are necessary. Increasing the size of battery will also not be useful here while it only adds extra buffer size, helping this continuously discharging device only last longer. While reduction of demand has been already analyzed, focus has to be on the

increase of the harvested energy. This can be reached by enlarging the PV panel or increasing the lighting intensity which will be analyzed hereafter.

6.2.1 Dimensioning the lighting

It has been shown in Fig. 3.20 that increasing E has a direct linear relation with the harvested current at the MPP. Therefore, if it is possible to increase the light intensity, perhaps PhyNode can be made energy-neutral. To check this, light intensities from the CPPS scenario are scaled from 1.5 to 4 times with 0.5 steps. Unfortunately, these multiplication only can reduce the PCD as presented in Fig. 6.7, but PhyNode will be still continuously discharging.

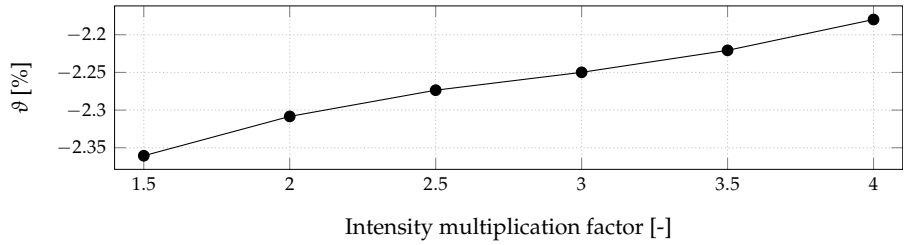

Fig. 6.7 Performance of PhyNode with multiplied light intensity.

Furthermore, multiplication of light intensity higher than 3 times is not feasible in this case because it leads to values which are too high for a warehouse. Therefore, a scenario is considered with a multiplication factor of 2 times of the present status leading to a maximum E =500 lx. Checking this new lighting condition combined with a zero idle current shows a very promising case with a PCD = -0.1125 % and $\sigma = 0.0310$ %.

In the next step, combination of these changes with different rest periods at 700 lx has been evaluated, leading to factors presented in Fig. 6.8.

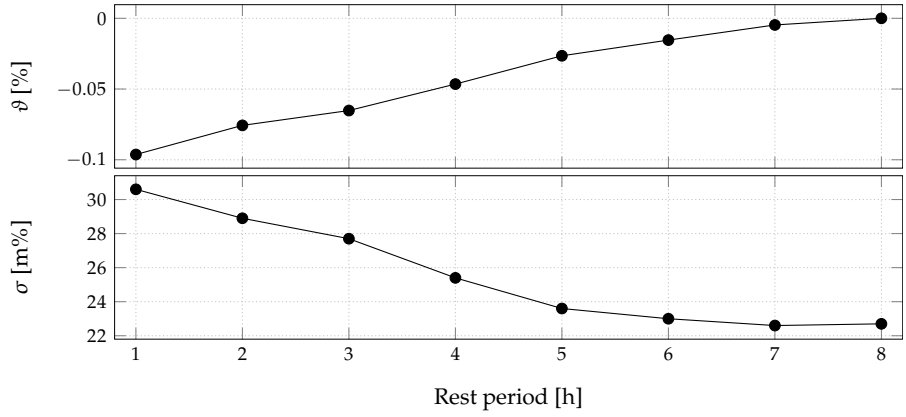

Fig. 6.8 Performance factors of PhyNode with doubled light intensity, zero idle current and different rest periods at 700 lx.

As can be seen in Fig. 6.8, increasing the rest period to 8 h within these conditions enables PhyNode to reach its initial SoC at the end of an operational period. A more detailed analysis of Fig. 6.8 shows that although the σ is reduced to 0.0226 % at 7 h, it increases again into 0.0227 % at 8 h. This means that there is an optimum point for the imbalance factor somewhere in between these two points. This can be understood better when the changes in the SoC for 8 h case shown in Fig. 6.9 are monitored.

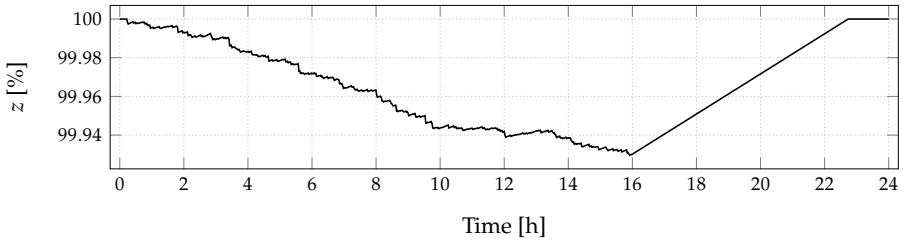

Fig. 6.9 Battery status of PhyNode during a complete day with doubled light intensity, zero idle current and 8 h of rest at 700 lx.

It is obvious from Fig. 6.9 that the SoC reaches its initial condition at a time shorter than end of one day period. This matches the hypothesis of having a minimum σ at some point less than 8 h rest which is the exact time of reaching the 100 % mark. However, it has to be noted that this is a single load profile of the CPPS and can be different based on the operation. Hence, although this exact point is an initial guess for the dimensioning, it has te be used with caution and extra considerations has to be added to assure reliable operation. Yet, this shows the benefit of used factors for analyzing the energy balance of system during design phase.

Although mentioned case is periodically energy-neutral, used assumptions are somehow extensive which include:

- Doubling the light intensity in the whole warehouse
- Use of zero idle current
- Having a rest period of 8 h with no operation and E =700 lx

It is very probable that a process designers not accept these conditions and requires modifications in the system to avoid these limitations. Hence, the only remaining factor will be increasing the size of PhyNode's PV module.

6.2.2 PV panel dimensioning

It is known that a larger PV module will generate more energy. However, the relation between size (S_{pv}) and energy has to be analyzed. Regardless of PV technology, a system designer can find this information from manufacturer datasheets. According to [263] from producer of the PhyNode's PV module, different sizes of modules with the same technology are available. Using this

data, effect of size on the harvested current at MPP (I_M) for this type of PV modules is presented in Fig. 6.10.

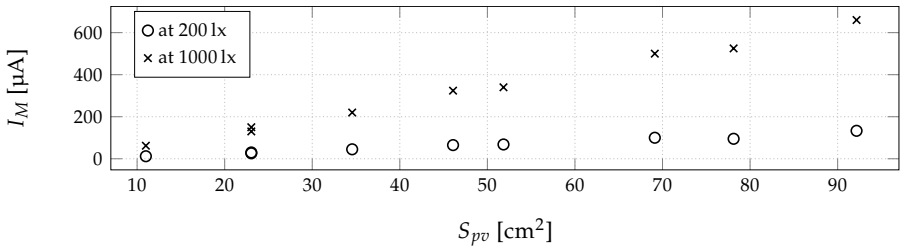

Fig. 6.10 Effect of S_{pv} on I_M. Based on data from [263].

Considering Fig. 6.10, it is clear that a linear relation is available between surface of PV module and its harvested current at MPP. Moreover, according to the manufacturer information in [263], voltage at MPP will remain constant. Hence, modification of voltage formulations will not be necessary. To find changes in currents due to the surface, similar process to the development of the single-point model of PV module can be used. By defining a reference case which is known with more details, relation for other surfaces can be written as (6.2), when ξ shows the lines slope in Fig. 6.10. To be noted that this line relation has no bias while a PV module with a zero surface produces no current.

$$I_M = \xi(E) \cdot \left(S_{pv} - S^*_{pv}\right) + I^*_M \tag{6.2}$$

Reason for relative formulation in (6.2) is to include dependencies of the PV module to the environmental conditions. In case of using absolute current instead of relative value, each calculated I_M value will be valid for the condition which the manufacturer has measured them. In contrary, formulation in (6.2) will only shift values found from real operational conditions within the desired lighting type.

Fitting lines to the available data in Fig. 6.10 gives a ξ of 1.427 µA cm^{-2} for 200 lx and 7.378 µA cm^{-2} for 1000 lx. Unfortunately, no exact value is available for any other lighting intensities. However, dependency of I_M to E has been formerly formulated in (3.40), providing a general explanation for the whole range including temperature effect. Anyhow, it can be considered that for intensities higher than 50 lx the changes in I_M are linearly related to the light intensities. Therefore, a linear relation for this change is considered which is tuned to (6.3) based on the available values.

$$\xi(E) = 7.4388 \cdot E - 60.75 \qquad [\text{nA cm}^{-2}] \tag{6.3}$$

Using single-point model of the PV module available from Chapter 3, it is possible to find the harvesting keypoints. Then, while it is possible to consider

similar voltage values, harvested current found from the single-point model can be transformed for each new surface value using (6.2) and (6.3).

With this method and holistic model, behavior of a range of S_{pv} are simulated which their performance factors are presented in Fig. 6.11.

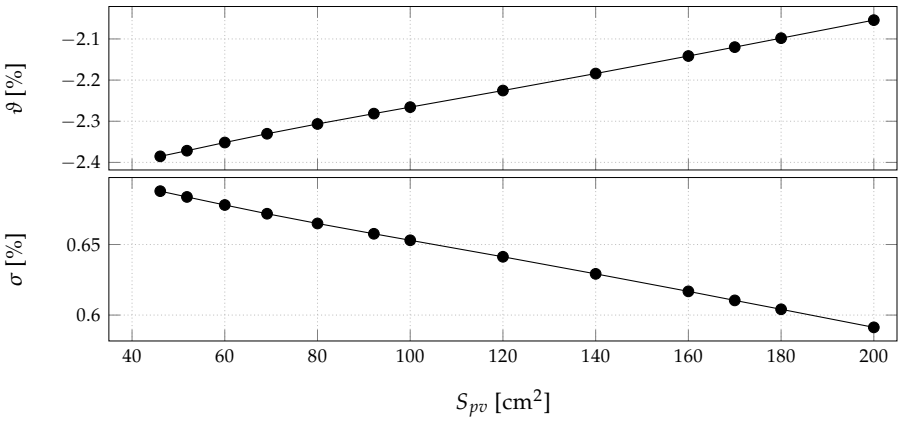

Fig. 6.11 Effect of S_{pv} on the PhyNode energy performance factors.

As it is clear from Fig. 6.11, even a roughly large PV panel of size 200 cm^2 is not able to fulfill the requirements of the present PhyNode's operational condition. Therefore, these simulations are repeated for the case with zero idle current, leading to performances shown in Fig. 6.12.

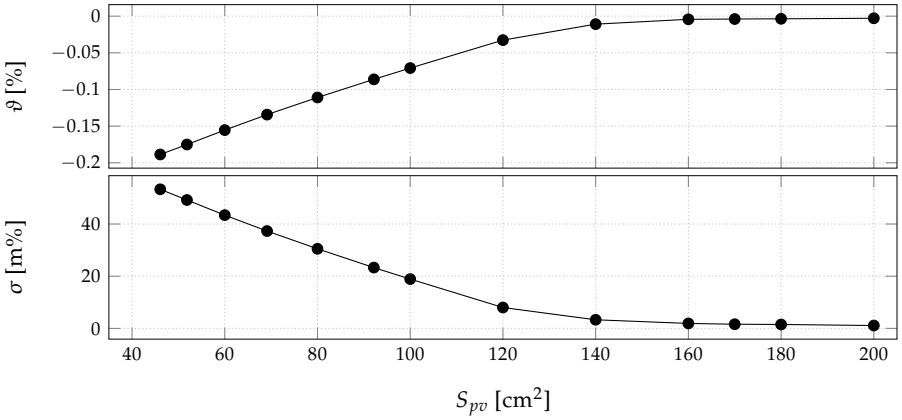

Fig. 6.12 Effect of S_{pv} with zero idle current on the system energy performance factors.

Based on these results, it can be considered that a PV panel with a size about 170 cm^2 will be very near to the balanced mode. Therefore, changes in the SoC of PhyNode for two highest considered S_{pv} are depicted in Fig. 6.13 for a better review.

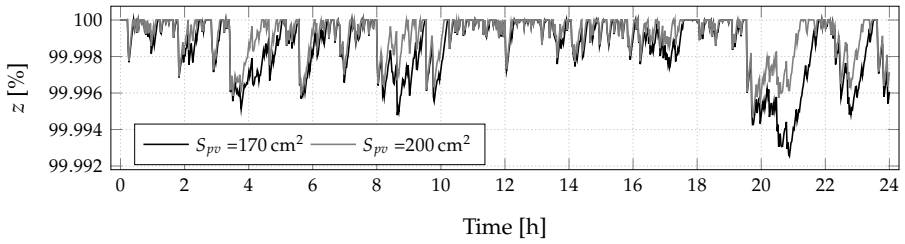

Fig. 6.13 Changes in the battery SoC with the cases of larger PV module and zero idle current.

Although there is a small deviation at the end point of one day simulation, a more detailed analysis of cases in Fig. 6.13 shows that there is a portion of time that the battery OV is reached. However, the PV module is still able to push current to the battery within these periods. Therefore, combination of the PV size with the zero idle current has to be analyzed at some other initial SoC values while it has the potential for balancing production and demand. Performance factors for some cases when starting from a SoC of 75 % can be seen in Fig. 6.14.

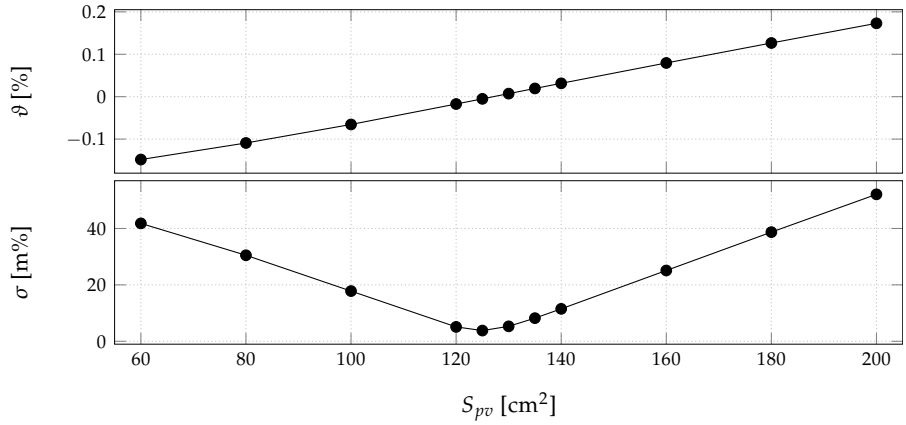

Fig. 6.14 Effect of S_{pv} with zero idle current on the system energy performance factors when starting from 75 % initial SoC.

Looking at Fig. 6.14, it is clear that there is an S_{pv} optimal point for both performance parameters. This shows both defined factors can be helpful for a system designer to select the most proper components.

For a more detailed overview, behavior of the SoC for surface values around the optimal point are shown in Fig. 6.15.

Based on these performances, selection of a PV module with S_{pv} =140 cm^2 will be acceptable when considering some extra buffer. Although this value is a bit over-dimensioned for the present current profile, it is able to compensate those cases when the load changes a bit or the lighting is partially smaller.

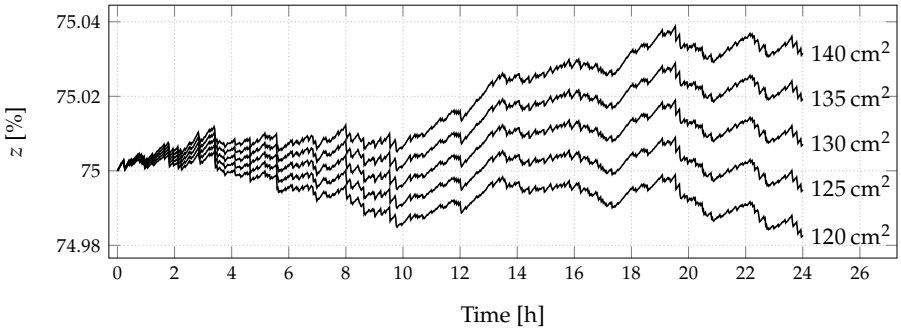

Fig. 6.15 Battery SoC for different S_{pv} and zero idle current starting from 75 % initial SoC.

All in all, based on different scenarios, it is clear that the main issue with the present status of PhyNode is its high idle demand. To balance the system design, reduction of this current is necessary which its best case will be a zero idle current by use of the wake-up system.

Two different cases has been shown that PhyNode will have a balanced ESU. First is by addition of a rest period during each operational day. Second is to modify the PV panel to have a size of about 140 cm^2. However, in both cases a zero idle current is essential.

Chapter 7
Sum up

There is no real ending.
It's just the place where you stop the story.

—Frank Herbert

The main aim of this work is development of a model to provide knowledge about the energy status of PhyNode as a CPS device in the field of materials handling and warehousing. This goal has been divided into two model sub-categories with different form of applications, each with its own characteristics. While the first type of model has to be implemented on-board of PhyNode to be used during operation, a more advanced and detailed model is required for the design phase by system and process designers who plan the hardware and operation of PhyNode. While on-board models has to be simple and fast due to PhyNode's extreme hardware constraints, detailed model can be complex and has no time, computation or energy limitations. Moreover, on-board models can have some kind of feedback from the system because it is possible to measure systems' real parameters. In contrary, detailed model has to operate in an open loop manner since it has no access to the real hardware.

7.1 Models

According to the structure of PhyNode's ESU with three main components including a PV EH module, a battery and a power management system with MPPT and a boost converter, a modular strategy is used to develop model for each device separately. These models are connected with each other to build a holistic model. Benefit of this scheme is its fast modification of the system model in case any module is swapped with another version. In addition, modular design of the model helps to evaluate each part separately, avoiding integration of errors into the whole system model.

7.1.1 IPV model

For the modeling of PV harvester a measurement platform is developed enabling high accuracy measurement of the module within controlled environmental conditions. Two different types of IPV technologies are measured to collect three different data-sets used for analysis of modules' characteristic

under pure indoor lighting. In addition to two IPV technologies, these datasets help to analyze not only effect of light intensity and its type, but also temperature. These data is utilized for evaluation of available knowledge about PV models and explaining relations which can replicate their behavior within this specific condition. Based on these evaluations, only three equations as in (7.1) are required to explain voltage and currents for the on-board model of a PV module.

$$\widetilde{V_x} = \frac{V_x}{V_x^*} = \alpha_1 + \alpha_2 \cdot \ln\left(\alpha_3 + \frac{\alpha_4}{\widetilde{E} + \alpha_5 \cdot \widetilde{T}}\right) + \alpha_6 \cdot \widetilde{T} \tag{7.1a}$$

$$\widetilde{I_{sc}} = \frac{I_{sc}}{I_{sc}^*} = \alpha_1 + \alpha_2 \cdot \widetilde{E} + \alpha_3 \cdot \widetilde{T} \tag{7.1b}$$

$$\widetilde{I_x} = \frac{I_x}{I_x^*} = \alpha_1 + \alpha_2 \cdot \widetilde{E} + \alpha_3 \cdot \widetilde{E}^{\alpha_4} + \alpha_5 \cdot \widetilde{T} \tag{7.1c}$$

When (7.1a) can be used for either V_{oc} or V_M. In (7.1c) I_x can be for both I_M or I_{80} which is the current at a voltage of 80 % of the V_{oc}. However, for each specific equation, α parameters are required separately in addition to the reference values. These equations require only the light intensity and temperature which both can be measured by available sensors on PhyNode. These equations are mathematically simple and can be calculated with low computational effort.

For the system level model, a two step strategy as in Fig. 7.1 is used.

Fig. 7.1 Two steps of a system level model of an IPV module.

In the first step, $\boldsymbol{\psi}$ as a vector of unknowns for the whole-curve model has to be found for each environmental condition. These unknowns are used in the second step to build the I-V curve, representing the overall behavior of the IPV curve. I-V relation is explained from deductive physical knowledge of PV system in one or two diode form. A general 2D formulation of I-V curve is as in (7.2) and (7.3) while one of I_d values has to be removed for the 1D model.

$$I_h = I_g - I_{d_1} - I_{d_2} - \frac{V_h + I_h \cdot R_s}{R_{sh}} \tag{7.2}$$

$$I_{d*} = I_{s*} \cdot \left[\exp\left(\frac{V_h + I_h \cdot R_s}{n_* \cdot V_t}\right) - 1\right] \tag{7.3}$$

These formulations can be expressed by an ECM as depicted in Fig. 7.2.

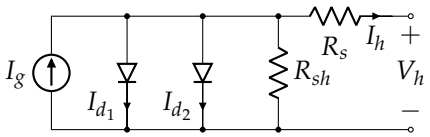

Fig. 7.2 Equivalent 2D circuit model of a PV cell including parasitic resistances.

To reduce numerical complexity of the data-sets because of large differences in signal ranges, PVNS is introduced as a normalization of each I-V curve according to its I_{sc} and V_{oc} using (7.4).

$$\overline{\mathbf{P}} = \left[V_h, V_t, R_s, R_{sh}, I_h, I_g, I_s\right]^{\mathsf{T}} \times \left[\frac{1}{V_{oc}}, \frac{1}{V_{oc}}, \frac{I_{sc}}{V_{oc}}, \frac{I_{sc}}{V_{oc}}, \frac{1}{I_{sc}}, \frac{1}{I_{sc}}, \frac{1}{I_{sc}}\right] \tag{7.4}$$

To make analysis of the performance for each whole-curve model, MANE as a new evaluation criteria is introduced which is explained by:

$$\text{MANE} = \frac{100}{I_{sc} \cdot V_{oc}} \cdot \int_0^{V_{oc}} \left|\delta\left(I_h\right)\right| \mathrm{d}V_h = 100 \cdot \int_0^1 \left|\delta\left(\overline{I_h}\right)\right| \mathrm{d}\overline{V_h} \tag{7.5}$$

Analyzing different numerical and AES based tuning methods for extraction of $\boldsymbol{\psi}$, it has been found that in addition to use of data in the normalized space, parameter values for IPV modules have to be bounded with values as shown in Table 7.1.

Table 7.1 Limits for IPV model's unknown parameters.

Parameter	Lower limit	Upper limit	Unit
I_g	0.9	1.1	[A]
R_s	ϵ	$(V_{oc} - V_M)/I_M$	[Ω]
R_{sh}	$V_M/(I_{sc} - I_M)$	∞	[Ω]
I_s	ϵ	1.1	[A]
n	1	10	[-]

Extraction of $\boldsymbol{\psi}$ for both types of models and both methods has shown that the 1D model parameters have a reliable relation to E and T. Though, 2D model parameters do not show a consistent relation according to E. Hence, relation of 1D model parameters according to the environmental factors are formulated empirically using (7.6).

$$\widetilde{I_g} = \frac{I_g}{I_g^*} = \alpha_{g1} \cdot \widetilde{E} + \alpha_{g2} \cdot \Delta T \tag{7.6a}$$

$$\widetilde{R_s} = \frac{R_s}{R_s^*} = \frac{\alpha_{s1} + \alpha_{s4} \cdot \Delta T}{\alpha_{s2} + \alpha_{s3} \cdot \widetilde{E}} \tag{7.6b}$$

$$\widetilde{R_{sh}} = \frac{R_{sh}}{R_{sh}^*} = \frac{\alpha_{p1} + \alpha_{p6} \cdot \Delta T}{\alpha_{p2} + \widetilde{E}} + \ln\left(\alpha_{p3} \cdot \widetilde{E} + \alpha_{p5}\right) \tag{7.6c}$$

$$\widetilde{I_s} = \frac{I_s}{I_s^*} = \alpha_{i1} + \alpha_{i2} \cdot \widetilde{E} + \frac{1}{\alpha_{i3} \cdot \widetilde{E}^{\left(\alpha_{i4} + \alpha_{i5} \cdot \widetilde{T}\right)}} + \alpha_{i6} \cdot \Delta T \tag{7.6d}$$

$$\widetilde{n} = \frac{n}{n^*} = \alpha_{n1} + \alpha_{n2} \cdot \widetilde{E} + \frac{1}{\alpha_{n3} \cdot \widetilde{E}^{\left(\alpha_{n4} + \alpha_{n5} \cdot \widetilde{T}\right)}} + \alpha_{n6} \cdot \Delta T \tag{7.6e}$$

For the evaluation of both models, an extra data-set is collected within PhyNetLab in the real operational condition of PhyNode including more than

120 I-V curves. Performance of the single-point on-board model on this data-set in the form of error for each single parameter is collected in Table 7.2.

Table 7.2 Performance of single-point on-board PV models to predict keypoints.

Parameter	V_{oc}	V_M	I_{sc}	I_M	I_{80}
MAPE [%]	0.1052	0.1607	1.1464	1.2680	1.3080

Furthermore, application of detailed system level model on this data-set shows an overall mean value of MANE performance factor of 1.2947 % when the worst case MANE is less than 6 %.

7.1.2 Battery model

For the measurement of the battery characteristics without a need for high accuracy cycler with specifications for ULP measurements, all experiments are programmed with use of a single SMU. A process for charging the battery to the fully charged state with a reduced time duration and hysteresis removal is defined. For analysis of the aging status of the battery a standard test is explained discharging the battery with I_n starting from a fully charged state. This test is measured before and after each characteristic measurement to normalize them and enable aging comparison.

For definition of operational range of battery in the context of PhyNode, exact demand of PhyNode for all its operations has been measured. This process is repeated for different voltage levels showing that the minimum allowed voltage for PhyNode is 3.54 V. PhyNode cannot start with lower voltage levels and system is in a non-deterministic state. Hence, operational voltage of PhyNode's battery is limited to this value instead of 3 V as the minimum allowed voltage for the battery.

SoC-V_e relation of the battery is measured using both discrete and continuous identification methods. Comparison of discrete method curve with continuous curve with I_e shows very similar forms except for small differences in the hyperbolic section. Different experiments have shown that this is a consequence of aging in the form of curve for low-budget batteries such as the one used for PhyNode. Using identified SoC-V_e relation, it is possible to prepare PhyNode's on-board battery model which can only measure the terminal voltage and provides an estimation of the SoC. While no current measurement is available on PhyNode, implementation of relation between V_b and SoC is more reliable than the SoC-V_e relation. Therefore, measured SoC-V_b relation for 12.5 mA as the nearest current to the average PhyNode demand is used. To avoid storage of this relation as a LuT requiring large memory space, it is formulated with a form from (7.7).

$$z(V_b) = \frac{\alpha_{b1} \cdot V_b^3 + \alpha_{b2} \cdot V_b^2 + \alpha_{b3} \cdot V_b + \alpha_{b4}}{V_b^4 + \alpha_{b5} \cdot V_b^3 + \alpha_{b6} \cdot V_b^2 + \alpha_{b7} \cdot V_b + \alpha_{b8}} \tag{7.7}$$

While this formulation explains the whole voltage range of the battery, a secondary relation as in (7.8) is tuned which is explicitly for the present status of PhyNode and shows $z = 0$ when the voltage of 3.54 V as the minimum allowed voltage of PhyNode is reached.

$$z(V_b) = \frac{7107 \cdot V_b^3 + 23790 \cdot V_b^2 + 26575 \cdot V_b + 10194}{V_b^4 + 24.68 \cdot V_b^3 + 247.3 \cdot V_b^2 + 394 \cdot V_b + 186.8} \tag{7.8}$$

Because SoC is required for the identification measurements, system level model requires a method to estimate the SoC. In contrary to most applications, this model has access only to I_b. In addition, this model has an open loop form while it will be used during the design phase for simulation. Hence, ampere-hour method has to be used for the estimation of the SoC. Nevertheless, it is possible to increase the accuracy of this estimation by inclusion of aging and current factors. Consequently, SoC formulation is advanced into a form in (7.9).

$$z(t) = z_0 - \frac{100}{Q_n} \cdot \int_0^t \zeta_a(\tau) \cdot \zeta_c(\tau) \cdot I_b(\tau)\, \mathrm{d}\tau \tag{7.9}$$

when ζ_a as the aging factor can be found using SoH curve of the battery or by use of standard tests in PhyNode. Moreover, ζ_c for PhyNode's battery is formulated from normalized discharge curves as in (7.10).

$$\zeta_c(I_b) = \frac{0.5287 \cdot \exp(1.089 \cdot I_b) - 0.5271}{0.5545 \cdot \exp(1.025 \cdot I_b) - 0.553} \tag{7.10}$$

The only missing information for the system level detailed battery model is the dynamics. Curves measured from discrete identification of SoC-V_e relation show that this can be explained using a $2RC$ model with the battery model as in Fig. 7.3.

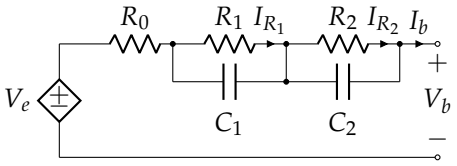

Fig. 7.3 An ECM with double RC set able to replicate PhyNode's dynamic behavior.

After identification of all parameters in this ECM for the whole SoC range, they can be stored in LuTs for the system level model.

Moreover, experiments have shown that consideration of a single aging factor for a whole discharge process adds extra error to the model. Hence, a linear dynamic aging factor is used in (7.9). Finally, the overall system level detailed dynamic model of the battery can be abstracted as in (7.11).

$$V_b[k] = V_e[k] - R_0(z[k]) \cdot I_b[k] - \sum_j \left(R_j(z[k]) \cdot I_{R_j}[k] \right) \tag{7.11a}$$

$$\chi[k] = \mathrm{LuT}_\chi(z[k]), \quad \chi \in \{V_e, R_0, R_j, C_j\}, \quad j \in \{1,2\} \tag{7.11b}$$

$$z[k+1] = z[k] - 100 \cdot \zeta_a[k] \cdot \zeta_c[k] \cdot I_b[k] \cdot \Delta t / Q_n \tag{7.11c}$$

$$\zeta_a[k+1] = \zeta_f + z[k] \cdot \left(\zeta_f - \zeta_l \right) / 100 \tag{7.11d}$$

$$I_{R_j}[k+1] = \exp(\tau_{rc_j}[k]) \cdot I_{R_j}[k] + \left(1 - \exp(\tau_{rc_j}[k]) \right) \cdot I_b[k] \tag{7.11e}$$

$$\tau_{rc_j}[k] = -\Delta t / \left(R_j(z[k]) \cdot C_j(z[k]) \right) \tag{7.11f}$$

For evaluation of these models two different loads are applied on the battery while its behavior is measured. First measurement uses a random generated load in the whole range of PhyNode load, while secondary measurement applies the exact PhyNode's load profile within its valid voltage range. Application of on-board model on these experiments subsequently shows a RMSE of 0.61 % and 0.3832 % for estimation of the SoC. System level performance on finding V_b has a RMSE of 0.08 % and 0.075 % on the relative error for these experiments.

7.1.3 BQ model

BQ as the management device in between EH transducer and battery has three responsibilities including: MPPT, voltage matching and battery protection. Due to simplicity of the battery protection function, it does not require any specific modeling. However, MPPT mechanism and converter require separate models. The overall control system of the BQ follows a state machine shown in Fig. 7.4. Yet, according to PhyNode hardware specifications, BQ will be operating only in the Normal Operation (NO) state.

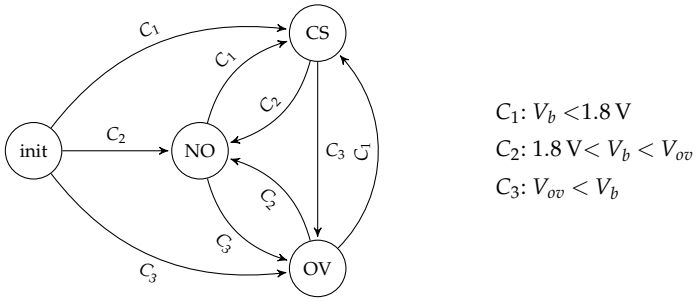

Fig. 7.4 A simplified state machine representing BQ's operational states.

For converter modeling in NO state its internal structure has been analyzed thoroughly showing a MPTC based on current with three levels at 50 mA, 100 mA and 230 mA. However, each cycle is made of pulses with only two of these peak currents which are selected according to (7.12).

$$I_{pl} = \max\{50, 100, 230\}[\text{mA}] \leq 2 \cdot \langle I_i \rangle \tag{7.12a}$$

$$I_{ph} = \min\{50, 100, 230\}[\text{mA}] \geq 2 \cdot \langle I_i \rangle \tag{7.12b}$$

Analyzing a large number of small-signal data collected at different operational conditions have shown that number of lower peak pulses is always equal to 3. In addition, based on analysis of switching mechanism a necessary condition as in (7.13) can be found for number of high peak pulses.

$$\mu_h \geq \left\lceil \frac{3 \cdot I_{pl} \cdot \left(2 \cdot \langle I_i \rangle - I_{pl}\right)}{I_{ph} \cdot \left(I_{ph} - 2 \cdot \langle I_i \rangle\right)} \right\rceil \tag{7.13}$$

Meanwhile, relation between idle phase duration ($\tau_{\varphi 3}$) and μ_h as in (7.14) in addition to physical conditions on these parameters helps to find a valid combination of them.

$$\begin{aligned} \tau_{\varphi 3} = & \frac{L \cdot \langle V_o \rangle}{\langle V_i \rangle \cdot (\langle V_o \rangle - \langle V_i \rangle)} \cdot \\ & \left[\mu_l \cdot I_{pl} \cdot \left(\frac{I_{pl}}{2 \cdot \langle I_i \rangle} - 1 \right) + \mu_h \cdot I_{ph} \cdot \left(\frac{I_{ph}}{2 \cdot \langle I_i \rangle} - 1 \right) \right] \end{aligned} \tag{7.14}$$

However, monitoring small-signals and their comparison with this deductive analysis shows that this is not always valid. It has two main reasons: on one hand, calculation of $\tau_{\varphi 3}$ is with ideal signals, ignoring all losses in the converter. This is mainly because this information is not available and has to be identified after explanation of switching mechanism. On the other hand, there are many abnormal signals available in small-signal data-set showing strange operational patterns of pulses. Although all these cases can be explained by analysis of small-signals, their reproduction will lead to a small-signal or Spice model which its usage is time and computational intensive. Consequently, a black-box approach is followed.

After definition of an experimental procedure, behavior of BQ at different operational conditions is measured, filtered and cleaned. Using these data, both converter and MPPT mechanisms of BQ are modeled.

For the modeling of BQ converter, different ANN structures have been checked and a network with two hidden layers is selected for the complete model which its signals are presented in Fig. 7.5.

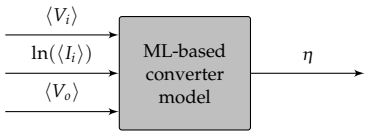

Fig. 7.5 Abstract representation of the ML-based model of the BQ converter.

Due to complexity of this model for implementation on PhyNode, it has been tried to replace the ANN-based model in Fig. 7.5 with a binary decision

tree. Although different form of them have shown promising performances on estimation of converter efficiency, a much simpler strategy is used for the on-board model of BQ converter. In this approach a single efficiency is selected by statistical analysis of data, showing 85.983 % as a good compromise for single efficiency value.

For the modeling of MPPT mechanism of BQ, a simple relation as in (7.15) is used because of FOCV principle implemented.

$$\langle V_i \rangle = \min\{0.8 \cdot V_{oc}, \langle V_o \rangle\} \tag{7.15}$$

Although simplicity of this model is perfect for implementation on PhyNode, its application on the data-set shows its shortcomings. Therefore, a more advanced form as in (7.16) is used for the system level model.

$$\langle V_i \rangle = \min\{0.8 \cdot V_{oc}, f(V_{oc}, \langle V_o \rangle, \ln(\langle I_i \rangle))\} \tag{7.16}$$

When the function f is made of ML-based model with either ANN or decision tree. Signals of these models are shown in Fig. 7.6.

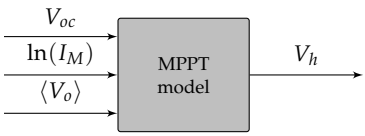

Fig. 7.6 Abstract representation of the BQ MPPT model in its full form.

For evaluation, both models are combined together to make the whole BQ model. To check this model on not trained situations, two new data-sets are measured with randomly selected operational conditions. First data-set is within the whole operational range of BQ, while conditions in the other data-set are limited to the PhyNode's operational range.

Combined on-board model show an RMSE of 10.40 % and 10.29 % subsequently for the whole range and PhyNode range. Best performing combined system level model is made by combination of both ANN models. It provides RMSE values of 4.628 % and 1.229 % subsequently on the whole and PhyNode ranges.

7.1.4 Holistic model

Finally, by combination of all system level models with a structure shown in Fig. 7.7, a holistic detailed model for the PhyNode's ESU is provided.

For the evaluation of this holistic model, a new environment is used to assure application validity of models in different conditions. After tuning PV EH model for the lighting in this new environment, PhyNode load is applied to the ESU and V_b is measured for three days. After subsequently repeating this experiment with four different combination of batteries and PV modules, worst case performance of the detailed holistic model has a MAPE of 0.938 %

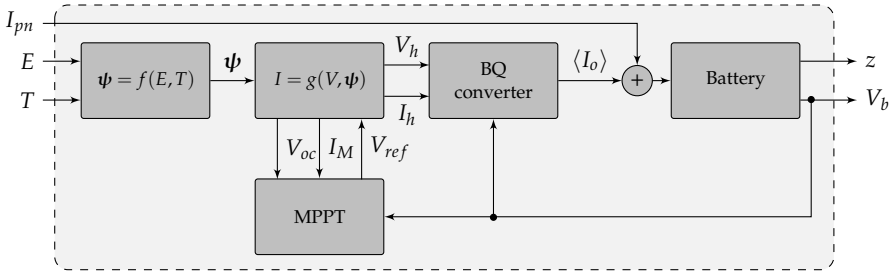

Fig. 7.7 The overall schematic of the holistic model for PhyNode's ESU.

on prediction of the battery terminal voltage. While this assures accurate model of the whole PhyNode ESU, it has been used for system dimensioning.

By use of real lighting, temperature and operational load profile for one complete day in CPPS platform, realistic performance of PhyNode is evaluated. For evaluation of energy balance, PCD and system imbalance factor are defined and used. By manipulation of lighting and operational conditions different fictive scenarios are simulated and compared. Furthermore, effect of changing the surface of PV module is formulated and integrated into the simulations of different conditions. Finally it has been shown that using these simulations in addition to balancing parameters, it is possible to dimension hardware and modify operation of PhyNode within a real materials handling application to operate it in an energy-neutral manner.

7.2 Contributions

In addition to solving the task of providing models for the PhyNode ESU, main contributions of this work can be listed as:

- Introducing Photovoltaic Normalized Space for analysis and parameterization of PV systems in indoor low light conditions.
- Use of a two-fold mechanism to estimate PV system parameters according to the environmental factors.
- Development of a setup for accurate measurement and analysis of PV modules in artificial low light conditions.
- Suggestion of an evaluation factor to quantify PV models performance regardless of their scale.
- Empirical formulation for estimation of PV module keypoints under different indoor lighting intensities and temperatures.
- Guidelines for computational process of extracting I-V curve parameters of a PV module.
- Formulating dependency of I-V curve parameters to the environmental parameters.
- A measurement setup for analysis and identification of batteries without using a cycler.

- Proving similar measured SoC-V_e relation for continuous and discrete discharge methods.
- Explaining relevance and scale of aging effect of low-budget batteries in ULP applications.
- Introducing a method for measurement of aging factor of batteries in ULP applications and its integration into the battery model.
- Introduction of battery normalized condition for calculation of SoC and current effects.
- Analysis of the aging factor on model's performance for low-budget batteries in ULP applications.
- Integration of a dynamic aging factor into the formulation of SoC for higher accuracy estimation in open loop battery models.
- Development of a partial deductive model for MPTC mechanism based on energy balance.
- Showing challenges on deductive modeling of ULP DC-DC converters operating in MPTC mode.

7.3 Future works

According to the limitations of this work there are different aspects which have not been addressed and can be topics for future research. Some of these topics are:

- Analysis of different IPV technologies and their behavior, based on the indoor environmental conditions.
- Trial for statistical analysis of number of parameters in a two diode model of PV systems.
- Advanced methods for inclusion of aging factor of low-budget batteries into the battery model.
- Analysis of aging factor in case of an energy neutral system which has no clear cycle.
- Inclusion of models for other operational states of the BQ device.
- Completion of analytical deductive model of the BQ converter by knowledge from the internal digital logic.

List of Publications

Parts of this work are published in the following data-set, technical reports, international conference and journal papers:

- M. Masoudinejad, "Data-sets for indoor photovoltaic behavior in low lighting conditions," *Data*, vol. 5, no. 2, p. 32, 2020, Number: 2 Publisher: Multidisciplinary Digital Publishing Institute. DOI: 10.3390/data5020032. [Online]. Available: https://www.mdpi.com/2306-5729/5/2/32
- M. Masoudinejad, *Data-sets for indoor photovoltaic behavior in low lighting condition*, type: dataset, Mar. 4, 2020. DOI: 10.5281/zenodo.3697105. [Online]. Available: https://zenodo.org/record/3697105
- M. Masoudinejad, M. Magno, L. Benini, and M. ten Hompel, "Average Modelling of State-of-the-Art Ultra-low Power Energy Harvesting Converter IC," in *2018 International Symposium on Power Electronics, Electrical Drives, Automation and Motion (SPEEDAM)*, 2018, pp. 99–104. DOI: 10.1109/SPEEDAM.2018.8445303
- M. Masoudinejad, *Large Signal Converter Data from Texas Instruments BQ25505*, 2018. DOI: 10.17877/fd72o6mn0g
- M. Masoudinejad, *Large Signal Converter Data from Texas Instruments BQ25570*, 2018. DOI: 10.17877/fd72wij6yo
- M. Masoudinejad, *Models and training datasets for texas instruments BQ25505 and BQ25570 ICs*, type: dataset, 2018. DOI: 10.17877/FE0O0YSXS0. [Online]. Available: https://bit.ly/2XSV4BI
- M. Masoudinejad, "Power analysis of PhyNode," TU Dortmund University, 2018
- M. Masoudinejad, A. K. Ramachandran Venkatapathy, D. Tondorf, D. Heinrich, R. Falkenberg, and M. Buschhoff, "Machine Learning Based Indoor Localisation Using Environmental Data in PhyNetLab Warehouse," in *European Conference on Smart Objects, Systems and Technologies (Smart SysTech)*, 2018, pp. 1–8
- R. Falkenberg, M. Masoudinejad, M. Buschhoff, A. K. Ramachandran Venkatapathy, D. Friesel, M. t. Hompel, O. Spinczyk, and C. Wietfeld, "PhyNetLab: An IoT-based warehouse testbed," in *Federated Conference on Computer Science and Information Systems (FedCSIS)*, 2017, pp. 1051–1055. DOI: 10.15439/2017F267
- M. Masoudinejad, "Automated Data Collection for Modelling Texas Instruments Ultra Low-Power Chargers," TU Dortmund, Dortmund, Technical Report, 2017
- M. Masoudinejad, "A Power Model for DC-DC Boost Converters Operating in PFM Mode," TU Dortmund University, Tech. Rep., 2017

- M. Masoudinejad, A. K. Ramachandran Venkatapathy, J. Emmerich, and A. Riesner, "Smart Sensing Devices for Logistics Application," in *Sensor Systems and Software*, M. Magno, F. Ferrero, and V. Bilas, Eds., vol. 205, Springer International Publishing, 2017, pp. 41–52, ISBN: 978-3-319-61562-2 978-3-319-61563-9. DOI: 10.1007/978-3-319-61563-9_4
- M. Masoudinejad, "Photovoltaic energy harvesting characteristics under ultra-low light," TU Dortmund University, Dortmund, 2016. [Online]. Available: https://bit.ly/2PFTkHC
- M. Masoudinejad, M. Kamat, J. Emmerich, M. ten Hompel, and S. Sardesai, "A gray box modeling of a photovoltaic cell under low illumination in materials handling application," in *3rd International Renewable and Sustainable Energy Conference (IRSEC)*, 2015, pp. 1–6. DOI: 10.1109/IRSEC.2015.7455081
- M. Masoudinejad, "A measurement platform for photovoltaic energy harvesting in indoor low light environment," TU Dortmund University, Dortmund, 2015
- M. Masoudinejad, J. Emmerich, D. Kossmann, A. Riesner, M. Roidl, and M. ten Hompel, "A measurement platform for photovoltaic performance analysis in environments with ultra-low energy harvesting potential," *Sustainable Cities and Society*, vol. 25, pp. 74–81, 2015, ISSN: 2210-6707. DOI: 10.1016/j.scs.2015.09.006
- M. Masoudinejad, J. Emmerich, D. Kossmann, A. Riesner, M. Roidl, and M. ten Hompel, "Development of a measurement platform for indoor photovoltaic energy harvesting in materials handling applications," in *6th International Renewable Energy Congress*, 2015, pp. 1–6, ISBN: 978-1-4799-7947-9. DOI: 10.1109/IREC.2015.7110938
- M. Roidl, J. Emmerich, A. Ramachandran Venkatapathy, A. Riesner, M. Masoudinejad, D. Kaulbars, C. Ide, C. Wietfeld, and M. ten Hompel, "Performance Availability Evaluation of Smart Devices in Materials Handling Systems," in *IEEE ICCC Workshops on Internet of Things*, 2014, pp. 6–10, ISBN: 978-1-4799-6707-0
- M. Roidl, J. Emmerich, M. Masoudinejad, A. Riesner, and M. T. Hompel, "Entwicklung eines Versuchsfelds für grosse Systeme intelligenter Behälter," *Logistics Journal*, vol. 2014, 2014, ISSN: 1860-7977. DOI: 10.2195/lj_Proc_roidl_de_201411_01
- M. Masoudinejad, "Open-loop dynamic modeling of low-budget batteries with low-power loads," Submitted to Batteries, Multidisciplinary Digital Publishing Institute. 2020.

References

[1] M. Masoudinejad, A. K. Ramachandran Venkatapathy, J. Emmerich, and A. Riesner, "Smart Sensing Devices for Logistics Application," in *Sensor Systems and Software*, M. Magno, F. Ferrero, and V. Bilas, Eds., vol. 205, Springer International Publishing, 2017, pp. 41–52, ISBN: 978-3-319-61562-2 978-3-319-61563-9. DOI: 10.1007/978-3-319-61563-9_4.

[2] O. Meyer-Rühle, S. Beige, A. Greinus, T. Erhardt, J. Bozuwa, J. Harmsen, R. Kok, C. Kille, N. Hua-Kellermann, M. Roth, R. Burg, and W. Röhling, "Statistical coverage and economic analysis of the logistics sector in the EU," SEALS Consortium, Basel Rotterdam Nürnberg Denzlingen, Tech. Rep., 2009.

[3] Ecorys, Fraunhofer, TCI, Prognos, and AUEB-RC/TRANSLOG, "Fact-finding studies in support of the development of an EU strategy for freight transport logistics; Lot 1: Analysis of the EU logistics sector," Ecorys, Fraunhofer, TCI, Prognos and AUEB-RC/TRANSLOG, Tech. Rep., 2015, p. 442.

[4] DVZ, *Statista: Marktvolumen des Logistikmarktes in Europa*, 2018.

[5] J. Macaulay, L. Buckalew, and G. Chung, "Internet of things in logistics," DHL Trend Research, Cisco Consulting Services, Troisdorf, Germany, Tech. Rep., 2015, p. 29.

[6] J. M. Müller, M. Erdel, and K.-I. Voigt, "Industry 4.0-Perspectives and challenges for project logistics," EurOMA Conference, Edinburgh, Scotland, 2017.

[7] H. Lasi, P. Fettke, H.-G. Kemper, T. Feld, and M. Hoffmann, "Industry 4.0," *Business & Information Systems Engineering*, vol. 6, no. 4, pp. 239–242, 2014, ISSN: 1867-0202. DOI: 10.1007/s12599-014-0334-4.

[8] P. Wang, R. Valerdi, S. Zhou, and L. Li, "Introduction: Advances in IoT research and applications," *Information Systems Frontiers*, vol. 17, no. 2, pp. 239–241, 2015, ISSN: 1572-9419. DOI: 10.1007/s10796-015-9549-2.

[9] J. Gubbi, R. Buyya, S. Marusic, and M. Palaniswami, "Internet of Things (IoT): A vision, architectural elements, and future directions," *Future Generation Computer Systems*, Including Special sections: Cyber-enabled Distributed Computing for Ubiquitous Cloud and Network Services & Cloud Computing and Scientific Applications Big Data, Scalable Analytics, and Beyond, vol. 29, no. 7, pp. 1645–1660, 2013, ISSN: 0167-739X. DOI: 10.1016/j.future.2013.01.010.

[10] A. Gluhak, S. Krco, M. Nati, D. Pfisterer, N. Mitton, and T. Razafindralambo, "A survey on facilities for experimental internet of things research," *IEEE Communications Magazine*, vol. 49, no. 11, pp. 58–67, 2011, ISSN: 0163-6804. DOI: 10.1109/MCOM.2011.6069710.

[11] D. Chen, J. Cong, S. Gurumani, W. m. Hwu, K. Rupnow, and Z. Zhang, "Platform choices and design demands for IoT platforms: Cost, power, and performance tradeoffs," *IET Cyber-Physical Systems: Theory Applications*, vol. 1, no. 1, pp. 70–77, 2016, ISSN: 2398-3396. DOI: 10.1049/iet-cps.2016.0020.

[12] A. Kamagaew, T. Kirks, and M. Ten Hompel, "Energy potential detection for autarkic Smart Object design in facility logistics," in *IEEE International Conference on Control System, Computing and Engineering, ICCSCE*, IEEE, 2011, pp. 285–290, ISBN: 978-1-4577-1642-3. DOI: 10.1109/ICCSCE.2011.6190538.

[13] E. A. Lee, "Cyber Physical Systems: Design Challenges," EECS Department, University of California, Berkeley, Tech. Rep. UCB/EECS-2008-8, 2008.

[14] N. Jazdi, "Cyber physical systems in the context of Industry 4.0," in *IEEE International Conference on Automation, Quality and Testing, Robotics*, 2014, pp. 1–4. DOI: 10.1109/AQTR.2014.6857843.

[15] J. Venkatesh, B. Aksanli, C. S. Chan, A. S. Akyürek, and T. S. Rosing, "Scalable-Application Design for the IoT," *IEEE Software*, vol. 34, no. 1, pp. 62–70, 2017, ISSN: 0740-7459. DOI: 10.1109/MS.2017.4.

[16] M. Brettel, N. Friederichsen, M. Keller, and M. Rosenberg, "How virtualization, decentralization and network building change the manufacturing landscape: An industry 4.0 perspective," *International Journal of Mechanical, Industrial Science and Engineering*, vol. 8, no. 1, pp. 37–44, 2014.

[17] M. Masoudinejad, J. Emmerich, D. Kossmann, A. Riesner, M. Roidl, and M. ten Hompel, "A measurement platform for photovoltaic performance analysis in environments with ultra-low energy harvesting potential," *Sustainable Cities and Society*, vol. 25, pp. 74–81, 2015, ISSN: 2210-6707. DOI: 10.1016/j.scs.2015.09.006.

[18] M. Roidl, J. Emmerich, A. Ramachandran Venkatapathy, A. Riesner, M. Masoudinejad, D. Kaulbars, C. Ide, C. Wietfeld, and M. ten Hompel, "Performance Availability Evaluation of Smart Devices in Materials Handling Systems," in *IEEE ICCC Workshops on Internet of Things*, 2014, pp. 6–10, ISBN: 978-1-4799-6707-0.

[19] M. Lewandowski, M. Gath, D. Werthmann, and M. Lawo, "Agent-based Control for Material Handling Systems in In-House Logistics - Towards Cyber-Physical Systems in In-House-Logistics Utilizing Real Size," in *European Conference on Smart Objects, Systems and Technologies (SmartSysTech)*, 2013, pp. 1–5.

[20] M. Masoudinejad, M. Kamat, J. Emmerich, M. ten Hompel, and S. Sardesai, "A gray box modeling of a photovoltaic cell under low illumination in materials handling application," in *3rd International*

Renewable and Sustainable Energy Conference (IRSEC), 2015, pp. 1–6. DOI: 10.1109/IRSEC.2015.7455081.

[21] J. S. Emmerich, M. Roidl, T. Bich, and M. ten Hompel, "Entwicklung von energieautarken, intelligenten ladehilfsmitteln am beispiel des inbin," *Logistics Journal*, vol. 2012, pp. 1–7, 2012, ISSN: 1860-7977. DOI: 10.2195/lj_Proc_emmerich_de_201210_01.

[22] A. K. Ramachandran Venkatapathy, A. Riesner, M. Roidl, J. Emmerich, and M. ten Hompel, "PhyNode : An intelligent, cyber-physical system with energy neutral operation for PhyNetLab," in *European Conference on Smart Objects, Systems and Technologies (Smart SysTech)*, VDE-Verl, 2015, pp. 1–8, ISBN: 978-3-8007-3996-7.

[23] A. K. Ramachandran Venkatapathy, M. Roidl, A. Riesner, J. Emmerich, and M. ten Hompel, "PhyNetLab: Architecture design of ultra-low power Wireless Sensor Network testbed," in *IEEE 16th International Symposium on A World of Wireless, Mobile and Multimedia Networks*, IEEE, 2015, pp. 1–6, ISBN: 978-1-4799-8461-9. DOI: 10.1109/WoWMoM.2015.7158206.

[24] R. Falkenberg, M. Masoudinejad, M. Buschhoff, A. K. Ramachandran Venkatapathy, D. Friesel, M. t. Hompel, O. Spinczyk, and C. Wietfeld, "PhyNetLab: An IoT-based warehouse testbed," in *Federated Conference on Computer Science and Information Systems (FedCSIS)*, 2017, pp. 1051–1055. DOI: 10.15439/2017F267.

[25] S. Beeby and N. White, *Energy Harvesting for Autonomous Systems*. Artech House, 2010, ISBN: 978-1-59693-719-2.

[26] H. G. Lee and N. Chang, "Powering the IoT: Storage-less and converter-less energy harvesting," in *The 20th Asia and South Pacific Design Automation Conference*, 2015, pp. 124–129. DOI: 10.1109/ASPDAC.2015.7058992.

[27] L. Ljung and T. Glad, *Modeling of Dynamic Systems*, 1st. Englewood Cliffs, N.J: Prentice Hall, 1994, ISBN: 978-0-13-597097-3.

[28] F. E. Cellier and J. Greifeneder, *Continuous System Modeling*. Springer Science & Business Media, 1991, ISBN: 978-1-4757-3922-0.

[29] C. L. Phillips, J. M. Parr, and E. A. Riskin, *Signals, Systems, and Transforms*. Prentice Hall, 2008, ISBN: 978-0-13-198923-8.

[30] P. P. J. v. d. Bosch and A. C. v. d. Klauw, *Modeling, Identification and Simulation of Dynamical Systems*, 1st. Boca Raton: CRC Press, 1994, ISBN: 978-0-8493-9181-1.

[31] P. Fritzson, *Introduction to Modeling and Simulation of Technical and Physical Systems with Modelica*. John Wiley & Sons, 2011, ISBN: 978-1-118-09424-2.

[32] C. A. Smith and S. W. Campbell, *A First Course in Differential Equations, Modeling, and Simulation*, 1st. CRC Press, 2011, ISBN: 13: 978-1-4398-5088-6.

[33] B. Girod, R. Rabenstein, and A. Stenger, *Signals and systems*. Wiley, 2001, ISBN: 978-0-471-98800-7.

[34] G. A. Bekey and B. J. Kogan, *Modeling and Simulation: Theory and Practice*. Springer Science & Business Media, 2012, ISBN: 978-1-4615-0235-7.

[35] A. V. Oppenheim, A. S. Willsky, and w. S. Hamid, *Signals and Systems*, 2nd edition. New Delhi: Pearson, 1997, ISBN: 978-81-7758-262-8.

[36] A. Castagnetti, A. Pegatoquet, C. Belleudy, and M. Auguin, "A framework for modeling and simulating energy harvesting WSN nodes with efficient power management policies," *EURASIP Journal on Embedded Systems*, vol. 2012, no. 1, p. 8, 2012, ISSN: 1687-3963. DOI: 10.1186/1687-3963-2012-8.

[37] P. Trebuna, A. Petriková, and M. Pekaríková, "Influence of physical factors of working environment on worker's performance from ergonomic point of view," *Acta Simulatio*, vol. 3, no. 3, pp. 1–9, 2017.

[38] A. E. F. Taylor, *Illumination Fundamentals*. NY, USA: Rensselaer Polytechnic Institute, 2000.

[39] A. Luque and S. Hegedus, *Handbook of Photovoltaic Science and Engineering*. John Wiley & Sons, 2011, ISBN: 978-0-470-97612-8.

[40] J. Randall, *Designing Indoor Solar Products*. John Wiley & Sons, 2006, ISBN: 978-0-470-01714-2.

[41] S. R. Wenham, *Applied Photovoltaics*. Routledge, 2012, ISBN: 978-1-84971-141-8.

[42] M. G. Villalva, J. R. Gazoli, and E. R. Filho, "Comprehensive approach to modeling and simulation of photovoltaic arrays," *IEEE Transactions on Power Electronics*, vol. 24, no. 5, pp. 1198–1208, 2009, ISSN: 0885-8993. DOI: 10.1109/TPEL.2009.2013862.

[43] S. Sengar, "Maximum Power Point Tracking Algorithms for Photovoltaic System: A Review," *International Review of Applied Engineering Research*, vol. 4, no. 2, pp. 2248–9967, 2014.

[44] V. Salas, E. Olias, A. Barrado, and A. Lazaro, "Review of the maximum power point tracking algorithms for stand-alone photovoltaic systems," *Solar Energy Materials and Solar Cells*, vol. 90, no. 11, pp. 1555–1578, 2006, ISSN: 0927-0248. DOI: 10.1016/j.solmat.2005.10.023.

[45] A. N. A. Ali, M. H. Saied, M. Z. Mostafa, and T. M. Abdel- Moneim, "A survey of maximum PPT techniques of PV systems," in *IEEE Energytech*, IEEE, 2012, pp. 1–17, ISBN: 978-1-4673-1836-5. DOI: 10.1109/EnergyTech.2012.6304652.

[46] H. J. El-Khozondar, R. J. El-Khozondar, K. Matter, and T. Suntio, "A review study of photovoltaic array maximum power tracking algorithms," *Renewables: Wind, Water, and Solar*, vol. 3, no. 1, pp. 1–8, 2016, ISSN: 2198-994X. DOI: 10.1186/s40807-016-0022-8.

[47] A. Gupta, Y. K. Chauhan, and R. K. Pachauri, "A comparative investigation of maximum power point tracking methods for solar PV system,"

Solar Energy, vol. 136, pp. 236–253, 2016, ISSN: 0038-092X. DOI: 10.1016/j.solener.2016.07.001.

[48] B. Subudhi and R. Pradhan, "A Comparative Study on Maximum Power Point Tracking Techniques for Photovoltaic Power Systems," *IEEE Transactions on Sustainable Energy*, vol. 4, no. 1, pp. 89–98, 2013, ISSN: 1949-3029. DOI: 10.1109/TSTE.2012.2202294.

[49] N. A. Kamarzaman and C. W. Tan, "A comprehensive review of maximum power point tracking algorithms for photovoltaic systems," *Renewable and Sustainable Energy Reviews*, vol. 37, pp. 585–598, 2014, ISSN: 1364-0321. DOI: 10.1016/j.rser.2014.05.045.

[50] B. Bendib, H. Belmili, and F. Krim, "A survey of the most used MPPT methods: Conventional and advanced algorithms applied for photovoltaic systems," *Renewable and Sustainable Energy Reviews*, vol. 45, pp. 637–648, 2015, ISSN: 1364-0321. DOI: 10.1016/j.rser.2015.02.009.

[51] T. T. N. Khatib, A. Mohamed, and N. Amim, "An Improved Indirect Maximum Power Point Tracking Method for Standalone Photovoltaic Systems," in *9th International Conference on Applications of Electrical Engineering*, 2010, pp. 56–62, ISBN: 978-960-474-171-7.

[52] H. E.-S. A. Ibrahim, F. F. Houssiny, H. M. Zein El-Din, and M. A. El-Shibini, "Microcomputer controlled buck regulator for maximum power point tracker for dc pumping system operates from photovoltaic system," in *IEEE International Conference on Fuzzy Systems*, vol. 1, IEEE, 1999, pp. I–406 – I–411, ISBN: 0-7803-5406-0. DOI: 10.1109/FUZZY.1999.793274.

[53] N. Javanmard, G. Vafadar, and A. Nasiri, "Indoor power harvesting using photovoltaic cells for low power applications," in *2009 13th European Conference on Power Electronics and Applications*, 2009, pp. 1–10.

[54] C. Alippi and C. Galperti, "An adaptive system for opimal solar energy harvesting in wireless sensor network nodes," *IEEE Transactions on Circuits and Systems I: Regular Papers*, vol. 55, no. 6, pp. 1742–1750, 2008, ISSN: 1549-8328. DOI: 10.1109/TCSI.2008.922023.

[55] S. Messalti, A. G. Harrag, and A. E. Loukriz, "A new neural networks MPPT controller for PV systems," in *The 6th International Renewable Energy Congress*, IEEE, 2015, pp. 1–6, ISBN: 978-1-4799-7947-9. DOI: 10.1109/IREC.2015.7110907.

[56] J. Binfet and B. Wilamowski, "Microprocessor implementation of fuzzy systems and neural networks," in *International Joint Conference on Neural Networks Proceedings*, vol. 1, IEEE, 2001, pp. 234–239, ISBN: 0-7803-7044-9. DOI: 10.1109/IJCNN.2001.939023.

[57] S. Daraban, D. Petreus, and C. Morel, "A novel global MPPT based on genetic algorithms for photovoltaic systems under the influence of partial shading," in *Proceedings Industrial Electronics Conference*, IEEE,

2013, pp. 1490–1495, ISBN: 978-1-4799-0224-8. DOI: 10.1109/IECON.2013.6699353.

[58] M. Adly and A. H. Besheer, "An optimized fuzzy maximum power point tracker for stand alone photovoltaic systems: Ant colony approach," in *7th IEEE Conference on Industrial Electronics and Applications*, IEEE, 2012, pp. 113–119, ISBN: 978-1-4577-2117-5. DOI: 10.1109/ICIEA.2012.6360707.

[59] K. Sundareswaran, P. Sankar, P. S. R. Nayak, S. P. Simon, and S. Palani, "Enhanced energy output from a PV system under partial shaded conditions through artificial bee colony," *IEEE Transactions on Sustainable Energy*, vol. 6, no. 1, pp. 198–209, 2015, ISSN: 1949-3029. DOI: 10.1109/TSTE.2014.2363521.

[60] A. S. Weddell, G. V. Merrett, and B. M. Al-Hashimi, "Photovoltaic sample-and-hold circuit enabling MPPT indoors for low-power systems," *IEEE Transactions on Circuits and Systems I: Regular Papers*, vol. 59, no. 6, pp. 1196–1204, 2012, ISSN: 1549-8328. DOI: 10.1109/TCSI.2011.2173393.

[61] A. M. AbdelAty, A. G. Radwan, A. Elwakil, and C. Psychalinos, "A fractional-order dynamic PV model," in *39th International Conference on Telecommunications and Signal Processing (TSP)*, 2016, pp. 607–610. DOI: 10.1109/TSP.2016.7760953.

[62] M. C. D. Piazza, M. Luna, and G. Vitale, "Dynamic PV Model Parameter Identification by Least-Squares Regression," *IEEE Journal of Photovoltaics*, vol. 3, no. 2, pp. 799–806, 2013, ISSN: 2156-3381. DOI: 10.1109/JPHOTOV.2012.2236146.

[63] M. C. D. Piazza and G. Vitale, *Photovoltaic Sources: Modeling and Emulation*. Springer Science & Business Media, 2012, ISBN: 978-1-4471-4378-9.

[64] K. A. Kim, C. Xu, L. Jin, and P. T. Krein, "A Dynamic Photovoltaic Model Incorporating Capacitive and Reverse-Bias Characteristics," *IEEE Journal of Photovoltaics*, vol. 3, no. 4, pp. 1334–1341, 2013, ISSN: 2156-3381. DOI: 10.1109/JPHOTOV.2013.2276483.

[65] S. Vinco, L. Bottaccioli, E. Patti, A. Acquaviva, and M. Poncino, "A Compact PV Panel Model for Cyber-Physical Systems in Smart Cities," in *IEEE International Symposium on Circuits and Systems (ISCAS)*, 2018, pp. 1–5. DOI: 10.1109/ISCAS.2018.8351764.

[66] M. Adel Hamdy, "A new model for the current-voltage output characteristics of photovoltaic modules," *Journal of Power Sources*, vol. 50, no. 1, pp. 11–20, 1994, ISSN: 0378-7753. DOI: 10.1016/0378-7753(93)01880-Q.

[67] G. Bhuvaneswari and R. Annamalai, "Development of a solar cell model in MATLAB for PV based generation system," in *Annual IEEE India Conference*, 2011, pp. 1–5. DOI: 10.1109/INDCON.2011.6139509.

[68] R. N. Hall, "Electron-Hole Recombination in Germanium," *Physical Review*, vol. 87, no. 2, pp. 387–387, 1952. DOI: 10.1103/PhysRev.87.387.

[69] W. Shockley and W. T. Read, "Statistics of the Recombinations of Holes and Electrons," *Physical Review*, vol. 87, no. 5, pp. 835–842, 1952. DOI: 10.1103/PhysRev.87.835.

[70] M. A. Green, *Solar cells: operating principles, technology, and system applications*. Prentice-Hall, 1982, ISBN: 978-0-13-822270-3.

[71] L. M. Fraas and L. D. Partain, *Solar Cells and Their Applications*. John Wiley & Sons, 2010, ISBN: 978-1-118-02405-8.

[72] A. Kassis and M. Saad, "Analysis of multi-crystalline silicon solar cells at low illumination levels using a modified two-diode model," *Solar Energy Materials and Solar Cells*, vol. 94, no. 12, pp. 2108–2112, 2010, ISSN: 0927-0248. DOI: 10.1016/j.solmat.2010.06.036.

[73] D. S. H. Chan and J. C. H. Phang, "Analytical Methods for the Extraction of Solar-Cell Single-and Double-Diode Model Parameters from I-V Characteristics," *IEEE Transactions on Electron Devices*, vol. 34, no. 2, pp. 286–293, 1987, ISSN: 1557-9646. DOI: 10.1109/T-ED.1987.22920.

[74] M. Wolf, G. T. Noel, and R. J. Stirn, "Investigation of the double exponential in the current-Voltage characteristics of silicon solar cells," *IEEE Transactions on Electron Devices*, vol. 24, no. 4, pp. 419–428, 1977, ISSN: 0018-9383. DOI: 10.1109/T-ED.1977.18750.

[75] A. D. Dhass, E. Natarajan, and L. Ponnusamy, "Influence of shunt resistance on the performance of solar photovoltaic cell," in *International Conference on Emerging Trends in Electrical Engineering and Energy Management (ICETEEEM)*, 2012, pp. 382–386. DOI: 10.1109/ICETEEEM.2012.6494522.

[76] V. Khanna, B. K. Das, D. Bisht, Vandana, and P. K. Singh, "A three diode model for industrial solar cells and estimation of solar cell parameters using PSO algorithm," *Renewable Energy*, vol. 78, pp. 105–113, 2015, ISSN: 1879-0682. DOI: 10.1016/j.renene.2014.12.072.

[77] D. Allam, D. A. Yousri, and M. B. Eteiba, "Parameters extraction of the three diode model for the multi-crystalline solar cell/module using Moth-Flame Optimization Algorithm," *Energy Conversion and Management*, vol. 123, pp. 535–548, 2016, ISSN: 0196-8904. DOI: 10.1016/j.enconman.2016.06.052.

[78] A. Sabadus, V. Mihailetchi, and M. Paulescu, "Parameters extraction for the one-diode model of a solar cell," *AIP Conference Proceedings*, vol. 1916, no. 1, p. 040 005, 2017, ISSN: 0094-243X. DOI: 10.1063/1.5017444.

[79] M. Jazayeri, S. Uysal, and K. Jazayeri, "A simple MATLAB/Simulink simulation for PV modules based on one-diode model," in *High Capacity*

Optical Networks and Emerging/Enabling Technologies, 2013, pp. 44–50. DOI: 10.1109/HONET.2013.6729755.

[80] M. V. Paukshto and K. Lovetskiy, "Invariance of single diode equation and its application," in *33rd IEEE Photovoltaic Specialists Conference*, 2008, pp. 1–4. DOI: 10.1109/PVSC.2008.4922501.

[81] W. Xiao, W. G. Dunford, and A. Capel, "A novel modeling method for photovoltaic cells," in *IEEE 35th Annual Power Electronics Specialists Conference*, vol. 3, 2004, pp. 1950–1956. DOI: 10.1109/PESC.2004.1355416.

[82] N. N. B. Ulapane, C. H. Dhanapala, S. M. Wickramasinghe, S. G. Abeyratne, N. Rathnayake, and P. J. Binduhewa, "Extraction of parameters for simulating photovoltaic panels," in *6th International Conference on Industrial and Information Systems*, IEEE, 2011, pp. 539–544, ISBN: 978-1-4577-0035-4. DOI: 10.1109/ICIINFS.2011.6038128.

[83] R. Chenni, M. Makhlouf, T. Kerbache, and A. Bouzid, "A detailed modeling method for photovoltaic cells," *Energy*, vol. 32, no. 9, pp. 1724–1730, 2007, ISSN: 0360-5442. DOI: 10.1016/j.energy.2006.12.006.

[84] A. N. Celik and N. Acikgoz, "Modelling and experimental verification of the operating current of mono-crystalline photovoltaic modules using four- and five-parameter models," *Applied Energy*, vol. 84, no. 1, pp. 1–15, 2007, ISSN: 0306-2619. DOI: 10.1016/j.apenergy.2006.04.007.

[85] W. De Soto, "Improvement and Validation of a Model for Photovoltaic Array Performance," M.S. thesis, University of Wisconsin-Madison, 2004.

[86] G. R. Walker, "Evaluating MPPT converter topologies using a MATLAB PV model," in *AUPEC 2000 : Innovation for Secure Power*, A. Krivda, Ed., vol. 1, Brisbane, Australia: Queensland University of Technology, 2000, pp. 138–143, ISBN: 978-1-86435-496-6.

[87] A. Bellini, S. Bifaretti, V. Iacovone, and C. Cornaro, "Simplified model of a photovoltaic module," in *2009 Applied Electronics*, 2009, pp. 47–51.

[88] K. Ding, X. Bian, H. Liu, and T. Peng, "A MATLAB-Simulink-Based PV Module Model and Its Application Under Conditions of Nonuniform Irradiance," *IEEE Transactions on Energy Conversion*, vol. 27, no. 4, pp. 864–872, 2012, ISSN: 0885-8969. DOI: 10.1109/TEC.2012.2216529.

[89] A. Hadj Arab, F. Chenlo, and M. Benghanem, "Loss-of-load probability of photovoltaic water pumping systems," *Solar Energy*, vol. 76, no. 6, pp. 713–723, 2004, ISSN: 0038-092X. DOI: 10.1016/j.solener.2004.01.006.

[90] M. A. de Blas, J. L. Torres, E. Prieto, and A. Garca, "Selecting a suitable model for characterizing photovoltaic devices," *Renewable Energy*, vol. 25, no. 3, pp. 371–380, 2002, ISSN: 0960-1481. DOI: 10.1016/S0960-1481(01)00056-8.

[91] W. De Soto, S. A. Klein, and W. A. Beckman, "Improvement and validation of a model for photovoltaic array performance," *Solar Energy*, vol. 80, no. 1, pp. 78–88, 2006, ISSN: 0038-092X. DOI: 10.1016/j.solener.2005.06.010.

[92] D. Sera, R. Teodorescu, and P. Rodriguez, "PV panel model based on datasheet values," in *IEEE International Symposium on Industrial Electronics*, 2007, pp. 2392–2396. DOI: 10.1109/ISIE.2007.4374981.

[93] S. Lineykin, M. Averbukh, and A. Kuperman, "An improved approach to extract the single-diode equivalent circuit parameters of a photovoltaic cell/panel," *Renewable and Sustainable Energy Reviews*, vol. 30, pp. 282–289, 2014, ISSN: 1364-0321. DOI: 10.1016/j.rser.2013.10.015.

[94] F. M. González-Longatt, "Model of photovoltaic module in Matlab," *Ii Cibelec*, vol. 2005, pp. 1–5, 2005.

[95] A. H. ALQahtani, "A simplified and accurate photovoltaic module parameters extraction approach using matlab," in *IEEE International Symposium on Industrial Electronics*, 2012, pp. 1748–1753. DOI: 10.1109/ISIE.2012.6237355.

[96] Q. Kou, S. A. Klein, and W. A. Beckman, "A method for estimating the long-term performance of direct-coupled PV pumping systems," *Solar Energy*, vol. 64, no. 1, pp. 33–40, 1998, ISSN: 0038-092X. DOI: 10.1016/S0038-092X(98)00049-8.

[97] M. T. Boyd, S. A. Klein, D. T. Reindl, and B. P. Dougherty, "Evaluation and Validation of Equivalent Circuit Photovoltaic Solar Cell Performance Models," *Journal of Solar Energy Engineering*, vol. 133, no. 2, pp. 021005–021005–13, 2011, ISSN: 0199-6231. DOI: 10.1115/1.4003584.

[98] V. Lo Brano, A. Orioli, and G. Ciulla, "On the experimental validation of an improved five-parameter model for silicon photovoltaic modules," *Solar Energy Materials and Solar Cells*, vol. 105, pp. 27–39, 2012, ISSN: 0927-0248. DOI: 10.1016/j.solmat.2012.05.028.

[99] A. Orioli and A. Di Gangi, "A procedure to calculate the five-parameter model of crystalline silicon photovoltaic modules on the basis of the tabular performance data," *Applied Energy*, Special Issue on Advances in sustainable biofuel production and use - XIX International Symposium on Alcohol Fuels - ISAF, vol. 102, pp. 1160–1177, 2013, ISSN: 0306-2619. DOI: 10.1016/j.apenergy.2012.06.036.

[100] Y. A. Mahmoud, W. Xiao, and H. H. Zeineldin, "A Parameterization Approach for Enhancing PV Model Accuracy," *IEEE Transactions on Industrial Electronics*, vol. 60, no. 12, pp. 5708–5716, 2013, ISSN: 0278-0046. DOI: 10.1109/TIE.2012.2230606.

[101] A. Chouder, S. Silvestre, N. Sadaoui, and L. Rahmani, "Modeling and simulation of a grid connected PV system based on the evaluation of

main PV module parameters," *Simulation Modelling Practice and Theory*, vol. 20, no. 1, pp. 46–58, 2012, ISSN: 1569-190X. DOI: 10.1016/j.simpat.2011.08.011.

[102] F. Adamo, F. Attivissimo, A. Di Nisio, A. M. L. Lanzolla, and M. Spadavecchia, "Parameters estimation for a model of photovoltaic panels," in *XIX IMEKO World Congress Fundamental Applied Metrology, Lisbon, Portugal, September*, 2009, pp. 6–11.

[103] M. U. Siddiqui, A. F. M. Arif, A. M. Bilton, S. Dubowsky, and M. Elshafei, "An improved electric circuit model for photovoltaic modules based on sensitivity analysis," *Solar Energy*, vol. 90, pp. 29–42, 2013, ISSN: 0038-092X. DOI: 10.1016/j.solener.2012.12.021.

[104] L. Peng, Y. Sun, and Z. Meng, "An improved model and parameters extraction for photovoltaic cells using only three state points at standard test condition," *Journal of Power Sources*, vol. 248, pp. 621–631, 2014, ISSN: 0378-7753. DOI: 10.1016/j.jpowsour.2013.07.058.

[105] M. Sheraz Khalid and M. A. Abido, "A novel and accurate photovoltaic simulator based on seven-parameter model," *Electric Power Systems Research*, vol. 116, pp. 243–251, 2014, ISSN: 0378-7796. DOI: 10.1016/j.epsr.2014.06.010.

[106] J. Appelbaum and A. Peled, "Parameters extraction of solar cells A comparative examination of three methods," *Solar Energy Materials and Solar Cells*, vol. 122, pp. 164–173, 2014, ISSN: 0927-0248. DOI: 10.1016/j.solmat.2013.11.011.

[107] L. Wu, Z. Chen, C. Long, S. Cheng, P. Lin, Y. Chen, and H. Chen, "Parameter extraction of photovoltaic models from measured I-V characteristics curves using a hybrid trust-region reflective algorithm," *Applied Energy*, vol. 232, pp. 36–53, 2018, ISSN: 0306-2619. DOI: 10.1016/j.apenergy.2018.09.161.

[108] J. Gow and C. Manning, "Development of a photovoltaic array model for use in power-electronics simulation studies," *IEE Proceedings - Electric Power Applications*, vol. 146, no. 2, pp. 193–200, 1999, ISSN: 1350-2352. DOI: 10.1049/ip-epa:19990116.

[109] M. A. Cappelletti, G. A. Casas, A. P. Cédola, E. L. Peltzer y Blancá, and B. Marí Soucase, "Study of the reverse saturation current and series resistance of p-p-n perovskite solar cells using the single and double-diode models," *Superlattices and Microstructures*, vol. 123, pp. 338–348, 2018, ISSN: 0749-6036. DOI: 10.1016/j.spmi.2018.09.023.

[110] K.-i. Kurobe and H. Matsunami, "New Two-Diode Model for Detailed Analysis of Multicrystalline Silicon Solar Cells," *Japanese Journal of Applied Physics*, vol. 44, no. 12R, p. 8314, 2005, ISSN: 1347-4065. DOI: 10.1143/JJAP.44.8314.

[111] T. Sudhakar Babu, J. Prasanth Ram, K. Sangeetha, A. Laudani, and N. Rajasekar, "Parameter extraction of two diode solar PV model using

Fireworks algorithm," *Solar Energy*, vol. 140, pp. 265–276, 2016, ISSN: 0038-092X. DOI: 10.1016/j.solener.2016.10.044.

[112] M. Hejri, H. Mokhtari, M. R. Azizian, M. Ghandhari, and L. Söder, "On the Parameter Extraction of a Five-Parameter Double-Diode Model of Photovoltaic Cells and Modules," *IEEE Journal of Photovoltaics*, vol. 4, no. 3, pp. 915–923, 2014, ISSN: 2156-3381. DOI: 10.1109/JPHOTOV.2014.2307161.

[113] R. Abbassi, A. Abbassi, A. A. Heidari, and S. Mirjalili, "An efficient salp swarm-inspired algorithm for parameters identification of photovoltaic cell models," *Energy Conversion and Management*, vol. 179, pp. 362–372, 2019, ISSN: 0196-8904. DOI: 10.1016/j.enconman.2018.10.069.

[114] K. Nishioka, N. Sakitani, Y. Uraoka, and T. Fuyuki, "Analysis of multicrystalline silicon solar cells by modified 3-diode equivalent circuit model taking leakage current through periphery into consideration," *Solar Energy Materials and Solar Cells*, vol. 91, no. 13, pp. 1222–1227, 2007, ISSN: 0927-0248. DOI: 10.1016/j.solmat.2007.04.009.

[115] R. C. Campbell, "A Circuit-based Photovoltaic Array Model for Power System Studies," in *39th North American Power Symposium*, 2007, pp. 97–101. DOI: 10.1109/NAPS.2007.4402293.

[116] H. Tian, F. Mancilla, and E. Muljadi, "A detailed performance model for photovoltaic systems," *National Renewable Energy Laboratory, USA NREL/JA-5500-54601*, 2012.

[117] N. Femia, G. Petrone, G. Spagnuolo, and M. Vitelli, *Power Electronics and Control Techniques for Maximum Energy Harvesting in Photovoltaic Systems*. CRC Press, 2012, ISBN: 978-1-4665-0690-9.

[118] A. Jain and A. Kapoor, "Exact analytical solutions of the parameters of real solar cells using Lambert W-function," *Solar Energy Materials and Solar Cells*, vol. 81, no. 2, pp. 269–277, 2004, ISSN: 0927-0248. DOI: 10.1016/j.solmat.2003.11.018.

[119] V. J. Chin, Z. Salam, and K. Ishaque, "Cell modelling and model parameters estimation techniques for photovoltaic simulator application: A review," *Applied Energy*, vol. 154, pp. 500–519, 2015, ISSN: 0306-2619. DOI: 10.1016/j.apenergy.2015.05.035.

[120] A. M. Humada, M. Hojabri, S. Mekhilef, and H. M. Hamada, "Solar cell parameters extraction based on single and double-diode models: A review," *Renewable and Sustainable Energy Reviews*, vol. 56, pp. 494–509, 2016, ISSN: 1364-0321. DOI: 10.1016/j.rser.2015.11.051.

[121] A. R. Jordehi, "Parameter estimation of solar photovoltaic (PV) cells: A review," *Renewable and Sustainable Energy Reviews*, vol. 61, pp. 354–371, 2016, ISSN: 1364-0321. DOI: 10.1016/j.rser.2016.03.049.

[122] R. Tamrakar and A. Gupta, "A Review : Extraction of solar cell modelling parameters," 2015.

[123] F. Dkhichi, B. Oukarfi, A. Fakkar, and N. Belbounaguia, "Parameter identification of solar cell model using LevenbergMarquardt algorithm combined with simulated annealing," *Solar Energy*, vol. 110, pp. 781–788, 2014, ISSN: 0038-092X. DOI: 10.1016/j.solener.2014.09.033.

[124] N. Moldovan, R. Picos, and E. Garcia-Moreno, "Parameter Extraction of a Solar Cell Compact Model usign Genetic Algorithms," in *Spanish Conference on Electron Devices*, 2009, pp. 379–382. DOI: 10.1109/SCED.2009.4800512.

[125] A. Harrag and S. Messalti, "Extraction of solar cell parameters using genetic algorithm," in *4th International Conference on Electrical Engineering (ICEE)*, 2015, pp. 1–5. DOI: 10.1109/INTEE.2015.7416775.

[126] X. Lingyun, S. Lefei, H. Wei, and J. Cong, "Solar Cells Parameter Extraction Using a Hybrid Genetic Algorithm," in *Third International Conference on Measuring Technology and Mechatronics Automation*, vol. 3, 2011, pp. 306–309. DOI: 10.1109/ICMTMA.2011.647.

[127] D. Oliva, E. Cuevas, and G. Pajares, "Parameter identification of solar cells using artificial bee colony optimization," *Energy*, vol. 72, pp. 93–102, 2014, ISSN: 0360-5442. DOI: 10.1016/j.energy.2014.05.011.

[128] L. Guo, Z. Meng, Y. Sun, and L. Wang, "Parameter identification and sensitivity analysis of solar cell models with cat swarm optimization algorithm," *Energy Conversion and Management*, vol. 108, pp. 520–528, 2016, ISSN: 0196-8904. DOI: 10.1016/j.enconman.2015.11.041.

[129] M. A. Mughal, Q. Ma, and C. Xiao, "Photovoltaic Cell Parameter Estimation Using Hybrid Particle Swarm Optimization and Simulated Annealing," *Energies*, vol. 10, no. 8, p. 1213, 2017, ISSN: 1996-1073. DOI: 10.3390/en10081213.

[130] K. L. Kennerud, "Analysis of Performance Degradation in CdS Solar Cells," *IEEE Transactions on Aerospace and Electronic Systems*, vol. AES-5, no. 6, pp. 912–917, 1969, ISSN: 0018-9251. DOI: 10.1109/TAES.1969.309966.

[131] Q. Jia, W. A. Anderson, E. Liu, and S. Zhang, "A novel approach for evaluating the series resistance of solar cells," *Solar Cells*, vol. 25, no. 3, pp. 311–318, 1988, ISSN: 0379-6787. DOI: 10.1016/0379-6787(88)90069-5.

[132] W. Zhou, H. Yang, and Z. Fang, "A novel model for photovoltaic array performance prediction," *Applied Energy*, vol. 84, no. 12, pp. 1187–1198, 2007, ISSN: 0306-2619. DOI: 10.1016/j.apenergy.2007.04.006.

[133] J. Quanxi and L. Enke, "A method for the direct measurement of the solar cell junction ideality factor," *Solar Cells*, vol. 22, no. 1, pp. 15–21, 1987, ISSN: 0379-6787. DOI: 10.1016/0379-6787(87)90066-4.

[134] H. Yu, Q. Yue, J. Zhou, and W. Wang, "A Hybrid Indoor Ambient Light and Vibration Energy Harvester for Wireless Sensor Nodes," *Sensors*, vol. 14, no. 5, pp. 8740–8755, 2014. DOI: 10.3390/s140508740.

[135] E. Saloux, A. Teyssedou, and M. Sorin, "Explicit model of photovoltaic panels to determine voltages and currents at the maximum power point," *Solar Energy*, vol. 85, no. 5, pp. 713–722, 2011, ISSN: 0038-092X. DOI: 10.1016/j.solener.2010.12.022.

[136] M. Bashahu and P. Nkundabakura, "Review and tests of methods for the determination of the solar cell junction ideality factors," *Solar Energy*, vol. 81, no. 7, pp. 856–863, 2007, ISSN: 0038-092X. DOI: 10.1016/j.solener.2006.11.002.

[137] Y. J. Maa and I. M. Abdel-Motaleb, "Analysis of the diode characteristics using the thermodynamic theories," *Solid-State Electronics*, vol. 46, no. 5, pp. 735–742, 2002, ISSN: 0038-1101. DOI: 10.1016/S0038-1101(00)00199-4.

[138] Y. B. Acharya, "Effect of temperature dependence of band gap and device constant on IV characteristics of junction diode," *Solid-State Electronics*, vol. 45, no. 7, pp. 1115–1119, 2001, ISSN: 0038-1101. DOI: 10.1016/S0038-1101(01)00139-3.

[139] S. Zhu, R. L. Van Meirhaeghe, C. Detavernier, F. Cardon, G.-P. Ru, X.-P. Qu, and B.-Z. Li, "Barrier height inhomogeneities of epitaxial CoSi2 Schottky contacts on n-Si (100) and (111)," *Solid-State Electronics*, vol. 44, no. 4, pp. 663–671, 2000, ISSN: 0038-1101. DOI: 10.1016/S0038-1101(99)00268-3.

[140] J. R. Sites and P. H. Mauk, "Diode quality factor determination for thin-film solar cells," *Solar Cells*, vol. 27, no. 1, pp. 411–417, 1989, ISSN: 0379-6787. DOI: 10.1016/0379-6787(89)90050-1.

[141] M. Müller, J. Wienold, W. D. Walker, and L. M. Reindl, "Characterization of indoor photovoltaic devices and light," in *IEEE Photovoltaic Specialists Conference*, IEEE, 2009, pp. 000 738–000 743, ISBN: 978-1-4244-2950-9. DOI: 10.1109/PVSC.2009.5411178.

[142] I. Corporation, *SLMD960H12L: IXOLAR High Efficiency SolarMD*, 2010.

[143] NREL, *Reference Air Mass 1.5 Spectra*, 2012.

[144] R. G. Vaughan, *Radiance Calculator program*.

[145] M. Masoudinejad, J. Emmerich, D. Kossmann, A. Riesner, M. Roidl, and M. ten Hompel, "Development of a measurement platform for indoor photovoltaic energy harvesting in materials handling applications," in *6th International Renewable Energy Congress*, 2015, pp. 1–6, ISBN: 978-1-4799-7947-9. DOI: 10.1109/IREC.2015.7110938.

[146] M. Masoudinejad, "Data-sets for indoor photovoltaic behavior in low lighting conditions," *Data*, vol. 5, no. 2, p. 32, 2020, Number: 2 Publisher: Multidisciplinary Digital Publishing Institute. DOI: 10.3390/data5020032. [Online]. Available: https://www.mdpi.com/2306-5729/5/2/32.

[147] Maxim Integrated, *MAX44009 Ambient Light Sensor Datasheet*, 2011.

[148] ams AG, *TSL2561 Ambient Light Sensor Datasheet*, 2018.

[149] Microchip Technology Inc, *MCP9808 Digital Temperature Sensor Datasheet*, 2011.

[150] M. Masoudinejad, *Data-sets for indoor photovoltaic behavior in low lighting condition*, type: dataset, Mar. 4, 2020. DOI: 10.5281/zenodo.3697105. [Online]. Available: https://zenodo.org/record/3697105.

[151] A. Jain and A. Kapoor, "A new method to determine the diode ideality factor of real solar cell using Lambert W-function," *Solar Energy Materials and Solar Cells*, vol. 85, no. 3, pp. 391–396, 2005, ISSN: 0927-0248. DOI: 10.1016/j.solmat.2004.05.022.

[152] N. Santakrus Singh, A. Jain, and A. Kapoor, "Determination of the solar cell junction ideality factor using special trans function theory (STFT)," *Solar Energy Materials and Solar Cells*, vol. 93, no. 8, pp. 1423–1426, 2009, ISSN: 0927-0248. DOI: 10.1016/j.solmat.2009.03.013.

[153] D. C. Wu, J. C. Shiao, C. H. Lin, C. H. Chen, C. H. Liao, W. C. Hsu, W. H. Lu, and C. W. Lan, "Fundamental parameters extraction from dark I-V characteristics: A comprehensive study on amorphous/crystalline silicon hetero-junction solar cell," in *IEEE Photovoltaic Specialists Conference*, IEEE, 2010, pp. 2751–2755, ISBN: 978-1-4244-5891-2. DOI: 10.1109/PVSC.2010.5616817.

[154] C. Zhang, J. Zhang, Y. Hao, Z. Lin, and C. Zhu, "A simple and efficient solar cell parameter extraction method from a single current-voltage curve," *Journal of Applied Physics*, vol. 110, no. 6, p. 064 504, 2011, ISSN: 0021-8979. DOI: 10.1063/1.3632971.

[155] H. Zhao, Q. Wu, S. Hu, H. Xu, and C. N. Rasmussen, "Review of energy storage system for wind power integration support," *Applied Energy*, vol. 137, pp. 545–553, 2015, ISSN: 0306-2619. DOI: 10.1016/j.apenergy.2014.04.103.

[156] K. S. Hariharan, P. Tagade, and S. Ramachandran, *Mathematical Modeling of Lithium Batteries: From Electrochemical Models to State Estimator Algorithms*. Springer International Publishing, 2018, ISBN: 978-3-319-03526-0.

[157] J. Hester, N. Tobias, A. Rahmati, L. Sitanayah, D. Holcomb, K. Fu, W. P. Burleson, and J. Sorber, "Persistent Clocks for Batteryless Sensing Devices," *ACM Trans. Embed. Comput. Syst.*, vol. 15, no. 4, 77:1–77:28, 2016, ISSN: 1539-9087. DOI: 10.1145/2903140.

[158] D. Briand, E. Yeatman, S. Roundy, O. Brand, G. K. Fedder, C. Hierold, J. G. Korvink, and O. Tabata, *Micro Energy Harvesting*. John Wiley & Sons, 2015, ISBN: 978-3-527-31902-2.

[159] C. Julien, A. Mauger, A. Vijh, and K. Zaghib, *Lithium Batteries: Science and Technology*. Springer, 2015, ISBN: 978-3-319-19108-9.

[160] S. Priya and D. J. Inman, *Energy Harvesting Technologies*. 2009, ISBN: 978-0-387-76463-4.

[161] M. T. Penella-López and M. Gasulla-Forner, *Powering Autonomous Sensors*. Dordrecht: Springer Netherlands, 2011, ISBN: 978-94-007-1572-1 978-94-007-1573-8.

[162] G. L. Plett, "Extended Kalman filtering for battery management systems of LiPB-based HEV battery packs: Part 2. Modeling and identification," *Journal of Power Sources*, vol. 134, no. 2, pp. 262–276, 2004, ISSN: 0378-7753. DOI: 10.1016/j.jpowsour.2004.02.032.

[163] W. Waag, C. Fleischer, and D. U. Sauer, "Critical review of the methods for monitoring of lithium-ion batteries in electric and hybrid vehicles," *Journal of Power Sources*, vol. 258, pp. 321–339, 2014, ISSN: 0378-7753. DOI: 10.1016/j.jpowsour.2014.02.064.

[164] T. Reddy, *Linden's Handbook of Batteries*, 4 edition. New York: McGraw-Hill Education, 2010, ISBN: 978-0-07-162421-3.

[165] M. R. Jongerden and B. R. Haverkort, "Which battery model to use?" *IET Software*, vol. 3, no. 6, pp. 445–457, 2009, ISSN: 1751-8806. DOI: 10.1049/iet-sen.2009.0001.

[166] R. Rao, S. Vrudhula, and D. N. Rakhmatov, "Battery modeling for energy aware system design," *Computer*, vol. 36, no. 12, pp. 77–87, 2003, ISSN: 0018-9162. DOI: 10.1109/MC.2003.1250886.

[167] A. Hausmann and C. Depcik, "Expanding the Peukert equation for battery capacity modeling through inclusion of a temperature dependency," *Journal of Power Sources*, vol. 235, pp. 148–158, 2013, ISSN: 0378-7753. DOI: 10.1016/j.jpowsour.2013.01.174.

[168] P. Marwedel, *Embedded System Design: Embedded Systems Foundations of Cyber-Physical Systems, and the Internet of Things*. Springer, 2017, ISBN: 978-3-319-56045-8.

[169] C. M. Shepherd, "Design of Primary and Secondary Cells II . An Equation Describing Battery Discharge," *Journal of The Electrochemical Society*, vol. 112, no. 7, pp. 657–664, 1965, ISSN: 0013-4651, 1945-7111. DOI: 10.1149/1.2423659.

[170] S. Moore and M. Eshani, "An Empirically Based Electrosource Horizon Lead-Acid Battery Model," SAE International, Warrendale, PA, SAE Technical Paper 960448, 1996. DOI: 10.4271/960448.

[171] L. E. Unnewehr and S. A. Nasar, *Electric Vehicle Technology*. New York: Wiley, 1982, ISBN: 978-0-471-08378-8.

[172] L. E. Unnewehr and C. W. Knoop, "Electrical Component Modeling and Sizing for EV Simulation," SAE International, Warrendale, PA, SAE Technical Paper 780215, 1978. DOI: 10.4271/780215.

[173] J. Manwell and J. McGowan, "Extension of the kinetic battery model for wind/hybrid power systems," *Proceedings of EWEC*, pp. 284–289, 1994.

[174] H. Fang, X. Zhao, Y. Wang, Z. Sahinoglu, T. Wada, S. Hara, and R. A. d. Callafon, "State-of-charge estimation for batteries: A multi-

model approach," in *American Control Conference*, 2014, pp. 2779–2785. DOI: 10.1109/ACC.2014.6858976.

[175] J. Meng, G. Luo, M. Ricco, M. Swierczynski, D.-I. Stroe, and R. Teodorescu, "Overview of Lithium-Ion Battery Modeling Methods for State-of-Charge Estimation in Electrical Vehicles," *Applied Sciences-Basel*, vol. 8, no. 5, p. 659, 2018, ISSN: 2076-3417. DOI: 10.3390/app8050659.

[176] T. Kim and W. Qiao, "A Hybrid Battery Model Capable of Capturing Dynamic Circuit Characteristics and Nonlinear Capacity Effects," *IEEE Transactions on Energy Conversion*, vol. 26, no. 4, pp. 1172–1180, 2011, ISSN: 0885-8969. DOI: 10.1109/TEC.2011.2167014.

[177] M. Doyle, T. F. Fuller, and J. Newman, "Modelling the Galvanostatic Charge and Discharge of the Lithium/Polymer/Insertion Cell," *Journal of the Electrochemical Society*, vol. 140, no. 6, pp. 1526–1533, 1992.

[178] J. Newman, *FORTRAN Programs for the Simulation of Electrochemical Systems*, 1998.

[179] J. F. Manwell and J. G. McGowan, "Lead acid battery storage model for hybrid energy systems," *Solar Energy*, vol. 50, no. 5, pp. 399–405, 1993.

[180] D. N. Rakhmatov and S. B. K. Vrudhula, "An Analytical High-level Battery Model for Use in Energy Management of Portable Electronic Systems," in *IEEE/ACM International Conference on Computer-aided Design*, ser. ICCAD '01, Piscataway, NJ, USA: IEEE Press, 2001, pp. 488–493, ISBN: 978-0-7803-7249-8.

[181] H. He, R. Xiong, and J. Fan, "Evaluation of Lithium-Ion Battery Equivalent Circuit Models for State of Charge Estimation by an Experimental Approach," *Energies*, vol. 4, no. 4, pp. 582–598, 2011. DOI: 10.3390/en4040582.

[182] J. Meng, M. Ricco, G. Luo, M. Swierczynski, D. Stroe, A. Stroe, and R. Teodorescu, "An Overview and Comparison of Online Implementable SOC Estimation Methods for Lithium-Ion Battery," *IEEE Transactions on Industry Applications*, vol. 54, no. 2, pp. 1583–1591, 2018, ISSN: 0093-9994. DOI: 10.1109/TIA.2017.2775179.

[183] F. Jin, H. Yongling, and W. Guofu, "Comparison Study of Equivalent Circuit Model of Li-Ion Battery for Electrical Vehicles," *Research Journal of Applied Sciences, Engineering and Technology*, vol. 6, no. 20, 2013, ISSN: 2040-7467.

[184] C. Gould, J. Wang, D. Stone, and M. Foster, "EV/HEV Li-ion battery modelling and State-of-Function determination," in *Automation and Motion International Symposium on Power Electronics Power Electronics, Electrical Drives*, 2012, pp. 353–358. DOI: 10.1109/SPEEDAM.2012.6264616.

[185] L. Tao, J. Ma, Y. Cheng, A. Noktehdan, J. Chong, and C. Lu, "A review of stochastic battery models and health management," *Renewable and*

Sustainable Energy Reviews, vol. 80, pp. 716–732, 2017, ISSN: 1364-0321. DOI: 10.1016/j.rser.2017.05.127.

[186] I. Kaj and V. Konané, "Modeling battery cells under discharge using kinetic and stochastic battery models," *Applied Mathematical Modelling*, vol. 40, no. 17, pp. 7901–7915, 2016, ISSN: 0307-904X. DOI: 10.1016/j.apm.2016.03.049.

[187] D. Panigrahi, C. Chiasserini, S. Dey, R. Rao, A. Raghunathan, and K. Lahiri, "Battery life estimation of mobile embedded systems," in *14th International Conference on VLSI Design*, 2001, pp. 57–63. DOI: 10.1109/ICVD.2001.902640.

[188] C. Chiasserini and R. R. Rao, "Energy efficient battery management," *IEEE Journal on Selected Areas in Communications*, vol. 19, no. 7, pp. 1235–1245, 2001, ISSN: 0733-8716. DOI: 10.1109/49.932692.

[189] V. Pop, H. J. Bergveld, D. Danilov, P. P. L. Regtien, and P. H. L. Notten, *Battery Management Systems: Accurate State-of-Charge Indication for Battery-Powered Applications*. Springer Science & Business Media, 2008, ISBN: 978-1-4020-6945-1.

[190] C. Unterrieder, M. Lunglmayr, S. Marsili, and M. Huemer, "Battery state-of-charge estimation using polynomial enhanced prediction," *Electronics Letters*, vol. 48, no. 21, pp. 1363–1365, 2012, ISSN: 0013-5194. DOI: 10.1049/el.2012.2773.

[191] W. Waag and D. U. Sauer, "Adaptive estimation of the electromotive force of the lithium-ion battery after current interruption for an accurate state-of-charge and capacity determination," *Applied Energy*, vol. 111, pp. 416–427, 2013, ISSN: 0306-2619. DOI: 10.1016/j.apenergy.2013.05.001.

[192] J. H. Aylor, A. Thieme, and B. W. Johnso, "A battery state-of-charge indicator for electric wheelchairs," *IEEE Transactions on Industrial Electronics*, vol. 39, no. 5, pp. 398–409, 1992, ISSN: 0278-0046. DOI: 10.1109/41.161471.

[193] S. Haykin, *Kalman Filtering and Neural Networks*. John Wiley & Sons, 2004, ISBN: 978-0-471-46421-1.

[194] J. Meng, G. Luo, and F. Gao, "Lithium Polymer Battery State-of-Charge Estimation Based on Adaptive Unscented Kalman Filter and Support Vector Machine," *IEEE Transactions on Power Electronics*, vol. 31, no. 3, pp. 2226–2238, 2016, ISSN: 0885-8993. DOI: 10.1109/TPEL.2015.2439578.

[195] M. Jinhao, "A Simplified Model based State-of-Charge Estimation Approach for Lithium-ion Battery with Dynamic Linear Model," *IEEE Transactions on Industrial Electronics*, 2019, ISSN: 0278-0046.

[196] X. Cui, Z. He, E. Li, A. Cheng, M. Luo, and Y. Guo, "State-of-charge estimation of power lithium-ion batteries based on an embedded micro control unit using a square root cubature Kalman filter at various

ambient temperatures," *International Journal of Energy Research*, vol. 0, no. 0, 2019, ISSN: 1099-114X. DOI: 10.1002/er.4503.

[197] L. Zheng, J. Zhu, G. Wang, D. D.-C. Lu, and T. He, "Differential voltage analysis based state of charge estimation methods for lithium-ion batteries using extended Kalman filter and particle filter," *Energy*, vol. 158, pp. 1028–1037, 2018, ISSN: 0360-5442. DOI: 10.1016/j.energy.2018.06.113.

[198] B. Xia, Z. Zhang, Z. Lao, W. Wang, W. Sun, Y. Lai, and M. Wang, "Strong Tracking of a H-Infinity Filter in Lithium-Ion Battery State of Charge Estimation," *Energies*, vol. 11, no. 6, p. 1481, 2018. DOI: 10.3390/en11061481.

[199] Z. Liu, X. Dang, and H. Sun, "Online State of Charge Estimation for Lithium-Ion Battery by Combining Incremental Autoregressive and Moving Average Modeling with Adaptive H-Infinity Filter," *Mathematical Problems in Engineering*, vol. 2018, pp. 1–16, 2018, ISSN: 1024-123X, 1563-5147. DOI: 10.1155/2018/7480602.

[200] C. Chen, R. Xiong, and W. Shen, "A Lithium-Ion Battery-in-the-Loop Approach to Test and Validate Multiscale Dual H Infinity Filters for State-of-Charge and Capacity Estimation," *IEEE Transactions on Power Electronics*, vol. 33, no. 1, pp. 332–342, 2018, ISSN: 0885-8993. DOI: 10.1109/TPEL.2017.2670081.

[201] M. Ye, H. Guo, R. Xiong, and Q. Yu, "A double-scale and adaptive particle filter-based online parameter and state of charge estimation method for lithium-ion batteries," *Energy*, vol. 144, pp. 789–799, 2018, ISSN: 0360-5442. DOI: 10.1016/j.energy.2017.12.061.

[202] C. Sbarufatti, M. Corbetta, M. Giglio, and F. Cadini, "Adaptive prognosis of lithium-ion batteries based on the combination of particle filters and radial basis function neural networks," *Journal of Power Sources*, vol. 344, pp. 128–140, 2017, ISSN: 0378-7753. DOI: 10.1016/j.jpowsour.2017.01.105.

[203] B. Xiong, J. Zhao, Y. Su, Z. Wei, and M. Skyllas-Kazacos, "State of Charge Estimation of Vanadium Redox Flow Battery Based on Sliding Mode Observer and Dynamic Model Including Capacity Fading Factor," *IEEE Transactions on Sustainable Energy*, vol. 8, no. 4, pp. 1658–1667, 2017, ISSN: 1949-3029. DOI: 10.1109/TSTE.2017.2699288.

[204] J. Du, Z. Liu, Y. Wang, and C. Wen, "An adaptive sliding mode observer for lithium-ion battery state of charge and state of health estimation in electric vehicles," *Control Engineering Practice*, vol. 54, pp. 81–90, 2016, ISSN: 0967-0661. DOI: 10.1016/j.conengprac.2016.05.014.

[205] J. Klee Barillas, J. Li, C. Günther, and M. A. Danzer, "A comparative study and validation of state estimation algorithms for Li-ion batteries in battery management systems," *Applied Energy*, vol. 155, pp. 455–462, 2015, ISSN: 0306-2619. DOI: 10.1016/j.apenergy.2015.05.102.

[206] P. Shen, M. Ouyang, X. Han, X. Feng, L. Lu, and J. Li, "Error Analysis of the Model-Based State-of-Charge Observer for Lithium-Ion Batteries," *IEEE Transactions on Vehicular Technology*, vol. 67, no. 9, pp. 8055–8064, 2018, ISSN: 0018-9545. DOI: 10.1109/TVT.2018.2842820.

[207] D. Zhang, S. Dey, L. D. Couto, and S. J. Moura, "Battery Adaptive Observer for a Single-Particle Model With Intercalation-Induced Stress," *IEEE Transactions on Control Systems Technology*, pp. 1–15, 2019, ISSN: 1063-6536. DOI: 10.1109/TCST.2019.2910797.

[208] P. Ascencio, K. Smith, C. W. Monroe, and D. Howey, "An Adaptive Observer Design for Charge-State and Crossover Estimation in Disproportionation Redox Flow Batteries undergoing Self-Discharge," 2019. arXiv: 1903.04073 [math].

[209] H. Yin, W. Zhou, M. Li, C. Ma, and C. Zhao, "An Adaptive Fuzzy Logic-Based Energy Management Strategy on Battery/Ultracapacitor Hybrid Electric Vehicles," *IEEE Transactions on Transportation Electrification*, vol. 2, no. 3, pp. 300–311, 2016, ISSN: 2372-2088. DOI: 10.1109/TTE.2016.2552721.

[210] A. J. Salkind, C. Fennie, P. Singh, T. Atwater, and D. E. Reisner, "Determination of state-of-charge and state-of-health of batteries by fuzzy logic methodology," *Journal of Power Sources*, vol. 80, no. 1, pp. 293–300, 1999, ISSN: 0378-7753. DOI: 10.1016/S0378-7753(99)00079-8.

[211] P. Singh, C. Fennie, and D. Reisner, "Fuzzy logic modelling of state-of-charge and available capacity of nickel/metal hydride batteries," *Journal of Power Sources*, Selected papers presented at the International Power Sources Symposium, vol. 136, no. 2, pp. 322–333, 2004, ISSN: 0378-7753. DOI: 10.1016/j.jpowsour.2004.03.035.

[212] C. Piao, X. Yang, C. Teng, and H. Yang, "An improved model based on artificial neural networks and Thevenin model for nickel metal hydride power battery," in *International Conference on Optics, Photonics and Energy Engineering (OPEE)*, vol. 1, 2010, pp. 115–118. DOI: 10.1109/OPEE.2010.5508184.

[213] T. Hansen and C.-J. Wang, "Support vector based battery state of charge estimator," *Journal of Power Sources*, vol. 141, no. 2, pp. 351–358, 2005, ISSN: 0378-7753. DOI: 10.1016/j.jpowsour.2004.09.020.

[214] J. C. Álvarez Antón, P. J. García Nieto, F. J. de Cos Juez, F. Sánchez Lasheras, M. González Vega, and M. N. Roqueñí Gutiérrez, "Battery state-of-charge estimator using the SVM technique," *Applied Mathematical Modelling*, vol. 37, no. 9, pp. 6244–6253, 2013, ISSN: 0307-904X. DOI: 10.1016/j.apm.2013.01.024.

[215] A. Zenati, P. Desprez, and H. Razik, "Estimation of the SOC and the SOH of li-ion batteries, by combining impedance measurements with the fuzzy logic inference," in *36th Annual Conference on IEEE Industrial*

Electronics Society, 2010, pp. 1773–1778. DOI: 10.1109/IECON.2010.5675408.

[216] S. Han and W. Chen, "The Algorithm of Dynamic Battery SOC Based on Mamdani Fuzzy Reasoning," in *5th International Conference on Fuzzy Systems and Knowledge Discovery*, vol. 1, 2008, pp. 439–443. DOI: 10.1109/FSKD.2008.166.

[217] M. Buschhoff, D. Friesel, and O. Spinczyk, "Energy Models in the Loop," *Procedia Computer Science*, The 9th International Conference on Ambient Systems, Networks and Technologies (ANT 2018) / The 8th International Conference on Sustainable Energy Information Technology (SEIT-2018) / Affiliated Workshops, vol. 130, pp. 1063–1068, 2018, ISSN: 1877-0509. DOI: 10.1016/j.procs.2018.04.154.

[218] Texas Instruments, *MSP430FR596x, MSP430FR594x Mixed-Signal Microcontrollers*, 2018.

[219] G. L. Plett, *Battery Management Systems, Volume I: Battery Modeling*. Artech House, 2015, ISBN: 978-1-63081-024-5.

[220] ——, "Extended Kalman filtering for battery management systems of LiPB-based HEV battery packs: Part 1. Background," *Journal of Power Sources*, vol. 134, no. 2, pp. 252–261, 2004, ISSN: 0378-7753. DOI: 10.1016/j.jpowsour.2004.02.031.

[221] D. Ma and R. Bondade, *Reconfigurable Switched-Capacitor Power Converters: Principles and Designs for Self-Powered Microsystems*. Springer Science & Business Media, 2012, ISBN: 978-1-4614-4187-8.

[222] M. Wens and M. Steyaert, *Design and Implementation of Fully-Integrated Inductive DC-DC Converters in Standard CMOS*. Springer, 2011.

[223] R. W. Erickson and D. Maksimovic, *Fundamentals of Power Electronics*, 2nd. Springer, 2012, ISBN: 978-1-4757-0559-1.

[224] S. Jaunay and J. Brown, "DC-to-DC Design Guide," *Vishay Siliconix, Application Note AN607*, 2002.

[225] A. J. Stratakos, "High-Efficiency Low-Voltage DC-DC Conversion for Portable Applications," Ph.D. dissertation, 1998.

[226] B. P. Schweitzer and A. B. Rosenstein, "Free Running-Switching Mode Power Regulator: Analysis and Design," *IEEE Transactions on Aerospace*, vol. 2, no. 4, pp. 1171–1180, 1964, ISSN: 0536-1516. DOI: 10.1109/TA.1964.4319737.

[227] R. Redl and J. Sun, "Ripple-Based Control of Switching Regulators - An Overview," *IEEE Transactions on Power Electronics*, vol. 24, no. 12, pp. 2669–2680, 2009, ISSN: 0885-8993. DOI: 10.1109/TPEL.2009.2032657.

[228] E. J. Carlson, K. Strunz, and B. P. Otis, "A 20 mV Input Boost Converter With Efficient Digital Control for Thermoelectric Energy Harvesting," *IEEE Journal of Solid-State Circuits*, vol. 45, no. 4, pp. 741–750, 2010, ISSN: 0018-9200. DOI: 10.1109/JSSC.2010.2042251.

[229] Linear Technology, *LTC3107: Ultra-Low Voltage Energy Harvester and Primary Battery Life Extender*, 2013.

[230] ——, *LTC3108: Ultralow Voltage Step-Up Converter and Power Manager*, 2010.

[231] ——, *LTC3588-1: Nanopower Energy Harvesting Power Supply*, 2010.

[232] ROHM Co., Ltd., *BD70522GUL: Ultra Low Iq Buck Converter For Low Power Applications*, 2017.

[233] EM Microelectronic-Marin, *EM8900: Ultra-low voltage DC-DC boost converter for thermal electrical generators*, 2017.

[234] A. Gomez, L. Sigrist, M. Magno, L. Benini, and L. Thiele, "Dynamic Energy Burst Scaling for Transiently Powered Systems," in *Conference on Design, Automation & Test in Europe*, ser. DATE '16, San Jose, CA, USA: EDA Consortium, 2016, pp. 349–354, ISBN: 978-3-9815370-6-2.

[235] R. A. Kjellby, L. R. Cenkeramaddi, T. E. Johnsrud, S. E. Løtveit, G. Jevne, B. Beferull-Lozano, and S. J, "Self-powered IoT Device based on Energy Harvesting for Remote Applications," in *2018 IEEE International Conference on Advanced Networks and Telecommunications Systems (ANTS)*, 2018, pp. 1–4. DOI: 10.1109/ANTS.2018.8710171.

[236] Q. Zhang, T. Lin, and J. Yang, "The acquisition and analysis of vibration energy signal generated by magnetic shape memory alloys," in *29th Chinese Control And Decision Conference (CCDC)*, 2017, pp. 7019–7022. DOI: 10.1109/CCDC.2017.7978447.

[237] Y. Ramadass, "Powering the internet of things," in *IEEE Hot Chips 26 Symposium (HCS)*, 2014, pp. 1–50. DOI: 10.1109/HOTCHIPS.2014.7478800.

[238] H. W. Pflug, H. J. Visser, and S. Keyrouz, "Practical applications of radiative wireless power transfer," in *IEEE Wireless Power Transfer Conference (WPTC)*, 2015, pp. 1–4. DOI: 10.1109/WPT.2015.7140131.

[239] M. Paoli, D. Spenza, C. Petrioli, M. Magno, and L. Benini, "Poster Abstract: MagoNode++ - A Wake-Up-Radio-Enabled Wireless Sensor Mote for Energy-Neutral Applications," in *15th ACM/IEEE International Conference on Information Processing in Sensor Networks (IPSN)*, 2016, pp. 1–2. DOI: 10.1109/IPSN.2016.7460708.

[240] I. Doms, P. Merken, R. Mertens, and C. V. Hoof, "Integrated capacitive power-management circuit for thermal harvesters with output power 10 to 1000 uW," in *IEEE International Solid-State Circuits Conference - Digest of Technical Papers*, 2009, 300–301, 301a. DOI: 10.1109/ISSCC.2009.4977427.

[241] Y. Qiu, C. V. Liempd, B. O. h. Veld, P. G. Blanken, and C. V. Hoof, "5 uW-to-10mW input power range inductive boost converter for indoor photovoltaic energy harvesting with integrated maximum power point tracking algorithm," in *2011 IEEE International Solid-State Circuits Conference*, 2011, pp. 118–120. DOI: 10.1109/ISSCC.2011.5746245.

[242] S. Bandyopadhyay, P. P. Mercier, A. C. Lysaght, K. M. Stankovic, and A. P. Chandrakasan, "A 1.1 nW Energy-Harvesting System with 544 pW Quiescent Power for Next-Generation Implants," *IEEE Journal of Solid-State Circuits*, vol. 49, no. 12, pp. 2812–2824, 2014, ISSN: 0018-9200. DOI: 10.1109/JSSC.2014.2350260.

[243] K. Kadirvel, Y. Ramadass, U. Lyles, J. Carpenter, V. Ivanov, V. McNeil, A. Chandrakasan, and B. Lum-Shue-Chan, "A 330nA energy-harvesting charger with battery management for solar and thermoelectric energy harvesting," in *IEEE International Solid-State Circuits Conference*, 2012, pp. 106–108. DOI: 10.1109/ISSCC.2012.6176896.

[244] Cypress Semiconductor Corporation, *MB39C831:Ultra Low Voltage Boost PMIC for Solar/Thermal Energy Harvesting*, 2017.

[245] Texas Instruments, *BQ25504: Ultra Low-Power Boost Converter With Battery Management for Energy Harvester Applications*, 2015.

[246] ——, *BQ25505: Ultra Low-Power Boost Charger With Battery Management and Autonomous Power Multiplexer for Primary Battery in Energy Harvester Applications*, 2015.

[247] ——, *BQ25570: Ultra Low-Power Boost Charger With Battery Management and Autonomous Power Multiplexer for Primary Battery in Energy Harvester Applications*, 2015.

[248] Linear Technology, *LTC3105: 400mA Step-Up DC/DC Converter with Maximum Power Point Control and 250mV Start-Up*, 2010.

[249] ——, *LTC3106: 300mA Low Voltage Buck-Boost Converter with PowerPath and 1.6μA Quiescent Current*, 2015.

[250] ST Microelectronics, *SPV1050: Ultralow power energy harvester and battery charger*, 2015.

[251] R. D. Middlebrook and S. Cuk, "A general unified approach to modelling switching-converter power stages," in *IEEE Power Electronics Specialists Conference*, 1976, pp. 18–34. DOI: 10.1109/PESC.1976.7072895.

[252] R. D. Middlebrook and S. Cuk, "A general unified approach to modelling switching-converter power stages," *International Journal of Electronics*, vol. 42, no. 6, pp. 521–550, 1977, ISSN: 0020-7217. DOI: 10.1080/00207217708900678.

[253] S. Cuk and R. D. Middlebrook, "A general unified approach to modelling switching DC-to-DC converters in discontinuous conduction mode," in *IEEE Power Electronics Specialists Conference*, 1977, pp. 36–57. DOI: 10.1109/PESC.1977.7070802.

[254] M. Wens and M. Steyaert, "Basic DC-DC Converter Theory," in *Design and Implementation of Fully-Integrated Inductive DC-DC Converters in Standard CMOS*, ser. Analog Circuits and Signal Processing, Springer Netherlands, 2011, pp. 27–63, ISBN: 978-94-007-1435-9 978-94-007-1436-6. DOI: 10.1007/978-94-007-1436-6_2.

[255] M. Telefus, A. Shteynberg, M. Ferdowsi, and A. Emadi, "Pulse Train, a novel digital control method, applied to a discontinuous conduction mode flyback converter," in *IEEE 34th Annual Power Electronics Specialist Conference*, vol. 3, 2003, 1141–1146 vol.3. DOI: 10.1109/PESC.2003.1216609.

[256] ——, "Pulse Train control technique for flyback converter," *IEEE Transactions on Power Electronics*, vol. 19, no. 3, pp. 757–764, 2004, ISSN: 0885-8993. DOI: 10.1109/TPEL.2004.826498.

[257] M. Ferdowsi and A. Emadi, "Pulse regulation control technique for flyback converter," in *Nineteenth Annual IEEE Applied Power Electronics Conference and Exposition, 2004. APEC '04*, vol. 3, 2004, 1745–1750 Vol.3. DOI: 10.1109/APEC.2004.1296102.

[258] G. Zhou, W. Tan, S. Zhou, Y. Wang, and X. Ye, "Analysis of Pulse Train Controlled PCCM Boost Converter With Low Frequency Oscillation Suppression," *IEEE Access*, vol. 6, pp. 68 795–68 803, 2018, ISSN: 2169-3536. DOI: 10.1109/ACCESS.2018.2879888.

[259] J. Sha, J. Xu, B. Bao, and T. Yan, "Effects of Circuit Parameters on Dynamics of Current-Mode-Pulse-Train-Controlled Buck Converter," *IEEE Transactions on Industrial Electronics*, vol. 61, no. 3, pp. 1562–1573, 2014, ISSN: 0278-0046. DOI: 10.1109/TIE.2013.2257145.

[260] J. Xu and M. Qin, "Multi-pulse train control technique for buck converter in discontinuous conduction mode," *IET Power Electronics*, vol. 3, no. 3, pp. 391–399, 2010, ISSN: 1755-4535. DOI: 10.1049/iet-pel.2009.0038.

[261] M. Masoudinejad, A. K. Ramachandran Venkatapathy, D. Tondorf, D. Heinrich, R. Falkenberg, and M. Buschhoff, "Machine Learning Based Indoor Localisation Using Environmental Data in PhyNetLab Warehouse," in *European Conference on Smart Objects, Systems and Technologies (Smart SysTech)*, 2018, pp. 1–8.

[262] F. Zeidler, *Beitrag zur Selbststeuerung cyberphysischer Produktionssysteme in der auftragsbezogenen Fertigung*. Praxiswissen Service, 2019, ISBN: 978-3-86975-149-8.

[263] Solems, *Solems thin-film solar cells for low and high illumination leaflet*, 2017.

[264] M. Masoudinejad, M. Magno, L. Benini, and M. ten Hompel, "Average Modelling of State-of-the-Art Ultra-low Power Energy Harvesting Converter IC," in *2018 International Symposium on Power Electronics, Electrical Drives, Automation and Motion (SPEEDAM)*, 2018, pp. 99–104. DOI: 10.1109/SPEEDAM.2018.8445303.

[265] M. Masoudinejad, *Large Signal Converter Data from Texas Instruments BQ25505*, 2018. DOI: 10.17877/fd72o6mn0g.

[266] ——, *Large Signal Converter Data from Texas Instruments BQ25570*, 2018. DOI: 10.17877/fd72wij6yo.

[267] ——, *Models and training datasets for texas instruments BQ25505 and BQ25570 ICs*, type: dataset, 2018. DOI: 10.17877/FE0O0YSXS0. [Online]. Available: https://bit.ly/2XSV4BI.

[268] ——, "Power analysis of PhyNode," TU Dortmund University, 2018.

[269] ——, "Automated Data Collection for Modelling Texas Instruments Ultra Low-Power Chargers," TU Dortmund, Dortmund, Technical Report, 2017.

[270] ——, "A Power Model for DC-DC Boost Converters Operating in PFM Mode," TU Dortmund University, Tech. Rep., 2017.

[271] ——, "Photovoltaic energy harvesting characteristics under ultra-low light," TU Dortmund University, Dortmund, 2016. [Online]. Available: https://bit.ly/2PFTkHC.

[272] ——, "A measurement platform for photovoltaic energy harvesting in indoor low light environment," TU Dortmund University, Dortmund, 2015.

[273] M. Roidl, J. Emmerich, M. Masoudinejad, A. Riesner, and M. T. Hompel, "Entwicklung eines Versuchsfelds für grosse Systeme intelligenter Behälter," *Logistics Journal*, vol. 2014, 2014, ISSN: 1860-7977. DOI: 10.2195/lj_Proc_roidl_de_201411_01.